CRANFIELD UNIVERSITY

MATTHEW T RUSH

DEVELOPMENT OF WELD REPAIR METHODS FOR RENE 80 NICKEL BASED SUPERALLOY

SCHOOL OF APPLIED SCIENCES

PhD THESIS

ACADEMIC YEAR 2011-2012

SUPERVISOR: DR PAUL A COLEGROVE

MARCH 2012

CRANFIELD UNIVERSITY

School of Applied Sciences

PhD Thesis

Academic year 2011-2012

Matthew T Rush

Development of weld repair methods for Rene 80 nickel based superalloy

Supervisor: Dr Paul A Colegrove

March 2012

Abstract

Nickel based superalloys are an integral material for gas turbines, where their excellent high temperature mechanical properties and corrosion resistance are utilised. Due to the increasing costs of raw materials, manufacturers are interested in repairing in-service and manufacturing defects in components. Unfortunately, superalloys such as Rene 80 are highly susceptible to welding defects such as liquation cracking and post-weld heat treatment cracking, which make repair welding highly difficult.

The aim of the research in this thesis was to develop an improved understanding of welding defect production in nickel-based superalloys. In particular, the effect of repair process and its parameters were examined, with the ultimate aim to produce crack-free repair welds.

The main theme of the work involved a large parametric study of the process parameter effects on welding defects in Rene 80 using a high power fibre laser. This work determined an optimised range of parameters which reduced the incidence of cracking. Furthermore, this work also identified a key relationship between the weld bead geometry aspect ratio and the incidence of cracking. This relationship was studied using neutron diffraction to determine the differences in strain and residual stresses between two welds with identical heat input but different geometry. An in-depth investigation of the cracks within the material, identified that as-welded cracks formed via liquation of secondary phases such as carbides, γ/γ' eutectics, and secondary gamma prime. The post weld heat treatment cracks formed by the strain-age mechanism in Rene 80.

From this work, a novel repair procedure avoiding the complications associated with using lower strength filler metal was developed, based on the optimised welding parameters. Finally, a number of advanced low heat input welding processes were also investigated for repair of superalloys.

Preface

Parts of this thesis have been published in the following:

M.T. Rush, P.A. Colegrove, Z. Zhang, and D. Broad. 2012, "Liquation and post-weld heat treatment cracking in Rene 80 repair welds". *Journal of Materials Processing Technology.* (212) 188-197.

M.T. Rush, P.A. Colegrove, Z. Zhang, and B. Courtot. 2010, "An investigation into cracking in nickel-base superalloy repair welds". *Advanced Materials Research.* (89-91) 467-472.

Acknowledgements

This research was supported financially by the EPRSC and Doncasters Group Plc.

I would like to extend my eternal thanks to my supervisor, Dr Paul Colegrove, who has supported me through all the highs and lows of my PhD. He has been so generous in giving advice, support, encouragement, and his dedication to his students is without question.

A special mention must go to David Yapp who offered some very helpful suggestions throughout my research. I also acknowledge the advice of Dr Supriyo Ganguly and Prof. Stewart Williams. The technical support offered by Flemming Nielsen, Brian Brooks and David Archer is also thanked. I also acknowledge the support of Andrew Dyer with metallography issues.

Dr Zhu Zhang, David Broad and Philip Postans of Doncasters Group all provided invaluable support to allow my research to progress so I offer thanks to them. Thanks also to Luis Baptista from Doncasters Precision Castings for helping with materials and heat treatments.

The work in Chapter 2 was developed to include work completed by Benoit Courtot in his MSc thesis. I acknowledge the use of the data contained in this work.

Without the friendly atmosphere created in the Welding Research Centre at Cranfield, my research would have been more difficult. Thanks to all members past and present. Special mention to the dear friends I have made for life with whom I started and finished at Cranfield: P Almeida, W Suder, H Wang, E Assuncao, and E Costa.

And now I turn to my family who have been the rock which I have leaned on many times. My parents Kevin and Alison, my sister Naomi, and my fiancée Sarah have been inspirational throughout my studies and I thank them for all the love, encouragement, support, enthusiasm and dedication which they have given to me. I would not be where I am right now if not for them.

I dedicate this thesis to them.

Contents

List of Figures

List of Tables

Nomenclature

a	lattice parameter
d	d-spacing
D	Grain diameter
h	Plank's constant
I	Current
P	Power
R^2	Coefficient of determination
V	Voltage
V_f	Volume fraction
γ	Gamma phase
γ'	Gamma prime
γ"	Gamma double prime
δ	Delta phase
ε	Strain
η	Eta phase
ϑ	Angle of diffraction
λ	Wavelength of neutrons
σ	Sigma phase

Acronyms

ACL	Average Crack Length	GE	General Electric
ANOVA	Analysis of Variance	GTCAW	Gas Tungsten Constricted Arc Welding
AR	Aspect Ratio	HAZ	Heat Affected Zone
AW	As Welded	HF	High Frequency
BSE	Back Scattered Electron	HIP	Hot Isostatic Pressing
BTR	Brittle temperature range	LCL	Longest Crack Length
CMT	Cold Metal Transfer	LFW	Linear Friction Welding
DC	Direct Current	MIG	Metal Inert Gas
DDC	Ductility Dip Cracking	OEM	Original Equipment Manufacturer
DS	Directionally Solidified	PAW	Plasma Arc Welding
DTR	Ductile temperature range	PMZ	Partially Melted Zone
EDM	Electrical Discharge Machining	PWHT	Post Weld Heat Treatment
EDX	Energy Dispersive X-ray	SEM	Scanning Electron Microscopy
EPRI	Electric Power Research Institute	SX	Single Crystal
FCC	Face Centred Cubic	TCL	Total Crack Length
FPI	Fluorescent Penetrant Inspection	TCP	Topologically Close Packed
FSP	Friction Stir Processing	TIG	Tungsten Inert Gas
FZ	Fusion Zone	TOF	Time of Flight
GB	Grain Boundary		

Chapter 1

Introduction and Literature review

1.1 Introduction

1.1.1 Gas turbines

Gas turbines have been a revolutionary technology improving energy generation and mass transportation. There are three main uses of gas turbines: aerospace, marine, and industrial turbines for energy generation. The evolution of this technology has been driven by the need to increase operating efficiency, thus improving both performance and environmental impact. Simple thermodynamic theory shows that improved performance and efficiency of the engines can be achieved by increasing the operating temperature (Treager, 1979). The evolution of gas turbine operation is shown in Table 1.1. This table clearly shows the need for materials that can operate at high temperature and under the oxidising and corrosive environments typically found in gas turbines.

Table 1.1 – Evolution of gas turbine operation conditions (Reed, 2006).

Year of introduction	1967	1972	1979	1990	1998
Turbine inlet temperature (°C)	900	1010	1120	1260	1425
Pressure Ratio	10.5	11	14	14.5	19-23
Exhaust temperature (°C)	427	482	530	582	593
Power (MW)	50-60	60-80	70-105	165-240	165-280
Efficiency, (%)	43	46	49	53	58

The design of a typical gas turbine (see Figure 1.1) sees the temperature increase from the air intake through to the exhaust. At the air intake, lighter materials such as titanium are used to improve operating efficiency, and the temperature at this stage is also relatively low. As the combustion and compressor stages are reached, the temperature increases significantly, and the combined effect of temperature and stresses require alloys which have good creep resistance. Typical centrifugal stresses

of approximately 137 MPa (Stoloff et al., 1987) are often observed although higher centrifugal loads can occur. The development of nickel-base superalloys and advanced coating technology has helped to improve the operation of this area.

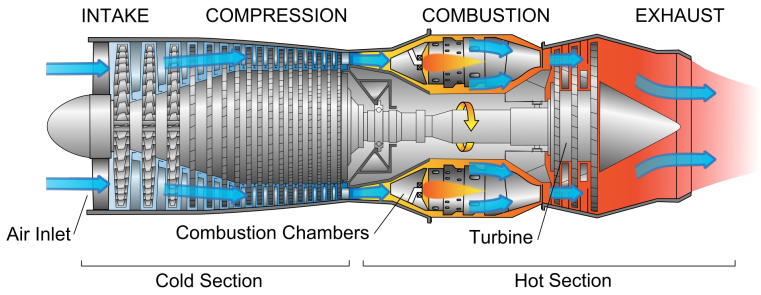

Figure 1.1 – Typical gas turbine design.

A summary of the typical materials used in each main section of a gas turbine is shown in Table 1.2

Table 1.2 – Summary of parts and materials used in gas turbine manufacture.

	Inlet	Compressor	Combustion cans	Turbines
Requirements	Impact strength, low density, fatigue and fracture strength	Creep resistance, resistance to thermal shocking	Creep resistance, oxidation resistance, thermal fatigue and buckling resistance	Creep resistance, Thermal fatigue resistance, impact strength, oxidation and corrosion resistance
Typical materials	Al alloys, Ti alloys, fibre reinforced composites	Entry - Ti alloys, Exit - Ni alloys	Ni alloys.	Ni alloys, advanced coating systems

Nickel-based superalloys were first developed during the 1940's as a material to cope with the extreme conditions of the newly invented gas turbine engines. Although it was the 1950's that saw significant development with the use of vacuum melting to produce better control of compositions (Stoloff et al., 1987). The development of gas turbines has driven the growth of superalloys into one of the largest groups of alloys, and certainly the most important high temperature and corrosion resistant material available. The alloy group has the advantages of possessing excellent creep and mechanical properties, resistance to high temperature oxidation and excellent corrosion resistance. Unfortunately they have high density (of around 8 to 9 g/cc). The cost of the raw materials used to produce the alloy is also high, with more advanced alloys using rare elements such as rhenium, hafnium and tantalum.

1.1.2 Interest in repair welding of superalloy components

Nickel base superalloys generally have poor weldability, although within the different sub-classes of this alloy (e.g. solid solution strengtheners, single crystal alloys etc) there are different problems with varying severities. The welding defects are summarised in Table 1.3. In general however, the most common issue when welding this alloy group is heat affected zone (HAZ) cracking. Cracking in the HAZ can be caused by a number of mechanisms, but the two most commonly occurring are liquation cracking, and post-weld heat treatment (PWHT) cracking (Kou, 2003b). These two defects severely affect the weldability of components made from the material, such as gas turbine components (Henderson et al., 2004). Often the component will not reach the required quality specification due to the crack formation.

Table 1.3 – Welding defects associated with Ni-based superalloys (Kou, 2003b).

Defect type	Superalloy types affected
Liquation cracking	All
PWHT cracking	Precipitation hardening alloys
Solidification cracking	All
Ductility dip cracking	Mainly solid solution, some precipitation hardened
Stray grain formation	Single crystal
Loss of strength in HAZ	Precipitation hardening alloys
Porosity	All

The combination of high raw material costs, high production costs, political pressure to increase recycling, and decreasing amount of raw material availability is leading to increasing interest in repair/rejuvenation of gas turbine components. As far back as the mid 1980s, gas turbine manufacturers have had an interest in repair of nickel-based superalloy gas turbine components (Schneider et al., 1985). A survey by TWI of gas turbine original equipment manufacturers (OEMs), repair companies and end users found that repair of superalloy components is of great current interest (Harvey, 1999; Gregori, 2003).

Recent interest in repair technologies for superalloy and gas turbine components from companies in the gas turbine sector is evident through papers by manufacturers Volvo Aero (Andersson and Sjoberg, 2012) , Siemens (Arjakine et al., 2008; Schnell et al., 2011), and Alstom (Henderson et al., 2004).

A simplified repair procedure is outlined in Figure 1.2. Although this is for a full repair of a used blade, it highlights that repair is a time consuming procedure and the weldability of the alloy is only considered for two parts of this.

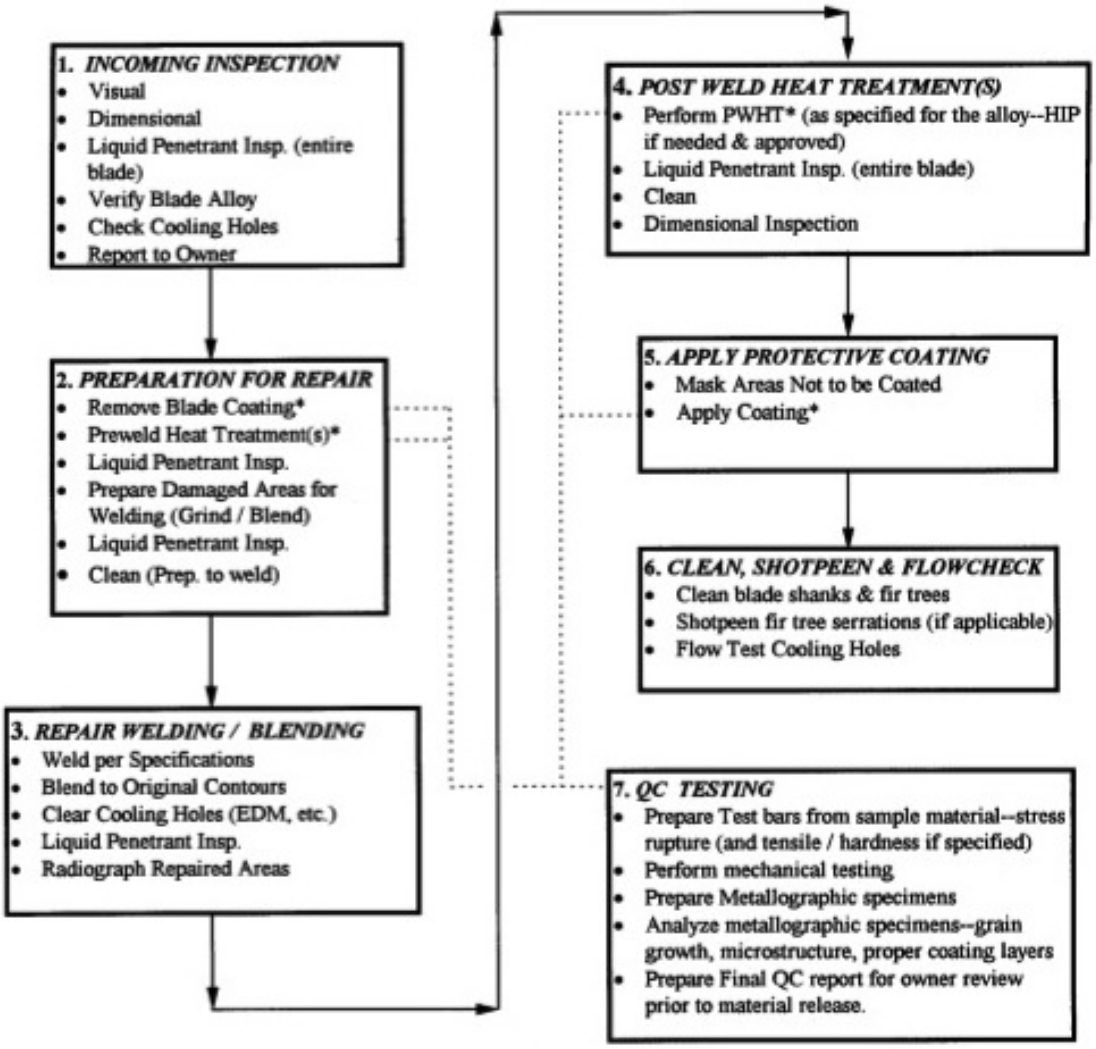

Figure 1.2 – Simplified flow diagram of a repair procedure for in-service blades as outlined by EPRI (Gandy et al., 2000).

Traditionally the interest in the weldability of nickel superalloys has been for both fabrication and manufacturing purposes and for repair of used components. Recently there has been interest in salvage repair of components that contain manufacturing defects. Examples of such defects include casting, e.g. porosities, inclusions, hot tears, cold shuts and freckles, and post casting, e.g. machining error.

Therefore, there is an increasing interest in understanding the welding metallurgy of nickel based superalloys such as Rene 80, which are considered difficult to weld due to being highly susceptible to liquation and PWHT cracking. This Chapter aims to review the literature related to nickel superalloy welding metallurgy, with more specific information on Rene 80 and similar alloys. This is followed by detailed descriptions of both liquation and PWHT cracking, together with a discussion on the impact of different factors on the defects.

1.2 Nickel base superalloy metallurgy

1.2.1 Metallurgy of superalloys used in gas turbines

Nickel has a face centred cubic (FCC) crystal structure (Callister, 2000) and has a high density compared to other commonly used metals (Table 1.4). It has a high melting point and is most commonly used in alloys, where it is found as a base element for most superalloys and in varying amounts in other important alloys e.g. steels. Most superalloys contain a combination of five to ten alloying elements such as Ti, Al, and Ta (Pollock and Tin, 2006) and typically around 40 % (weight) of the alloy is made up of these elements (Table 1.7). Superalloys are capable of stable operation at up to 80 % of their melting temperatures (Meetham, 1989; Reed, 2006).

Table 1.4 – Properties of nickel compared to other important metals (compiled from data in Callister, 2000).

	Density at 20°C (g/cc)	Crystal structure at 20°C	Melting point (°C)	Modulus of elasticity (GPa)	Yield strength (MPa)**	Tensile strength (MPa)**
Nickel	8.9	FCC	1455	207	138	480
Iron	7.87	BCC	1538	207*	130	262
Aluminium	2.71	FCC	660	69	35	90

* Value based on data for steels. ** Value based on material in annealed state

Nickel superalloys are grouped depending on their main strengthening mechanism. There are solid solution strengthened, precipitation hardened, and oxide dispersion alloys. The main mechanism for an alloy depends on the alloying elements. Typical alloying elements and their roles in nickel superalloys are shown in Table 1.5. These provide a range of phases within the alloy which are summarised in Table 1.6.

Table 1.5 – Role of alloying elements in Ni-based superalloys (Adapted from Table 2 in Gregori, 2003).

Elements	Effect on microstructure and properties
Co, Cr, Fe, Mo, W, Ta, Re	Solid solution strengthening
C, Ti, W, Mo, Ta, Nb, Hf, Cr	Carbide formers
Al, Ti	Gamma prime (γ') formers
Nb, Ta	Gamma double prime (γ") formers
Al, Cr, Y, La, Ce	Increase oxidation resistance
La, Th	Increase hot corrosion resistance
Cr, Co, Si	Increase sulphidation resistance
B, Ta	Increase creep properties
B	Improves rupture strength
B, C, Zr, Hf	Grain refiners

Table 1.6 – Phases in Ni-based superalloys (Adapted from Table 3 in Gregori, 2003).

Phase	Chemical formula (examples shown)	Temperature range (°C)	Crystal structure	Lattice parameters (Å)
Gamma (γ)	-	-	FCC	a = 3.58-3.62
Gamma prime (γ')	$Ni_3(Al,Ti)$	>600	FCC	a = 3.58-3.62
Gamma double prime (γ")	Ni_3Nb	600-920	BCT	a=3.62, c=7.41
M_6C Carbide	Fe_3Nb_3C	<630	FCC	a=10.85-11.75
M_7C_3 Carbide	Cr_7C_3	900-1050	Hexagonal	a=13.98, c=4.52
$M_{23}C_6$ Carbide	$Cr_{23}C_6$	650-950	FCC	a=10.56-10.65
MC Carbide	TiC	750-1040	Cubic	a=4.47
Boride	$(Mo_3Fe)B_2$	-	Tetragonal	-
M_2SC Sulfocarbide	(Ti,Zr)SC	-	-	-
Laves	$(Nb,Ti)(Fe,Ni,Cr)_2$	<1150	Hexagonal	a=4.74, c=7.72
η phase	$Ni_3(Ti,Nb)$	650-1000	HCP	a=5.10, c=8.31
σ phase	CrFeMoN	540-980	Tetragonal	a=8.80, c=7.70
δ phase	Ni_3Nb	750-1010	Orthorhombic	a=5.14, b=4.25

Superalloys can also be defined by the grain structure they exhibit. Directionally solidified (DS) alloys are produced using innovative casting techniques to align all the grain boundaries in a direction useful to improve the creep properties. Similarly, single crystal (SX) alloys are cast to produce a microstructure free of grain boundaries. This improves the creep resistance of the alloy (Donachie and Donachie, 2002; Reed, 2006). These alloys are less susceptible to liquation (see section 1.4.2), but present other difficulties when welding such as stray-grain formation (David et al., 1997; Babu et al., 2004).

The work contained in this thesis focuses on one particular alloy, Rene 80.

1.2.2 Metallurgy of Rene 80

Rene 80 is a precipitation hardened nickel-base superalloy developed by General Electric (GE) and patented in the 1970's (Electric, 1971). Its composition is listed in Table 1.7 together with some other superalloys. The composition of the alloy is similar to IN738, although it has a higher content of tungsten and molybdenum. By comparison, CMSX-4 (a single crystal alloy) shows significantly lower carbon and boron content – both grain boundary precipitate formers – highlighting the lack of grain boundaries. IN718, an alloy which is strengthened by gamma double prime (γ"), contains very little aluminium and titanium, but high niobium and iron.

Rene 80 was designed for higher temperature operation, and although it is designed to operate up to 980°C (Neidel et al., 2005), it has good rupture strength up to 1040°C. A comparison of the high temperature strengths of Rene 80 and other alloys is shown in Table 1.8, which indicates it has very high tensile strengths, but poorer yield strengths than competing alloys.

Table 1.7 – Composition of Rene 80 and other commonly used superalloys (weight %).

Alloy	Ni	Co	Cr	W	Mo	Al	Ti	Fe	C	Zr	B	Ta	Nb	Re	Hf	Ru	Ref
Rene 80	Bal	9.0	14.0	4	4	3	4.7	<0.35	0.15	0.01	0.015	<0.1	-	-	<0.1	-	Doncasters (2006)
IN939	Bal	19	22.5	2	-	1.9	3.7	-	0.15	0.1	-	1.4	1	-	-	-	Gregori (2003)
MarM247	Bal	10	8	10	0.6	5.5	1	-	0.15	0.03	0.015	3	-	-	1.5	-	Gregori (2003)
IN718	Bal	-	19	-	3.0	0.5	0.9	18.5	<0.08	-	-	-	5.1	-	-	-	Gregori (2003)
IN738LC	Bal	8.5	15.84	2.48	1.88	3.46	3.47	0.07	0.11	0.04	0.012	1.69	0.92	-	-	-	Egbewande et al. (2009)
TMS-162	Bal	5.8	2.9	5.8	3.9	5.8	-	-	-	-	-	5.6	-	4.9	0.09	6	Zhang et al. (2004)
CMSX-4	Bal	9.6	6.6	6.4	0.6	5.6	1	-	<60ppm	<75ppm	<30ppm	6.5	-	3	0.1	-	Gregori (2003)

Table 1.8 – Comparison of high temperature strengths of Rene 80 and other Ni-based superalloys.

	Ultimate tensile strength (MPa)			0.2% yield strength (MPa)			Elongation in 25mm (%)		
(Temperature °C)	650	760	871	650	760	871	650	760	871
IN738	1055	965	772	910	793	551	7	6.5	11
U520	1172	724	517	793	723	517	7	15	20
U500	883	855	662	703	703	600	18	9	9
IN939	986	917	641	696	634	400	7	7	18
Rene 80	1027	993	703	724	717	531	8	10	12

Rene 80 is used in aerospace and land-based turbines. It is predominantly used in the standard polycrystalline form, although a directionally solidified (DS) form has been developed and used in various weldability studies (Sidhu et al., 2009a,b; Osoba et al., 2011). The benefits of the DS form of Rene 80 were shown to be an increase of 10 % to 15 % in tensile strength, and two to four times improvement in creep rupture strength (Nakagawa et al., 1976). Note that these increases are when testing in the direction of the elongated grains.

Rene 80 consists of a high combined amount of aluminium and titanium. It also has a high ratio of titanium to aluminium compared to other alloys such as IN738LC (see Table 1.7), which according to Ross (1971) inhibits the oxidation resistance of the alloy. The high Al/Ti ratio also produces a high volume fraction of the γ' secondary precipitate, which is partly responsible for the alloy's superb high temperature strength. Rene 80 is reported to contain 49.3 % (Watanabe and Kuno, 1975) volume fraction of γ', whilst Dyrkacz (1979) reports that the GE class A heat treatment produces 47 %.

The rest of the elements act either as solid solution strengtheners, or form secondary phases such as carbides and borides. Typically Rene 80 contains (depending on the heat treatment) carbides in the form of MC type, borides in the form of M_3B_2, and sulfocarbides in the form of M_2SC (Safari and Nategh, 2006; Sidhu et al., 2009a).

1.2.2.1 Gamma phase (γ)

Rene 80, like all nickel-based superalloys, contains an austenitic gamma (γ) matrix phase which contains all elements that are in solution. It is significant that the majority of elements which are found in solution in the matrix phase have high melting temperatures. Titanium, tungsten and molybdenum are favoured for solution strengthening due to their high melting temperature, in addition to their high strengthening effect. However, if the elements are segregated at the grain boundaries then their effect is to reduce the strength (unless as part of a secondary precipitate as discussed later).

A major benefit of the solid solution elements is the increase in strength (both

at low and high temperature), which is due to dislocations being impeded. This is as a result of distortion and of differences in shear modulus within the matrix; which are caused by the solute atoms having a larger diameter than nickel (Jena and Chaturvedi, 1984). Elements with high melting points are preferred for creep resistance as they offer lower diffusivity, although this may also affect the stiffness of the alloy.

To summarise, the creep resistance of the solution strengthened gamma phase is increased for the following reasons (Jena and Chaturvedi, 1984):

1. Low diffusivity of atoms;
2. Low stacking fault energies;
3. High stiffness of solute elements.

Austenitic nickel matrices are renowned for having excellent ductility, and for the ease with which they form secondary phases such as γ' and γ" (Donachie and Donachie, 2002). They are also favourable due to their high tolerance for alloying without phase instability; their tendency (when chromium is present) to form a protective Cr_2O_3 scale which helps in lowering diffusion of oxygen into the material; and the formation (at high temperature) of an Al_2O_3 rich scale which possesses exceptional oxidation resistance. The latter is certainly of benefit in high temperature applications in an environment such as that found in a gas turbine.

1.2.2.2 Gamma prime (γ')

The gamma prime (γ') phase is an intermetallic precipitation-hardening phase, which is finely dispersed within the matrix. The compound has an ordered FCC $L1_2$ (an intermetallic crystallographic structure) form, in the style of A_3B, with A nickel, and B titanium and/or aluminium. The $L1_2$ structure is preferred over the $D0_{22}$ system (which is found as γ" in IN718 alloys) due to a higher number of slip systems, giving it higher ductility at higher temperatures (Milman et al., 2001; Wang et al., 2001), although it has limited ductility at lower temperatures. It also has more rapid precipitation kinetics than the γ" precipitate (Donachie and Donachie, 2002)

Typically, the B (e.g. Al/Ti) atoms sit at the corner points of the cube, with the A (Ni) atoms positioned in the faces, as shown in Figure 1.3. It is of benefit that these FCC crystals have identical lattice parameters (see Table 1.6) to the matrix FCC phase because the optimum strength is achieved when the precipitates are coherent with the matrix phase.

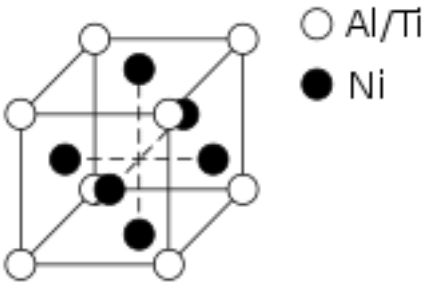

Figure 1.3 – Cubic structure of γ'.

Gamma prime can form in a number of morphologies, with spheres being the initial type and often the smallest. From this, cuboidal morphologies form, followed by distorted cubes and more commonly arrays of cubes. Often the final morphology after service or ageing is dendritic. The strengthening benefit of this phase increases with higher volume fractions (V_f) (Pollock and Tin, 2006).

1.2.2.3 Carbides

The role of carbides (see Table 1.6 for types in superalloys) is complex but necessary to achieve the required properties. There are many different types of carbides formed in superalloys. The type, morphology, and location of formation typically depends on the level of alloying additions as well as the thermal cycle during the casting process and subsequent heat treatments.

Carbides in superalloys can be any one of four types and are found to exist jointly in nearly all superalloys due to their formation through sequential reactions e.g. MC to $M_{23}C_6$ (actual reaction is more complex). Their presence in superalloys is beneficial, giving improved creep properties compared to superalloys that are just solution and precipitation strengthened (Jena and Chaturvedi, 1984).

Carbides are most advantageous when formed on grain boundaries (GBs) of equiaxed cast superalloys, although in some cases they can precipitate within the matrix phase (this is disadvantageous). They increase the creep resistance by preventing GBs from sliding and migrating (Reed, 2006). An example of improved creep performance in the alloy Nimonic 80A is reported by Betteridge and Franklin (1957), who showed that when a discrete chain of globular $M_{23}C_6$ forms on the GBs, the creep-rupture life was significantly improved.

However other studies, such as those reported by Donachie and Donachie (2002) showed that if the $M_{23}C_6$ forms as a continuous grain boundary film, the impact strength was reduced, and if MC forms as films then the rupture life and ductility was lowered. Hence it is important to ensure that the carbides, particularly MC type, form in globular form to ensure maximum benefit to the mechanical properties. Note that generally carbon and boron are eliminated from single crystal superalloys due

to the lack of grain boundaries (See CMSX-4 and TMS-162, Table 1.7).

The working temperatures of the carbides are shown in Table 1.6. During long service periods, carbide reactions can occur, for example conversion of MC to $M_{23}C_6$ at around 750 °C (see below):

$$MC + \gamma \rightarrow M_{23}C_6 + \gamma'$$

During solidification in the casting process, Rene 80 forms M(Ti)C type carbide, which according to Ross (1971) breaks down slowly during heat treatment and operation to form the M_6C and $M_{23}C_6$ grain boundary carbides.

Österle et al. (2008) found the presence (on grain boundaries) of MC type carbides enriched with Ti, Mo and W, and thin films of $M_{23}C_6$ enriched with chromium in Rene 80. Safari and Nategh (2006) reported that in Rene 80 alloys, the M_6C is formed from molybdenum, nickel, cobalt and chromium, and has a higher solutionisation temperature than $M_{23}C_6$ which confirms the order of stability discussed previously.

1.2.2.4 Other phases

The content of boron is usually lower than carbon, and typically 50-500 ppm in most superalloys. Boron usually forms borides on the GBs to improve the creep properties in a similar manner to carbides. Österle et al. (2008) found M_3B_2 particles enriched with Mo, W and Cr present in Rene 80. However, too much boron can be detrimental as it is a melting point suppressor.

Gamma double prime (γ") generally forms in nickel-iron alloys such as IN718 and IN706, particularly with greater than 5 % of niobium. It has a different structure to γ' and has more sluggish precipitation kinetics (Donachie and Donachie, 2002). As a result, alloys containing this phase are generally less prone to PWHT cracking, although the alloys are not able to operate at temperatures as high as those strengthened with γ'.

Topologically close packed (TCP) phases are undesirable phases that are less common in γ' alloys. Table 1.6 lists four examples of this phase (laves, σ, δ and η). They are a common source of crack initiation and propagation due to their effect on reducing toughness and ductility.

Sulfo-carbides are formed during the solidification of superalloys. In studies on IN100 and IN713LC, they were found in interdentric regions, which led the authors to suggest that they form as a result of carbon and sulphur segregating to the liquid alloy during solidification (Wallace et al., 1973). The particle is a crack initiation site and has been shown to reduce the tensile strength (Wallace et al., 1973).

Recent studies found sulfocarbides present in IN738LC (Ojo et al., 2006), and in directionally solidified Rene 80 (Sidhu et al., 2009a), where they were found to be

enriched with titanium and zirconium, and formed as rod shaped particles around 20 μm to 30 μm in length. These studies have also shown that the Ti-Zr rich M_2SC particles were a source of constitutional liquation in DS Rene 80 and in IN738LC.

1.2.3 Heat treatment

The reasons for heat treatments with respect to nickel-base superalloys are summarised by Safari and Nategh (2006) below:

1. Homogenising – The as-cast microstructure can suffer from chemical alloy segregation, and homogenising substantially reduces this;
2. Solution heat-treatment – This involves dissolving the coarse precipitates (γ') and the γ-γ' eutectic into the matrix phase. Both of these are products of the last stages of alloy solidification;
3. Carbide reactions – To dissociate MC type carbides from other carbides, and to form them on grain boundaries;
4. Serration - To promote grain boundary serration, which helps to enhance creep resistance;
5. Ageing – Precipitation of fine γ' from the solutionised matrix to improve strength.

For the Rene 80 alloy, there are three classes of heat treatments outlined by General Electric specification GE C50TF28, (found in Dyrkacz, 1979). Class A is a full heat treatment producing the peak strength conditioned alloy, utilising a solution treatment followed by two stage ageing (. Class B uses a solution treatment followed by one ageing cycle, producing a lower strength alloy, whilst class D is a solution cycle only. For full details of each, please see Table 1.9.

Table 1.9 – Table illustrating the different heat treatments applied to Rene 80 as outlined by Dyrkacz (1979). Note that AC stands for air cool.

Heat treatment	Class A	Class B	Class D
	Fully heat treated	Solution treated and primary age	Solution treated only
Step 1	1191 - 1204 °C, 2 hr in vacuum; furnace cool in vacuum, Ar or He to 1079 - 1107 °C within 10 mins (a, b)	Same	Same
Step 2	Hold at 1079 - 1107 °C, 4 hr in vacuum; furnace cool to 650 °C in vacuum, Ar or He within 60 mins, hold at 650 °C for 10 mins	Same	(c)
Step 3	Raise temp to 1050°C and hold for 2 to 12 hr in vacuum, Ar or He; cool to 650 °C within 15 to 60 mins, and hold at 650 °C for 10 mins (d)	Furnace or AC to room temperature	-
Step 4	Raise temp to 845 °C and hold for 16 hr in vacuum, Ar or He; furnace or AC to room temp	-	-
(a) Cooling to 650 °C within 60 mins is optional			
(b) Cooling to room temperature is optional			
(c) Continue furnace cool to 650 °C in vacuum, Ar, or He within 60 minutes; furnace or AC to room temperature			
(d) When parts are coated, the treatment is omitted			

The microstructure of Rene 80 after class A heat treatment contains approximately 47 % γ', about 2 % MC carbide, and minor amounts of M_3B_2 and $M_{23}C_6$ (Dyrkacz, 1979). The same information for the class B and D heat treatments is not available. The effect of the heat treatment on the weldability of superalloys is discussed in subsequent sections.

1.3 Repair welding of superalloys

A review of repair methods by EPRI (Gandy et al., 2000) concluded that low heat input methods are generally the preferred route that manufacturers take for repair of turbine components. The report lists laser, tungsten inert gas (TIG) and plasma arc welding (PAW) as the most commonly used processes for this application (Gandy et al., 2000). A detailed description of these and other joining process can be found in Norrish (1992).

The majority of published works regarding studies on superalloy weldability involve the use of TIG, laser and electron beam processes.

Recently an interest in additive layer manufacturing processes (both laser and arc welding, with powder and/or wire as the filler) has developed with manufacturers aiming to combine this with accurate control systems to enable more automated and cost effective repair procedures (Clark et al., 2008; Pinkerton et al., 2008; Hussein et al., 2008; Dinda et al., 2009). A list of all processes that can be used for joining

and repair of superalloy components in gas turbines is listed in Table 1.10.

Table 1.10 – Summary of processes used for joining and repair of superalloys.

Fusion welding	Brazing	Solid state
TIG	Brazing	Friction*
Laser	Diffusion brazing	Friction taper plug
Electron beam	Wide gap diffusion brazing	Diffusion*
Plasma arc	Transient phase liquid bonding*	
Laser powder deposition		
Additive layer manufacturing		
MIG		

Note that processes marked with an * are generally used for manufacturing processes and not repair.

1.4 Liquation cracking

1.4.1 Proposed mechanisms

Liquation cracking is a type of hot cracking (Kou, 2003b). It has been referred to by other names, such as HAZ cracking (Gittos and Scott, 1981), edge of weld cracking (Dudas and Collins, 1966) and base metal cracking (Metzger, 1967) but is in general a form of microfissuring. There are other mechanisms that cause cracking which can occur in the HAZ, for example ductility dip cracking which is discussed in section 1.6.2. As well as affecting nickel base superalloys, it also affects aluminium alloys (Huang and Kou, 2002, 2004), and some steels (Pepe and Savage, 1967).

Liquation is defined as melting of localised regions in the microstructure and typically occurs along the grain boundaries. Liquation cracking occurs with the combination of a liquation mechanism, and a force pulling apart the weakened liquated area (Kou, 2003b). The latter is generated immediately after welding, when the weld pool begins solidifying, and the contraction occurring in the weld pool pulls the solid material immediately surrounding the fusion boundary inwards. This is illustrated in Figure 1.4.

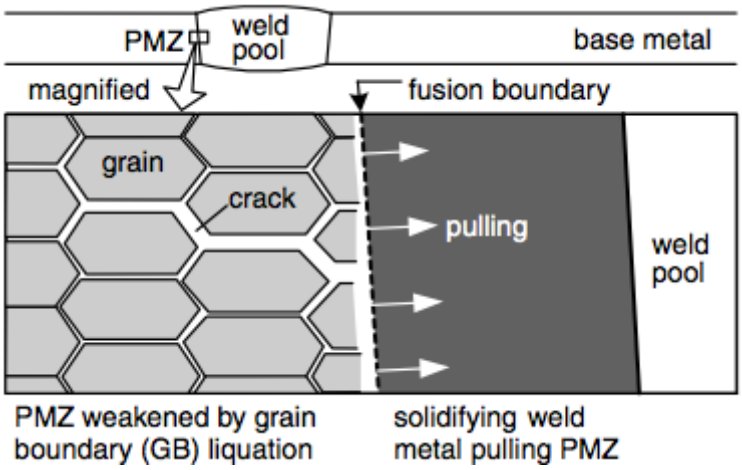

Figure 1.4 – An illustration of the formation of a liquation crack in the HAZ of a weld (Kou, 2003b).

Liquation can occur but with no cracks forming, as found by Idowu et al. (2007), which suggests that there is a requirement for both stress and liquation to form the crack. HAZ liquation occurs by either of the following:

1. Supersolidus melting;
2. Non-equilibrium subsolidus melting.

The latter type is more common and is also more harmful as it is this which increases the melting temperature range in the weld and surrounding material, thus increasing the chance of liquation. Subsolidus melting can occur by two different methods:

- Constitutional liquation of secondary phase particles present on grain boundaries;
- Liquation of low melting point segregates formed on the grain boundaries during solidification and pre-weld heat treatments.

Both of these are discussed in the following subsections.

1.4.1.1 Subsolidus constitutional liquation

Constitutional liquation in nickel-base superalloys was first proposed by Owczarski et al. (1966). As the name suggests, the mechanism involves constituent particles (secondary phases present in the microstructure). However, the melting of the particle itself does not occur (most of the secondary phase particles in superalloys have melting temperatures similar to/greater than the matrix). A more complex eutectic-type reaction occurs at the interface between the matrix and particle. The slow heating rate (equilibrium) conditions that occur in heat treatments allow the precipitate phases to fully dissolve into the matrix phase. Conversely, under extremely rapid heating (exceeding the rates observed during welding) there is insufficient time for any dissolution to occur. Thus in either of these cases the

constitutional liquation is avoided. Welding however has a heating rate which falls between those described above.

According to DuPont et al. (2009), the following must be operative for the mechanism to occur:

1. The particle must react with the matrix to create a composition gradient around the particle;
2. The reaction zone composition must undergo melting below the melting temperature of the surrounding matrix.

The mechanism is explained with the aid of a simple hypothetical binary phase diagram (Figure 1.5), and an illustration of the constitutional liquation at the precipitate/matrix interface in Figure 1.6.

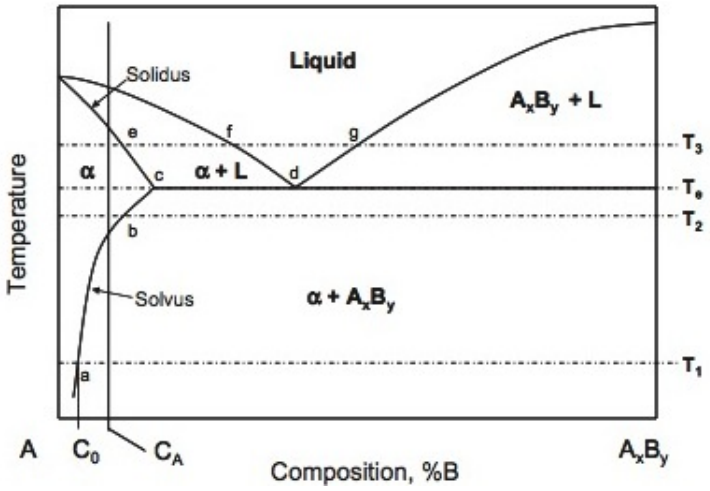

Figure 1.5 – A binary phase diagram illustrating constitutional liquation (From DuPont et al., 2009).

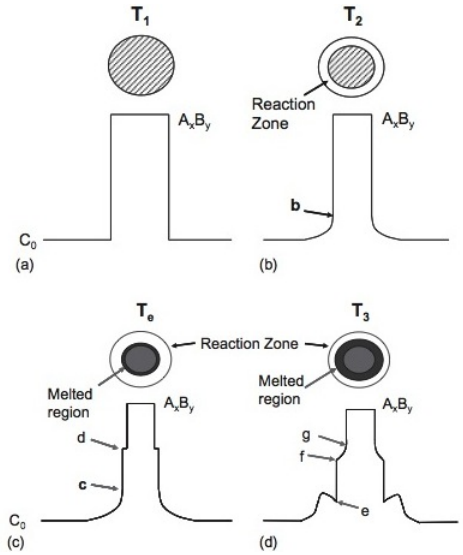

Figure 1.6 – An illustration of the constitutional liquation mechanism at the precipitate/matrix interface (From DuPont et al., 2009).

The phase diagram illustrates the particle phase A_xB_y, which could be a carbide, or even a γ' precipitate. This is contained within the matrix, represented by α (of composition C_0). Assume that an alloy of composition C_A (α + A_xB) is welded. During welding, there are four different temperatures passed, T_1, T_2, T_e(the eutectic) and T_3 (above the eutectic). The following microstructural changes occur at each temperature:

Temperature	Stage of mechanism
T_1	The alloy consists of the particle A_xB_y within the matrix phase of composition α.
T_2	At this temperature, under the rapid heating conditions, the A_xB_y starts to react with the matrix now of composition b (on the solvus line/T_2 intersection), forming a reaction zone (illustrated in Figure 1.6(b)). There is now a composition gradient in this reaction zone due to the partial dissolution of the precipitate.
T_e	As the eutectic temperature is reached, the composition of the interface follows the solvus to point c in the phase diagram, also denoted c in Figure 1.6(c). Also at the eutectic point, a liquid, of composition d is present, which produces a liquid region between the particle and the reaction zone. It is this liquid which starts the constitutional liquation.
T_3	Further heating to this temperature increases the amount of liquid in the system. However, there are now two liquid compositions present, denoted in the phase diagram and illustration as f and g. These two are simply the compositions at the matrix and particle interfaces respectively. At this temperature, the composition of the matrix in contact with the liquid is denoted e (at the solidus line). Above T_3, further reactions of this type will occur around particles until the alloy is fully liquid (above the solidus) and full matrix melting occurs. Upon cooling from temperature T_3, the reaction products (e.g. a eutectic of γ/γ' or γ/MC carbide) solidify, forming weakened films which under the contraction stresses result in the formation of cracks.

Chaturvedi (2007) cites two factors which significantly influence constitutional liquation:

1. Heating rate: - When the heating rate is at an intermediate range (e.g. below the very rapid heating rates previously stated which avoid dissolution, but above the equilibrium rates observed during heat treatments), a greater concentration of the eutectic forming element is produced at the particle/matrix interface;
2. Solute diffusivity: - Elements with slow diffusivity produce greater concentra-

tion of the eutectic element at the particle/matrix interface.

Therefore, optimising the heating rate such that it avoids the intermediate range which significantly affects the liquation mechanism is a productive method for avoiding liquation. Unfortunately, the heating rates involved in welding are commonly within the intermediate ranges associated with influencing liquation. Carbides and intermetallic compounds (as predominantly observed in Rene 80) are slower to dissolve and therefore are inevitably going to constitutionally liquate unless extremely slow heating is used (Chaturvedi, 2007).

A table of constitutionally liquating phases for the most relevant alloys based on a review of literature is shown in Table 1.11.

Table 1.11 – Phases associated with constitutional liquation in various multi-phase superalloys.

Alloy	Liquating phases	Reference
IN718	NbC and laves phase	Radhakrishnan and Thompson (1993)
Allvac 718Plus	MC-type carbides	Vishwakarma et al. (2005)
IN738	MC-type carbides, M_3B_2-type borides, γ', and M_2SC-type sulfo-carbides	Ojo et al. (2006)
Rene 80	MC-type carbides (solutionised condition), MC-type carbides, M_3B_2 (overaged condition), MC-type carbides and γ/γ' eutectic islands (as-cast condition)	Shahsavari et al. (2007)
	M_2SC-type sulfo-carbides	Sidhu et al. (2009a)

Examples of liquation of the Allvac 718Plus and IN738 phases described in Table 1.11 are shown in Figure 1.7. It is clear that liquation cracks show evidence of resolidified products around their edges, and often contain partially melted precipitates within them.

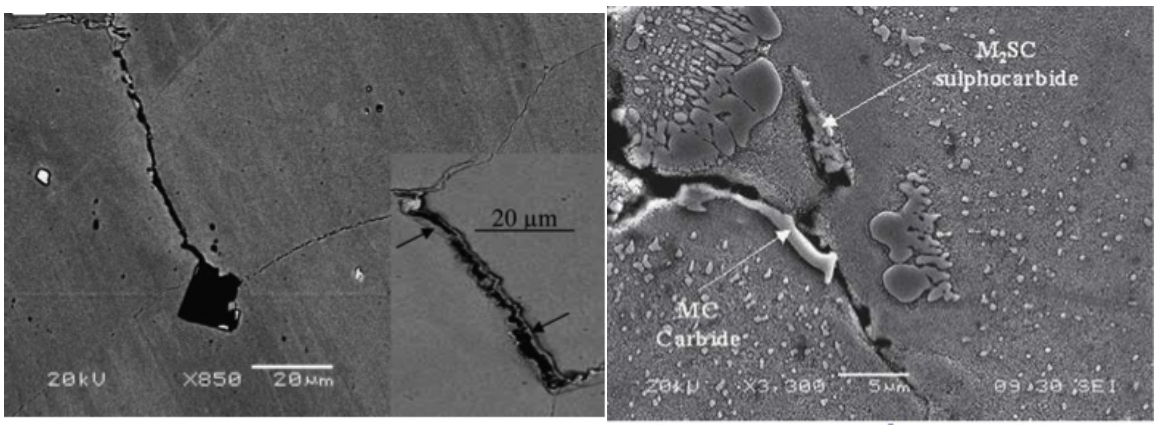

(a) **(b)**

Figure 1.7 – (a) Example of a liquation crack in Allvac 718Plus with inset image showing resolidified constituents around the edge of crack (in this case Ti,Nb (C, N)), from Idowu et al., 2007 and (b) Example of liquation of MC carbide and M_2SC sulphocarbide in IN738, from Ojo et al., 2006.

In summary, during the rapid thermal cycle during welding, constitutional liquation on the grain boundaries in nickel base superalloys results in a partial dissolution of a precipitate into the matrix, which forms a eutectic composition liquid. The liquid is weak, and, (especially if there are a number of reactions occurring along the same grain boundary, forming a film) weakens the grain boundary. Due to the stresses caused by cooling and the volume change, the weakened liquid film is liable to form a crack.

1.4.1.2 Subsolidus liquation of grain boundary segregation

This mechanism is a consequence of the pre-weld processing conditions rather than in the constitutional liquation mechanism, and it could be argued it is easier to reduce the probability of this type occurring. However, Chaturvedi (2007) suggests that even when conditions for constitutional liquation are avoided, there is still a risk of grain boundary melting by low melting point segregates.

The dynamics of casting, particularly for an alloy with such a vast range of elements as found in superalloys, will often result in segregation of various items, such as tramp elements, secondary phases, and eutectic phases at the grain boundaries. It is common for such phases to have a melting point lower than the surrounding matrix.

The complex mechanisms by which the segregates are formed on the grain boundary are not discussed in detail here. However the segregation can occur either in equilibrium or non-equilibrium. The former occurs when the material is held at a high temperature, allowing diffusion of material from the matrix to the grain boundaries, while the non-equilibrium occurs during cooling from an elevated temperature,

such as during the cooling of casting, solutionisation or HIP treatment. Factors affecting this second mechanism include the peak temperature prior to cooling, the rate of cooling, and bulk concentration of solutes (Chaturvedi, 2007). Chen et al. (1998) found that the cooling rate is critical, requiring either rapid or very slow cooling rates to avoid formation of the segregates. Unfortunately it is difficult to use such rates without avoiding other issues such as thermal shock, distortion, or adding additional complexities such as variable cooling rates within the one component.

Most castings are subjected to further thermal cycles prior to welding, such as hot isostatic pressing (HIP), solutionisation, and/or solution and ageing. These are used to homogenise the microstructure, producing a more stable material with optimum properties for the welding process. Therefore it is likely that the cooling rates could induce segregation at the grain boundaries by the above mentioned processes. Although attempts are made to minimise macro-segregation, micro-level segregation is more difficult to avoid. Macro-level is avoided by optimum control of the casting process, heat treatments, and chemical composition to minimise segregation on the grain boundaries.

As a result, although this form of liquation is likely to occur even when constitutional liquation is avoided, it is perhaps easier to avoid by careful control of compositions, casting, and heat treatments. This is perhaps why there is little published on this mechanism, and why constitutional liquation is reported as the dominant mechanism that causes liquation cracking in superalloys.

1.4.2 Factors affecting liquation cracking

1.4.2.1 Weld contamination

Contamination is a common source of welding defects. It can cause porosity, liquation and solidification cracks. In the review of mechanisms of liquation in Section 1.4.1, the role of lower melting point segregates in forming liquation cracks was discussed. In nearly all published works, there is clear emphasis on ensuring the surface prior to welding is cleaned thoroughly. This always includes degreasing, and often involves removal of the surface oxides by wire brushing.

Contamination of low melting point elements is obviously a serious issue when trying to avoid liquation cracking. A list of the elements most commonly found as contaminants which cause liquation in superalloys, together with recommended maximum levels, can be found in Table 1.12 (Donachie and Donachie, 2002).

Table 1.12 – Suggested maximum level of impurity elements for avoiding liquation cracking in superalloys (Table 9.2 From Donachie and Donachie (2002)).

Element	Maximum level (% weight)
Sulphur	0.015
Phosphorus	0.015
Silicon	0.02
Oxygen	0.005
Nitrogen	0.005

Other elements, such as copper, lead and boron can also lead to liquation by contamination. However, the latter is a known alloying element and its level is generally controlled as such to avoid liquation. Thus, ensuring surfaces are thoroughly cleaned prior to welding helps avoid liquation cracking.

1.4.2.2 Weld bead geometry

Little work has centred around investigating the effect of the weld bead on HAZ cracks. Shinozaki et al. (2000) state that when analysing cracking results it is important to consider the weld bead aspect ratio (penetration to width) and cross sectional area.

Boucher et al. (1976, 1977) investigated the effect of weld pool morphology on cracking in IN718 and Waspaloy. They found that the amount of cracking reduced with increasing aspect ratio (see Figure 1.8). This is reportedly due to lower stresses generated at the fusion boundary.

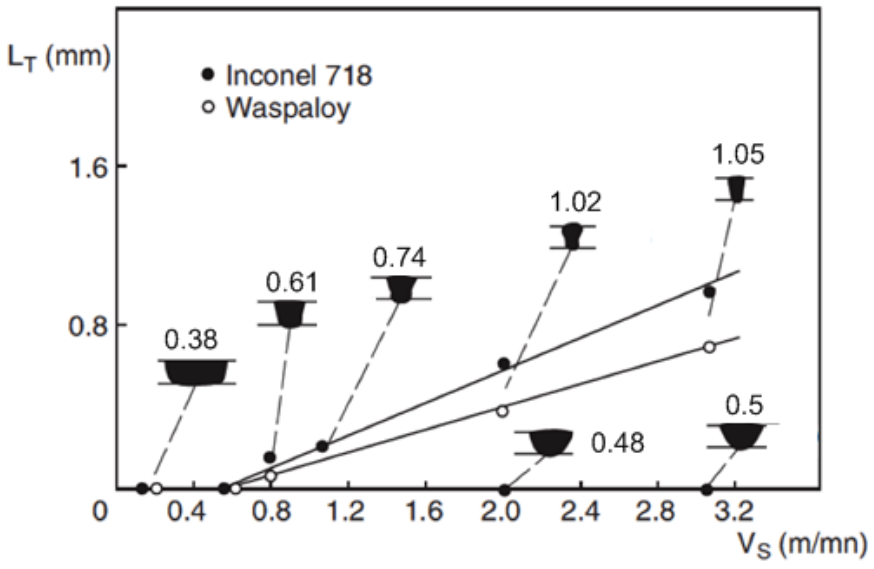

Figure 1.8 – Influence of welding speed and aspect ratio (penetration/width) on total crack length (y-axis) occurring in the heat-affected zone for the TIG process (After Boucher et al., 1977).

Additionally, the necking feature (see Figure 1.9) observed in some weld bead geo-

metries is reportedly the most common region for HAZ crack initiation in superalloys (Shinozaki et al., 2000). This type of feature is commonly observed in high energy density processes such as keyhole laser welding.

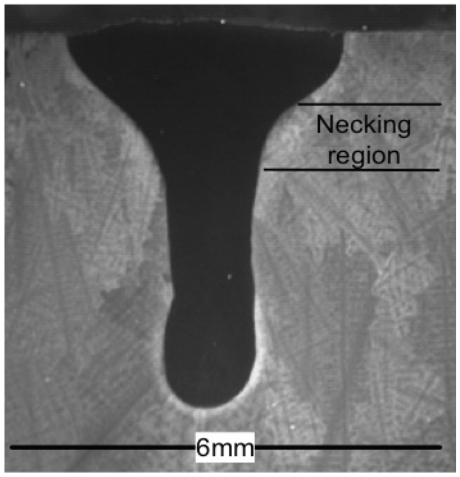

Figure 1.9 – Illustration of necking feature.

1.4.2.3 Welding parameters

Welding heat input (defined as the input power divided by the welding speed) and the resulting thermal cycle, are both critical in determining the size of the fusion zone and the HAZ. A high level of heat input will lead to more energy input to the weld, causing a larger HAZ. Kou (2003a) recommends the use of multipass welding or low heat input processes such as laser and electron beam welding to help reduce the size of the HAZ and partially melted zones (PMZs) and therefore reduce the potential for liquation occurring.

Kim et al. (2000) found that by decreasing the heat input in TIG welding (from 0.990 kJ/mm to 0.550 kJ/mm) the level of cracking decreased to zero, and with autogenous laser welds heat input ranges from 0.2 kJ/mm to 0.8 kJ/mm produced crack free welds. Thus lower total heat input is a possible method of lowering cracking.

However, other studies have shown that lowering heat input may not reduce cracking in superalloys. Idowu et al. (2007) found that lower heat input (0.137 kJ/mm) produced more cracking than higher heat input (0.472 kJ/mm) laser welds on Allvac718 alloy, proposing that the higher heat input welds had a shallower thermal gradient, which reduced the susceptibility to crack formation. This is despite the higher heat input microstructure showing evidence of grain boundary liquation. Danis et al. (2010) also proposed that cracking decreases with shallower thermal gradients. There have also been studies on the influence of power and welding speed in isolation.

Welding speed effects also appear to be inconclusive, with Egbewande et al. (2010) finding that cracking increased at lower welding speeds due to process instabilities (laser welding), and using numerical analysis, Dye et al. (2001a) suggested that liquation cracking is promoted when welding speed is increased. However, Richards et al. (1994) and Shinozaki et al. (2000) found that cracking decreased with lower welding speeds (which could be as a result of shallower thermal gradients). Danis et al. (2010) proposed that (for constant heat input rate) decreasing the welding speed and power reduced cracking. Power effects have also been investigated, Danis et al. (2010) finding lower cracking with lower powers, whilst Richards et al. (1994) suggest the opposite.

Therefore there is disagreement in the literature on the effects of the welding parameters on cracking. In general, studies related to parameter effects on crack susceptibility of nickel superalloys are generally limited to a small window of parameters, which may explain the different findings.

Other factors that effect the crack susceptibility include filler wires, with more ductile filler wires reducing cracking (Banerjee et al., 2005; Sidhu et al., 2005, 2008). Additionally, pre-heating above 600 °C for both TIG and plasma arc welding, and above 900 °C for electron beam welding was shown by Haafkens and Matthey (1982) to reduce cracking.

Jahnke (1982) proposed that applying pre-heating at the homogenisation temperature (1120 °C) for the alloy IN738 during welding and then subsequently applying hot isostatic pressing (HIP) can produce successful crack free welds without filler alloys. Danis et al. (2010) found that cracking in IN738LC could only be avoided by using pre-heating at temperatures high enough to significantly reduce temperature gradients during welding.

Therefore, the role of pre-heating is to reduce the thermal gradient. However, using preheating is complex; the furnaces required are expensive and often unavailable. Additionally, most repairs are performed manually, and using the pre-heating temperatures described above presents many health and safety problems.

Finally, one of the reasons why pre-heating and/or optimising the process parameters reduces liquation cracking is shallow heating/cooling rates allow the elements with slow diffusivity to solutionise without forming the eutectic at the particle/matrix interface, as was outlined by Chaturvedi (2007) in section 1.4.1.

1.4.2.4 Alloy chemistry

The alloy chemistry significantly influences the crack susceptibility of nickel superalloys, as outlined in the discussion of the mechanisms in section 1.4.1. Tramp elements, minor and major alloying elements, and the secondary precipitate phases

all influence an alloy's weldability.

Alloys with high aluminium and titanium content are generally considered to be more susceptible to liquation cracking because of their higher hardness (and lower ductility), which influences the resistance to stresses which cause both liquation and the PWHT cracking. This relationship is shown in Figure 1.10. Note that this plot was developed for PWHT cracking rather than liquation cracking, however it is still a good representation of general crack susceptibility.

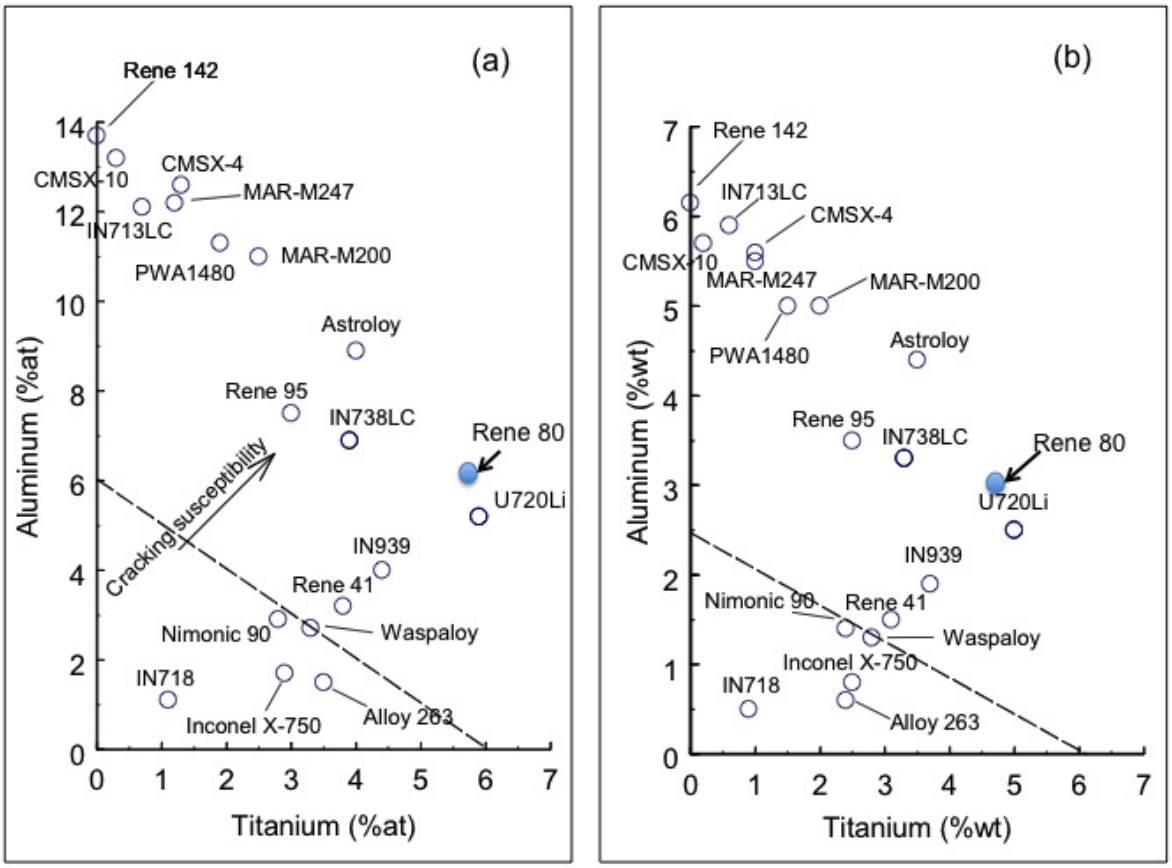

Figure 1.10 – Relationship between aluminium and titanium content and alloy crack susceptibility for various superalloys. Different plots show (a) atomic % and (b) weight % (Modified from Gregori, 2003).

Boron has been shown to increase the possibility of liquation occurring, although it does offer benefits to the high temperature properties of superalloys (as borides). As a result, the content of this element is generally limited to ensure minimal cracking. Boride particles are found to be constitutionally liquated in IN738 (Ojo et al., 2006) and Rene 80 (Shahsavari et al., 2007).

Similarly, carbon affects the formation of secondary precipitates. Thompson et al. (1991) found that in IN718 an increase in carbon from 0.02 % to 0.06 % (by weight) caused a 70 % increase in the measured volume fraction of NbC - a phase

which leads to liquation in the alloy – with a corresponding 18 % increase in liquation cracking. However, because of its role in forming the carbides, which ensure high temperature creep properties, it is difficult to reduce the content of this element.

Modern processing of components typically ensures that castings rarely include high levels of elements with low melting points that would contribute to grain boundary segregation mechanism. Kelly (1990) suggests that sulphur and phosphorus should be kept below 0.015 %, silicon below 0.02 %, and oxygen and nitrogen below 0.005 % (all by weight).

1.4.2.5 Grain size and structure

The general consensus is that a large grain size, typical of cast superalloys, will lead to a greater level of cracking. This is reported by Kou (2003a,b) who emphasised that the coarser the structure, the smaller the grain boundary area, which means that there will be a greater concentration of liquating items (e.g. secondary phases, impurities and low melting point segregates) on the grain boundaries. In addition, a coarser grain structure will produce a material that has low ductility, and this will impact the material's intrinsic resistance to the stresses that occur during weld solidification, which cause the cracking to occur.

Lingenfelter (1997) reports that when grain size exceeds ASTM number 5, (e.g. ASTM 4 to ASTM 00) the material becomes more sensitive to liquation cracking. Note that ASTM method (ASTM, 1988) of annotating grain size dictates the average grain size with a number, with e.g. 00 having a nominal average diameter of 510 μm, and number 8 a size of 22 μm.

An actual quantification of the effect of grain size by Thompson et al. (1985) on wrought IN718 found that the grain size does affect the level of liquation microfissures. Using a test method known as a spot varestraint test, the level of cracking in the alloy, which was treated to have grain sizes in the range 20μm to 200 μm (ASTM numbers 8 to 1) was assessed. It was found that for every 1 μm increase in grain size, the level of microfissuring increased by 0.4 %. However, there are limited studies on the influence of grain size in cast alloys, which have significantly coarser grain structures than wrought alloys.

The role of the grain structure has also been found to affect the crack susceptibility. Directionally solidified (DS) alloys utilise advanced casting techniques to grow the grains in orientations that improve the creep properties by alignment of the grain boundaries. The weldability of DS alloys Rene 80 (Sidhu et al., 2009a) and IN738 (Sidhu et al., 2007a) was improved compared to their conventionally cast counterparts due to the reduced number of grain boundaries intersecting the fusion zone.

Nickel-base superalloys generally have their grain boundaries engineered to maximise high temperature creep resistance. In addition to the decoration of grain boundaries with precipitates such as carbides, this also involves ensuring the grain boundaries are serrated (Safari and Nategh, 2006). In addition to the improvement in high temperature properties, grain boundary serration has recently been shown to improve the resistance to liquation cracking in nickel base superalloys (Hong et al., 2011)

1.4.2.6 Pre-weld microstructure

The microstructure of the component is as important as the amount of liquation susceptible phases on the grain boundaries, and will vary depending on the heat treatment, or the amount of service the component has seen.

Welding superalloys in the as-cast condition is not advised as the microstructure will contain a significant amount of the liquation inducing phases and elements, all decorated along grain boundaries. This was found in investigations on IN738 (Ojo, 2007) and Rene 80 (Shahsavari et al., 2007).

Unfortunately, repair welding is often dictated by the limitation of avoiding pre-welding heat treatments due to time and cost. However, a study by Thakur et al. (2003) comparing different pre-weld microstructures in IN738 concluded that to minimise HAZ cracking the following steps must be taken:

1. Reduction of volume fraction of γ' (compared to the as-cast condition);
2. Reduction in the level of carbides present at GBs, avoiding the formation of films of carbides;
3. Ensuring the grain boundary morphology is serrated.

Thakur et al. (2003) developed a heat treatment based on these three points, which used the standard solution treatment for IN738 (1120 °C for two hours followed by argon quenching) but had an additional period of ageing at 1025 °C for 16 hours. The effect of this heat treatment was compared with the standard solution treatment by Sidhu et al. (2007b) (see Figure 1.11 for a comparison of the two treatments), who found that the standard heat treatment had a microstructure consisting of coarse cuboidal primary γ' of 40-50 nm, and finer spheroidal secondary γ' of ~10 nm. The newer heat treatment (with the additional ageing) resulted in an increase in the size of the coarse primary γ' to 70-80 nm, and increase of the secondary γ' to <50 nm (Sidhu et al., 2007b). The result was an increase in volume fraction comparing the two heat treatments (~21 % standard heat treatment, ~30 % with ageing) but the as cast condition was ~42 % (Sidhu et al., 2007b). Additionally, the overaged microstructure had a hardness of 280±12 HV_{10}, whilst the standard solutionised material had a hardness of 380 ±12 HV (Sidhu et al., 2007b).

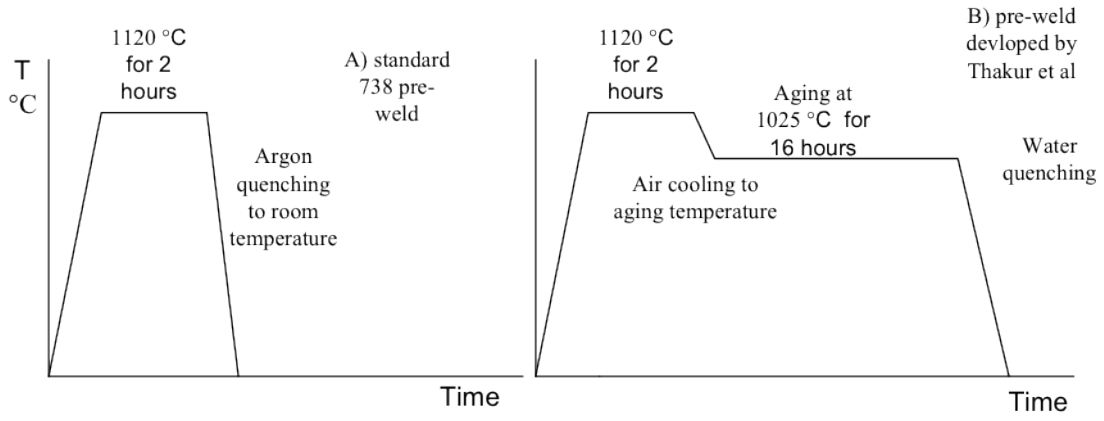

Figure 1.11 – Different pre-weld heat treatment cycles applied to IN738LC in work by Sidhu et al. (2007b).

After welding and PWHT, the overaged condition resulted in approximately 43 % less cracking compared with the standard pre-weld solutionised condition (Sidhu et al., 2007b). The combination of the reduction in hardness (caused by the over-ageing), the grain boundary serration, and the optimised microstructure of other secondary phases clearly contributed to this improvement in crack resistance.

However, a more recent study by Egbewande et al. (2009) found that the pre-weld heat treatment developed by Thakur et al. (2003) still resulted in significant cracking in IN738 (although as was discussed previously, it was reduced compared to a standard solution treatment). The authors applied a different heat treatment, utilising water quenching after solution treatment followed by a longer period of ageing at a slightly higher temperature, which produced a microstructure with reduced cracking. This was reported to reduce the intergranular boride particles which were forming in the previous heat treatment, which are susceptible to constitutional liquation.

A study on Rene 80 produced contrasting findings to those reported above. Shahsavari et al. (2007) found that the solutionised condition resulted in lower liquation crack susceptibility compared to an overaged microstructure. The solutionised condition did however show some cracking, but it was unclear whether it was via the liquation mechanism. However, it is interesting to note that the overaged alloy showed evidence of liquation of carbides and borides close to the fusion zone boundary. The overageing treatment used in this study was different to that developed by Thakur et al. (2003).

An alternative method of changing the pre-weld microstructure was investigated by Mousavizade et al. (2009). They applied friction stir processing (FSP) to a plate of as cast IN738, which through a combination of plastic deformation and heat homogenised the microstructure, reducing liquation cracking observed in the

processed zone of the material, after laser welding. This type of process however, is difficult to apply to castings of more complex shapes. Additionally, the vast improvement observed may be due to the base material being in the as-cast condition, which of course will offer a significantly more susceptible microstructure. If the base material was solutionised prior to the FSP treatment, then the difference in crack susceptibility may be reduced.

1.4.3 HAZ cracking in Rene 80

Whilst Rene 80 is similar in composition and strength to IN738 (and its variant IN738LC), the latter alloy has seen a greater focus of research. The limited works available on Rene 80 focus on the metallurgical aspects and not on the relationship between processing parameters and the incidence of cracking. In addition, the number of parameters studied is very small.

HAZ cracking in Rene 80 has until recently been proposed to be by the liquation mechanism only. Shahsavari et al. (2007) found that it is the constitutional liquation of secondary precipitates, with the exact precipitates depending on the pre-weld microstructure condition. It was found that constitutional liquation of MC-type carbides and γ/γ' eutectics in the as-cast condition, and MC-type carbides and borides in the overaged condition caused the cracking. There was also evidence of MC-type carbides in the solutionised condition, however there was significantly less cracking in this condition.

However, the same authors concluded that in the solution treated condition, the cracks had a morphology unlike those in the other conditions, and suggested these were not produced via a liquation mechanism.

Directionally solidified (DS) Rene 80 alloy has been studied by various authors. Sidhu et al. (2009a) found that (after overageing) the alloy contained liquation cracks formed from constitutional liquation of coarsened γ', M_5B_3 borides, MC-type carbides and M_2SC sulfo-carbides. A follow up study by Osoba et al. (2011) found that cracking was significantly reduced in the DS Rene 80 when optimising a pre-weld heat treatment to eliminate the M_5B_3 borides.

It is therefore slightly uncertain as to the exact particles that are liquated to form cracks in this material. However, it is clear that the majority of the secondary precipitates have been found to be constitutionally liquated in the different references.

1.4.4 Summary of solutions

Most of the methods to minimise liquation cracking are related to the factors which were discussed in section 1.4.2. Therefore, a summary of methods is shown in Table 1.13 below.

Table 1.13 – Summary of methods for minimising liquation crack susceptibility.

Solution	Method	Reference
Overage	Pre-weld heat treatment	Thakur et al. (2003)
Reduce heat input	Welding process selection, parameter optimisation	-
High ductility weld zone	Ductile filler wire	Sidhu et al. (2005)
Control chemistry	Reduce B and C content, minimise tramp elements	-
Reduce grain boundary segregation	Reduce grain size	Thompson et al. (1985)

1.5 Post weld heat treatment cracking

1.5.1 Mechanism

Post-weld heat treatment (PWHT) cracking is a solid state cracking mechanism and is typically intergranular in nature. Whilst it is known as PWHT cracking (Kou, 2003b; Henderson et al., 2004), the mechanism by which it occurs in superalloys is referred to as strain-ageing, hence it is sometimes called strain-age cracking (Kou, 2003b). It predominately occurs in the HAZ of a weld, and is known to extend into both the fusion zone and the base material. It has similarities with liquation cracking, which include being severely affected by stresses and occurring on the grain boundaries (although it can occur within the grains as well). It affects precipitation hardened nickel alloys.

The need for PWHT of nickel base superalloy welds is to:

1. Relieve residual stresses within the material left after cooling from welding;
2. Homogenise and age the microstructure to the desired strength level.

A typical PWHT will involve heating to the solutionisation temperature, followed either by cooling or any number of ageing cycles depending on the requirements (an example PWHT is shown in Figure 1.12). The solutionisation will achieve both the stress relief and homogenisation described above, but unfortunately it is during heating to the solutionisation temperature that the cracking occurs.

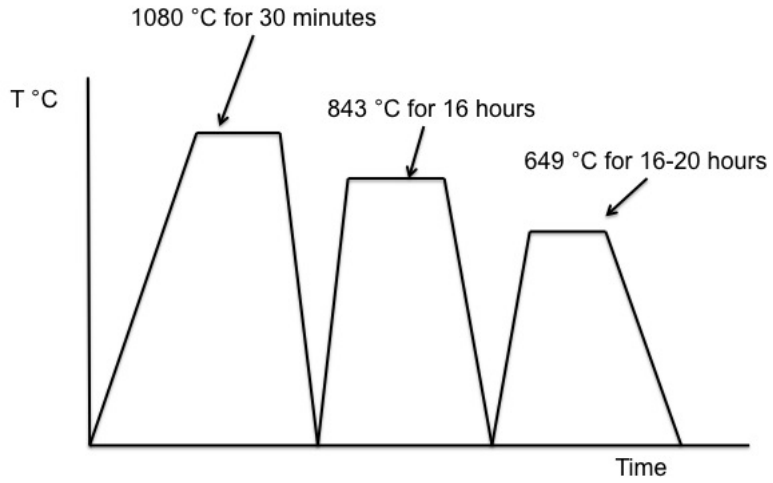

Figure 1.12 – An example PWHT cycle for Rene 80 alloy as described in Lim et al. (2002c).

The following mechanism description is aided by the use of Figure 1.13. During welding, the temperature (T_2) reached in the HAZ causes dissolution of the precipitate phase, and after cooling at time t_1, there is high residual stress contained within the microstructure (Kou, 2003b). As the alloy is heated to solutionisation temperature (above T_2), the γ' precipitation temperature range - T_1 to T2 - is passed. During this time (t_2), fine coherent γ' precipitates are formed, which depletes the surrounding matrix of those elements - nickel, aluminium and/or titanium. This results in a a decrease in the lattice parameter of the matrix, and causes the formation of ageing contraction stresses(Lim et al., 2002c). As a consequence of the precipitation of the γ', the ductility of the alloy will be lower. At this time, the microstructure will not yet be relieved of the welding residual stresses (Kou, 2003b).

Thus, the combination of the low ductility, coupled with the welding residual stresses and ageing contraction stresses, results in the formation of strain-age cracks(Kou, 2003b; Lim et al., 2002c). The issue is exacerbated where the section is thick, where there is high restraint in the weldment, or by brittle zones (embrittled grain boundaries or liquated phases) which are often found in the HAZ due to the rapid thermal cycle of the weld (Kou, 2003b).

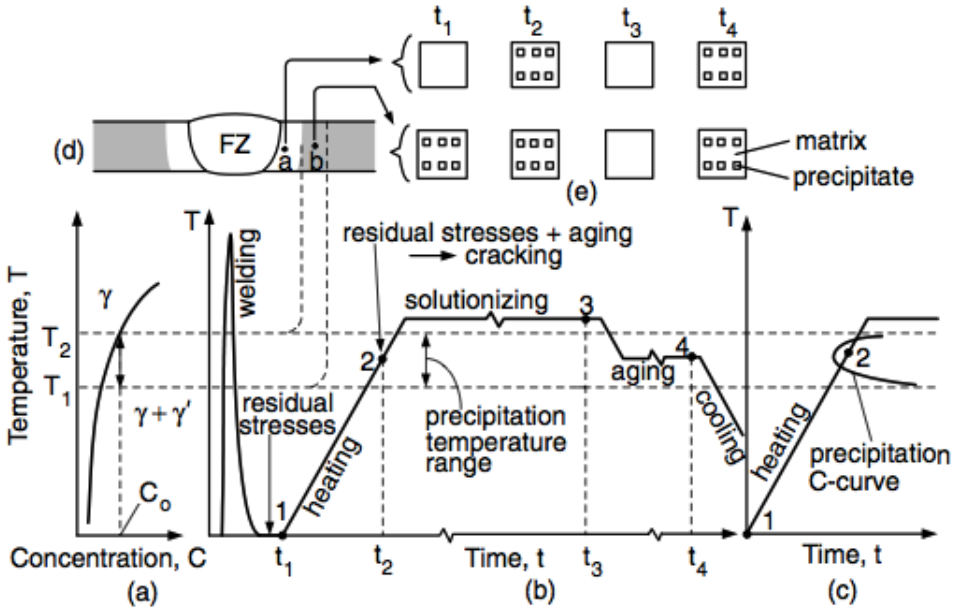

Figure 1.13 – General illustration of strain-age mechanism, (a) phase diagram, (b) thermal cycles during welding and heat treatment, (c) precipitation C curve, (d) weld macro section and (e) microstructural changes, from Kou (2003b).

Despite the solutionisation temperature being reached (at t_3), the cracks will already have formed. The subsequent ageing (t_4) will not induce further PWHT cracks as the residual stresses will be relieved, and the brittle areas of the microstructure will be dissolved.

There are three major factors that affect the strain-age mechanism:

1. The magnitude and distribution of residual stresses after welding;
2. The ductility of the microstructure;
3. The amount of ageing occurring in the alloy during heating to solutionisation.

The mechanism of PWHT cracking in Rene 80 was found to be as described previously (Lim et al., 2002c). However, it was also found that the mechanism in Rene 80 is highly localised, and is also affected by the constitutionally liquated and resolidified grain boundaries that are present in the HAZ (Lim et al., 2002c). The regions where these grain boundaries are present showed full dissolution of the γ' phase, together with a high concentration of the solutes which form this phase. During the PWHT, the surrounding matrix (further away from the grain boundaries) is much stronger. As mentioned previously, this factor together with the volume contraction stress caused by the precipitation of γ', forms the cracks.

There are a number of factors that affect the susceptibility of an alloy to PWHT cracking, including: the chemistry, the ductility (of the weld zone and surrounding base material) and the thermal cycle of the weld. The full thermal cycle leading to

the formation of PWHT is shown in Figure 1.13. The following subsections discuss these factors.

1.5.2 Factors affecting PWHT cracking

1.5.2.1 Aluminium and titanium content

As discussed previously, work by Prager and Shira (1968) found that there is a maximum combined amount of aluminium and titanium (around 6 % atomic) above which an alloy will be susceptible to PWHT cracking. A plot of this relationship for various superalloys with crack susceptibility is shown in Figure 1.10. Additionally, the γ' precipitation kinetics are a significant factor in the mechanism. This phase precipitates more rapidly than the γ" phase (Donachie and Donachie, 2002) and the rate at which it does so is influenced by the content of aluminium and titanium (DuPont et al., 2009). The rate of precipitation is often illustrated by a C-curve. A theoretical illustration of the C-curve of the γ' phase is illustrated for low and high Al+Ti content in Figure 1.14(a). This plot has three heating rates illustrated, with the first (1) a very fast rate which avoids the range at which the secondary precipitates form in both the high and low content alloys. The subsequent two heating rates pass through the C-curve of the high Al+Ti alloy, which illustrates that there would be some precipitation of γ' in these heat treatments, with the likely formation of strain-age cracks. Additionally the comparison between Waspaloy (γ' former) and IN718 (γ" former) is shown in Figure 1.14(b). It illustrates that the latter has slower ageing rates, requiring greater time to precipitate the phase.

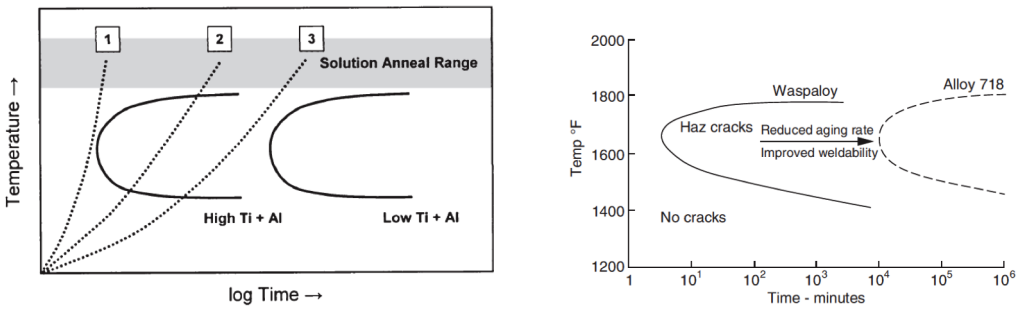

Figure 1.14 – (a) theoretical C-curve comparison of low and high Al+Ti content, with three curves showing how different heating rates in a thermal cycle would pass or avoid the precipitation range (From DuPont et al. (2009)), and (b) C-curve comparison of Waspaloy and IN718 alloy (From DuPont et al., 2009).

By comparing the two different material C-curves (Figure 1.14(b)), for the same heating rate in a PWHT, the IN718 will avoid intersecting the C-curve and therefore will not be as susceptible to ageing. Hence this alloy is less susceptible to PWHT cracking.

1.5.2.2 PWHT cycle

As discussed in the previous section, the precipitation rate of the γ' phase is a significant influence on cracking, and is illustrated by the C-curve (DuPont et al., 2009). There is also a relationship between this C-curve and the heating rate used to reach the solutionisation temperature. An illustration of a C-curve and different heating rates is shown in Figure 1.15. The illustration shows that if the heating rate is fast enough, then the ageing temperature is passed before intersecting the tip of the C-curve (where the earliest signs of ageing will occur). However, if the heating rate is insufficient, then it will pass through the C-curve and cracking will occur.

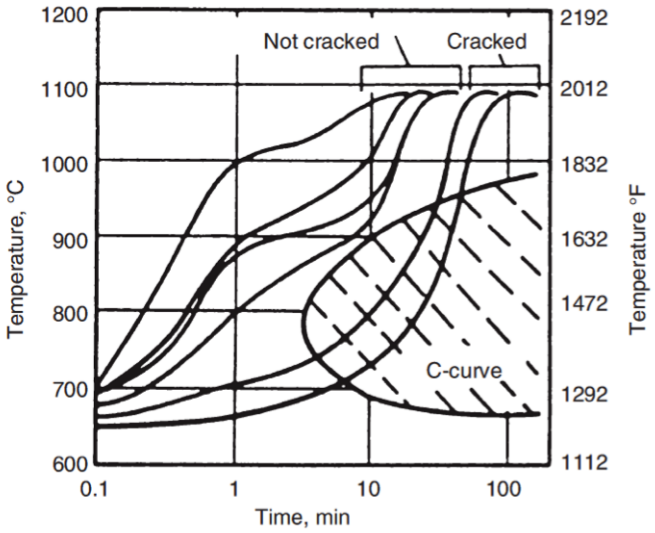

Figure 1.15 – Illustration of C-curve with different heating rates causing/avoiding cracking (courtesy of Hughes and Berry, 1967).

The environment used during the heat treatment is also an influencing factor in cracking during PWHT. Selection of the gas type used in the furnace is crucial, for example using oxygen containing gases (whether deliberate or accidental) was found to lead to embrittlement of grain boundaries, increasing crack susceptibility (Prager and Sines, 1970; Carlton and Prager, 1970).

1.5.2.3 Grain size

The role of grain size in PWHT crack susceptibility is similar to its effect on liquation cracking. In general a large grain size is believed to yield greater crack susceptibility (Lim et al., 2002c; Thakur et al., 2003; Sidhu et al., 2007b). This is due to the influence the grain size has on the alloy ductility, and the level of grain boundary embrittlement during welding. A coarser grain structure causes an increase in both intergranular fracture and a reduction in high temperature ductility, both influencing the crack susceptibility (Norton, 2002).

The grain size also influences the level of grain boundary embrittlement during

the welding cycle, which can act as crack initiation points during PWHT. Like liquation cracking, larger grain sized material reduces grain boundary area, which leads to a greater concentration of embrittled phases, which are more likely to link to form larger embrittled areas.

1.5.2.4 Pre-weld microstructure

The pre-weld microstructure of the alloy often proves vital to the production of crack free or near crack free welds. The ductility of the alloy is an important factor in resistance to PWHT cracking. As a result of this, it has been shown that the amount of ageing in the alloy prior to welding influences the subsequent cracking during the PWHT.

There do however appear to be different opinions on the right pre-weld microstructure, with some researchers suggesting pre-weld overageing, whilst others preferring an optimised solutionisation treatment.

As reported earlier, Sidhu et al. (2007b) found that using a pre-weld heat treatment developed by Thakur et al. (2003) produced a microstructure consisting of coarse overaged γ'. After welding and PWHT, the overaged condition resulted in approximately 43 % less cracking compared with the standard pre-weld solutionised condition.

A different proposal for pre-weld overageing treatment called cyclic overageing was proposed by Lim et al. (2002b,a) and is shown in Figure 1.16. The principle is to produce a microstructure consisting of equiaxed and uniformly dispersed coarse γ' producing maximum ductility. The application of the cyclic heat treatment to Rene 80 alloy found that PWHT cracking was eliminated in all six test coupons, in comparison to 50 % of the standard pre-weld weld heat treated samples showing cracking (Lim et al., 2002b).

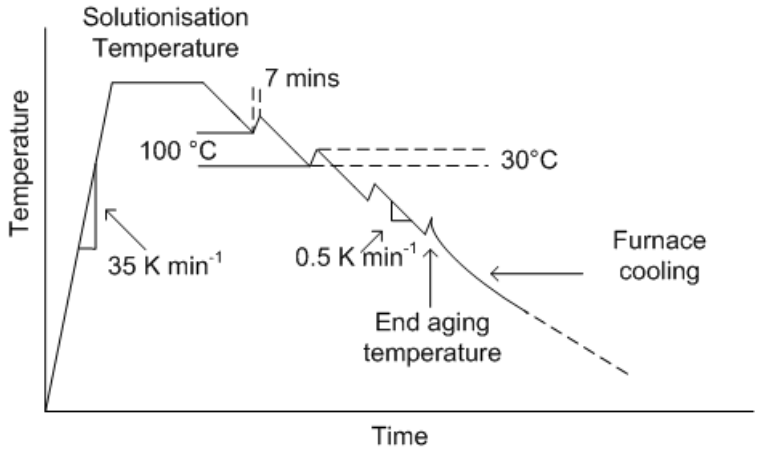

Figure 1.16 – Cyclic overageing pre-weld heat treatment proposed by Lim et al. (2002b) for avoiding PWHT cracking in Rene 80.

However, others propose that an optimised solutionisation treatment is better. Kayacan et al. (2004) investigated the role of various pre-weld heat treatment variables and found that having a relatively slow cooling rate from the solutionisation temperature (after holding for 30 mins) resulted in an optimum microstructure, and after using the same heat treatment cycle post weld, the material contained no cracks.

Although it appears that different pre-weld heat treatments appear to influence PWHT cracking, it is clear that a microstructure which is either as-cast or in the peak strength condition is most susceptible to PWHT cracking.

1.5.2.5 Filler metal

An additional aspect of the weld microstructure prior to PWHT is the use of filler metals, which affect the ductility of the fusion zone relative to the parent. The lower the ductility of the fusion zone often results in greater PWHT cracking. This is confirmed by work by Sidhu et al. (2007b) who found that an autogenous weld was more susceptible to PWHT cracking (note that this will be considered as having the same composition in the fusion zone as the base metal). However, an often-used technique is to use a filler alloy with lower strength relative to the base, to aide in reducing crack susceptibility.

It was also found that crack susceptibility reduced with decreasing Al+Ti content of the filler (Sidhu et al., 2008). Whilst this indicates that increased ductility helps reduce crack susceptibility, it is also possible that the addition of the filler material reduces the stresses during cooling in the welding cycle. The work found that the microhardness in welds with a filler alloy was similar to the autogenous welds. Only the alloy (IN625) with less than 1 % combined weight of aluminium and titanium had a significantly softer weld metal compared to the autogenous weld (Sidhu et al., 2008).

1.5.3 Summary of solutions

Most of the methods to minimise PWHT cracking are related to the factors that were discussed in section 1.5.2. Therefore, a summary of methods is shown in Table 1.14.

Table 1.14 – Summary of methods for minimising PWHT crack susceptibility.

Solution	Method	Reference
Overage	Pre-weld heat treatment	Thakur et al. (2003)
Reduce heat input	Welding process selection and parameter optimisation	Kou (2003b)
High ductility weld zone	Ductile filler wire	Sidhu et al. (2008)
Control chemistry	Optimise content of Al and Ti	Prager and Shira (1968)
Reduce weld residual stresses	Optimisation of welding process, stress engineering	-
Reduce grain size	Casting	Kou (2003b)
Reduce number of as-welded cracks	Welding procedure optimisation	Prager and Sines (1970); Carlton and Prager (1970)
Optimise PWHT	Modify heating rates to avoid intersecting γ' precipitation curve	Hughes and Berry (1967)

1.6 Other defects

1.6.1 Solidification cracking

Solidification cracking, also referred to as centreline cracking and weld metal cracking, occurs in the centre of the fusion zone (Kou, 2003b). The crack is formed due to a combination of shrinkage stress and a material structure which is not fully solidified, which results in the conditions for intergranular cracking. Because of this, the freezing range of the alloy is critical to the occurrence of this defect (Kou, 2003b). An alloy with a large freezing range (affected by the composition) will be more susceptible than one with a smaller range. The factors affecting the crack formation are listed in Table 1.15.

Table 1.15 – Factors affecting solidification cracking. Note that these are not specific to superalloys. (Kou, 2003b).

Metallurgical factor	Other factor
Freezing range	Restraint of weld
Amount of liquid during final stage of solidification	Contraction stresses
Ductility of weld metal	Weld aspect ratio
Primary solidification phase	
Grain structure of weld metal	
Surface tension of grain boundary liquid	

Contamination of the weld pool is therefore a factor which can influence the freezing range and amount of liquid during the final stage of solidification. The impurity elements listed in Table 1.12 will also influence solidification cracking. Therefore, ensuring the surface is thoroughly cleaned will also help to minimise the

occurrence of this defect.

Welding parameters also influence the occurrence of this defect. In their numerical analysis of the weldability of superalloys, Dye et al. (2001a) suggest that solidification cracking is prevalent when low welding speeds and high powers are employed.

Additionally, the weld bead shape (which is influence by the welding parameters) may also significantly influence the alloy's susceptibility to solidification cracking. As illustrated in Figure 1.17, a weld with a high penetration to width ratio is more likely to crack than one with a lower aspect ratio. This is because of the large angle formed between the opposite sides of columnar grain growth in the weld pool, whereas a lower aspect ratio has a shallower angle (Kou, 2003b).

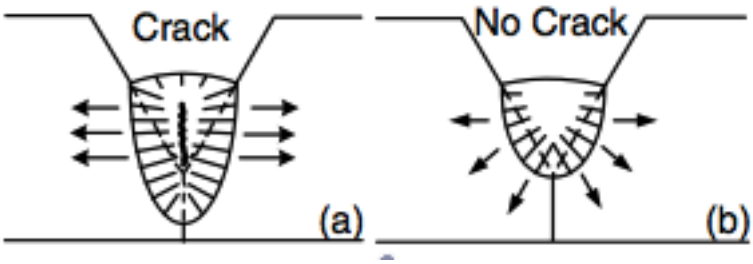

Figure 1.17 – Effect of weld bead geometry on solidification cracking susceptibility (a) too high penetration causing cracking and (b) optimised geometry avoiding cracking (Kou, 2003b).

1.6.2 Ductility dip cracking

This form of defect has been a major issue with solid solution strengthened superalloys. However, recent work has suggested the mechanism can occur in precipitation hardened alloys, in particular Rene 80 (Shahsavari et al., 2007; Österle et al., 2008). This form of cracking can occur in the weld metal, HAZ, or in the reheated weld metal, although it is most common in the weld metal (DuPont et al., 2009). It occurs in the ductility-dip temperature range (DTR), which is below the brittle temperature range (BTR) where segregation based mechanisms such as liquation and solidification cracking occur.

The mechanism by which ductility dip cracking (DDC) occurs is controversial, with numerous authors appearing to provide differing opinions on the exact mechanism (DuPont et al., 2009). It is clear that the mechanism is similar to creep-rupture, with the formation of micro-voids which weaken the grain boundary, allowing some grain boundary sliding and eventually formation of cracks. It is related to a temperature range between 0.5 and 0.8 of the melting point of the superalloy, where a ductility drop is often recorded. An illustration of the ductility range of an alloy as a function of temperature is shown in Figure 1.18, which shows the regions where

segregation cracking (note this includes liquation and solidification cracking) and DDC occur.

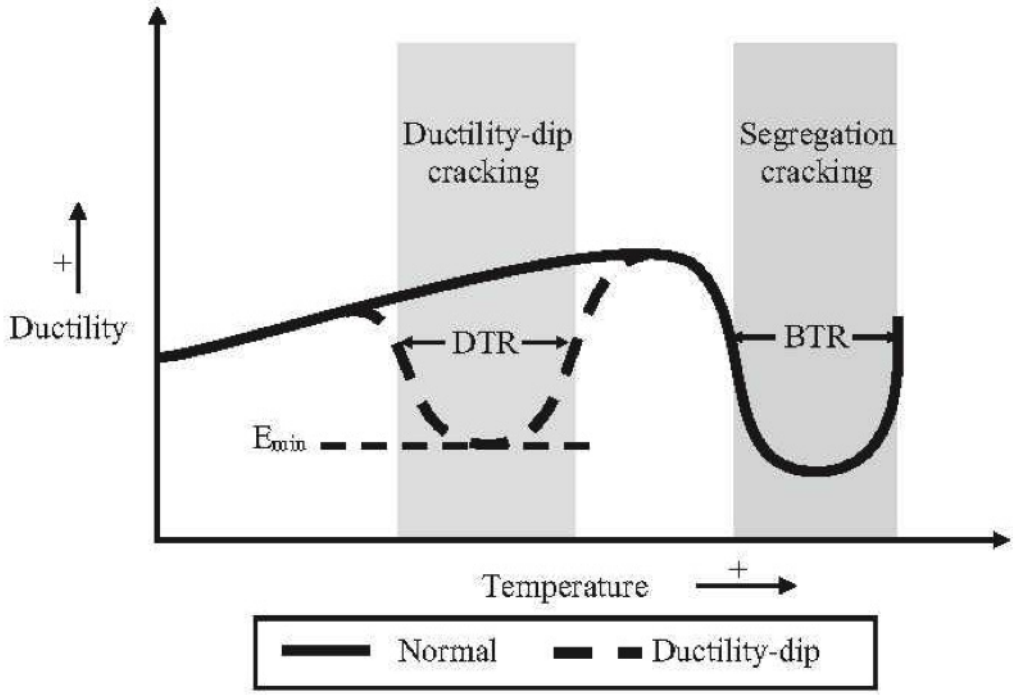

Figure 1.18 – Illustration of ductility as a function of temperature, and the regions where hot cracking and DDC occur. DDC occurs in the ductility-dip temperature range (DTR) and liquation and solidification cracking occur in the brittle temperature range (Nissley, 2006).

In Rene 80 it was found that the temperature range where ductility dip cracking occurs was roughly 750 °C to 1170 °C (Figure 1.19(a)) (Czech et al., 1997). However, alloys like Rene 80 are less susceptible to DDC cracking than alloys such as IN625. This could be due to the lower chromium content in the alloy, as proposed by Young et al. (2008) who found that higher chromium containing alloys are more susceptible due to their tendency to form chromium based carbides. Rene 80 is primarily an MC (titanium/molybdenum/tungsten) type carbide former, and this together with the engineered grain structure (e.g. serrated GBs) prevent grain boundary sliding leading to low DDC susceptibility.

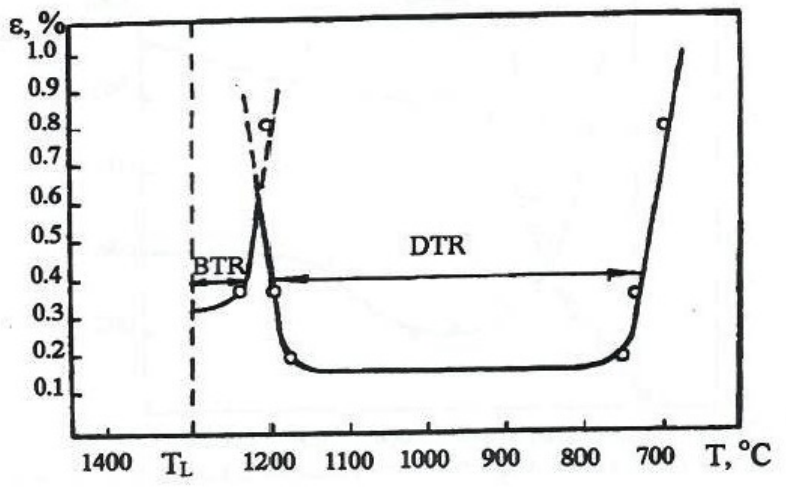

(a)

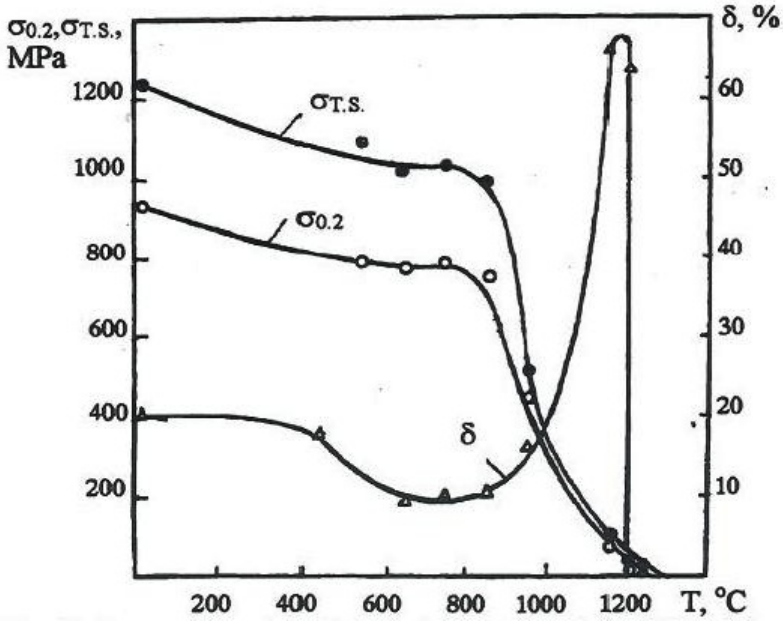

(b)

Figure 1.19 – (a) Temperature ranges where ductility dips in Rene 80 and (b) Temperature dependence of strength and ductility for Rene 80 (Czech et al., 1997).

1.6.3 Porosity

Porosity in weld metal occurs due to gas pockets or voids, which are trapped in the liquid state of the fusion zone (Kou, 2003b). However, they can also arise from poor joint fit-up. In repair welding of superalloys, this factor is not common. Often they can occur due to poor gas quality/welding equipment, and contamination of the surfaces and consumables used. Generally this defect type is rare in nickel superalloys due to the additional care taken to avoid contamination to eliminate cracking in this material.

1.7 Summary

This chapter introduced the metallurgy and welding metallurgy of nickel-base superalloys, and in particular Rene 80. This alloy is precipitation hardened and contains the secondary phases γ', carbides of the form MC (enriched with Ti, Mo and W), M_6C (enriched with Mo, Ni, Co and Cr), and $M_{23}C_6$ (enriched with Cr). Additionally, the alloy contains borides of the form M_3B_2 (enriched with Mo, W and Cr), and sulfo-carbides of the form M_2SC (enriched with Ti and Zr).

There are two HAZ cracking mechanisms affecting Rene 80: liquation cracking, and PWHT cracking. Liquation cracking occurs by one of two mechanisms; the constitutional liquation of secondary phase particles present at grain boundaries, or by liquation of low melting point elements/segregates formed on grain boundaries during solidification. The former mechanism is considered more common.

In Rene 80, it has been reported that the microstructure condition affects the precipitate phase which is constitutionally liquated. In the as-welded condition, it is MC type carbides and γ/γ' eutectics, whilst in the overaged condition it is MC-type carbides and borides, and MC type carbides in the solutionised condition. However, other work has shown that other secondary phases, such as the sulfo-carbides discussed above are susceptible to constitutional liquation in this alloy.

Whilst liquation cracking occurs during the welding cycle, PWHT cracking occurs in the subsequent heat treatments typically applied to superalloy components. It occurs by the strain-age mechanism. During welding, there is partial dissolution of the γ' close to the fusion zone. Additionally, after welding there is a residual stress, which will be relieved during the solutionisation stage of the PWHT. However, during the PWHT, as the temperature passes through the γ' ageing range, there is a combination of nucleation of new γ' precipitates, and growth of existing ones. The precipitation results in a depletion γ' forming elements from the matrix, which reduces the lattice parameter of the matrix and induces ageing contraction, which imparts an additional stress in the microstructure. An additional effect of this γ' ageing is a further reduction in ductility of the alloy. This reduction in ductility, coupled with the combined residual/contraction stress, results in the formation of cracks.

The effect of welding parameters on crack susceptibility appears to be unclear. Whilst some work suggested that increasing power increases cracking, others have shown the opposite. This is also true of welding speed effects, where different work has shown that cracking increased at lower welding speeds due to process instabilities (laser welding) whilst others found that cracking decreased with lower welding speeds. It has also been proposed that, (for constant heat input rate) decreasing the

welding speed and power reduces cracking. A detailed investigation on the effect of welding parameters on cracking susceptibility is required to resolve these conflicting findings.

The effect of pre-weld heat treatment on liquation cracking susceptibility appears to be contrasting. The development of an optimum overageing type heat treatment, which when applied to IN738, appears to reduce the susceptibility to cracking. The same treatment has not been applied to Rene 80.

However a cyclic overageing heat treatment was applied to Rene 80 and proved to be effective at reducing PWHT cracking due to an optimised microstructure. In general, overageing an alloy prior to welding is an effective method for minimising the PWHT crack susceptibility.

1.8 Thesis aims and outline

There is a conflicting message in the literature regarding the effect of welding parameters on cracking in nickel based superalloys. This is due in part to the narrow and limited range of parameters studied in a particular set of trials, and particularly on Rene 80. There also appears to be uncertainty over the exact mechanism of HAZ welding cracks, with some recent publications suggesting that a stress induced mechanism such as ductility dip cracking might occur under some microstructural/thermal/stress conditions. Additionally, there appears to be some ambiguity in the secondary phases which have been reported to constitutionally liquate in the previous studies.

The mechanism of PWHT cracking is significantly affected by weld residual stresses, but the number of published works which help develop a deeper understanding of these stresses in superalloys is limited. This is particularly true for high strength superalloys with more advanced chemistries, with large thickness and grain sizes.

Most repair procedures, whether arc or laser based, use a lower strength filler metal (wire or powder). This offers improvements in reducing the crack susceptibility, but also reduces the range of areas which can be repaired due to reduced strength of the repaired area. There does not appear to be a suitable repair procedure which does not require the use of filler material, which would bypass the disadvantages of using such a material. Additionally, it appears that nearly all repair procedures use a power beam or TIG based processes, with very few published works studying the use of MIG processes for repair. This is despite there being significant developments to this process in recent years that give low heat input which could be suitable for repair.

Therefore to address these limitations, the aims of this thesis are:

1. To assess advanced arc welding processes (low heat input MIG and high frequency pulsed TIG welding processes) for their suitability for repair of superalloys;
2. To understand the effect of laser process parameters (such as power, beam diameter and welding speed) on the incidence of cracking in the as-welded and PWHT condition, in Rene 80 superalloy;
3. Resolve uncertainties associated with mechanisms and phases related to crack formation in Rene 80;
4. Develop a repair procedure which can avoid the formation of HAZ cracks and also avoid the use of low strength filler material;
5. Gain a deeper understanding of welding residual stresses produced during thick section cast nickel based superalloy welding.

To achieve these aims, the thesis will be structured in the following way: Chapter 2 describes a set of experiments which primarily studied the suitability of a low heat input MIG process for crack free repair of superalloys. This chapter also studied the influence of grain size on liquation cracking in cast superalloys. In Chapter 3, a systematic study of the effects of process parameters on liquation and PWHT cracking is described. This study used a large parameter window, and analysed the effect of weld bead geometry.

In Chapter 4, cracks from a selection of welds produced in Chapter 3 are characterised to help determine the mechanisms causing cracking. Chapter 5 describes the measurement of residual stresses from a few conditions in Chapter 3 that did and did not produce cracks.

Chapter 6 describes how the knowledge gained from the previous chapters is then applied with a HIP treatment to develop a novel repair procedure that avoids the use of filler material. Finally, in Chapter 7, a series of experiments that aimed to transfer the optimised weld bead geometry finding (from Chapter 3) to arc based processes is described. In addition, the suitability of a high frequency pulsed TIG process for repair is also studied. It is important to note that Chapter 7 is positioned here and not after Chapter 2 (despite the link of arc based processing) because Chapters 3-6 are a continuation of a linked theme and Chapter 7 is based on findings from Chapter 3.

Chapter 2

Effect of grain size and CMT welding on Rene 80 superalloy

2.1 Introduction and scope

A review of the literature in Chapter 1 found that crack susceptibility of superalloys was influenced by the grain size, but most of the previous literature had concentrated on wrought alloys with average grain sizes less than one millimetre. A significant difference between wrought and cast superalloy components is the latter often have grain sizes above one millimetre, which has significant implications for crack susceptibility.

In addition, a review of the welding processes used on superalloys revealed that TIG and power beam processes are the most commonly used. However, MIG welding offers a number of advantages over the conventionally used TIG processes, such as higher deposition rates and much simpler wire feeding. However, MIG welding also has much higher heat input and generally lower quality welds than TIG welding, which makes it unsuitable for superalloys. The Cold Metal Transfer (see description later in chapter), or CMT process overcomes some of these issues. CMT welding is a variant of MIG welding, offering lower heat input welding whilst still utilising the advantages of MIG.

Metal inert gas (MIG) welding is a high productivity welding process, where the arc is formed between the workpiece and a continually-fed consumable electrode (Figure 2.1).

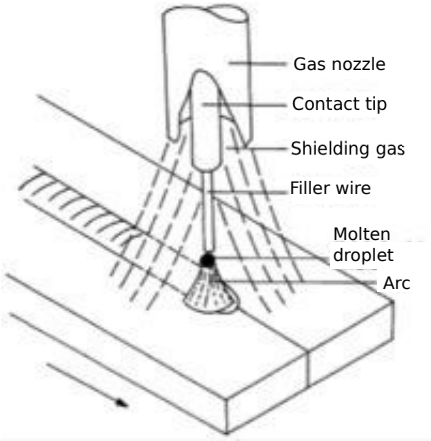

Figure 2.1 – Illustration of MIG welding (After Norrish, 1992).

The wire feed rate (or melting rate) is related to the welding current in Eq 2.1, developed by Halmoy (1979). The terms in the equation represent the wire feed rate (metres per min) stick out of the wire (s), the α term is a constant related to the localised arc heating the wire tip, the β is a constant related to the mean resistivity of the electrode stick out (Modenesi, 1990), and I is the current (amperes). This equation demonstrates that for an increased wire feed rate, there is a necessary increase in arc current.

$$w = \alpha.I + \beta.sI^2. \tag{2.1}$$

An important aspect of MIG welding is the various mechanisms of material transfer that can be used. These are all defined by operating parameters and are illustrated in Figure 2.2. CMT welding operates using short circuiting transfer mode.

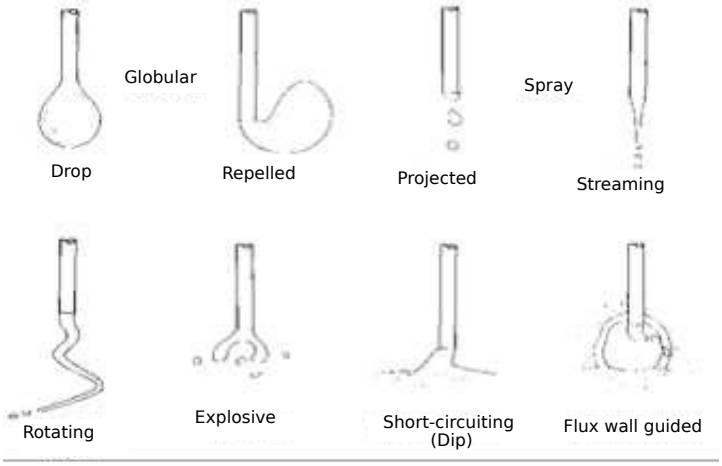

Figure 2.2 – Illustration of various modes of material transfer for MIG welding (After Messler, 2004).

Short-circuit (or dip) transfer generally encompasses the lowest range of current

and electrode diameters (Messler, 2004), and therefore the heat input for this transfer mechanism is lower than for spray and globular. The dipping of the electrode into the molten weld pool causes a drop in voltage. This coincides with an increase in current due to the short circuit, causing metal transfer to occur by surface tension (Messler, 2004).

CMT was developed by Fronius (Bruckner, 2005) and works on the principles of controlled dip transfer (or short circuit) (Pickin and Young, 2006; Pickin et al., 2011). Whilst this is the key point of the process, it is actually more complex (see Figure 2.3).

The power source is controlled by a high speed digital processor. An innovative wire feed system which operates on a push-pull mechanism, oscillates the wire backwards and forwards in and out of the melt pool. During the first stage (Figure 2.3(a)) there is an arc between the wire and the weld pool. As the wire is fed at a faster rate than the melting rate, it soon touches the weld pool where it short circuits (Figure 2.3(b)). The controller detects the short circuit, and reduces the current. When the wire is dipped into the weld pool, the molten metal on the end of the wire is transferred to the weld pool by surface tension. The controller then retracts the wire (Figure 2.3(c)), re-establishes the arc and the process is repeated (Figure 2.3(d)).

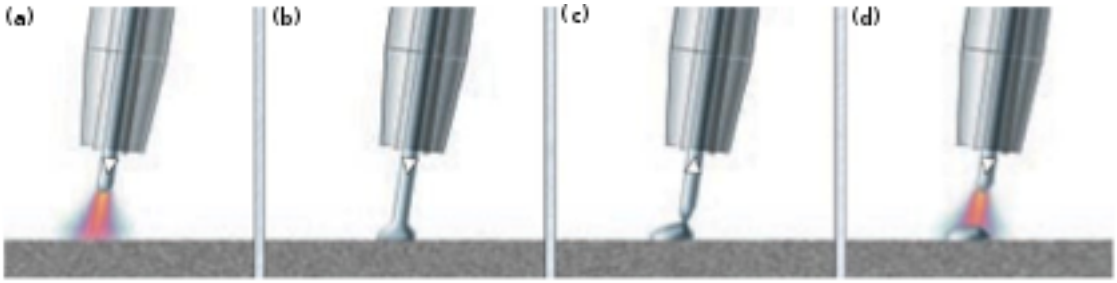

Figure 2.3 – Illustration of CMT process (Bruckner, 2005) (a) Arc established between wire and weld pool. (b) Wire is 'pushed' into weld pool by controller, the arc is short-circuited, and the voltage and current are reduced. (c) The controller 'pulls' back the wire, and the molten material at the end of wire is transferred to weld pool by surface tension. (d) The process repeats.

A typical CMT waveform is shown in Figure 2.4(a). It illustrates the arcing phase where there is a constant voltage, and shows how the voltage drops as the wire is dipped into the molten pool, i.e. the short circuiting phase. The process can also operate in a hybrid mode, known as CMT/Pulse mix. An example waveform is shown in Figure 2.4(b). The advantage of this over standard CMT is that thicker section material can be welded, for minimal increase in arc energy. The application of the pulses is typically during the CMT arcing phases.

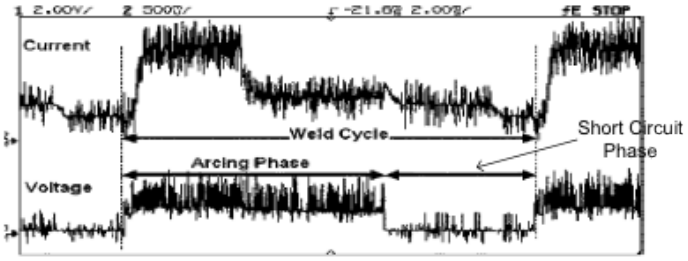

(a)

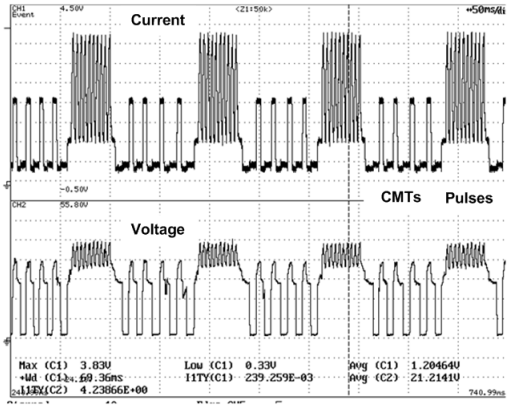

(b)

Figure 2.4 – (a) An example CMT waveform (Pickin and Young, 2006) and (b) Example CMT/Pulse hybrid waveform with 5 CMTs and 10 Pulses.

A recent study (Benoit et al., 2011) applied the CMT process to IN718, which is a superalloy considered more weldable than Rene 80. The authors reported that the process produced a sound weld bead with reduced HAZ, reduced residual stress levels, which was also free of defects (e.g. cracks or porosity). However, it is difficult to comment on how suitable the process is to welding superalloys in general because they only analysed one weld bead.

Therefore this study aimed to investigate the feasibility of using CMT MIG welding for the repair of Rene 80 nickel superalloy.

The aims of this chapter were:

1. To investigate the effect of grain size on HAZ crack susceptibility in Rene 80 castings;
2. To undertake an initial study on the influence of welding parameters on crack susceptibility of Rene 80;
3. To examine the potential of the low heat input CMT welding process for repair welding.

This chapter is a continuation of work on Rene 80, started in a MSc project by Courtot (2007) and includes the data from this thesis for comparison with the data obtained in this PhD.

2.2 Methodology

2.2.1 Materials

In this chapter, large grain sized Rene 80 nickel-based superalloy was studied, and was compared with data from an MSc thesis (Courtot, 2007) that used the same material, but with a smaller grain size. The material was supplied having been hot isostatically pressed and then solutionised (Figure 2.5).

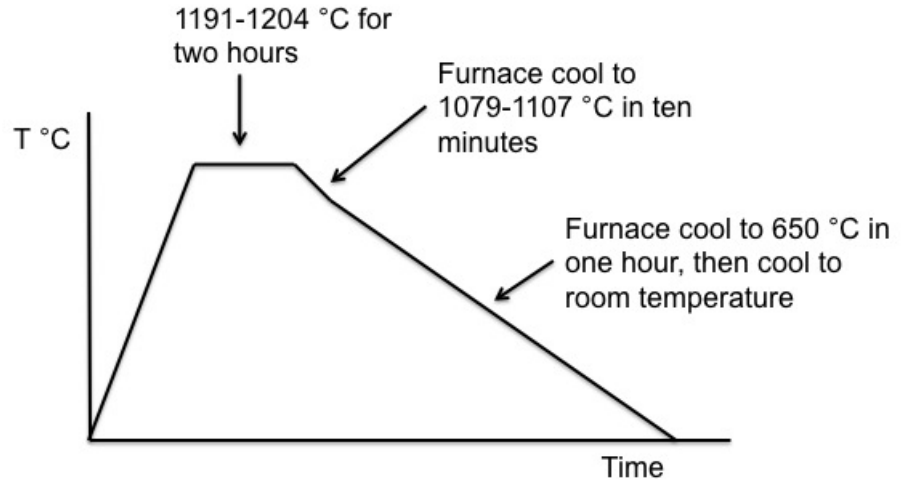

Figure 2.5 – Solution heat treatment applied to material prior to welding. This treatment is based on data from the GE specification GE C50TF28 discussed in Chapter 1, referenced by Dyrkacz (1979). Note that exact numbers are proprietary information of the material supplier.

The smaller grain size material was cast at 1380 °C, and the larger was cast at 1420 °C. The material was supplied as blocks with dimensions 110x70x22 mm. The consumable filler wire is IN625 of 1.2 mm diameter. Details of the standard nominal chemical composition of the filler and base materials are listed in Table 2.1.

Table 2.1 – Specification chemical composition (in % weight) of Rene 80 and IN625.

Alloy	Cr	Co	Mo	W	Al	Ti	Hf	C	B	Zr	Ni
Rene 80 (Substrate)	14	9	4	4	3	4.7	0.8	0.16	0.015	0.01	Bal
IN625 (Filler)	23	1	10		0.4	0.4		0.1			Bal

2.2.2 Welding trials

Prior to welding, the blocks were cleaned using an angle grinder, then wire brushed and finally wiped with acetone. The blocks were placed on a flat surface, and clamped at either end of the length of the blocks. No backing bar was required due to the large thickness of the material and the lack of full penetration expected. A Fronius TransPulse Synergic 500 power source with the Fronius VR700 CMT wire feeder and a Fronius Robotica Drive CMT torch was used for the trials. The power

source was connected to an ABB IRB2400 M96 six axis robot. For shielding gas, argon with 2.5 % CO_2 was used.

Single pass bead-on-plate welds of 70 mm in length were laid on the blocks of material, as illustrated in Figure 2.6. This figure also illustrates the plane (grey dashed lines) through with the material was cut to produce an as-welded and PWHT block for subsequent metallographic analysis.

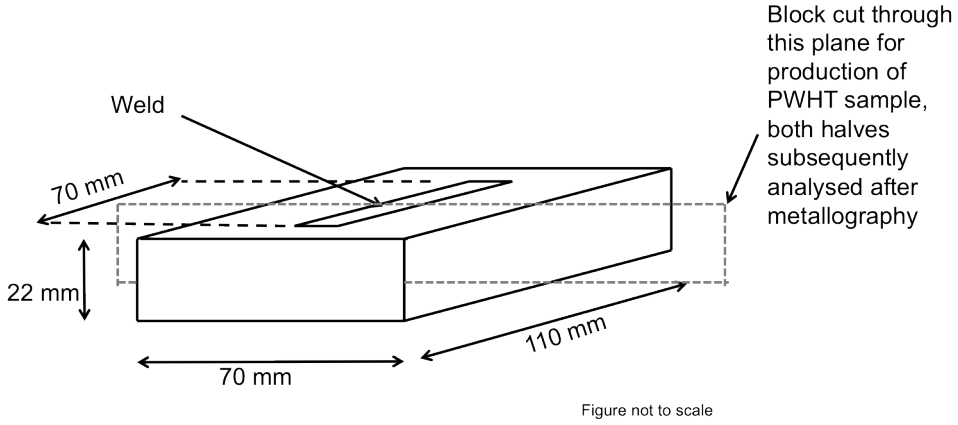

Figure 2.6 – Illustration of material dimensions, location and size of weld relative to plate, and plane through with material is cut for production of as-welded and PWHT samples.

The welding parameters were originally used in an MSc project on the smaller grain sized material (Courtot, 2007). The same parameters were then applied to the larger grain sized material in this study. Note that the parameters were split into CMT and the hybrid CMT/Pulse version. The pure CMT used a synergic mode setting in the machine for the filler wire diameter (although as there was not one for the specific wire, a high chromium steel program was used). The CMT/pulse mode was controlled manually, with CMT/Pulses and the pulsing parameters defined individually. The parameters were designed using the Design of Experiments technique and further details on this can be found in Courtot (2007) and the parameters are listed in Tables 2.2 and 2.3. Note that the arc length correction factor is a method for adjustment of the distance of the end of the electrode to the weld pool. In the CMT/pulse waveform, the CMTs and pulses per cycle are adjusted as outlined in the table. In the CMT/pulse waveform, the wire feed speed was set as a constant.

Table 2.2 – Combinations of CMT mode parameters used in trials.

Wire feed speed	Welding speed	Arc length correction factor
m/min	m/min	%
6	0.6	10
6.5	0.4	10
6.5	0.6	-20
6	0.4	-20

Table 2.3 – Combinations of CMT/Pulse mode parameters used in trials.

Wire feed speed	Welding speed	No of CMTs	No of Pulses	Time at base
m/min	m/min			(ms)
6.5	0.3	5	30	2
6.5	0.5	5	30	2
6.5	0.5	1	10	4
6.5	0.5	5	10	2
6.5	0.3	1	10	2
6.5	0.5	1	30	2
6.5	0.3	5	10	4
6.5	0.3	1	30	4
6.5	0.5	5	30	4

The transient waveforms were monitored for calculation of arc power. The waveforms were recorded on an AMV 4000 arc watch monitoring system with voltage and current monitoring devices. The arc power was calculated by the average instantaneous method, as described by Joseph et al. (2003), and was calculated as per Eq. 2.2.

$$P_{AI} = \sum_{i=1}^{n} \frac{I_i V_i}{n} \tag{2.2}$$

Where I is the current (A), V is the voltage (V), and n the time step. Note that the work in this thesis is only interested in the relative difference in power between the parameters of this process only, so efficiency was ignored.

2.2.3 Post weld heat treatment

After welding, the substrates with welds were sectioned into two halves, as illustrated in Figure 2.6. One half of each substrate was then sectioned for as welded analysis (see section 2.2.4.1 for details), whilst the other section was given a post-weld heat treatment (PWHT). This heat treatment was applied to the material by the industrial sponsors. The heat treatment was near identical to the solution cycle illustrated in Figure 2.5, but with a faster cooling rate from the solution cycle. The heat treatment was performed in a pure argon environment. Note that the exact details are proprietary information of the sponsor company. Only the welds produced

on the large grain sized material were given the PWHT.

2.2.4 Metallography

2.2.4.1 Sample preparation

Both the PWHT and as-welded samples then had one section cut from each weld, generating a sample in each condition for metallographic examination for each set of parameters.

The samples were cut using a Struers Discotom-65, and then mounted using epoxy resin. Three-stage grinding (120, 240 and 1200 grit) followed by polishing at 6 µm diamond suspension and 0.05 µm colloidal silica was used. The samples were etched using Kalling's number 2 waterless reagent (2 g of $CuCl_2$, 40 ml of HCl and 80 ml of methanol).

Weld bead macros were captured using a Nikon Prysm system, and microstructural investigations to detect cracks were by a Nikon Optiphot microscope with x2.5 to x40 objective lenses. Carl Zeiss Axiovision software was used for all measurements. The weld bead geometry values were measured, and a typical macro showing these measurements is shown in Figure 2.7(a). The dilution ratio was also calculated from the measurement of the area of weld above the surface (A1), to the total weld bead areas (A1+A2). Figure 2.7(b) illustrates the method for measuring a typical crack.

Savage et al. (1977) discussed the merits of total (TCL), average (ACL), and longest crack length (LCL) for indicating crack susceptibility. The longest crack length was suggested as the most sensible indicator of cracking, but it is also the most sensitive to variation and therefore requires more than one section per weld to form an average of a number of sections. As only one section per weld was analysed, it was more expedient to use ACL for the analysis. In addition, the ACL is less affected by the weld size, unlike TCL which is likely to scale with the weld bead size.

The total crack length (TCL) was calculated by summing all the cracks measured in the section. The average crack length was calculated by dividing the TCL by the total number of cracks in the section measured. Cracking is presented in either the as-welded (AW, predominantly liquation cracking), or post-weld heat treated (PWHT) form.

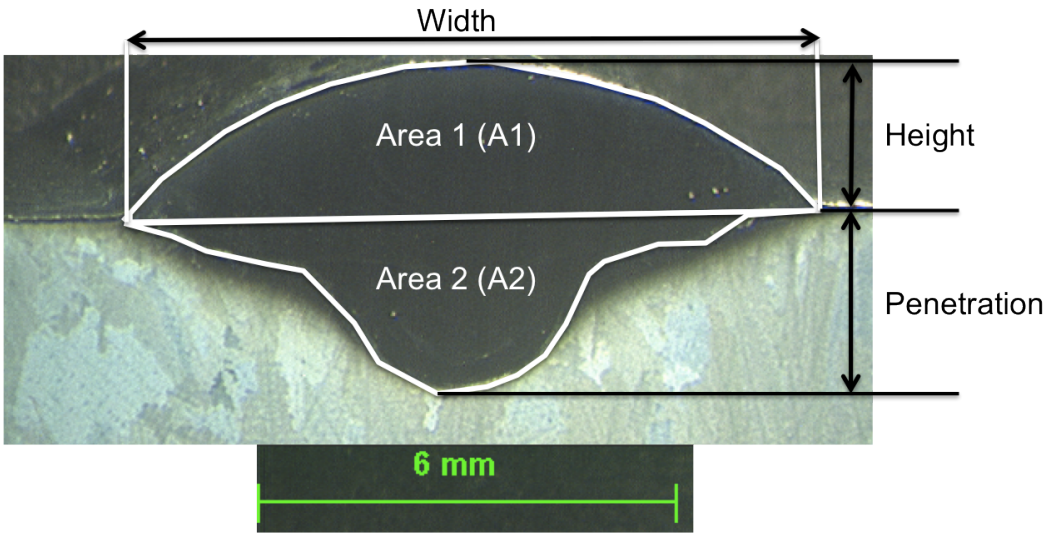

(a)

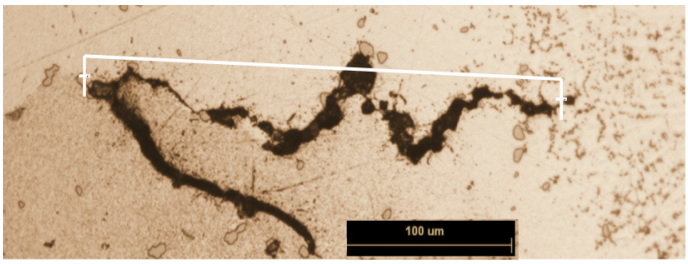

(b)

Figure 2.7 – Illustration of (a) weld geometry showing the width, height, penetration, and areas A1 and A2, and (b) An example illustration of how a crack's length was measured.

2.2.4.2 Grain size measurement

There are many different procedures for calculating grain size in multiphase alloys. In this study, the linear intercept method was used, based on work by Wurst and Nelson (1972) and is similar to the method described in the ASTM technical report E112-88 (ASTM, 1988).

The method involves drawing a line that intersects through the image of the grain structure. The number of grain boundaries that are intercepted was counted, and this data was then put into Eq. 2.3, to calculate the average grain diameter, D:

$$D = 1.56\frac{C}{MN} \tag{2.3}$$

Where C is the total length of the line, N the number of intercepts on this line, and M is the magnification.

The grain size was measured from the bulk of the material. For each grain size measurement, one sample was sectioned and prepared using the standard metallographic preparation described previously. For each sample, three lines were used and intercepts counted. The lines were positioned at different orientations and different positions within the bulk, therefore ensuring a fair overview of the whole bulk structure, and including any effect of elongated columnar grains. Note that the grain size around the periphery was significantly smaller and was not measured.

2.2.5 Statistical analysis

Due to the significant issues caused by the variability in cracking observed (as will be illustrated in the results section), the cracking data was also analysed using a statistical analysis software package, Design Expert 7.1 (STAT-EASE, 2008). This software is useful for experimental design as well as regression analysis on data produced from the experiments. As in the present case, this is accomplished using the surface response historical data function. This involves identifying factors (e.g. welding parameters) and responses (e.g. ACL), and inputting the data into the software. The software attempts to fit a model of best fit and produces various statistics from analysis of variance, or ANOVA. There are a number of different statistical terms which are produced, and the important ones are outlined in Table 2.4.

Table 2.4 – Descriptions of the statistical terms used in ANOVA in the analysis of the data studied using Design Expert software. Note that value required column and description refer to the comments from the handbook of the software (STAT-EASE, 2008). Please see Appendix A.1 and A.2 for exact excerpts from the software's handbook.

Term	Value required	Comments
Model p-value	<0.05	A measure of whether the model applied to the data is significant, based on the model f-value. If this value is <0.05 then the model is significant.
Factor p-values	<0.05	A measure of whether a particular factor is significant. A value of less than 0.05 indicates that a factor is significant.
Model f-value		A value comparing the variance in the model with the variance in the error. The larger the better.
Adeq Prec	> 4	Signal to noise ratio.
R^2	As close to 1 as possible	Measure of variation around mean explained by the model.
Pred R^2	"	Measure of variation in new data explained by the model. Pred $R^2$and Adj R^2should be within 0.2 of each other otherwise there is either a problem with the model or the data.
Adj R^2	"	Measure of variation around the mean explained by the model, adjusted for the number of terms in the model.

In some cases, the software recommends a transformation is applied to the response data, to help produce a better fit to a model. However, in this Chapter, there was no requirement for this. Also, the types of models which can be used range from linear, two factorial interactive, to more advanced quadratic and cubic.

For this Chapter, the software was used to (1) study the influence of the grain size on as welded (liquation) cracking, (2) study the influence of welding parameters on ACL in both the as-welded and PWHT conditions, and (3) study the influence of weld bead geometries on ACL in both conditions. Note that the grain size was set as a categoric factor, which is useful for when the data is not considered numerical.

2.3 Results

2.3.1 Grain size

The average grain size measurements for the bulk size, which were taken from the middle of the material, are reported in Table 2.5. The large size was approximately 4.85 mm, and the smaller was an average of 3.53 mm.

Table 2.5 – Results of average bulk grain size measurements.

Average large grain size				Average small grain size			
Line no	Length (mm)	No of intercepts	D (mm)	Line no	Length (mm)	No of intercepts	D (mm)
1	14.67	9	5.08	1	14.67	13	3.52
2	15.67	9	5.43	2	15.67	13	3.76
3	11.67	9	4.04	3	11.67	11	3.31
Average	-	-	4.85	Average	-	-	3.53

In Figure 2.8(a) and (b) the macros for small and large grain sized materials are shown respectively. It is clear from comparing these that there is a substantial difference between the overall grain structures. In general, both show elongated grain growth from the chill grains towards the bulk (centre) of the material. In Figure2.8(c) and (d), it is clear that the size of the bulk grains are different.

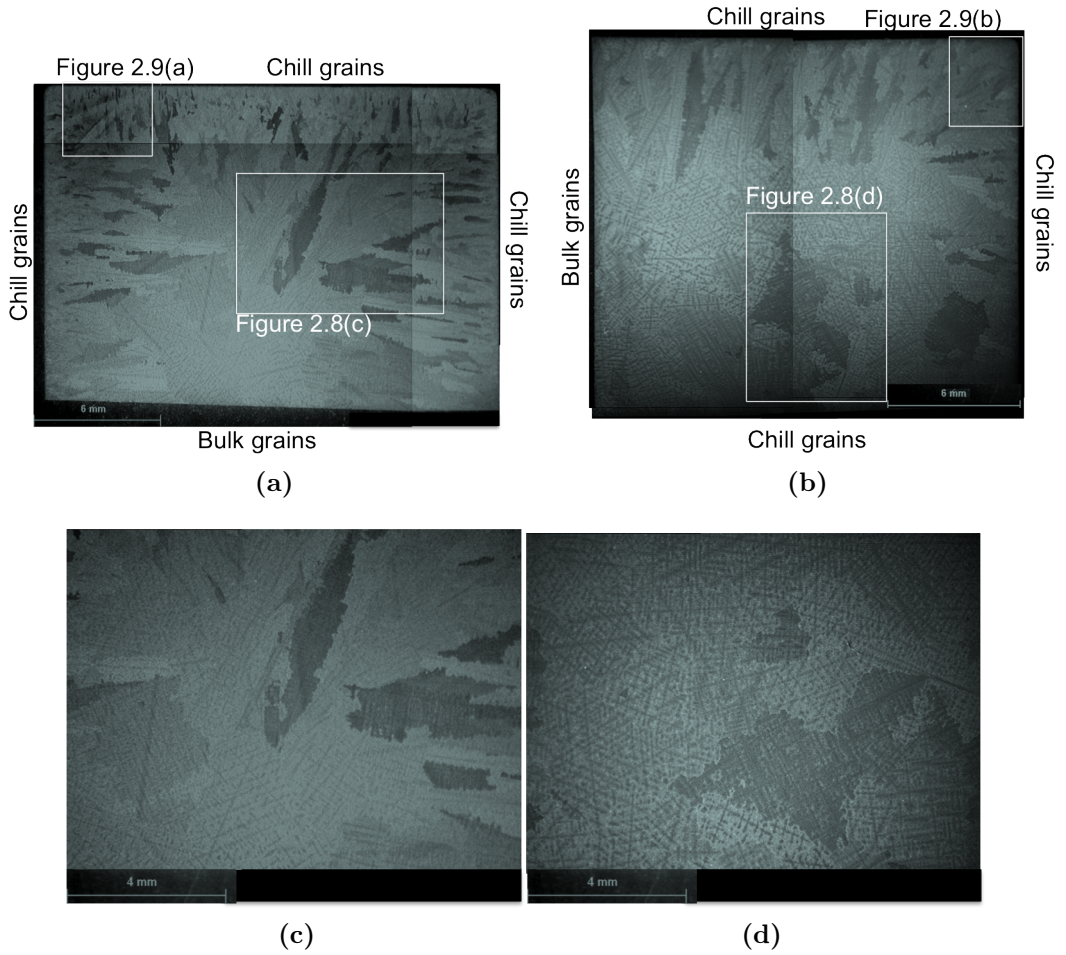

Figure 2.8 – A comparison of the two different material's grain structures. (a) Macro of small grain size structure and (b) Macro of large grain size structure. (c) A higher magnification of the bulk grain sized region of the smaller grain sized material, and (d) A higher magnification of the bulk grain sized region of the larger grain sized material.

The grains at the edges, known as the chill grains, are illustrated in Figure 2.9. Again here, there is a visual difference in the size and structure of these in the two material batches. The smaller grained material (Figure 2.9(a)) has smaller chill grains than the larger material (Figure 2.9(b)).

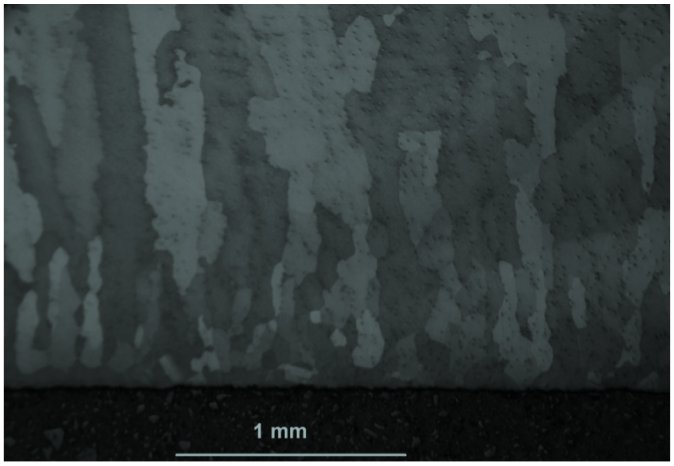

(a)

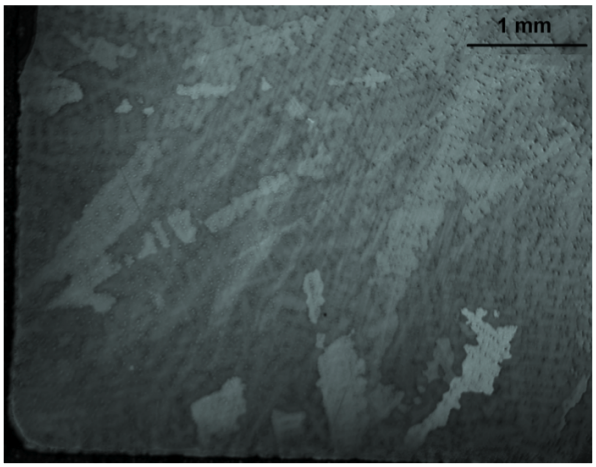

(b)

Figure 2.9 – Higher magnification images of chill grain regions as outlined in Figure 2.8. (a) small grain size and (b) large grain size structures.

2.3.2 Cracking results

2.3.2.1 Effect of grain size and parameters on as-welded cracking

The ACL versus power is plotted in Figure 2.10(a) for both process types and grain sizes. The first thing that is apparent is the large statistical variation, which makes interpretation difficult. The results indicate that there may be a correlation between power and ACL for both processes, with the exception of a couple of outliers. Additionally, the plot appears to indicate that the larger grain size possibly increases the ACL for both the CMT and CMT/Pulse processes.

The ACL versus welding speed plot in Figure 2.10(b) appears to show no obvious relationship. There also appears to be a lot of variation in cracking values for the CMT/Pulse, which may be as a result of the ranges of powers used at these speeds.

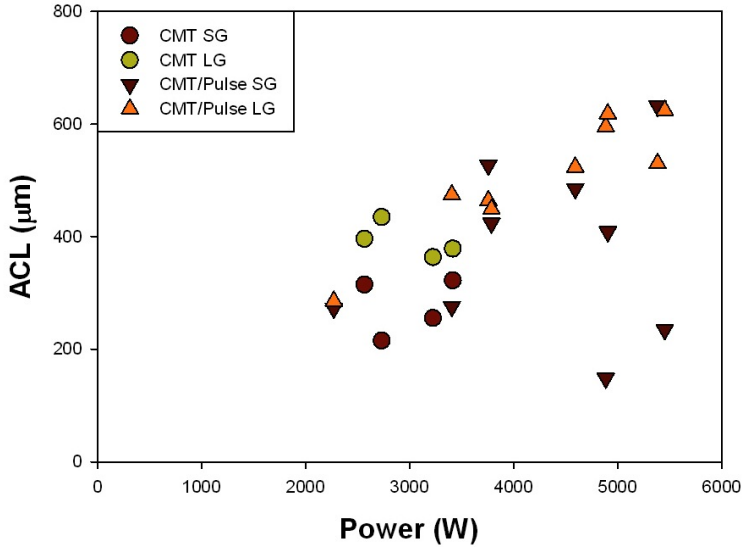

(a)

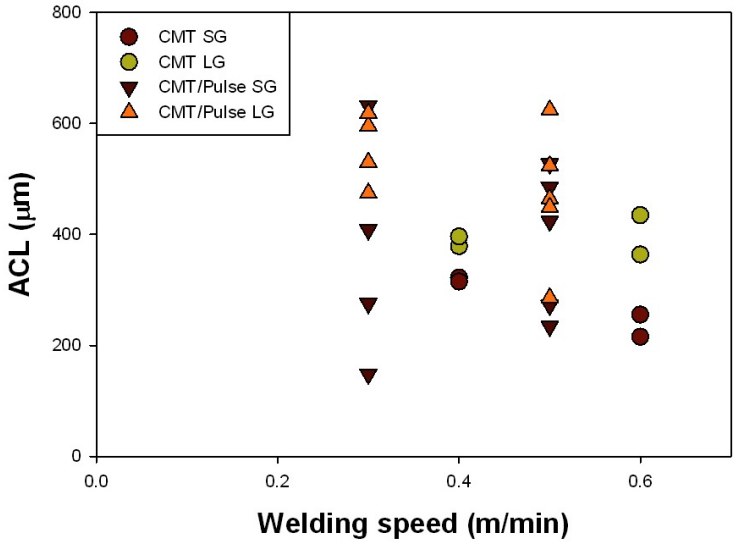

(b)

Figure 2.10 – Scatter plots showing (a) ACL versus arc power, and (b) ACL versus welding speed, for the as-welded condition. Note small grains (SG) and large grains (LG) are differentiated in the key. Please note that the small grain size data used in this plot was taken from the MSc project by Courtot (2007).

Because of the difficulties in obtaining a clear relationship between welding parameters and cracking, the data was analysed using the Design Expert 7.1 statistical analysis software as discussed in section 2.2.5. In Figure 2.11, it is shown that there is a clear relationship between increasing welding power and increasing ACL, and the ANOVA also reports this term as being statistically significant (see p-values, Table 2.6). Figure 2.11 also shows that there is no relationship between welding speed and the ACL, and this factor also is shown to be statistically insignificant

(Table 2.6). In the figure, the minimum and maximum values of the welding speed ranges (0.3 m/min and 0.6 m/min respectively) are plotted, and because the lines overlap each other, this indicates that the factor is not significant.

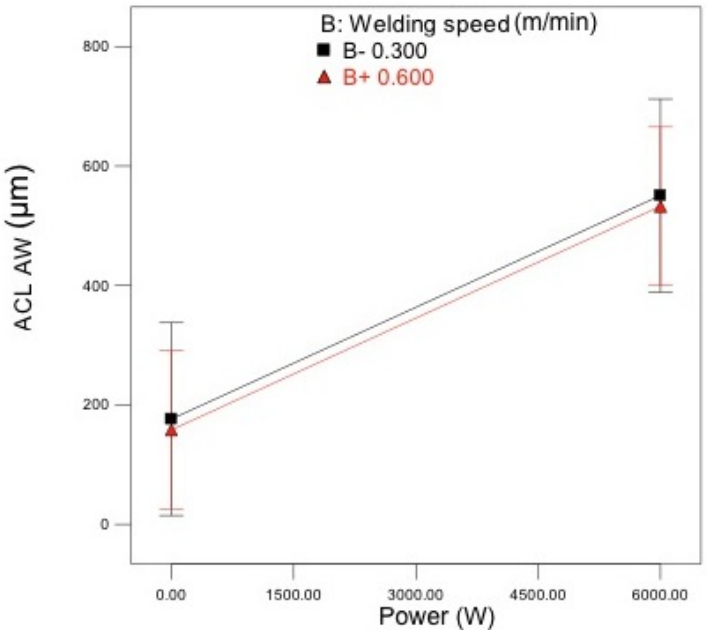

Figure 2.11 – Relationship between power, welding speed, and ACL for as-welded condition, from the statistical analysis. The welding speed is represented by the two lines, each of which represent the minimum and maximum welding speed range. Please note that the small grain size data used in this plot was taken from the MSc project by Courtot (2007).

The statistical analysis software was also used to assess the true influence of grain size. In Figure 2.12, it shows that the larger grain sized material generated larger ACL values. However, perhaps more significantly, the ANOVA results in Table 2.6 illustrate that the grain size is termed to be a statistically significant factor influencing the ACL.

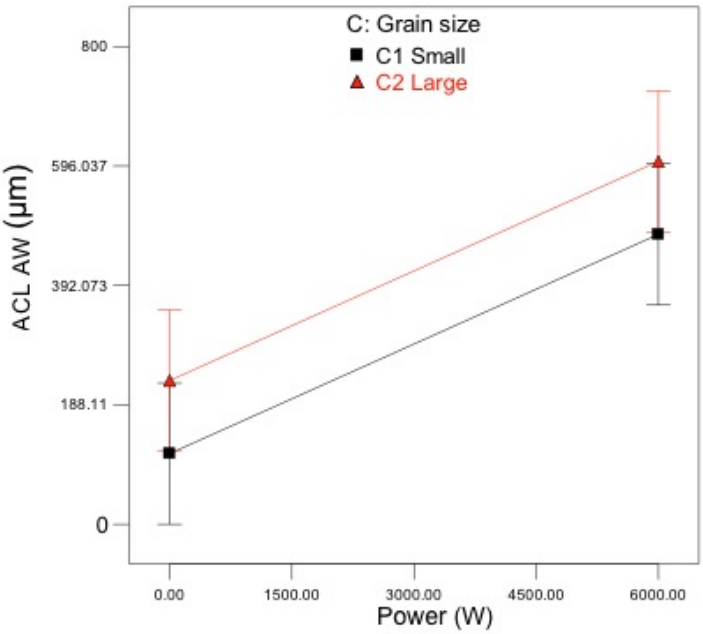

Figure 2.12 – Relationship between power, grain size, and ACL for as-welded condition, from the statistical analysis. Please note that the small grain size data used in this plot was taken from the MSc project by Courtot (2007).

Table 2.6 – Details of the model type and respective information from the statistical analysis on the effect of welding parameters and grain size on ACL for as welded condition, and the effect of welding parameters on ACL in PWHT condition. The power, welding speed and grain size are all factor p-values.

	As welded	PWHT
Model type	Linear	Linear
Transformation	None	Power
Adeq Prec	8.019	5.105
Model f-value	6.6	4.38
Model p-value	0.0024	0.0258
R^2	0.4737	0.2942
Pred R^2	0.4019	0.0895
Adj R^2	0.2461	0.2269
Power (A)	0.01	0.0155
Welding speed (B)	0.779	0.9927
Grain size (C)	0.0062	Not in Model

2.3.2.2 Effect of PWHT on cracking

In this section of results, only data from the large grain sized material was studied. Again, all results have an issue with variability and therefore this was considered when assessing the plots.

A plot of the ACL versus power in the as welded and PWHT specimens is shown in 2.13(a). As per the comparison of grain size effects results, there does appear to be a trend between the power and increasing ACL, although there is more scatter.

It is also clear from Figure 2.13(b) that there is no relationship between the welding speed and the ACL in the PWHT results either.

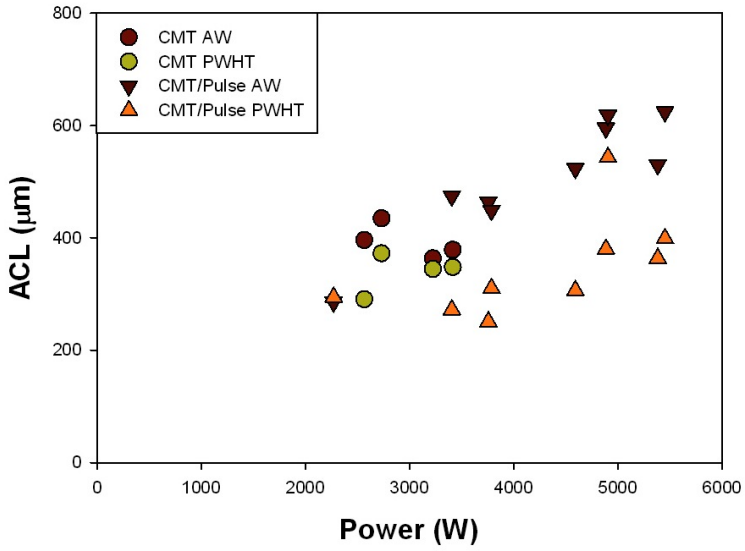

(a)

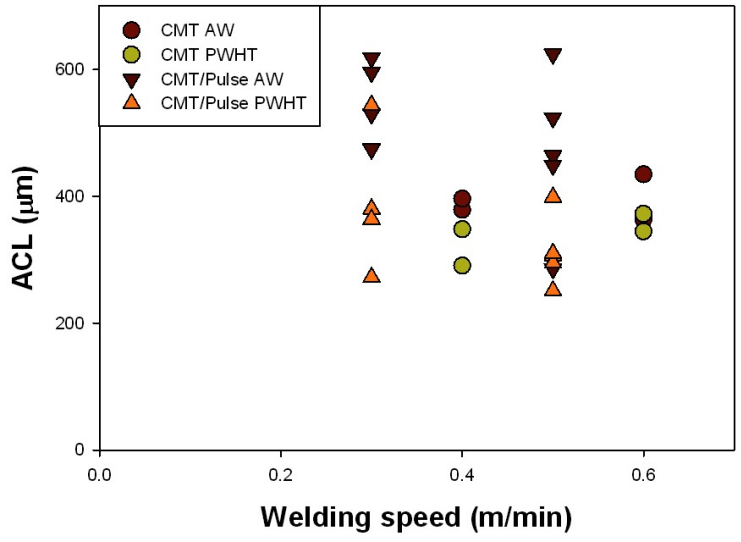

(b)

Figure 2.13 – Scatter plots showing (a) ACL versus arc power, and (b) ACL versus welding speed, comparing the as-welded and PWHT conditions.

Again, because of the lack of clarity from the plots in Figure 2.13, the statistical analysis software was used to assess the influence of the power and welding speed on PWHT cracking. When viewing Figure 2.14, care must be taken due to the application of the power transformation (see Equation 2.4) to the response data, which converts a value of 200 µm to approximately 0.001, and a value of 800 to 0.00002. Taking this into account, the plot illustrates that cracking increases with power (as per the as-welded samples) and is statistically significant (see factor p-

value Table 2.6). Note that error bars with high power were greater. There is still no influence of the welding speed which was also shown to be statistically insignificant (see Table 2.6). As with the as-welded results, the welding speed is represented by the two curves in Figure 2.14, with the minimum and maximum welding speeds plotted. As there is a near overlap of the plots, the term is assumed to be insignificant in its effect on the response.

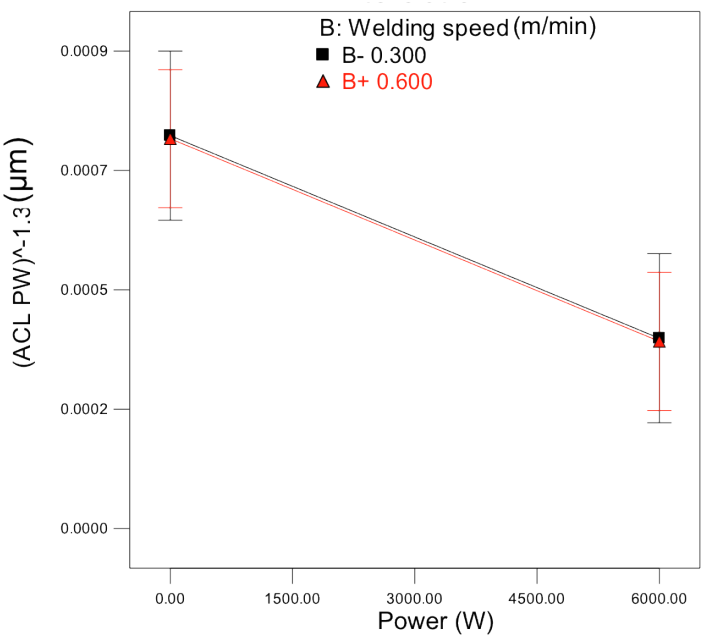

Figure 2.14 – Relationship between power, welding speed, and ACL for PWHT condition, from the statistical analysis. The welding speed is represented by the two lines, each of which represent the minimum and maximum welding speed range.

$$y' = (ACL)^{-1.3} \tag{2.4}$$

The PWHT appears to have reduced the ACL, which is observed in Figure 2.13. This is interesting, because when the total crack length is plotted for each weld as in Figure 2.15, the cracking is shown to have increased.

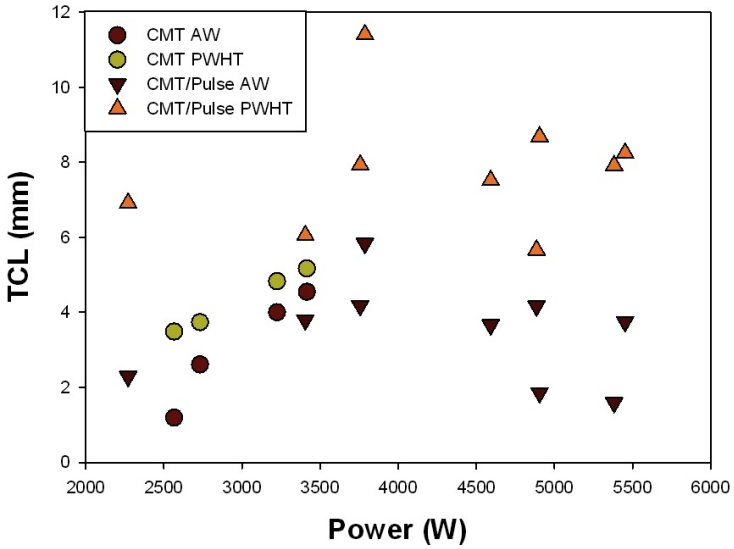

Figure 2.15 – Scatter plot showing the effect of PWHT on TCL versus power.

Despite there being an increase in total cracking, the reduction in ACL is due to a greater number of small cracks present in the sample after the PWHT. To illustrate this, two samples were analysed to show the variation in lengths of the cracks within the section. The results (Figure 2.16) show that there are a significantly greater number of small cracks (less than 400 μm) in the PWHT condition when compared with the as-welded condition.

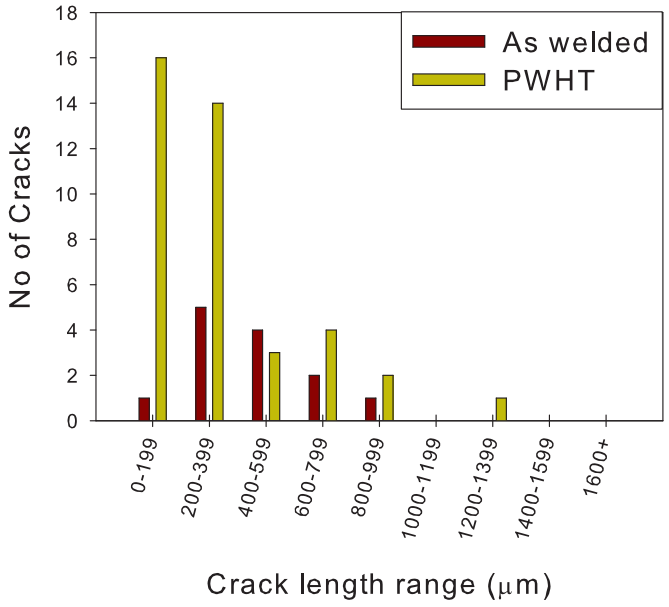

(a)

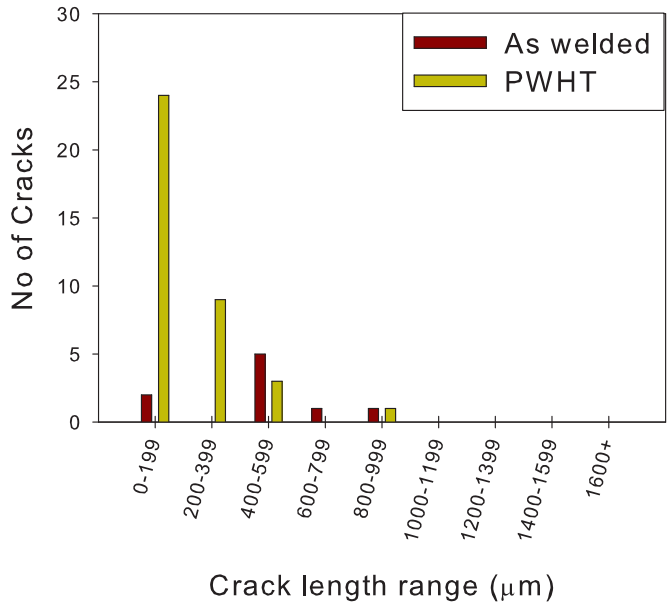

(b)

Figure 2.16 – Distribution of crack lengths in two separate CMT/pulse mix welds with similar processing conditions, both produced at 0.45 kJ/mm heat input and 0.5m/min welding speed. (a) CMT/Pulse mix ratio of 5/30 and (b) CMT/Pulse mix ratio of 1/10.

2.3.2.3 Effect of weld geometry on cracking

As an additional point of interest, the relationship between weld bead geometry and ACL was studied using the statistical analysis software. In Figure 2.17 the

relationship for the ACL with the height, width, and penetration for both conditions, is plotted as a perturbation plot. The perturbation plot shows how each factor affects the response, with a normalised X-axis. In Figure 2.17(a), the most interesting thing is that cracking appears to increase with increasing weld width. This term has a p-value of 0.0772 (Table 2.7), which is above the 0.05 limit that the software recommends a term is significant, but is below a value of 0.1 which the software terms as insignificant (STAT-EASE, 2008). Therefore, the terms which are within this range are still considered. However, the weld penetration and height are shown to be statistically insignificant, so their influence on the response in the figure is to be ignored. Similarly, Figure 2.17(b) plots the same, but from the ANOVA statistics it is now only the weld height which is a statistically significant term, with ACL increasing with increasing height.

Table 2.7 – Details of the model type and respective information from the statistical analysis on the effect of weld bead geometry on ACL for as welded and PWHT condition. Again, the width, penetration, height, dilution ratio and fusion zone area terms are the p-values. Note that the software's manual (STAT-EASE, 2008) suggests that a p-value of below 0.05 is a significant term, whilst only above 0.1 is a term insignificant. As a result, there is some uncertainty as to whether some of the terms in this table are significant.

	Penetration/Width/Height		Fusion zone area/Dilution ratio	
	As welded	PWHT	As welded	PWHT
Model type	Linear	Linear	Linear	Linear
Transformation	None	None	None	None
Adeq Prec	5.135	6.942	4.019	7.414
Model f-value	2.69	6.73	2.37	8.66
Model p-value	0.0772	0.0031	0.1204	0.0021
R^2	0.3095	0.5286	0.1997	0.4770
Pred R^2	-0.2546	0.2959	-0.1393	0.2420
Adj R^2	0.1944	0.4501	0.1155	0.4220
Width (A)	0.0783	0.5078		
Penetration (B)	0.6940	0.3309	Not in model	Not in model
Height (C)	0.6360	0.0451		
Dilution ratio (A)	Not in model	Not in model	0.0969	0.0020
Fusion zone area (B)			0.4357	0.2743

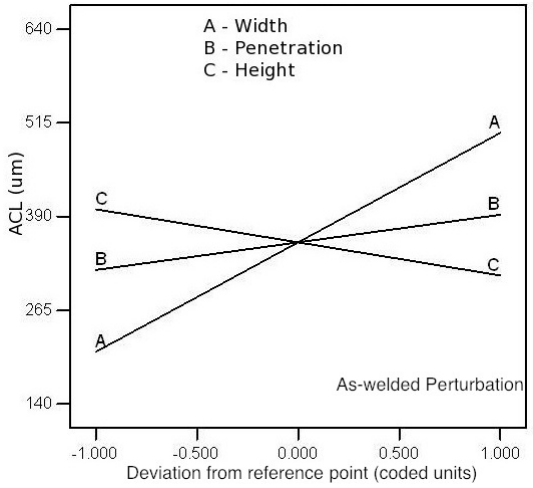

(a)

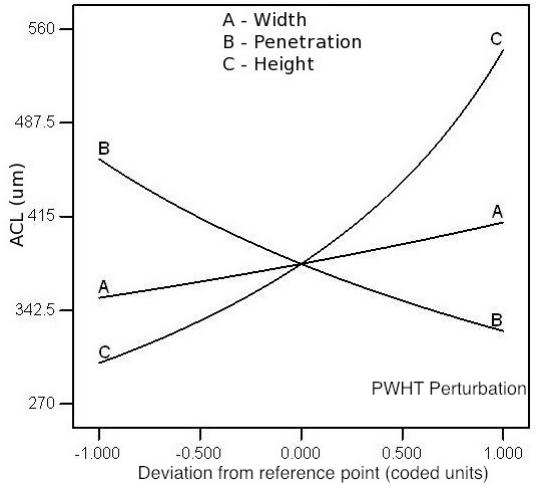

(b)

Figure 2.17 – Perturbation plots illustrating how each weld bead geometry measurement relates to the ACL value for (a) as welded condition, and (b) PWHT. The x-axis corresponds to a generalised variation from the minimum (-1) to maximum (+1) for each factor. For example, in (a), the ACL increases as the width (A) and penetration (B) increase, but decreases as the height (C) increases.

The weld bead fusion zone area and dilution ratio have also been studied, and this is shown in Figure 2.18 for both conditions. First of all, the statistics in Table 2.7 indicate that the dilution ratio has a p-value (for the as-welded condition) within the range where the software doesn't rule out the term as being significant or otherwise, and is a significant factor on the PWHT response. However, the fusion zone area is not significant, for both conditions. In both Figure 2.18(a) and (b), the ACL increases with increasing dilution ratio.

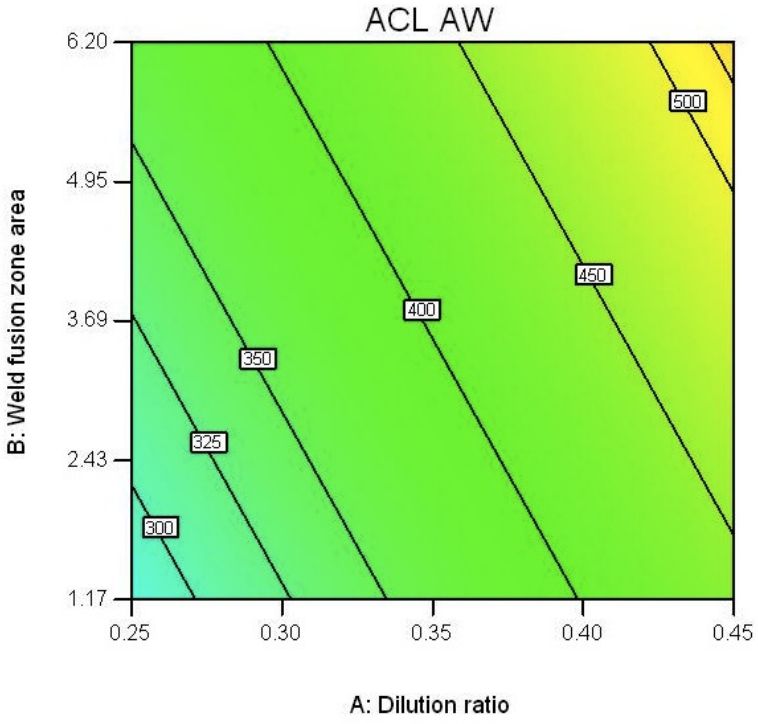

(a)

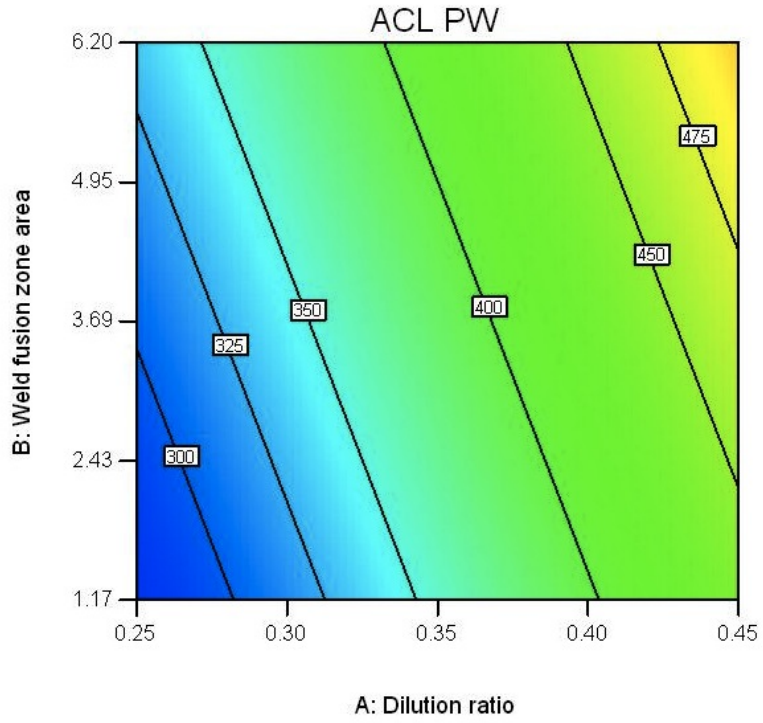

(b)

Figure 2.18 – Contour plots showing the relationship between ACL and weld bead fusion zone area and dilution ratio, for (a) as-welded condition and (b) PWHT condition. The contour lines represent the ACL value.

2.4 Discussion

2.4.1 The influence of grain size on cracking

Within this chapter, the effects of grain size are described on the average crack length in the as-welded condition only. The influence of the grain size on cracking in the study was initially unclear. The CMT process results appeared to show a clearer trend (although this had less data) than the CMT/Pulse mix results. However, there is clear evidence of statistical variability in the cracking results, causing difficulties in trying to determine the key factors. Therefore, the statistical analysis was performed. This variability is due to the location of the weld bead relative to the grain boundaries and is discussed in the subsequent chapters.

This analysis demonstrates that the grain size does have an effect, across all the data. The larger grain sized data shows a general increase in cracking compared to the smaller grain size. The statistics for this analysis, shown in Table 2.6, appear at first glance to be adequate but not excellent. This is due to the low R-Squared values. The variability in the cracking values means that it is difficult to fit a function through the outputs. Hence the R-squared term (which indicates the difference between the model and experimental values) is low. It is also possible that the R-squared value is low because not all of the influencing factors have been identified. However, the purpose of this study was not to produce a model from which we would predict the cracking susceptibility, and therefore as long as the predicted and adjusted R-Squared are within 0.2 of each other, this is acceptable (STAT-EASE, 2008). The model and the factors are shown to be statistically significant (through the f-value and p-values), and the signal to noise ratio (Adeq precision) is also acceptable. Additionally, the grain size was shown to be a significant factor, having p-value of 0.0062. Therefore, from the analysis it is clear that the grain size is a significant factor influencing the response.

It is interesting to compare this work with that of others related to the effects of grain size. As discussed in section 1.4.2, an increase in grain size leads to a decrease in the grain boundary area (Kou, 2003b), which also increases the concentration of liquating phases. The increased concentration inevitably leads to the increase in liquation susceptibility. A similar adverse effect of the coarser grain structure is the reduction in ductility, inhibiting the ability to withstand the high stresses developed during welding and cooling, which contributes to crack formation.

Thompson et al. (1985) and Lingenfelter (1997) both reported works on grain size effects in wrought alloys. These generally have much finer grain sizes, and it is difficult to compare with these results. However, the findings reported in this chapter agree with the theory of increased cracking susceptibility with increased

grain size.

Thompson et al. (1985) reported that every one micrometer increase in the grain size yielded an increase of 0.4 % in total crack length measured. For the present work, assuming a difference in grain size of 1320 μm, this should produce 528 % increase in cracking in the larger grain sized material. The results clearly do not show this. A key difference is that the work by Thompson et al. (1985) only studied grain sizes between 20 μm and 200 μm. It is possible that this relationship is not applicable above a certain threshold. It could also be due to other factors as discussed next.

One significant question is the variation in grain size from the surface of the cast blocks to the bulk and their relative influence on cracking. In both grain sizes studied in this chapter, the measurements occurred such that the majority of the measurement line was placed through the bulk of the material, where the grain size is significantly larger than around the edges (see Figure 2.8(a)). The size, and structure of these smaller chill grains (formed first during solidification of casting) was illustrated in Figure 2.9. Even without a quantitative study on these images, it is clear that the chill grains in the smaller sized material are indeed smaller than the chill grains in the larger sized material. Therefore the relative difference between the two materials should remain consistent.

The influence of the variation in grain size and structure should also include a consideration of the penetration of the weldments. All the welds were measured as having penetrated into the material in the range of 1.5 to 3 mm. In Figure 2.9, it is clear that the transition from the very fine grains to the elongated and larger grains is also in the range of 1 to 3 mm.

2.4.2 The effect of welding parameters on cracking

The use of the statistical analysis software has proven to be a useful tool for understanding the trends in the data, and has offered additional benefits in determining the statistical significance of a factor (e.g. power) against the responses (cracking).

The effects of welding process parameters on both types of cracking provided some interesting results. As would be expected, increasing welding power appears to increase the ACL for both conditions. This is as suggested by Danis et al. (2010), but as was discussed in Chapter 1 there is contradictory evidence to suggest that cracking decreases with increasing power (Richards et al., 1994). The power was shown to be a statistically significant term on the ACL in both conditions (Table 2.6). However, in both conditions the welding speed was not a significant factor, and therefore suggests that it offers no influence over cracking. This is as Danis et al. (2010) suggested, but there are many other studies which suggest that it does

have an influence, although these are contradictory as was discussed in section 1.4.2. Additionally, the narrow range of welding speeds studied may also have contributed to the lack of significance of this term in this study.

The effects of weld geometry on cracking in both conditions was unclear. The perturbation plots in Figure 2.17 illustrate the variation a factor has (from its minimum to maximum values) on the cracking. There is no obvious trend, particularly as the statistics of this analysis in Table 2.7 suggest that only the width on as-welded, and height on PWHT were significant terms. Both of these effects may be a reflection of increasing power which will cause both to increase, although the reason for the width being more significant for the AW samples and the height for the PWHT samples is unclear. Similarly, the relationship between dilution ratio, fusion zone area, and cracking in Figure 2.18 showed increased cracking with dilution ratio (and this is a significant term) but no significant relationship between fusion zone area and cracking. The fusion zones of welds with greater dilution ratios will have a greater proportion of base material which has poorer ductility and will therefore be more susceptible to cracking. This analysis illustrates that there is uncertainty in the relationship between weld geometry and cracking, which is in contrast to the discussion in section 1.4.2, which reviewed various literature which suggests there maybe a relationship between the two.

The results here clearly show problems in determining the effect of the welding parameters, which is corroborated by the discussion on the published works studying the parameter effects. To resolve these inconsistent findings, a systematic series of experiments will be reported in Chapter 3 which were completed using a laser and used a wider range of parameters.

Finally, it is important not to neglect the shielding gas used in these trials. For all the welds, argon with a small (2.5 %) amount of CO_2 was used. This is in contrast to most publications on welding of superalloys, where either pure argon or helium is used. Therefore, all subsequent work used a high purity argon gas.

2.4.3 The effect of PWHT on cracking

The results clearly indicate a significant effect of PWHT on cracking. However, the most interesting aspect is that the ACL appears to have reduced in all samples, possibly more substantially in the CMT/Pulse mix samples. However, the TCL plotted in Figure 2.15, shows clearly that the effect of the PWHT actually increases the overall cracking in the welds.

The reduction in ACL could, in a reasoned argument, be proposed as being due to the variation typically observed along the length of welds. In these trials, for all the samples, the half of the weld which was treated with the PWHT was always the

second half. It is logical to suggest that the reduced ACL after PWHT observation is due to a difference occurring in the second half of the weld, e.g. a greater build up of heat input.

An alternative reason for the reduction in ACL is related to the mechanism of strain age cracking. The PWHT will not only propagate existing cracks, it will also nucleate new cracks. Li (2007) found that cracks in PWHT samples contained a dual morphology, with one section possessing similar shape and liquid like interface with the matrix, whilst the second section had a sharper interface, indicating this was formed during the PWHT (which is a solid state form of cracking). The overall increase in the TCL is driven by the addition of new cracks, and the extension of existing cracks. Distinguishing between these different crack types is discussed further in Chapter 4.

The theory of reduced ACL by nucleation of smaller cracks is confirmed by the charts in Figure 2.16, which plot the distribution of cracks measured in two different samples. In both welds, there were a large number of cracks observed in the small crack length categories (0-199 μm and 200-399 μm) for the PWHT samples, whereas in the as-welded condition this was not the case. It is likely to be this second reason that is causing the observed reduction in ACL after PWHT.

2.5 Conclusions

The CMT welding process has been investigated for suitability of repair welding crack susceptible superalloy Rene 80. In this study, the influence of the grain size, the welding parameters, and the effect of PWHT have been investigated. The main findings from this chapter are:

1. Cracking is highly variable which makes interpretation of results difficult. The use of a statistical analysis software such as Design Expert can be a useful tool when interpreting such highly variable data. The software is able to indicate statistically significant terms;
2. The terms which appeared to have an effect are the power and grain size (on as-welded condition only), while the welding speed term was shown to not be a significant factor;
3. There was greater uncertainty over the influence of the weld bead geometry on cracking;
4. Finding metrics to assess cracking susceptibility is difficult. While ACL has the advantage that it is less affected by the weld bead fusion zone area and variability, it obviously had limitations when used to assess the severity of cracking in the PWHT samples;

5. There is a need to do a larger systematic study to more clearly identify the factors that affect cracking. This study will need to investigate a larger range of powers and welding speeds.

Chapter 3

Laser welding of Rene 80 nickel-base superalloys

3.1 Introduction

The review in Chapter 1 on liquation and PWHT cracking in Rene 80 indicated that there is still a lot to be learnt about this alloy's susceptibility to HAZ defects. Although there have been studies on the effect of alloy chemistry and pre-weld heat treatments, there is little knowledge of the influence of welding parameters on the crack susceptibility of polycrystalline Rene 80. In Chapter 2, it was concluded that the influence of welding heat input on cracking susceptibility is unclear. Additionally, the majority of papers available which have studied this alloy show a narrow window of parameters, and concentrate more on the metallurgical aspects. This is also broadly true for most studies on superalloy weldability.

It is important to understand the relationship between process parameters and the crack susceptibility of this alloy for repair of turbine components, to be able to produce effective repair procedures. Laser welding is an extremely useful welding process for studying the effect of welding parameters due to the ability to adjust the power and beam diameters independently. These parameters in combination with the welding speed enables the production of a range of thermal cycles, cooling rates, and heat inputs. In this chapter, a range of process conditions have been applied to Rene 80, and the influence on the as-welded and PWHT cracking has been assessed.

3.2 Laser welding

3.2.1 Laser welding of superalloys

Laser beam welding is a very flexible process. Whilst equipment is generally expensive and there are a number of safety issues, these factors are outweighed by the benefits offered. An excellent review of the technology, from first principles

to general operation is provided by Ion (2005) and another good overview is also provided by Steen (2010).

With regards to welding of superalloys, in particular gas turbine components, a report by Gandy et al. (2000) summarised the following advantages and disadvantages of the process for repair (Table 3.1).

Table 3.1 – Advantages and disadvantages of laser welding for superalloy repair (Gandy et al., 2000).

Advantages	Disadvantages
Localised heating and melting resulting in small HAZ	Expensive system costs
Automated process, typically faster than TIG	Typically inefficient systems (in terms of energy usage)
Allows easy application of inline powder delivery	Significant safety issues that need to be controlled

The application of laser welding is generally simpler than arc welding due to the reduced number of process parameters. The main parameters are power, beam diameter, and welding speed.

3.2.2 Laser welding of Rene 80

There are very few published works on laser processing of Rene 80. Österle et al. (2008) reported the cracking related to laser drilling of turbine blades made from the alloy, but laser drilling requires completely different processing conditions to laser welding.

Sexton et al. (2002) completed a study of laser powder cladding for repair of turbine blades and included Rene 80 as a substrate material. However, the only conclusion was that there was no cracking in the base material, but few results were presented. However, from the work presented (a total of five different substrate materials were used), laser powder deposition was found to be better than TIG cladding for repair due to better mechanical properties (caused by less dissolution of γ') and less porosity. A more recent study investigated laser powder deposition of Rene 80 onto stainless steel (Liu et al., 2010). It was found that cracking occurred in the deposited material with high-energy inputs.

A parametric study on the effect of laser processing on weld geometry in thin cast Rene 80 suggests it is easily applicable, but doesn't outline the effects of these parameters on cracking (Moradi and Ghoreishi, 2010). Additionally, the material's thickness is 1.4 mm; substantially smaller to what is used in this study (22 mm), so it is difficult to compare the processing conditions.

A recent study on directionally solidified Rene 80 focused on secondary factors such as pre-weld heat treatments, and their influence on cracking (Osoba et al.,

2011). It appears that only one combination of processing conditions was applied and therefore it is difficult to comment on their influence.

This brief review outlines that laser welding is applicable to Rene 80 alloy, but a full understanding of the laser processing parameters effects on cracking in the as-welded and PWHT is not available presently. This is also partly true of similar alloys such as IN738LC, where the process window used in published works is often narrow.

3.3 Methodology

3.3.1 Material

The material used in this investigation was produced to have the same grain size as the fine grained material in Chapter 2. The material was solutionised as outlined in Figure 2.5. The welding trials were split into four sets which are described in the next section. The first set was performed on a different batch of material to the rest of the trials. The chemical compositions of the batches are illustrated in Table 3.2. The material was prepared for the welding trials as per the trials in Chapter 2.

Table 3.2 – Chemical composition of the batches of Rene 80 used in the trials. Note in some cases the material was rounded to 0 decimal places to protect the proprietary information of the sponsors.

Batch/ Element	Al	B	C	Co	Cr	Fe	Mo	Ni	S	Si	Ti	W	Zr
Spec	3	0.02	0.16	9	14	<0.35	4	Bal	2ppm	-	4.7	4	0.01
Set 1	3	0.01	0.15	9	14	0.81	4	Bal	0.003	0.17	4.8	4	0.02
Sets 2,3 & 4	3	0.01	0.16	9	14	0.17	3	Bal	0.003	0.16	4.9	4	0.01

3.3.2 Parameter selection

As outlined in the previous section, there were four sets of experiments performed. The parameters investigated are the power, the welding speed, and the beam diameter. The first set of trials used small beam diameters of 0.7 mm and 1.71 mm. The second and third set used 2.5 mm and 5 mm. The third set of trials focused on smaller power and welding speeds, similar to those used for repair welding. Table 3.3 summarises the ranges of parameters used in sets one to three, and the full list of parameters can be found in Appendix B.1. The fourth set of welds used material from the batch used in sets two and three, with parameters selected from the first set of trials, and these are outlined in Table 3.4. This was done to understand whether there was any difference in crack susceptibility between the batches, and was compared with samples of identical parameters used in set one.

Table 3.3 – Summary of parameters used in trials. A full detailed list of parameters can be found in Appendix B.1.

Set	Beam diameter (mm)	Powers (kW)	Welding speeds (mm/min)	Total
1	0.7 1.71	0.4, 0.86, 1.725, 2.6 1.72, 3.44, 6.9	100, 200, 400, 600, 800, 1000, 2000, 4000	56
2	2.5 5.0	0.5, 1, 2, 4, 8	200, 600, 1000, 2000, 4000	50
3	2.5 5.0	0.5, 0.6, 0.8, 1, 1.5	50, 100, 150	30

Table 3.4 – Parameters used for set 4. These were selected at random from those used in Set 1.

Beam diameter (mm)	Power (kW)	Welding speed (mm/min)
0.7	0.86	2000
0.7	2.6	600
0.7	2.6	400
0.7	1.725	100
1.71	1.72	600
1.71	3.44	400
1.71	3.44	2000
1.71	6.9	100

3.3.3 Experimental set up

The welding trials were performed using an IPG YLR-8000 ytterbium doped fibre laser. This operates at an emission wavelength of 1070 nm, and a maximum power output of 8 kW. The beam is delivered through a 250 μm core diameter fibre which is coupled (using an Optoskand f50-f60 fibre coupler) to a process fibre of 300 μm and ends in a Precitec YW50 processing head. The beam is collimated with a lens of 125 mm focal length, and focused using a 250 mm focal length lens to an in focus beam diameter of 0.64 mm. The process head is mounted on a Fanuc M-170iB/45T robot.

In these trials, the laser beam is defocused to produce an energy density which is near Gaussian, resembling that of a typical repair weld using an arc-based process such as TIG welding. To achieve this, the beam profile was measured using a Primes GmbH Focus Monitor with Primes Laser Diagnostic Software 2.73. The laser was positioned above the device in the focal position (250 mm), and then the software ran a beam profile at varying positions away from the lens. This produced a profile of the beam diameter at varying distances from the lens. The beam diameter is determined by the radius which contains 86 % of the beam energy. To protect from

back reflection, the laser head is tilted at a 10 ° angle to the normal of the plate surface.

Each set of welding parameters were applied as autogenous single pass bead-on-plate welds. More than one weld was laid on each block of material, but assurances were taken to ensure that there was no overlap of the weld's HAZs.

3.3.4 Metallography

After welding, each sample was cut into two halfs, using the same procedure as described in Chapter 2, and illustrated in Figure 2.6: one half was analysed in the as-welded condition, whilst the second half was treated with the PWHT which was outlined in the previous chapter. This is the same heat treatment as the solution cycle, but with faster cooling rates. Note that the sections of the weld which were analysed for each condition were now randomised. The same metallographic procedure was also applied, including measurement of welds and crack lengths.

For assessing the repeat weld samples in set 4 (the repeat weld data), five sections were taken from each weld - both set 4 and the respective same parameters in set 1 - by grinding approximately one millimetre away from the previous site of inspection. The variability in cracking was assessed based on the average data from these.

The average crack length parameter was chosen as the main criterion for assessing the defects in the welds, based on the same reasoning given in Chapter 2.

3.3.5 Statistical analysis

Due to having a significantly large number of data points for both as-welded (liquation cracking) and post weld (strain-age cracking) conditions, statistical analysis software was used to investigate the relationship between the dependent and response variables, e.g. how the crack length depended on the experimental parameters. The same software as previously used in Chapter 2 was used for this purpose with the historical data analysis function.

Two model types were used on both the as-welded and post-weld heat treated data. The first model type investigates the power, beam diameter, and welding speed, while the second investigates the fusion zone area and aspect ratio. The fusion zone area was chosen because it was indicative of the absorbed power per mm, and will be related to the absorbed heat input.

Different transforms were applied to the data during the analysis. The transforms were applied to the data because it allowed for easier and better fitting of models to the data using the least-squares regression analysis technique. The transforms chosen in the present case are illustrated in Equation 3.1 for the as-welded condition, and the PWHT data was transformed using Equation 3.2. Both are also illustrated in Figure 3.1. The transforms work by simply illustrating whether cracking has

occurred or not by condensing the magnitude of the ACL. For example in the as-welded condition, zero cracking is illustrated by a transformed response of 0.365. As further examples of how the transforms work, a value of 100 μm yields a transformed response of 0.096, whist an ACL value of 500 μm produces a transformed value of 0.044. This illustrates how the transformed data simply shows whether a factor causes cracking or not, and ignores how much cracking it has produced.

$$y'_{AW} = \frac{1}{\sqrt{ACL + 7.5008}} \tag{3.1}$$

$$y'_{PW} = \frac{1}{\sqrt{ACL + 26.53}} \tag{3.2}$$

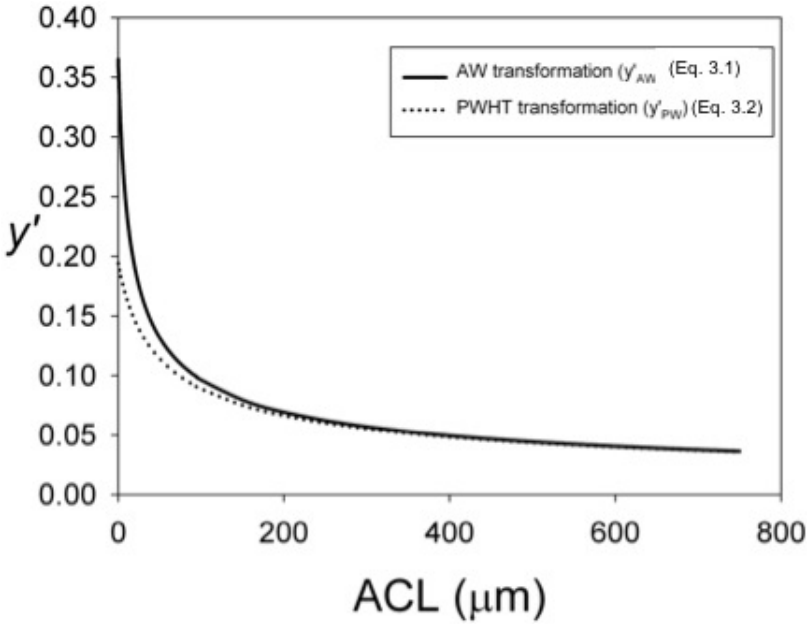

Figure 3.1 – Transformations applied to the cracking data during the statistical analysis.

3.4 Results

3.4.1 Statistics

The statistics for the models which relate the ACL to the welding parameters are shown in Table 3.5. The models are for both the as-welded (AW) and PWHT results. Note that it was only possible to generate a statistically significant model for the PWHT results for set 1, which is why no models are included for the other data sets. The table shows the p-values corresponding to the factors which are significant. An empty space against a particular factor indicates that it is not significant and removed from the model where possible. Also, some terms/interactions were

removed from the model and are not represented at all in the analysis. An example of this is the interaction between power (A) and welding speed (C), which would be designated as AC. The first three experimental sets are shown separately as well as combined because of the different materials and parameters used for the sets. The same statistics for the models related to the influence of weld bead geometry on ACL are illustrated in Table 3.6.

Table 3.5 – Details of the model type and respective p-values from the statistical analysis of the effect of the welding parameter on average crack length.

	All data AW	Set 1 AW	Set 2 AW	Set 3 AW	Set 1 PWHT
Model type	Quadratic	Linear	Two-Factorial interactive	Linear	Two-Factorial interactive
Transformation	Inverse Square root	Log_{10}	Inverse Square root	Inverse Square root	Inverse Square root
Adeq Prec	10.350	12.582	4.412	7.041	14.362
Model f-Value	9.06	12.01	2.33	7.72	14.26
Model p-Value	<0.0001	<0.0001	0.0706	0.0008	<0.0001
R^2	0.2997	0.4094	0.1715	0.4713	0.5279
Pred R^2	0.1912	0.3267	-0.0492	0.2966	0.4229
Adj R^2	0.2667	0.3753	0.0978	0.4103	0.4909
Power (A)	0.0014	<0.0001	0.7432	0.5657	<0.0001
Beam diameter (B)	0.5661	0.0315	0.0964	<0.0001	0.0034
Welding speed (C)	0.6712	0.0255	0.5122	0.1945	0.0006
Interaction AB	<0.0001	-	0.1222	-	0.0072
Interaction BC	0.054	-	-	-	-
B^2	0.0063	-	-	-	-

Table 3.6 – Details of the model type and respective p-values from the statistical analysis of the effect of weld geometry on average crack length.

	All AW	Set 1 AW	Set 2 AW	Set 3 AW	All PWHT	Set 1 PWHT
Model type	Cubic	Quadratic		Linear	Two-Factorial Interactive	Cubic
Transformation	Inverse Square root	Log_{10}	Inverse Square root		Inverse Square root	
Adeq Prec	Inverse square root	14.013	7.844	10.647	16.132	13.508
Model f-Value	11.472	11.02	5.31	11.72	16.63	21.97
Model p-Value	6.08	<0.0001	0.0014	0.0002	<0.0001	<0.0001
R^2	<0.0001	0.4636	0.3207	0.4647	0.2057	0.729
Pred R^2	0.3062	0.365	0.2004	0.3893	0.1249	0.6617
Adj R^2	0.1601	0.4216	0.2604	0.425	0.1874	0.6958
Aspect ratio (A)	0.2559	0.9178	0.0002	0.0001	0.8316	0.3698
Log Fusion zone area (B)	0.1693	0.0425	0.0026	0.0007	<0.0001	<0.0001
Interaction AB	0.1302	0.0236	0.0042	-	0.0019	0.0028
A^2	0.0058	-	-	-	-	0.0139
B^2	0.0001	0.0174	0.0018	-	-	0.0152
A^2B	0.021	-	-	-	-	-
B^2A	0.0128	-	-	-	-	0.0011
A^3	0.0039	-	-	-	-	-
B^3	0.0323	-	-	-	-	-

3.4.2 Repeat welds

A plot of the repeat weld conditions comparing the first material batch against the second is shown in Figure 3.2. For each data point, five sections were taken from each weld and analysed, with the average plotted in Figure 3.2. The error bars in the plot are the standard deviation of the five sections per weld used to produce the data points. This plot and the error bars clearly show the high statistical variability associated with cracking in nickel based superalloy welds. This statistical variation is significant on the interpretation of all the results in this work.

Note that the extremely large ACL sample contained significant solidification cracking. This sample was also a high aspect ratio (1.25) weld.

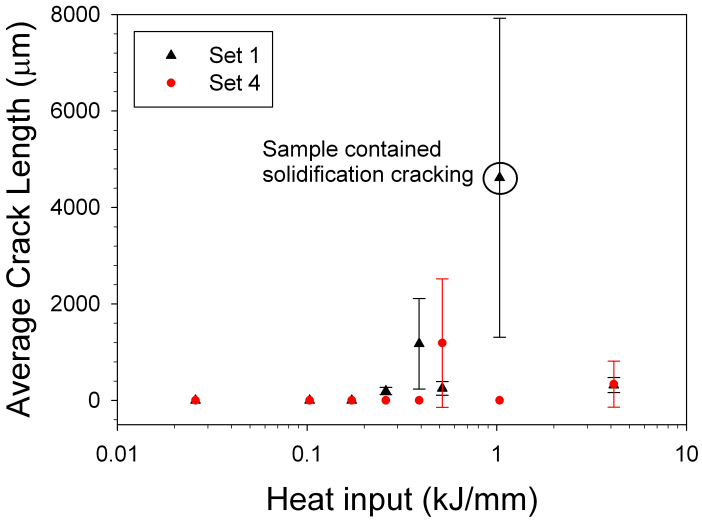

Figure 3.2 – Plot showing the mean ACL versus heat input for the welds in set 4 and identical parameter samples from set 1, error bars showing the standard deviation of five readings used to create the mean. Note one sample showed solidification cracking (circled).

To assess whether the difference in materials was statistically significant, the data were analysed using the statistical analysis software, based on the previous procedure. The p-value was 9.95 %, and to be statistically significant the p-value needs to be less than 5 %. Therefore it is unclear whether or not there is a statistically significant difference between the batches.

3.4.3 As-welded (liquation) cracking condition

3.4.3.1 Effect of welding parameters

A plot showing the effect of power and welding speed on cracking for a beam diameter of 2.85 mm is shown in Figure 3.3. Note that the inverse square root transformation is used, where a value of 0.365 indicates no cracking, and values less than 0.365 indicate that cracking has occurred. In this plot, the welding speed is plotted as the two curves, with the black curve indicating the minimum (50 mm/min) welding speed, and the red as the maximum (4000 mm/min). This plot shows that welding speed has little effect on the incidence of cracking as the two curves are nearly overlapping. The plot does show that the power is significant, illustrating that increasing the welding power increases the likelihood of cracking occurring.

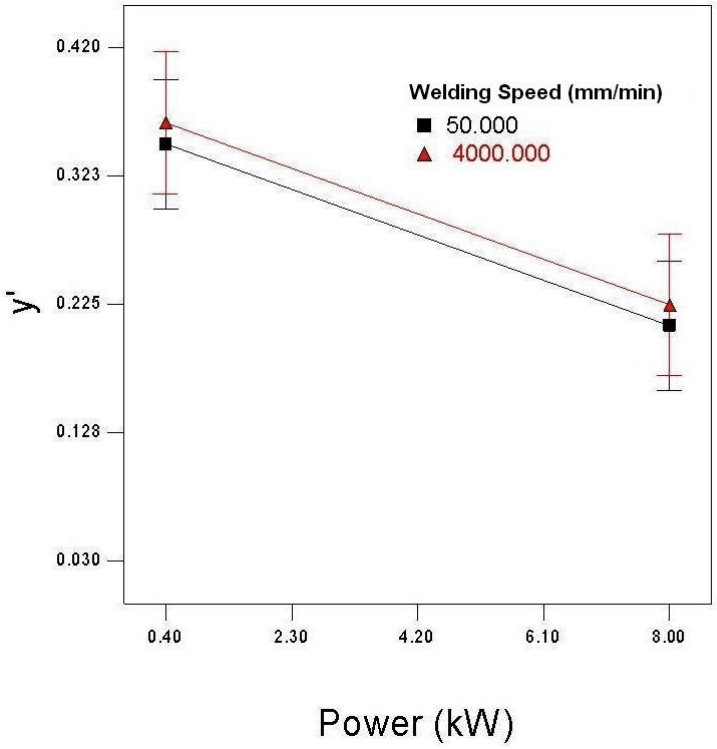

Figure 3.3 – Interaction of power and welding speed with ACL for all weld data, as-welded condition.

Since the welding speed has little effect on the results, the key parameters are the power and beam diameter. A plot showing the effect of these parameters is shown in Figure 3.4. According to this, the average crack length will be either at zero or less than 100 μm at beam diameters from 0.7 mm to approximately 3.75 mm, when the power is less than 2.5 kW. Outside this region, cracking starts to occur even at low powers, particularly when the beam diameter is large. Interestingly, the cracking decreases with higher power at the largest beam diameter. Similar plots for each individual set of data can be found in Appendix B.2.

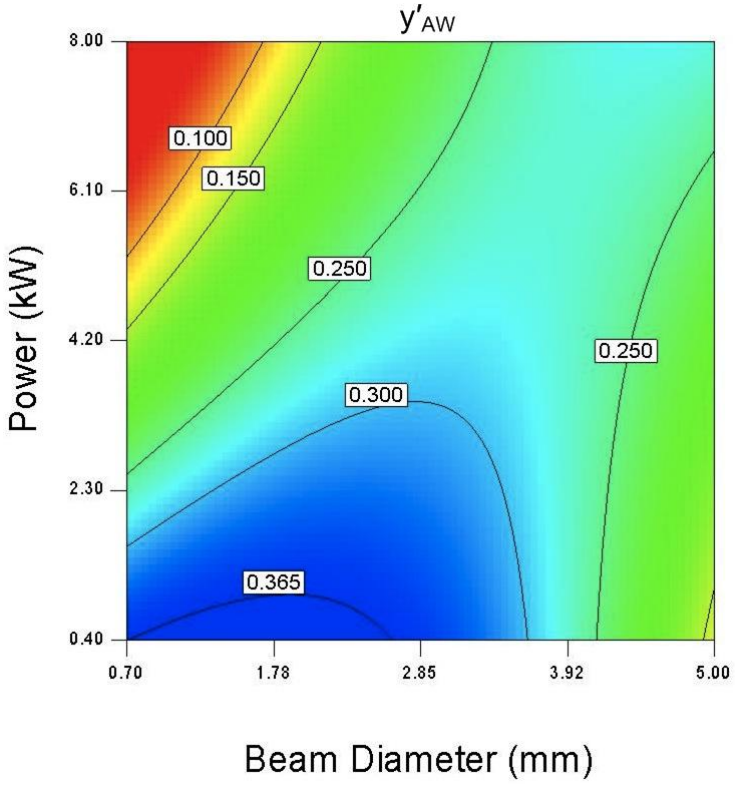

Figure 3.4 – Contour plot of ACL data for the as-welded samples vs. beam diameter and power for all weld data. Note a value of 0.300 corresponds to an ACL value of approximately 100 μm.

3.4.3.2 Effect of weld bead geometry

To better understand the factors causing cracking, the ACL was plotted against the aspect ratio (penetration to width) shown in Figure 3.5. This shows that there is a region with little cracking between aspect ratios of 0.25 and 0.65. Note that there are many samples with aspect ratios outside this region that have no cracking, emphasising the statistical nature of the cracking phenomenon. As before, the plots for each individual set are found in Appendix B.2.

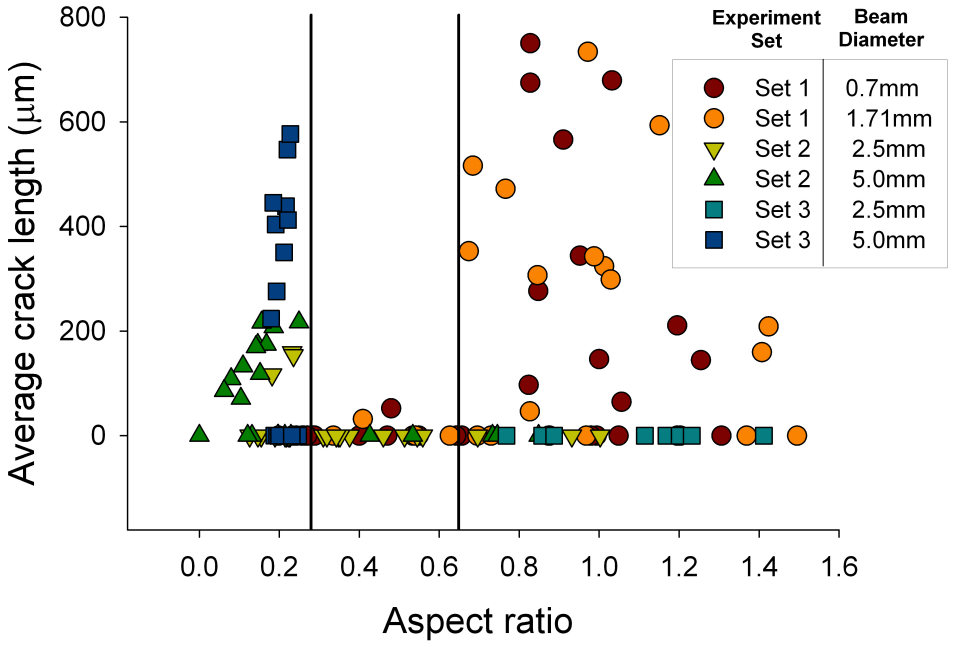

Figure 3.5 – Aspect ratio versus ACL scatter plot, all data, as-welded condition.

To better understand the effect of the heat input on the weld, the fusion zone area is included as a factor with the aspect ratio in a statistical analysis of the results. Since the real data points are unevenly dispersed across the plot, they are indicated with red dots. To make the data easier to interpret, the fusion zone area was plotted using a log scale. There are two regions, one in the top left and the other in bottom right, where there are no data points due to physical limitations of the laser welding process. Hence the predictions are blanked out in these regions

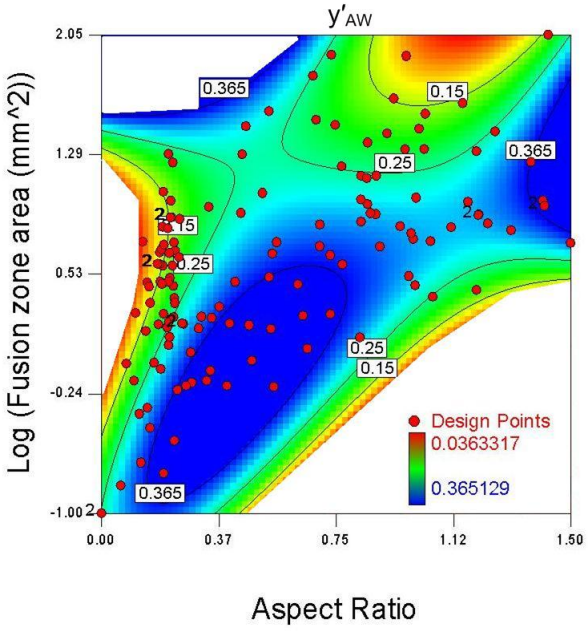

Figure 3.6 – Contour plot showing the ACL of the as-welded samples versus the log of fusion zone area and aspect ratio for all data.

From Figure 3.6 there is a near linear region of increasing aspect ratio and fusion zone area where cracking is found to be at its lowest. This is broadest around an aspect ratio of 0.5. This region also contains a number of data points so this can be confidently claimed.

3.4.4 PWHT condition

3.4.4.1 Effect of welding parameters

An analysis of the results from the PWHT condition was only feasible for set 1 data as no statistically significant model could be obtained for all data combined, or the individual sets 2 and 3. This analysis is shown in Figure 3.7 which is split into two plots for each beam diameter. These plots suggest that for constant power, cracking decreases with increasing welding speed. Also, the plots show that the smaller beam diameter had lower crack susceptibility than the larger diameter. This is illustrated by the difference in values within the two plots in Figure 3.7.

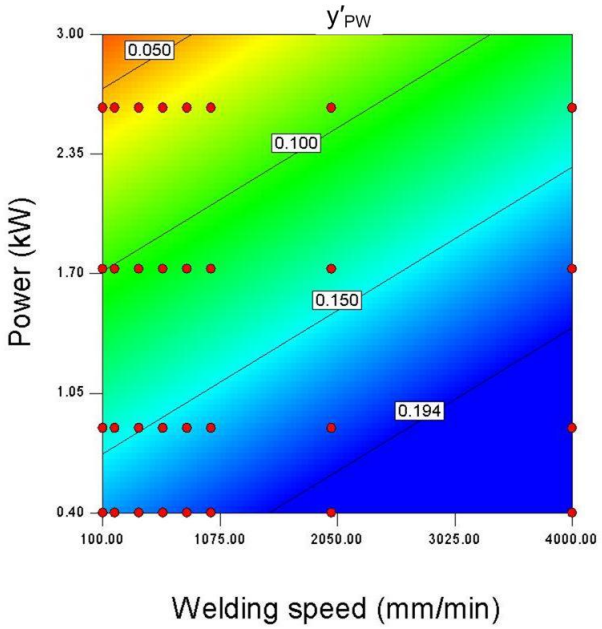

(a)

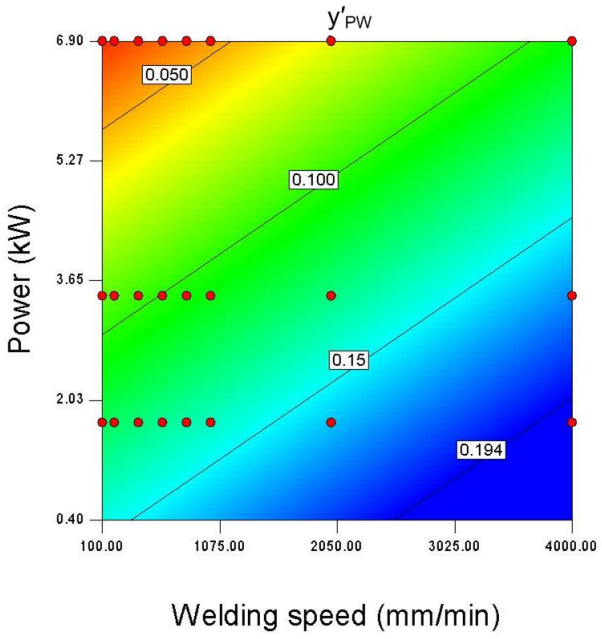

(b)

Figure 3.7 – Contour plot of the ACL after the PWHT versus welding speed and power for beam diameters of (a), 0.7 mm, and (b) 1.7 mm, (set 1 only). Note how the region for zero cracking (0.194) in (a) is much larger, particularly in range of welding speed, than in (b). Note that in (a) there were no data points above 3 kW and as such interpretation of the response above here is not recommended, hence why the scale on this graph (a) is not the same as that in (b).

3.4.4.2 Effect of weld bead geometry

The effect of weld bead geometry on PWHT is similar to the as-welded condition. As Figure 3.8 shows, there is a defined region of aspect ratio where little or no cracking occurred. However, with PWHT the width of this region is significantly narrower.

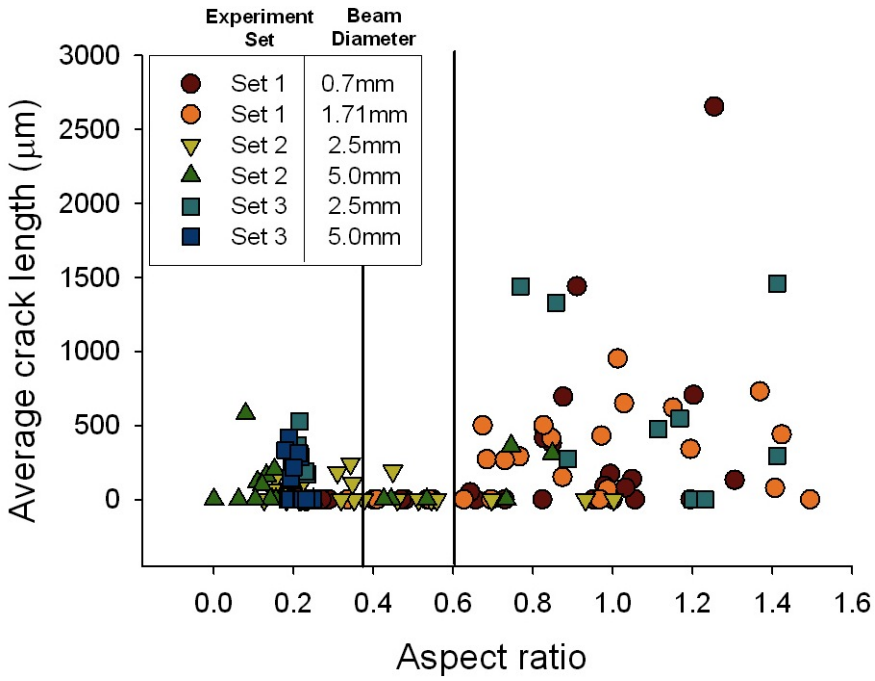

Figure 3.8 – Aspect ratio versus ACL scatter plot, all data, PWHT condition.

The relationship between weld bead aspect ratio and fusion zone area was also studied. This time a model was fitted to all the PWHT data and to set 1 only; a statistically significant model was not possible with sets 2 and 3. There appears to be a small trend of cracking increasing with increasing fusion zone area and aspect ratio, although this is more obvious in the set 1 data (Figure 3.10) than the all data plot (Figure 3.9).

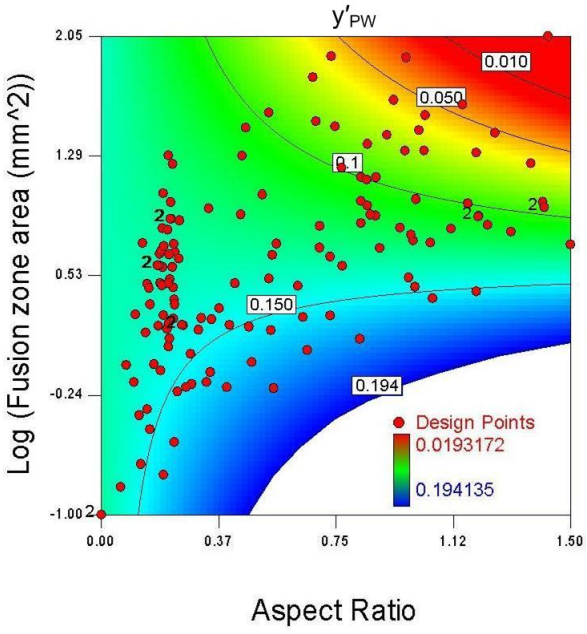

Figure 3.9 – Contour plot showing the ACL per section (for all PWHT data) versus the log of fusion zone area and aspect ratio.

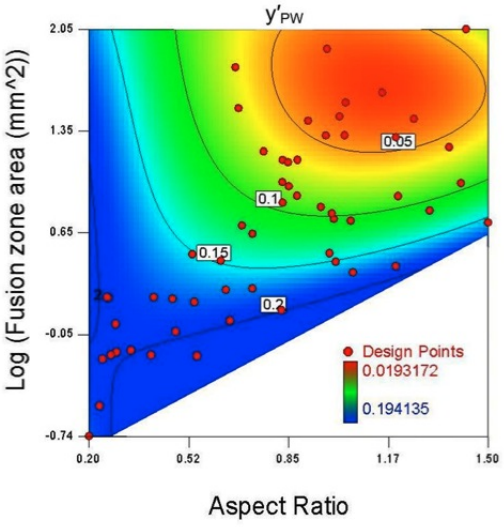

Figure 3.10 – Contour plot showing the ACL per section (for set 1 PWHT data) versus the log of fusion zone area and aspect ratio.

3.4.5 Differences between cracking in AW and PWHT condition

For this analysis, the samples were split into five categories (listed in the legend of Figure 3.11). For this, the data was split such that crack length of a sample in its as-welded and PWHT condition was compared, and the category it fits into in Figure

3.11 is logged. For example, a sample which had an TCL of 0.5 mm as-welded, and 1 mm after PWHT is put as cracked - cracked more, and a sample which had 1.5 mm as-welded and 0.7 mm after PWHT would be cracked - cracked less. This figure shows that approximately one third of the welds showed no cracking in either the as-welded or PWHT condition. In addition, a further 29 % showed cracking only after PWHT. However, it is the final 37 % of samples which are of most interest, as these appear to show the susceptibility to variation in cracking that affects the analysis of the data. Some of this data showed cracking in the as-welded section, but none in the PWHT, and the rest of the data showed increasing or decreasing amounts of cracking after PWHT.

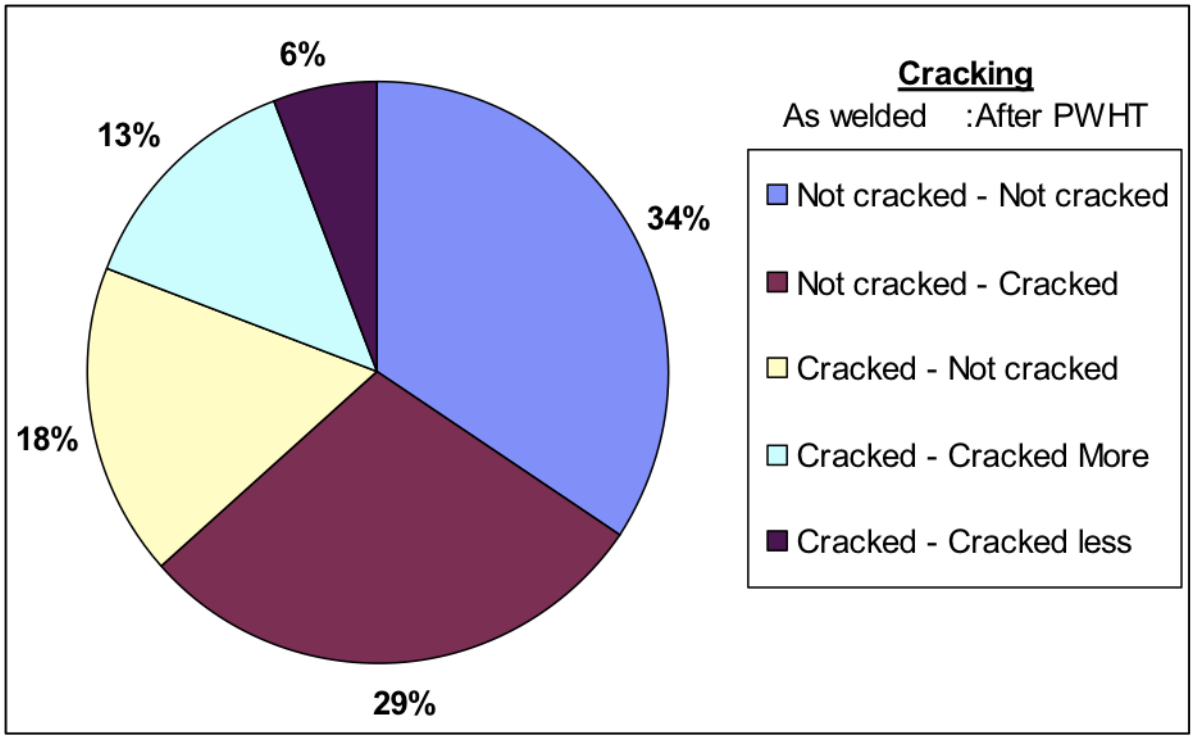

Figure 3.11 – Chart showing the differences in cracking between AW and PWHT conditions, split into different categories.

It is interesting to compare the individual sets of welds, as outlined in Figure 3.12. In set 1, about a third were not cracked in both the as-welded and PWHT conditions, and only 21 % that were not cracked showed cracking afterwards. In set 3 there were fewer that were not cracked in both conditions (20 %) and a very large proportion that cracked with PWHT. Also of interest from this figure, is that it appears that the set 2 data (same power and welding speed range as set 1 but larger beam diameter) showed a greater amount of samples with no cracking in both conditions.

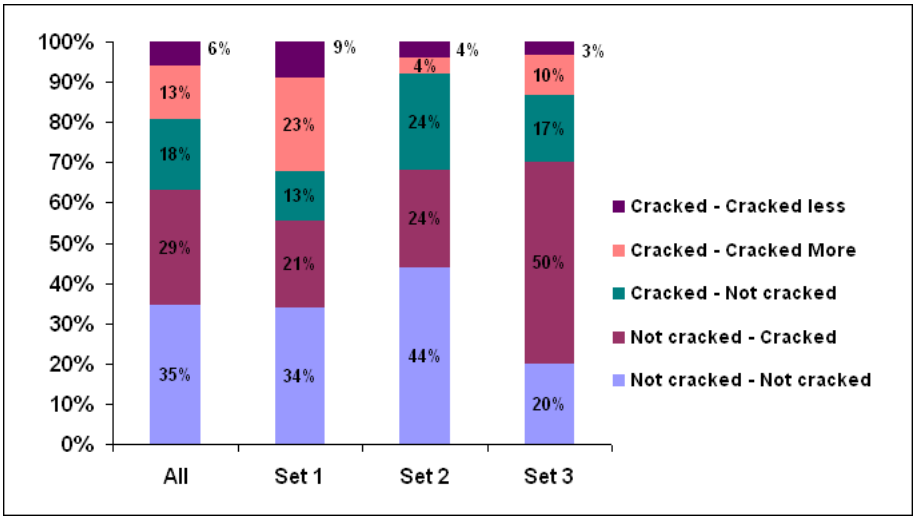

Figure 3.12 – Chart showing breakdown into individual sets, of the differences in cracking between AW and PWHT conditions, as per Figure 3.11.

Perhaps a simple method of comparing the individual sets is with a parameter denoted as the PWHT ratio, or ψ_{PWHT} as in Eq. 3.3:

$$\psi_{PWHT} = \frac{N_{PWHT/NAW}}{N_{NAW}} \tag{3.3}$$

Where $N_{PWHT/NAW}$ is the number of samples which showed PWHT cracking but no as-welded (liquation) cracking, and N_{NAW} is the number of samples which show no as-welded (liquation) cracking. For each individual set of data, the values are 38 %, 35 % and 71 %, indicating that set 3 has a higher tendency to crack during the PWHT than sets 1 or 2 given no cracking in the as-welded state.

3.4.6 Relationship between HAZ size and cracking

For each weld section, the average HAZ size was calculated by averaging the width (either side of the weld) and below the fusion zone, by optical microscopy. The HAZ size for each sample has been plotted in a histogram (Figure 3.13) which shows the distribution of the HAZ sizes for each of the categories. The clearest observation from this chart is that the samples which showed no cracking in either condition generally had small (<200 μm) HAZ sizes. The larger HAZ sizes are typically dominated by the samples which had cracking in the as-welded condition. This plot therefore shows further evidence of a relationship between HAZ size and cracking.

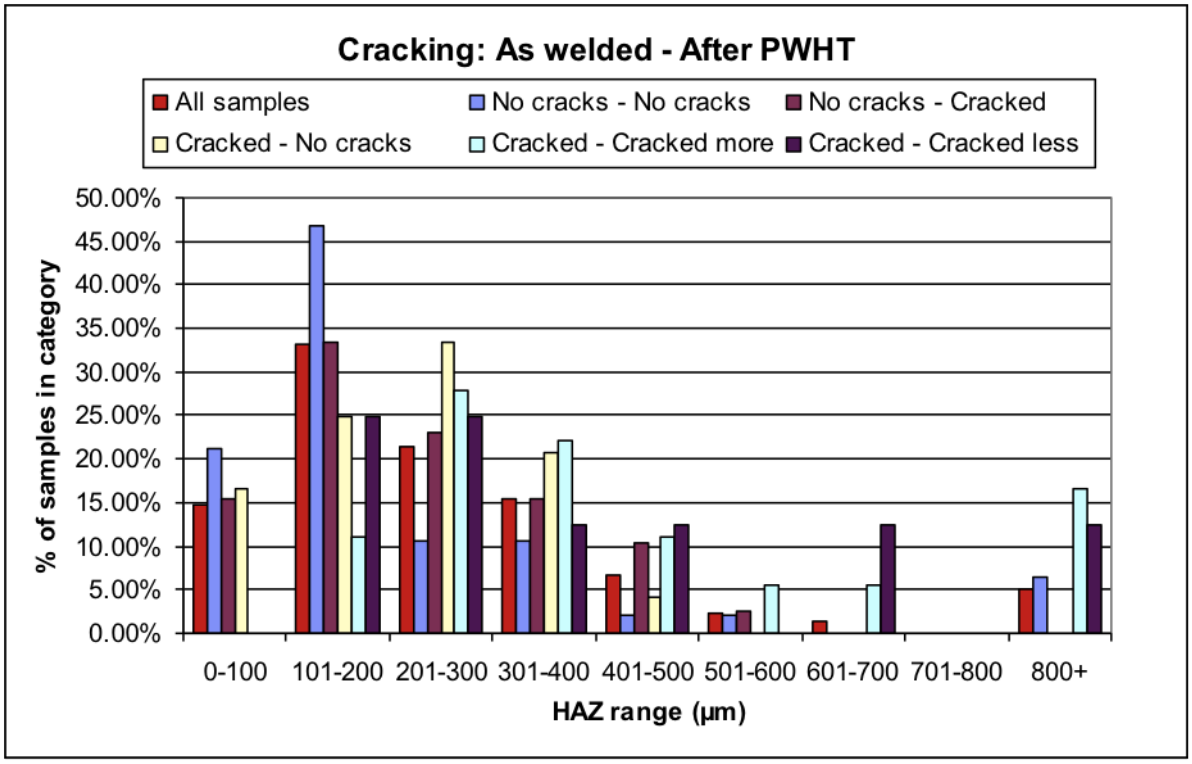

Figure 3.13 – Comparison of HAZ sizes for different cracking categories outlined in Figure 3.11. The X-axis plots the range of HAZ size that a sample fits into, whilst the y-axis plots the distribution of samples (as a %) in the HAZ range.

3.5 Discussion

3.5.1 Difference between material batches

One of the problems when using more than one batch of material is the effects that are observed may be due to differences in the material as well as differences in processing conditions. By undertaking a statistical analysis, the results in section 3.4.2 suggest that it is unclear whether there is any statistically significant difference between the two material batches. The chemical analysis data outlined in Table 3.2 has shown that there is only a large difference in the iron content. Cao (2005) reported that iron is a driver for the formation of liquation inducing laves phase in IN718, however there is no evidence to suggest this is true for Rene 80 and similar alloys. The role of iron in most superalloys is reported to be a solid solution strengthener, although as reported above it does form the detrimental laves and sigma phases in certain alloy groups. Therefore the iron content differences can be discounted as having an effect.

The error bars in Figure 3.2 represents the standard deviation, and it is clear that there is significant variability in the measured cracking across the five sections measured per weld. This underlines the difficulties associated with attempting any

statistically sound analysis of the crack susceptibility and the determination of the important factors. The average crack length parameter is selected because this is not affected by the size of the weld bead, whereas the total crack length could vary significantly between two weld beads simply because of the difference in weld cross sectional area.

Throughout the study, it is clear that the microstructure is a significant factor in influencing both forms of cracking. The grain size of the material is large – typically 3.5 mm bulk, and the grain boundary location undoubtedly affects both cracking phenomena (as discussed in section 3.5.5). Hence the location of the grain boundaries relative to the fusion region and HAZ is likely to be one of the main causes of the cracking variability.

3.5.2 Analysis of variance from statistical analysis

As with the statistical analysis of grain size effect in Chapter 2, there is also some interesting data to discuss with regards to the statistical analysis completed in this chapter. The critical statistics are as before: the adjusted and predicted R-Squared values, the model f-value, and the p-values for both the model and factors.

The R-Squared values for all models in both Table 3.5 and Table 3.6 are lower than desirable, as was the case for Chapter 2. However, as discussed Chapter 2, a number of reasons could cause this: First, there may be other factors influencing the relationship which are not described in the model. Second, the inherent variability of the material's susceptibility to cracking is also a contributing factor. The error bars plotted in Figure 3.2 show this clearly. Also, the correlation between the data points and the fit of the model to the data is important. This is best represented with Figure 3.14, which shows a plot of transformed ACL versus power. The significant variability related to cracking has resulted in a poor fit between the model and experimental values which resulted in the low value of R^2.

Ideally, the statistics could be improved greatly by taking many more sections and estimating the probability of cracking. This however was not possible within the timescale of this project as there were over 130 different parameter combinations for both the as-welded and PWHT conditions that would produce a minimum of over 800 weld sections (if six sections were taken per sample).

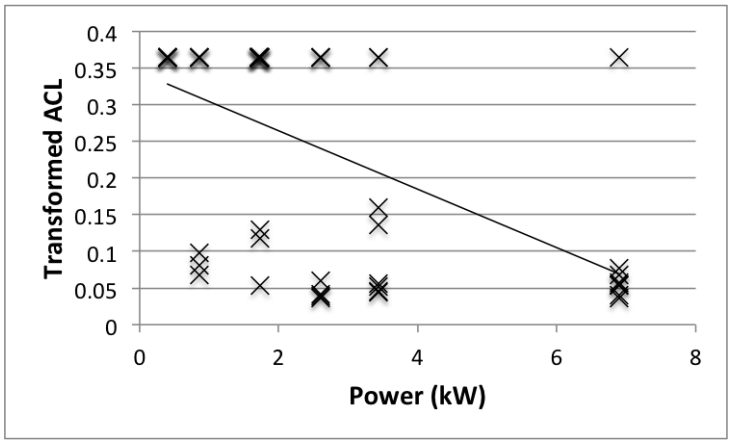

Figure 3.14 – How the R^2 value is affected by the variation of the data to the model. This is a plot of the transformed ACL for set 1 laser data (at beam diameters of 0.7 mm and 1.7 mm) for the range of powers applied. The plot shows how the data varies considerably from the line of best fit, particularly at higher powers. Note that an ACL of 0 μm is equal to a transformed value of 0.364. See Equation 3.1 for this transform.

The statistics were first used to understand whether the factors are significant in influencing the responses. This is illustrated by the p-values for each factor. As discussed in Chapter 2, the R-Squared values have no influence on whether the models are acceptable for this purpose; it is the other model statistics as described below, which are important.

For the models outlined in Table 3.5, the only model which has what could be considered poor model statistics is the set 2 as-welded. The adequate precision (noise to background ratio) is only just above the recommended minimum level of four, and the model f-value is very low relative to the other models. The model p-value is also the poorest. This poor data is also demonstrated by the poor R-Squared values for this particular model.

The data for aspect ratio and fusion zone area as factors was illustrated in Table 3.6. All of the models appear to be acceptable for the purposes used to describe any significance of the factors on cracking.

3.5.3 As-welded results

As has previously been emphasised, studying cracking in welds made in nickel-based superalloys is inherently difficult due to the significant statistical variability. This was discussed in both Chapter 2, and in section 3.5.1.

The study of the welding parameters illustrated that there is little influence of the welding speed on observed cracking. This is in line with the findings of Danis et al. (2010) but contradicts the findings of Egbewande et al. (2010), who proposed that increasing welding speed for a constant power reduces the cracking, whilst Richards et al. (1994) and Shinozaki et al. (2000) both suggest that decreasing welding speed

for a constant power leads to a reduction in cracking. Shinozaki et al. (2000) also suggested that the welding speed strongly influences the weld bead cross sectional shape for a given power. In all of these publications, the range of parameters that the authors studied was very small. Therefore, some of the differences maybe due to the changes in weld bead shape between the different published works.

Assuming the independence of the results from welding speed effects, it was shown in Figure 3.4 that the effect of power depended on the beam diameter. At small beam diameters, cracking decreased with decreasing power, whilst at large beam diameters cracking decreased with increasing power. Both effects have been shown by different authors, Danis et al. (2010) indicating lower power resulted in lower cracking, whilst Richards et al. (1994) found that cracking decreases with increasing power.

As shown in Figure 3.5, there is an intermediate range of aspect ratios where the likelihood of cracking is minimised. Either very high or very low aspect ratios increase the likelihood of cracking. Therefore when using large beam diameters with small powers, the aspect ratio is very low and the likelihood of cracking is high. Similarly, when using the small beam diameter and high powers, the intensity is high enough to induce a keyhole which will inevitably create deeper penetration welds and therefore high aspect ratios that are outside the optimum range, which also have a high likelihood of cracking. This, and the data in Figure 3.5, leads to the conclusion that to minimise liquation cracking, the aspect ratio needs to be between 0.25 and 0.65.

This finding is backed up by Boucher et al. (1976, 1977) who investigated electron beam and TIG welding of lower crack susceptible alloys. They suggest that higher weld aspect ratios produce greater cracking, finding that an aspect ratio of 0.5 eliminates cracking in TIG welded IN718 samples. This is in extremely good agreement with the findings reported in this thesis. Richards et al. (1994) also found that higher aspect ratios increased the amount of cracking. None of the reported literature have found increased cracking with low aspect ratios, which was found in this thesis.

Despite this interesting and potentially significant finding, it is unclear as to why it is occurring. Perhaps, as supported by Shinozaki et al. (2000), liquation crack susceptibility is strongly dependant on the weld bead cross section. In addition, Shinozaki et al. also hypothesised that for high aspect ratio welds, the necking region (where the weld shape transitions from high width to narrow but deep penetration) is a location where cracking is at its highest probability of occurring. In the high aspect ratio welds, this necking feature occurs frequently and could be attributed to

the high cracking susceptibility in these welds.

The weld bead shape has a significant effect on the transient stresses in the HAZ (and weld zone) during cooling, which are significant drivers in the formation of liquation cracks, as suggested by Koren et al. (1982). The shape will also affect the cooling gradients, which are significant in controlling the stresses and subsequent cracking. Therefore it is likely that there is a significant relationship between the weld geometry, transient stresses, and cracking susceptibility.

Alternatively, the optimum aspect ratio may be influencing the strain within the HAZ, which influences the formation of liquation cracking. Recent work studied the influence of compressive strain on liquation in superalloys using the linear friction welding (LFW) process (Ola et al., 2011b,c,a). The authors found that where linear friction welding is previously thought to avoid liquation, this is not strictly true as the microstructures showed evidence of liquation. However, there was no cracking present in the microstructure, which was found to be as a result of the compressive strain applied during the processing. This was validated by using gleeble simulations, both with and without the compressive strain applied.

It was suggested that the compressive strain increased the rate at which solute atoms in the liquid diffused into the surrounding solid material. This reduced the amount of non-equilibrium liquid (i.e. liquated secondary phases), and was a significant contributory factor to the reduced amount of liquation cracking in the LFW samples.

Whilst the magnitudes of compressive strains observed in the autogenous welds in this thesis are not the same as those applied in the LFW process, there is a possibility that the localised strains present in the optimal aspect ratio samples are higher than those observed in the welds outside of the optimal region. It is however only a small chance that the optimal aspect ratio influence is because of the same compressive strain type effect observed in the cited works (Ola et al., 2011b,c,a). But, it is interesting to observe that liquation mechanisms can be reduced by more than optimising the chemistry/heat input, and by modifying the stress/strain profile in the weld area.

The statistical analysis technique was used to study the combined effect of the aspect ratio and fusion zone area on the cracking incidence (Figure 3.6). Perhaps the most significant finding here is that the region of fusion zones that also show lowest cracking is at its broadest around an aspect ratio of 0.5. This plot also demonstrates how the combination of low heat input and an aspect ratio of around 0.5 give conditions that minimise cracking.

At low aspect ratios, it is shown that cracking is only minimised when the fusion

zone area is very small. It is difficult to obtain low fusion zone areas with high aspect ratios. This is related to the working capabilities of the laser process. The intensities required to create the keyhole driving the formation of deep penetrations and high aspect ratios also cause large weld beads to form. The plots however must be analysed with care. For instance, regions have been blocked because no data (red dots) were produced so the model is likely to be very inaccurate in these areas.

There is a region shown in Figure 3.4 which suggests an optimum beam diameter of approximately 2.5 mm for the range of parameters used in this study. Note that this has been demonstrated with the exception of one or two points. Interestingly, Zhong et al. (2005) found that an optimum beam diameter of 2 mm minimised cracking in IN738 laser deposition welding. Therefore, this parameter is a logical starting point for further work.

3.5.4 Post-weld results

Obtaining statistically significant models for the PWHT data proved more difficult. Many more samples have demonstrated cracking, especially for sets 2 and 3 which is why this may have proved more difficult. The significant variability in PWHT cracking was highlighted by Figure 3.11, i.e. some samples that were cracked in the AW condition then showed no cracking after PWHT.

The relationship between welding parameters and cracking in the PWHT condition was only analysed for the set 1 data. Interestingly, this data suggests that the welding speed does have an effect, with the cracking decreasing with increasing welding speed. There also appears to be a marginal reduction in crack susceptibility when increased beam diameters are used (Figure 3.7). Power appears to have the same effect as with the AW results.

Perhaps the welding speed influence on the PWHT is due to a reduced size of the HAZ and thermally stressed area. However, another theory by Shinozaki et al. (2000) suggests that the welding speed influences the weld bead geometry, with faster welds producing lower aspect ratio welds.

The effect of the weld bead geometry, particularly the aspect ratio, observed in the as-welded samples is also visible in the post-weld heat treatment cracking results, Figure 3.8. This finding, coupled with the previous finding for the as-welded condition confirms the reasoning that the aspect ratio influences the stresses generated during cooling in both the weld bead and surrounding material.

The range of aspect ratios which are shown to reduce cracking is reduced in the PWHT results. This is likely to be due to the complex relationship between the residual stresses after cooling, the metallurgical condition (i.e. the amount of solute in solution which can precipitate during ageing) and the subsequent heat treatment

which is extremely critical to the formation of post-weld heat treatment cracks.

The relationship between aspect ratio and fusion zone area for the PWHT condition in Figure 3.9 illustrates the importance of minimising the fusion zone area in addition to obtaining an aspect ratio of around 0.5.

The study of the differences in cracking levels between as-welded and PWHT conditions shows that a third of all welds showed no cracking in both conditions (Figure 3.11). This suggests that in these conditions, the thermal cycle was both sufficient to produce a weld, without causing the HAZ to form liquation cracks, and subsequently low residual stresses to avoid strain-age cracks to form in the PWHT.

The effect of the size of the HAZ is also critical to crack susceptibility in this alloy. As was shown in Figure 3.13, cracking in both conditions is avoided when the HAZ is small (e.g. less than 200 μm). This is perhaps also a significant finding because it suggests that to ensure avoidance of cracking, the welding parameters selected to produce the optimised aspect ratio should also be chosen to produce a smaller HAZ.

It is during the heating to solutionisation treatment that PWHT cracking occurs. The exact mechanism involves a generation of strain caused by the volume contraction due to precipitation and/or growth of the γ' particles. The size of the HAZ is therefore important because if it is small, the amount of γ' which can be aged during the cycle is small, and therefore chances of cracking is reduced. Conversely, if it is large, then it is also likely that there would be a higher chance of PWHT cracks forming.

3.5.5 Effect of local microstructure

It is clear that there is variability in all the results reported herein. This is a problem that is associated with any welding metallurgy investigation where cracking is the point of interest.

The localised segregation of liquating phases, as well as the distribution of carbides on grain boundaries, is related to the grain structure (including grain size and orientation). Sidhu et al. (2009a) found that a directionally solidified Rene 80 alloy was less susceptible to cracking than an equiaxed cast IN738, subjected to the same welding parameters. They found that this was due to reduced number of grain boundaries intercepting the fusion zone. The same authors reported a similar finding in directionally solidified IN738 alloy (Sidhu et al., 2007a). Therefore it could be argued that both the grain orientation and the localised chemistry are significant factors in variability found in cracking in these samples.

The localised chemistry of the alloy may also have a significant impact on the susceptibility to cracking during PWHT. Lim et al. (2002c) reported that PWHT

cracking is a very localised phenomenon due to the mechanism involving volume contraction stresses induced by the precipitation of γ'. Therefore this localised effect could be a factor.

The γ' phase has the designated formula $Ni_3(Al,Ti)$. There are a number of factors related to the variability of PWHT cracking which could be affected by this phase:

1. Localised variation in Al/Ti content affects the amount of γ' precipitation during the PWHT;
2. The morphology and size of existing γ' in the HAZ prior to PWHT could vary resulting in variation in volume change during the PWHT.

Therefore it is possible that the strength of the HAZ will vary, as will the amount of γ' that will nucleate during the PWHT, resulting in variation in strain ageing volume contraction which has been shown previously to be a dominant factor in the cracking occurring during PWHT.

As a result, the above could be a reason for why there is significant variation in the observed cracking after PWHT from sample to sample, and a possible reason for why the results indicated in section 3.4.5 of some samples showing cracking in the as-welded condition but less or none after PWHT.

3.6 Conclusions

In this study, it has been shown that:

1. Autogenous welding of highly crack susceptible alloy Rene 80, can produce welds which are crack free;
2. The welding power is shown to significantly affect the incidence of cracking in the as-welded condition. Low powers at small beam diameters, and high powers with large beam diameters both resulted in minimal or no cracking. An optimum beam diameter of around 2.5 mm was found for the range of powers studied in this thesis;
3. Cracking is shown to be dependent on the shape of the weld bead, in both conditions. The likelihood of cracking occurring is reduced when the weld bead aspect ratio (penetration divided by the width) is between 0.25 and 0.65 in the as-welded condition, and 0.35 and 0.65 in the PWHT;
4. It is also shown that when the weld bead fusion zone area is included in the analysis, this factor influences the cracking. When this is reduced, the incidence of cracking is also reduced;
5. The welding speed was shown to have no affect on the incidence of cracking in the as-welded condition, but did appear to have an influence on the incidence of PWHT cracking. Lower welding speeds resulted in lower amounts of PWHT cracking, observed in the only set of PWHT data statistically analysed;
6. The size of the HAZ appears to be important when aiming to have zero cracking in both conditions. It was shown that when there was no cracking in a sample in either condition, the HAZ size is small, compared to those samples that did contain cracking. It is also apparent that where there is variability in the amount of cracking, the HAZ size is larger.

Chapter 4

Characterisation of welding defects in laser welds of Rene 80

4.1 Introduction

In Chapter 3 it was shown that by controlling the weld parameters, and producing welds of an optimum weld bead aspect ratio, cracking susceptibility in Rene 80 is significantly reduced. Despite these conclusions, it is interesting that cracks still form in some welds even with optimal parameters. The review in Chapter 1 discussed the different types of cracking occurring in the weld metal and HAZ of welds. Due to the uncertainty as to the exact mechanism by which HAZ cracks occur in solutionised Rene 80 (see sections 1.4.3 and 1.6.2), a selection of samples generated in Chapter 3 are analysed using a scanning electron microscope (SEM) and energy dispersive x-ray spectroscopy (EDX) to understand by what mechanism the cracks occur, in both the as welded and PWHT conditions.

4.2 Methodology

4.2.1 Sample selection

Low, intermediate and high aspect ratio welds were chosen for the analysis, as detailed in Table 4.1. The welds were selected from the samples produced in Chapter 3. Note that the high aspect ratio weld was also analysed after the PWHT.

Table 4.1 – Details of samples that have been analysed using SEM/EDX in this chapter.

Description	Aspect ratio	Power (kW)	Beam diameter (mm)	Travel speed (mm/min)
Low aspect ratio	0.11	2	5.0	2000
Optimal aspect ratio	0.55	3.44	1.7	2000
High aspect ratio	0.83	2.6	0.7	400
PWHT	0.83	2.6	0.7	400

4.2.2 Sample preparation

Sample integrity is critical to ensuring good quality SEM images and accurate EDX data. This means that the sample has to be highly polished, and throughly cleaned of any polishing media and other contaminants. The samples were prepared using the same metallographic preparation techniques described previously in Chapter 2 . For the SEM, the samples were un-etched to ensure minimal interference between the etchant and the EDX analysis. This also enables clearer back-scattered electron images. A JOEL JSM-7000F SEM with EDX running Oxford INCA (a software which processes and analyses the data generated by the SEM/EDX) was used. Macros of the weld beads were produced using a Nikon Optiphot microscope.

EDX analysis is however limited when attempting to quantify light elements. Additionally, any quantification of carbon is also difficult, and as such the numbers presented for this element are not necessarily an accurate representation. For all the measurements, semi-quantitative analysis was used, with a pure nickel sample used as a reference.

4.3 Analysis

Figure 4.1 shows the macros of each weld analysed. The low aspect ratio weld (Figure 4.1(a)) is very shallow, illustrating why this sample has a low aspect ratio. There was only one region of the sample which contained any cracks, on the left of centre at the bottom of the weld.

In Figure 4.1 (b), the intermediate (or optimal) aspect ratio macro is shown. This has a higher penetration than the in the low aspect ratio, but it is also a slightly narrower width. The cracking in this sample was again limited to one region, on the left side of the macro as viewed. There are no significant features within these two samples which would be considered stress raisers.

The high aspect ratio macro is shown in Figure 4.1(c). There is a distinct 'necking' region on either side of the weld, where the width of the fusion zone transitions from the wide top section to the narrow keyhole section. Note the clearly visible cracking in this 'necking feature'. In the high aspect ratio sample, there are

some small pores dotted around the fusion zone, including a large pore visible at the bottom end of the fusion zone.

In all of the macros, there is a dispersion of black small marks. These appear throughout the base material, and are also visible within the fusion zone near to the fusion boundary. As the material has been HIP'ed and solution treated prior to welding, it is highly unlikely that those dispersed in the base material are porosity, and are likely to be secondary precipitates such as carbides.

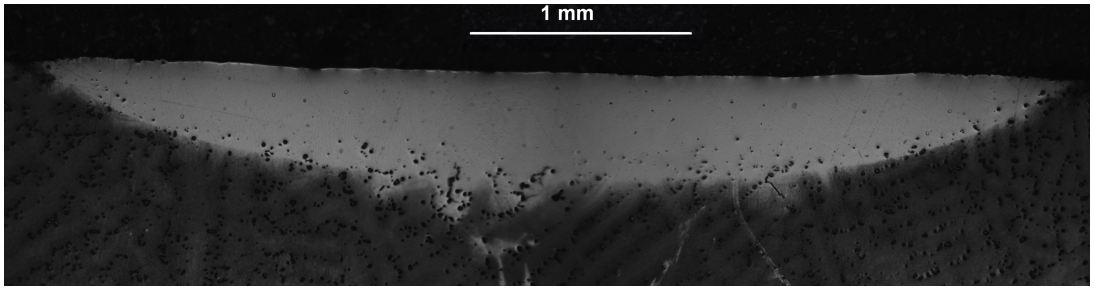

(a)

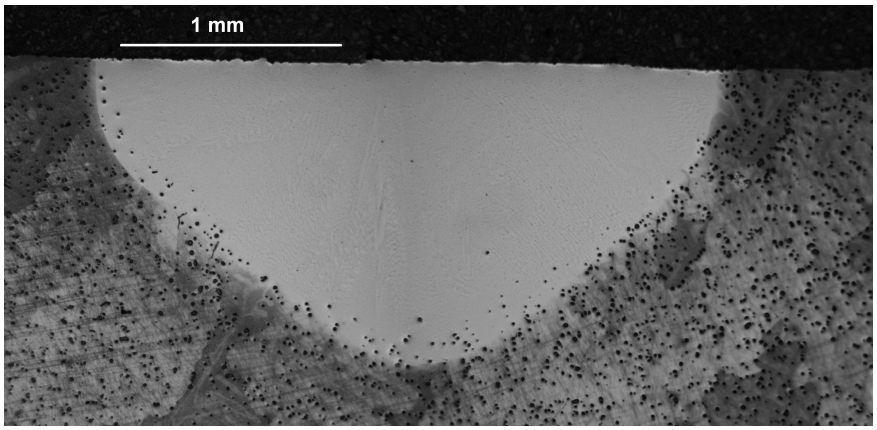

(b)

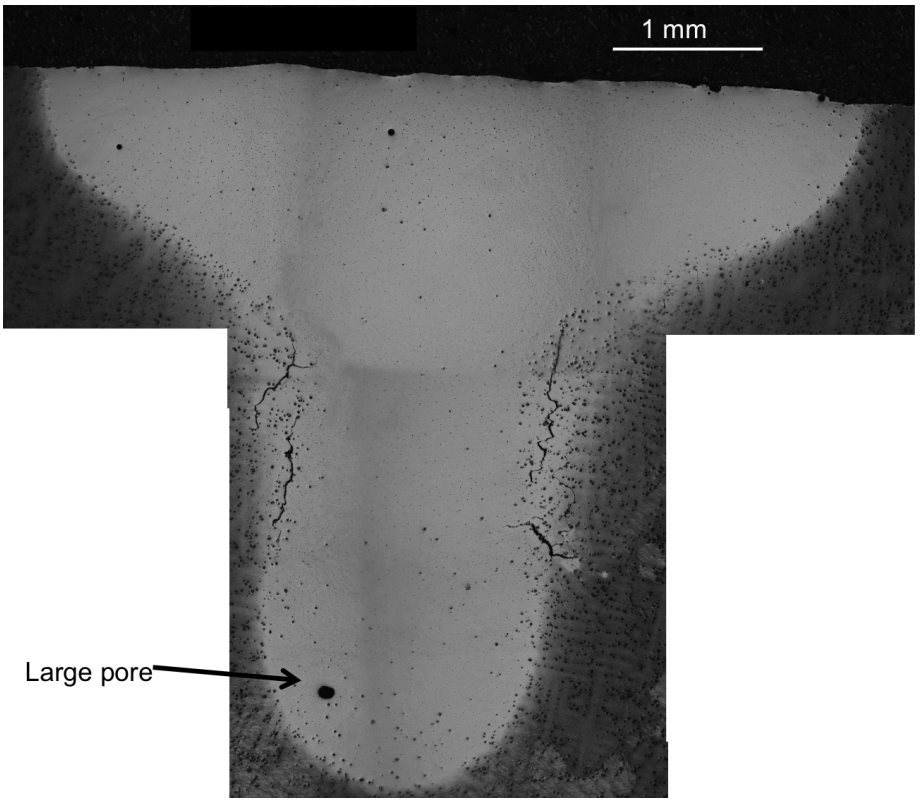

(c)

Figure 4.1 – Macro images illustrating the profiles of (a) low aspect ratio sample, (b) intermediate (optimal) aspect ratio sample and (c) high aspect ratio sample.

4.3.1 Low aspect ratio as-welded sample

The following sample is a low aspect ratio weld, produced using the parameters described in Table 4.1. Figure 4.2(a) illustrates where two distinct cracks are visible. The cracks appear to extend from the fusion line into the HAZ, following a path along grain boundaries. One of the cracks from this sample was selected for further analysis and is shown in greater detail in Figure 4.2(b) and (c).

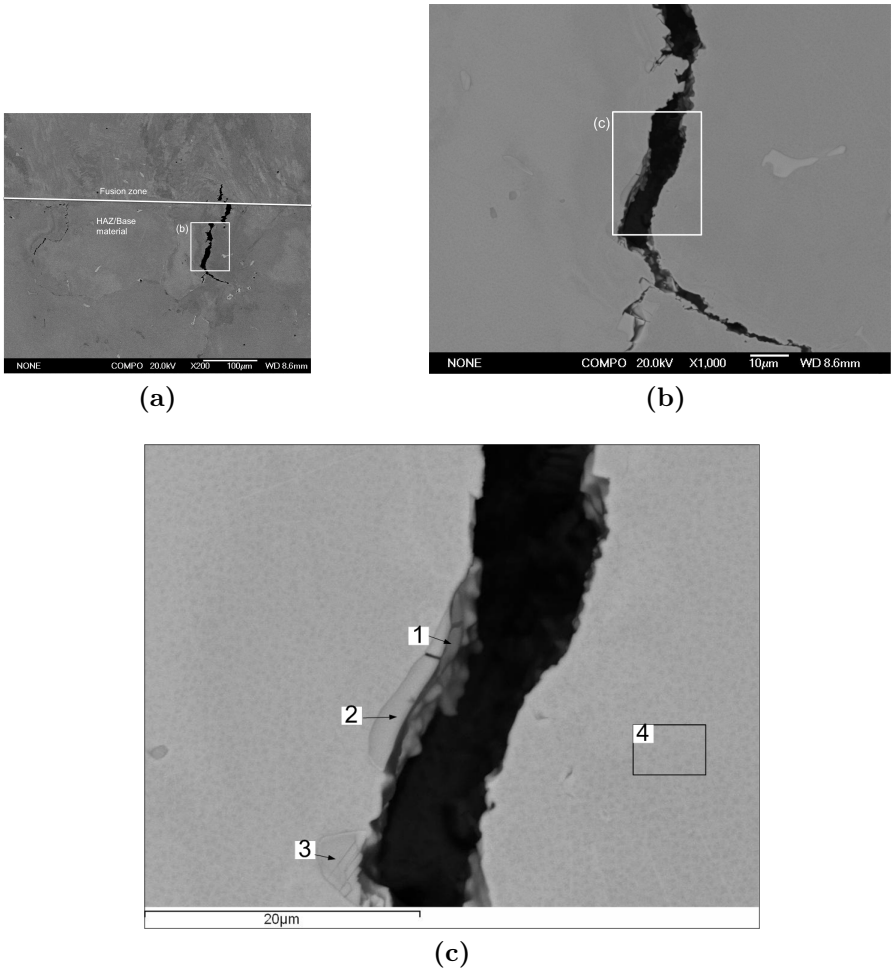

Figure 4.2 – (a) Back-scattered electron image of region showing cracks in low aspect ratio sample, (b) higher magnification of one of the cracks and (c) further detail of crack, including points for EDX analysis.

For the following data in Table 4.2 (and all subsequent tables of EDX results), care must be taken when assessing the values of carbon, due to the difficulties in accurately measuring this element using EDX analysis. In Table 4.2, the details of the EDX analysis illustrate that the analysis points 1, 2 and 3 are M(Ti, Mo, W)C-type carbides, due to the high content of titanium, molybdenum and tungsten compared to the matrix, with little or no content of the other elements found in the matrix. There is evidence of liquation of secondary phases (the carbides) at the

edges of the crack, marked as points 1 and 2 in Figure 4.2(c). It appears that the carbides in points 1 and 2 are an extension of the same carbide, but partial melting occurred allowing some of the liquid to run into the crack face, visible at point 1. The morphology of the crack is irregular, with evidence of melting (liquation), and is quite wide in places. This is as has been observed by Montazeri and Ghaini (2012) in IN738LC.

Table 4.2 – Results of EDX of points illustrated in Figure 4.2(c).

No	C	O	Na	Al	Ti	Cr	Co	Ni	Mo	W	Phase
1	27.43	3.5	-	-	34.11	1.85	0.72	5.86	11.05	15.48	M(Ti, Mo, W)C type carbide
2	27.51	6.65	0.71	-	36.02	0.89	-	2.18	16.07	9.98	M(Ti, Mo, W)C type carbide
3	24.28	-	-	-	43.08	1.41	-	2.7	17.78	10.75	M(Ti, Mo, W)C type carbide
4	5.36	-	-	2.66	4.56	14.12	9.41	56.74	3.98	3.18	Matrix

4.3.2 Optimum aspect ratio as-welded sample

Of the 136 different welds produced in the laser trials, 22 were within the optimised aspect ratio range. Of these, four samples did contain a small amount of cracking, one sample of which has been analysed. Only two cracks were observable, on the left hand side of the weld as outlined in Figure 4.3(a).

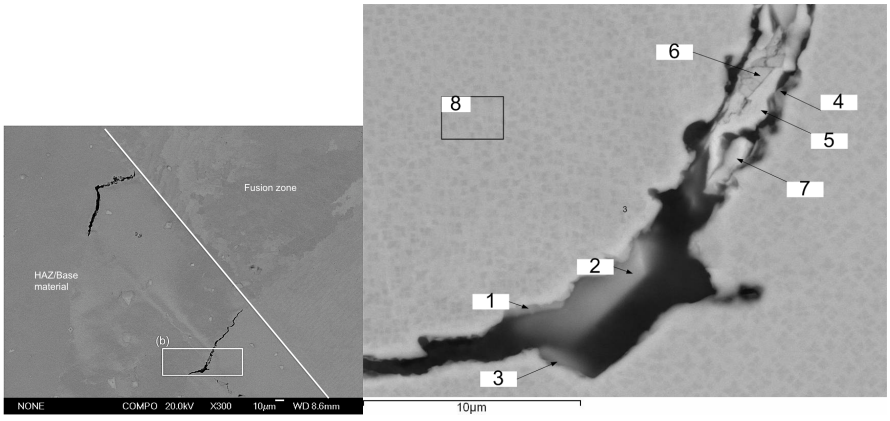

(a) **(b)**

Figure 4.3 – (a) Back-scattered electron image showing cracks in sample with intermediate (or optimal) aspect ratio and (b) Further detail of crack, including points for EDX analysis.

On Figure 4.3(a) the fusion zone boundary is annotated, and it can be observed how the cracks extend from this into the HAZ. This is also visible from the macro image of this sample (Figure 4.1(b)). There is further evidence of the liquation mechanism forming the cracks observed in the sample (resolidified precipitates within the crack). The crack morphology is similar to that observed in section 4.3.1. The EDX analysis of the points marked in Figure 4.3(b) is further detailed in Table 4.3. The data indicates that the cracks were formed from constitutional liquation of MC type

carbides (enriched in Ti, Mo and W), and additionally have a product of γ/γ' eutectic, which suggests there is also liquation of γ'. This is because the composition of the material at points 1, 3, 4, 5 and 7 is higher in aluminium and/or titanium, and lower in cobalt and chromium than the matrix material. This suggests that it is a composition of the eutectic material expected when liquation of a secondary phase γ' occurs.

Table 4.3 – Results of chemistry of points illustrated in Figure 4.3(b) analysed using EDX.

No	C	O	Na	Al	Si	Ti	Cr	Fe	Co	Ni	Mo	W	Phase
1	28.91	8.79	2.39	2.66	0.9	6.66	5.63		3.75	31.2	5.13	3.97	Mixture of carbide and γ/γ' eutectic
2	29.63	10.11	2.38			29.51	0.88			2.62	9.87	15	M(Ti, Mo, W)C Type carbide
3	19.74	3.61	2.62	0.37	0.44	8.22	11.18	0.58	6.37	36.54	8.19	2.14	Mixture of carbide and γ/γ' eutectic
4	6.66	4.13		4.97	1.71	6.08	9.14		6.28	53.85	4.13	3.05	Mixture of carbide and γ/γ' eutectic
5	6.84	1.2		3.99		4.69	11.66		7.7	56.06	3.97	3.9	Mixture of carbide and γ/γ' eutectic
6	17.94			0.7		30	6	0.5	3.11	21.79	7.99	11.97	M(Ti, Mo, W)C Type carbide
7	6.9	1.97		3.61	0.76	5.98	8.67		6.72	58.69	3.42	3.27	Mixture of carbide and γ/γ' eutectic
8	5.49			2.45		4.42	13.49	0.61	8.05	57.71	4.26	3.51	Matrix

4.3.3 High aspect ratio as-welded sample

The high aspect ratio geometry welds were shown to be highly susceptible to cracking (Chapter 3). The cracking was observed in the HAZ in the region just below the necking, on either side of the fusion boundary, as illustrated by Figure 4.4. An interesting observation is the significantly finer grain structure observed in the fusion zone compared to the base material.

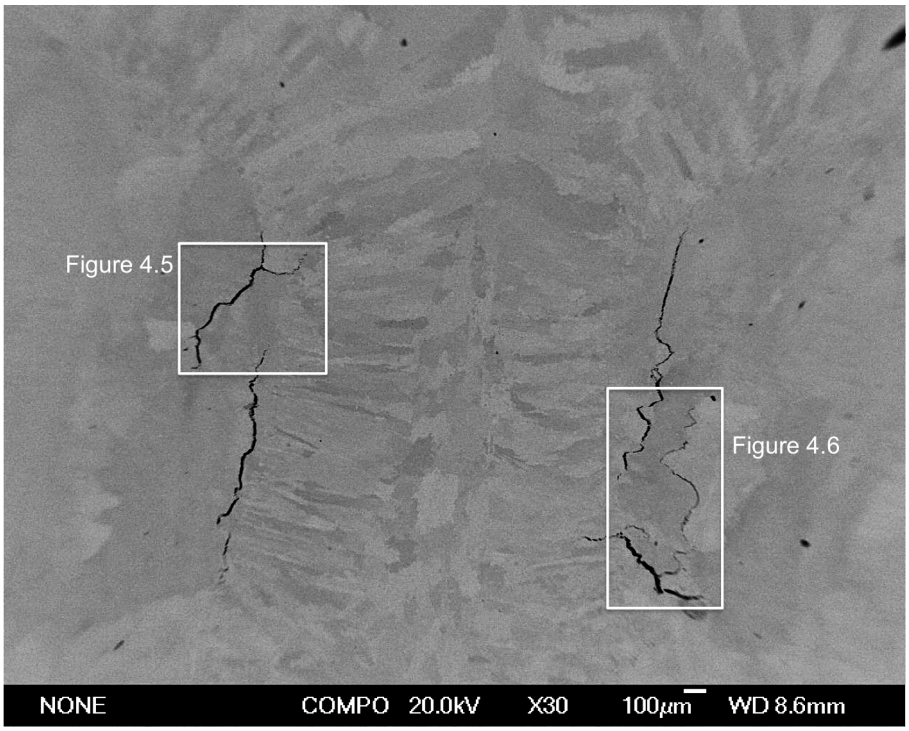

Figure 4.4 – Back scattered electron image showing regions of the welds where cracks formed, for the as-welded sample of high aspect ratio conditions.

A crack from the left hand side of Figure 4.4 is shown in more detail in Figure 4.5(a). Figure 4.5(b) shows the crack tip, which has extended slightly into the fusion zone. It shows that it has narrowed slightly compared to the bulk of the crack. The irregular shape of the crack and lack of voids at the tip indicate that this is a liquation crack.

Two distinct and separate areas of the crack have been analysed using EDX and are illustrated in greater detail in Figure 4.5(c) and (d). Both images show features of liquation – wide cracks with irregular but smooth edges, with resolidified material within the cracks shown by smooth surfaces. The EDX results are illustrated in Table 4.4 and Table 4.5 respectively, and indicate that there are unmelted carbides around the edges of the crack, and within the cracks the chemistry suggests resolidified liquation products consisting predominantly of γ/γ' eutectic, with some residual MC-type carbides.

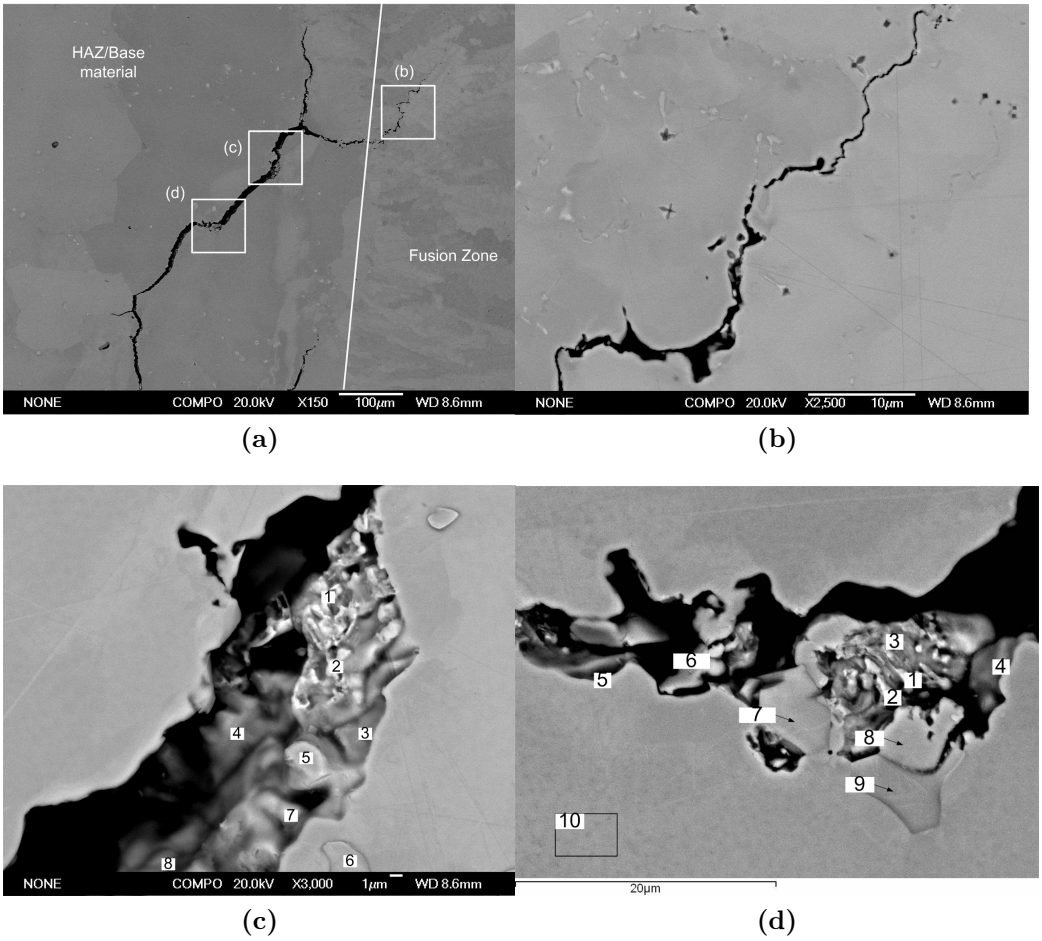

Figure 4.5 – (a) Crack on left of Figure 4.4, (b) tip of crack in (a) having extended into fusion zone, (c) higher magnification of part of (a) showing evidence of liquation and (d) another location of (a) showing evidence of liquation and EDX analysis points marked. Note how the crack has propagated along grain boundary, with some extension into the fusion zone.

The crack in Figure 4.6 is from the right side of the weld section, and shows different features from those observed so far. This crack appears to have formed along the grain boundary (see Figure 4.6(a)). It is narrower than those determined to be formed via liquation, and there is no evidence to suggest any liquation occurring. There is however evidence of fracture (Figure 4.6(c), points 3 and 4) which are carbides (see Table 4.6), but there is no evidence of melting and resolidification. Around the crack there are fine voids which are features found in stress cracks. These characteristics all indicate that this is a stress induced crack formed at low temperature.

Table 4.4 – Results from EDX analysis as illustrated in Figure 4.5(c).

No	C	O	Na	Al	Si	Ti	Cr	Fe	Co	Ni	Mo	W	Phase
1	8.64	4.77		3.35	1.85	6.72	9.43		7.14	53.08	3.16	1.86	Mixture of carbide and γ/γ' eutectic
2	7.87	2.89		2.77	0.64	5.27	12.04		8.13	53.2	3.92	3.27	Mixture of carbide and γ/γ' eutectic
3	2.97	2.6	0.52	0.77	1.61	5.45	13.03		8.83	62.79	0.88	0.53	Mixture of carbide and γ/γ' eutectic
4	4.18	1.49		0.49	0.47	3.89	12.65		9.15	65.88	1.21	0.6	Mixture of carbide and γ/γ' eutectic
5	2.94			2.71		5.73	14.3		8.34	59.46	3.97	2.56	Mixture of carbide and γ/γ' eutectic
6	18.95					44.73	1.44			2.56	16.22	16.1	M(Ti, Mo, W)C Type carbide
7	2.62	1.14		0.31		4.5	14.34		9.26	66.44	0.72	0.67	Mixture of carbide and γ/γ' eutectic
8	9.6	3.54		0.66	1.34	3.3	11.36	0.62	7.79	60.63	0.72	0.45	Mixture of carbide and γ/γ' eutectic
9	3.61			2.77		4.3	14.33	0.55	8.6	58.73	3.7	3.42	Matrix

Table 4.5 – Results from EDX analysis as illustrated in Figure 4.5(d).

No	C	O	Al	Ti	Cr	Fe	Co	Ni	Mo	W	Phase
1	1.69	0.5	1.04	5.66	13.64		9.87	64.52	1.88	1.2	Mixture of carbide and γ/γ' eutectic
2	3.57	1.23	1.26	5.54	14.167		9.53	63.13		1.54	Mixture of carbide and γ/γ' eutectic
3	6.72	1.02	2.87	4.67	12.85	0.51	8.16	56.70	3.51	3.00	Mixture of carbide and γ/γ' eutectic
4	4.89	1.09	0.98	4.69	13.52	0.60	9.14	63.63	1.45		Mixture of carbide and γ/γ' eutectic
5	3.83	0.95	0.87	4.65	13.78	0.61	8.77	63.56	1.54	1.11	Mixture of carbide and γ/γ' eutectic
6	10.84	1.84	3.34	6.22	11.59	0.47	7.18	51.13	4.20	3.20	Mixture of carbide and γ/γ' eutectic
7	20.36			45.09	0.85			1.99	9.99	21.72	M(Ti, Mo, W)C Type carbide
8	3.89		2.9	5.69	14.48	0.53	8.94	60.51		3.07	Residual of γ/γ' eutectic
9	19.73			46.68	0.91			2.25	13.03	17.41	M(Ti, Mo, W)C Type carbide
10			3.00	4.81	15.18	0.62	9.43	62.60		4.35	Matrix

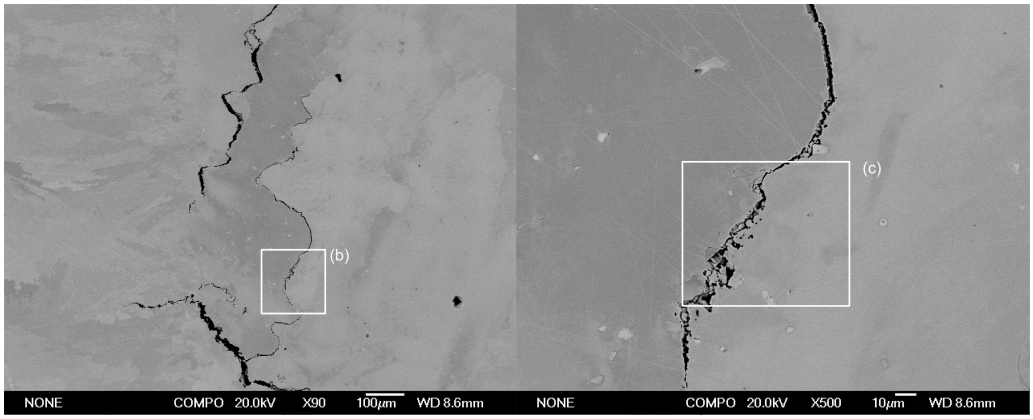

(a) **(b)**

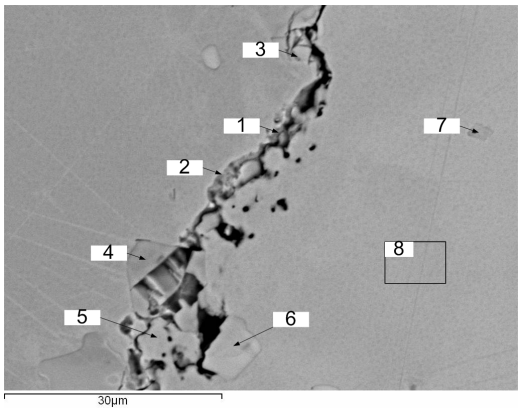

(c)

Figure 4.6 – (a) SEM image of a crack on the right side of Figure 4.4, (b) further detail of crack in (a), and (c) further enlargement with points for EDX analysis marked. Note that the cracks in (a) are all placed on grain boundaries.

Table 4.6 – Results from EDX analysis as illustrated in Figure 4.6(c).

No	C	O	Al	Ti	Cr	Fe	Co	Ni	Mo	W	Phase
1	7.21	5.34	2.69	3.96	12.45	0.46	7.99	51.02	3.63	3.02	Gamma
2	9.13	2.94	3.04	3.88	13.61	0.68	7.62	50.58	4.18	3.58	Gamma
3	19.62			43.82	13.6		0.67	3.62	11.76	19.15	M(Ti, Mo, W)C Type carbide
4	22.48			45.33	0.97			2.18	19.54	9.50	M(Ti, Mo, W)C Type carbide
5	2.75		2.80	3.88	16.05	0.80	9.86	59.73		4.12	Gamma
6	17.91			41.39	1.32			2.62	11.10	25.66	M(Ti, Mo, W)C Type carbide
7	13.89			58.03	1.55			4.58		21.95	M(Ti, Mo, W)C Type carbide
8	2.79		2.63	4.64	14.7		9.68	61.06		4.51	Matrix

4.3.4 High aspect ratio PWHT sample

This is the same weld that was analysed in section 4.3.3, but after being given the PWHT treatment. A low magnification back scattered electron image showing the regions of crack formation is shown in Figure 4.7.

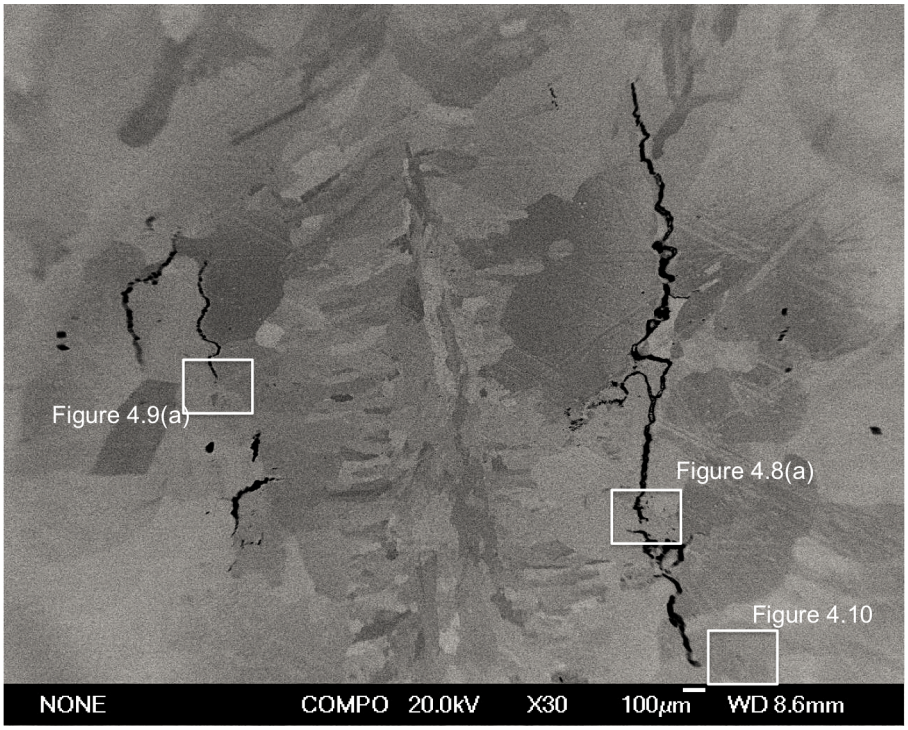

Figure 4.7 – BSE image showing regions of the welds where cracks formed, for the PWHT high aspect ratio sample.

This sample showed two different morphologies of cracks (see Figure 4.8), formed by the different mechanisms behind liquation and PWHT cracking. The liquation cracks show evidence of re-solidified precipitate phases, and are often a lot wider than the PWHT cracks, whereas the PWHT are significantly thinner and do not show any evidence of melting. Additionally, around the cracks which have a morphology which suggests they formed via liquation mechanism (like those illustrated in the previous sections), there are some unusual fine precipitate type features (Figure 4.8). These features appeared dark when viewed under back-scattered electron mode in the SEM.

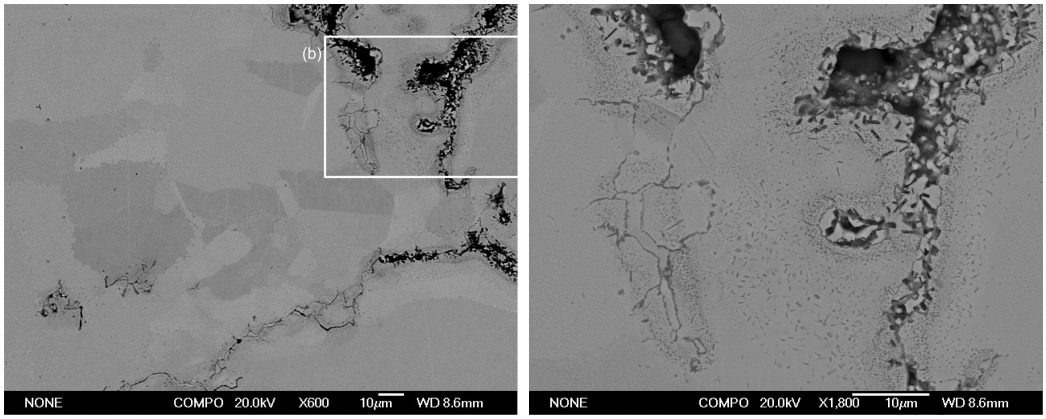

(a) **(b)**

Figure 4.8 – (a) Different morphology of as welded and PWHT cracks in PWHT sample, and (b) higher magnification of region showing further details of difference.

In Figure 4.9, an example of a liquation crack that has extended after the PWHT is shown. In Figure 4.9(b), there is further evidence of the fine particles which appeared around liquation-type crack, but these are not present around the crack tip. The crack appears to have extended during the PWHT, and the voids in front of the crack tip (Figure 4.9(a)) suggest a stress-induced mechanism has occurred.

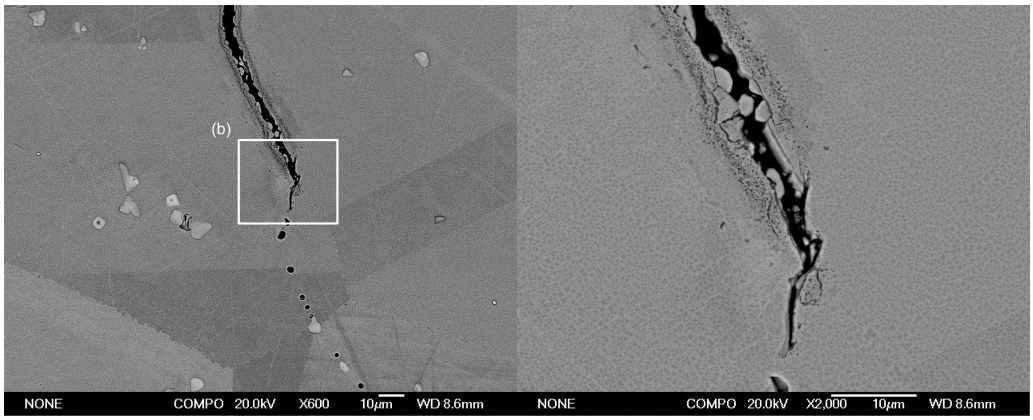

(a) **(b)**

Figure 4.9 – (a) The tip of a crack after PWHT and (b) higher magnification of crack tip showing evidence of oxidation surrounding liquated crack with a thin extension of the crack.

A final example of the cracks formed during the PWHT is shown in Figure 4.10, with subsequent EDX analysis in Table 4.7. There is no evidence of liquation occurring in this crack. This is also confirmed by the chemistry of points 1 and 2 which are very similar to point 3, but show a higher level of titanium, indicative of an influence of the secondary phase gamma prime. The crack shows a narrow, continuous morphology. There are also some fine voids formed at the front of the

crack tip formed by the stresses which dominate the formation of this type of crack. It is therefore concluded that this crack is a stress-induced crack, most likely formed by the strain-age mechanism.

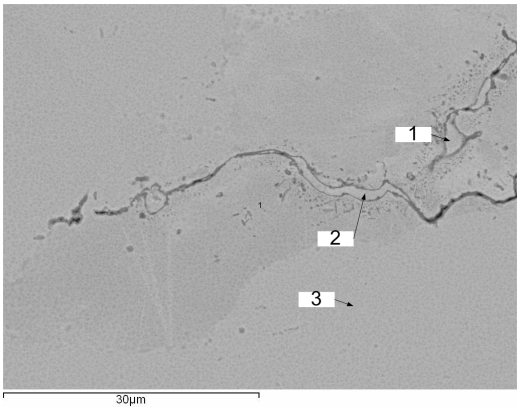

Figure 4.10 – A high magnification back scattered electron image of a PWHT crack showing no evidence of liquation with EDX points marked.

Table 4.7 – Results from EDX analysis as illustrated in Figure 4.10.

No	C	Al	Ti	Cr	Fe	Co	Ni	Mo	W	Phase
1	4.62	2.55	10.88	12.40	0.69	7.90	53.09	4.20	3.66	Gamma prime
2	6.06	2.75	7.85	13.00	0.51	7.48	54.40	3.68	4.27	Gamma prime
3	4.59	2.67	3.79	14.04	0.5	8.66	58.04	4.17	3.56	Matrix

4.4 Discussion

This analysis of the four samples provided some very interesting information regarding the cracking mechanisms occurring in the laser welds produced in Chapter 3. However, it is interesting that even where welds are produced in the aspect ratio range where the probability of cracking was shown to be significantly reduced, cracks could still be observed in some welds.

From the literature review (Chapter 1), there are different types of cracking occurring in nickel-base superalloys. They are usually defined by their location (i.e. weld metal/HAZ), but perhaps more importantly, by the type of mechanism by which they occur by, e.g. either hot cracks, or stress-induced cracks.

Hot cracks in superalloys are either solidification (weld metal), or liquation (HAZ). Of the four samples analysed using the SEM/EDX characterisation system, none of them contained any solidification cracks. In fact, of all the samples analysed in Chapter 3, less than 8 % showed any evidence of these cracks. These cracks also tended to form in deep penetration weld conditions, i.e. the higher aspect ratio conditions. As reported in the literature review, high aspect ratio conditions can be one of the causes for solidification cracking. Hence there is limited discussion here relating to this type of cracking in this alloy.

Of the as-welded samples analysed, all showed evidence of liquation cracking. All of these cracks show similar morphologies: wide, irregular in shape, with smooth edges (as opposed to sharp edges associated with fracture type cracks), with evidence of liquid running into the crack and resolidifiying. This final feature - evidence of liquid running into the crack - would have occurred due to the contraction forces pulling open the weak liquated grain boundaries to form the cracks, whilst at the same time the final stage of solidification of the liquated product would be occurring. The mechanism of constitutional liquation is best illustrated in Figure 4.3(b), which shows a carbide (point 6) surrounded by the partially liquated and solidified mixed material (points 4, 5 and 7). This crack also shows the features of a solidified liquid boundary around the crack, typical of a hot crack. The cracks also appeared on grain boundaries that are heavily decorated with secondary phases. The majority of the cracks analysed show evidence of constitutional liquation of secondary phases, with products primarily resolidified γ/γ' eutectic, but there is also evidence of liquated MC type carbide enriched with Ti, Mo and W. It is therefore possible that the resolidified γ/γ' eutectic observed in the EDX results is actually a product of constitutional liquation of γ'.

Constitutional liquation of γ' has been reported in IN738 (Ojo et al., 2004; Ojo and Chaturvedi, 2005). Also, Ojo et al. (2004) found that a high volume fraction of γ' is a contributory factor to liquation of this phase. Other work reported liquation of γ' in directionally solidified Rene 80 (Osoba et al., 2011). Osoba et al. (2011) also found the liquation of γ' to be affected by a high Ti content, which raises the γ' solvus (in Rene 80 this is around 1170 °C (Doncasters, 2006)) and also reduces the initiation temperature of γ/γ' eutectic formation (Osoba et al., 2011)). As a result, the difference in temperature between these events is reduced, and the usual window for dissolving γ' is reduced, resulting in conditions likely for liquation of the γ'.

Other works on the liquation of secondary phases in different heat treated conditions of Rene 80 found that in the solutionised condition (as in this work), the intensity of liquation was not enough to induce liquid film formation (Shahsavari et al., 2007). However, it is clear from the present work that there does appear to be enough liquation to induce cracks. What Shahsavari et al. may be suggesting is that in comparison to the microstructures which are more susceptible to liquation (as-cast and overaged) there is a significant reduction in cracks, and sample size was not high enough to produce enough quality samples to find suitable samples.

In addition to the hot cracks discussed above, there are also lower temperature stress-induced cracks which can occur in nickel-based superalloys. As highlighted in

section 1.6.2, there is some discussion as to the occurrence of stress-induced cracks forming during welding in nickel-base superalloys. It is interesting to note that one crack showed evidence of this type of mechanism, observed in Figure 4.6. This crack shows differences from the liquation cracks: thinner, with sharper edges, and there is no evidence of any partial melting of secondary phases or the grain boundary itself. Additionally, there are some voids surrounding the crack, which are associated with this type of crack. The chemical analysis (Table 4.6) along the crack shows only whole phases with no mixtures as observed in the liquation cracks. This may be a ductility dip crack, although normally this type of crack is observed in solid solution strengthened alloys.

Generally, precipitation hardened alloys are less susceptible to stress-induced cracks during welding due to the microstructure being engineered to resist grain boundary sliding, particularly at higher temperatures, through pinning by the carbides and also serration of the grain boundaries themselves. Hence this may be why there are less occurrences of this crack type occurring in this alloy, both in this thesis and in previous published works. Therefore, observing a crack of this type in this alloy is unique and it is unclear why this occurred in preference to the normal liquation cracks.

The PWHT sample provides some further interesting results. The type of cracks typically occurring during the PWHT are stress-induced, occurring via the strain-age mechanism. However, the sample also contained cracks formed during the welding cycle via liquation mechanism, these are observed in Figure 4.8 and Figure 4.9. Surrounding the wide and black cracks is what appears to be some form of particles which appear dark under the back scattered electron (BSE) image. This indicates that they are containing light atomic number elements, such as oxygen or carbon. These features do not appear at the tip of cracks, which appear with different morphology (thinner) and therefore propagated during the heat treatment. Without having undertaken further analysis of these features, it is difficult to comment on what they are.

Figure 4.9 shows an example of a crack which appears to have a small extension during PWHT (lack of oxidation), characterised by being narrower (Figure 4.9(b)) whilst there is evidence of stress voids (Figure 4.9(a)) further down the grain boundary where this crack propagated. In Figure 4.10, a high magnification image shows the tip of a crack propagated during the PWHT. It is clear that this crack shows no evidence of melting, and it is also significantly thinner than the cracks observed previously. The EDX (Table 4.7) confirms that there are a number of secondary precipitates on the grain boundary, but no evidence of liquation of any of these. In

this instance, the EDX at points 1 and 2 are marked as γ' because of the increased level of titanium. There is however similar traces of other elements found in the base of the material, and this is as a result of the interference caused by x-rays from the matrix material.

From this work, it is observed that the dominant cracking mechanism in the laser welds is constitutional liquation. This is because of all the cracks observed in the as-welded samples, it appears to be the most commonly occurring type, with perhaps the occasional occurrence of the stress-type cracks. However, the liquation cracks also impact the cracking in the PWHT condition of the material, because they not only propagate during the heat treatment via the strain-age cracking, but they also have an impact on the overall microstructure of the alloy, leading to weakened areas where new strain-age cracks may nucleate.

The very nature of the constitutional liquation mechanism means that often the cracks are difficult to avoid, however much the process is optimised as seen in Chapter 3. At least by the knowledge that the cracks are formed via this mechanism, the only way of freely avoiding their occurrence is by optimising the base metal chemistry/microstructure via the methods discussed in Chapter 1 to produce optimised microstructures, but this then loses the key properties of the alloy required for high temperature applications.

4.5 Conclusions

1. The as welded cracking in all three aspect ratio samples appears to occur predominantly through constitutional liquation of secondary phases. The cracking appears inter-granular, with a wide and irregular morphology, with smooth edges often showing re-solidified product;
2. The study of cracking using back scattered electron imaging and EDX characterisation reveals that the cracks are rich in products indicating liquation of γ/γ' eutectic, and MC type carbides enriched with titanium, molybdenum and tungsten. There is additional evidence of liquated MC type carbides in the low aspect ratio sample;
3. One as-welded sample appears to show a HAZ crack formed via a low temperature mechanism. This crack showed features of stress-induced cracking with voids and fracture surfaces appearing together with a narrower and straighter morphology. This could be an example of a ductility dip crack;
4. The PWHT sample shows existing cracks formed via liquation, with some of these appearing to propagate during PWHT, and new cracks shown to have nucleated during the PWHT. These are via a stress-induced cracking mechanism such as strain-age cracking. The cracks observed during PWHT are narrower with no evidence of melting, with additional stress-induced voids surrounding the cracks.

Chapter 5

Strain and residual stress measurement of laser welded Rene 80 samples with different aspect ratios

5.1 Introduction

The relationship between aspect ratio and HAZ cracking in superalloys is critically important in any future development of repair procedures which avoid defects forming in welds. All prior studies do not explain why the aspect ratio is critical to minimising cracking. The weld bead shape affects the stresses generated during welding as well as the residual stresses generated afterwards, which in turn affects the formation of both liquation and PWHT cracks.

5.1.1 Residual stresses in superalloy welding

There are various techniques applied to measure residual stresses in welds; and these are categorised into destructive (e.g. hole drilling, contour method and crack compliance) and non-destructive (e.g. diffraction, ultrasonic) (Withers and Bhadeshia, 2001). Diffraction techniques for characterisation of materials have been in use for over 80 years, having initially been via X-ray and latterly neutrons (Krawitz, 2011).

5.1.2 Neutron diffraction measurement of residual stresses

Diffraction techniques employ the Bragg equation (Eq. 5.1) to relate changes in interplanar spacing (Δd_{hkl}) with elastic strain, when the incident wavelength (λ) and diffraction angle θ_{hkl} are known.

$$\lambda = 2d_{hkl} \sin \theta_{hkl} \tag{5.1}$$

The interplanar spacing, d, is related to the cubic lattice parameter (a) by Eq. 5.2 for cubic crystals:

$$d = \frac{a}{\sqrt{(h^2 + k^2 + l^2)}} \tag{5.2}$$

Where h, k and l are the miller indices that define the Bragg plane.

The changes in measured d-spacing (or lattice spacing) are then related to strain by Eq. 5.3 :

$$\varepsilon = \frac{d - d_0}{d_0} = \frac{a - a_0}{a_0} \tag{5.3}$$

Where ε is the strain, d and a are the measured interplanar spacing and lattice parameter respectively, and d_0 and a_0 are the stress-free references. The result is the use of the atomic spacings as 'strain gauges', due to the fundamental way that stress relates to strain, which relates to changes in d spacing, which affects the diffraction peaks.

The significant benefit of neutrons over X-rays is their ability to travel deeper into a material's structure than X-rays. This was realised in the mid 1970's when the first development of neutron diffraction was published (Krawitz, 2011). Following this, rapid development lead to the first generation of modified X-ray diffraction equipment. Krawitz (2011) also presents a list of the dedicated instruments for neutron diffraction, and the sources may be either pulsed or a reactor source. Reactor sources are more stable, but offer fixed wavelengths. Pulsed sources offer a greater range of wavelengths, allowing results from multiple peaks to be captured at once. This study used a pulsed source of neutrons.

The neutrons from the pulsed sources have a range of energies and wavelengths, and the procedure to measure interplanar spacing is defined as time-of-flight (TOF) whereby the diffraction angle (ϑ) is fixed (Withers and Bhadeshia, 2001), enabling a whole diffraction pattern to be recorded. The length of the time of flight is related to the time difference between the arrival of the most energetic neutrons, and the last to arrive (Withers and Bhadeshia, 2001). The wavelength (λ) of the neutrons is determined by:

$$\lambda = \frac{h}{m(L_1 + L_2)}t \tag{5.4}$$

Where h is Planck's constant, m is the mass of the neutron, t is its time of flight, and L_1 and L_2 are the flight paths.

The Engin-X instrument at ISIS (the name of the neutron source at the Rutherford-

Appleton Laboratory), which was used for these trials, operates using the TOF principle. A schematic illustration of the ENGIN-X layout with the flight paths annotated is found in Figure 5.1.

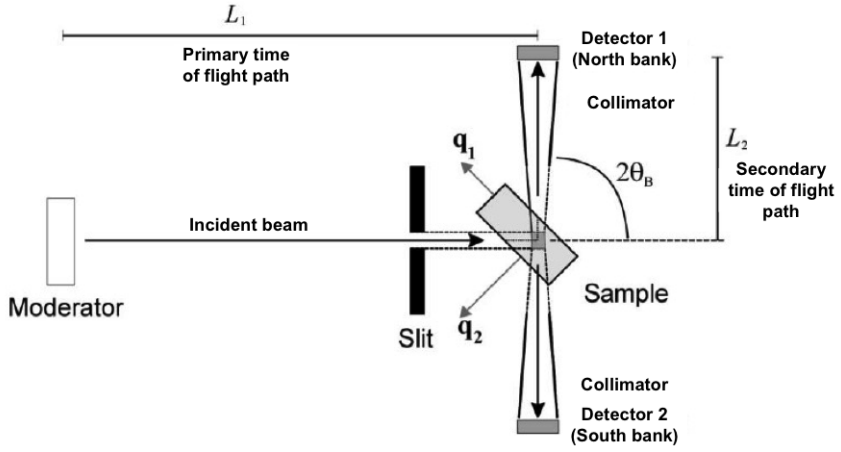

Figure 5.1 – Schematic diagram of time-of-flight diffraction of the ENGIN-X instrument at ISIS. (Modified from Santisteban et al. (2006)).

An example time-of-flight (TOF) diffraction profile is shown in Figure 5.2. This shows the different peaks and the corresponding crystallographic planes, for stainless steel.

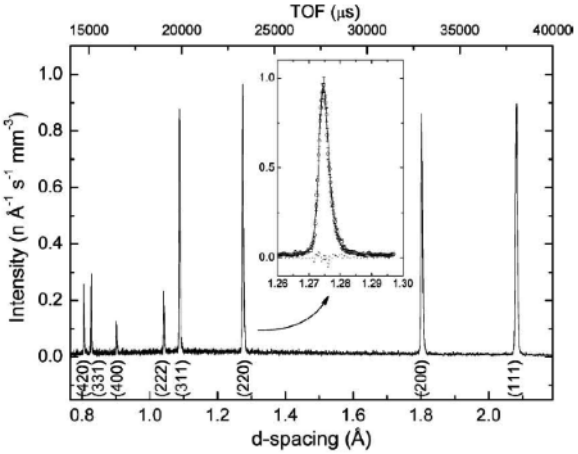

Figure 5.2 – Example diffraction profile for a stainless steel, with the d-spacing and corresponding TOF related to the various crystallographic peaks. (Santisteban et al., 2006).

Each peak of the diffraction pattern in Figure 5.2 corresponds to a crystallographic plane {hkl}, and applying Eq. 5.1 to Eq. 5.4, the d-spacing can be calculated thus:

$$d_{hkl} = \frac{h}{2\sin\theta(L_1 + L_2)m} t_{hkl} \tag{5.5}$$

Where the t_{hkl} is the position of the peak in the TOF spectrum, and other items are listed previously.

The above equation can be used to calculate the d-spacing for each individual peak, or can produce an average over a number of peaks as required. This then allows the strain to be calculated with Eq. 5.3. However, by using a Rietveld or Pawley refinement across the whole diffraction peak, the average lattice parameters can be calculated. This latter approach is considered more accurate as it gives an approximate value based on a larger range of crystallographic planes. In this case, Eq. 5.3 is still used, but instead of d spacing, the lattice parameter (designated as a) is used.

The ENGIN-X instrument used in this study positions the sample in line with the incident beam (Figure 5.1). Two detector banks are placed at 90° to the incident beam, which ensures that the same volume of material is measured for each orientation (Santisteban et al., 2006). The use of two detectors means that two perpendicular strain orientations can be measured simultaneously.

The volume of material from which the diffraction pattern is obtained is defined as the gauge volume. This volume is produced from the intersection of the incident and diffracted beams. The size of the incident beam is controlled by the slits, and radial collimators are used in line with the detectors to control the dimensions of the scattered beams. The gauge volume influences the quality of measured data, and also the amount of time required per measurement. As a result, there is often a compromise between the size of the gauge volume to ensure the data obtained is of good quality, whilst minimising the measurement time.

Measuring residual stresses in welds of various materials has been a major application of the technique. A variety of processes including laser, arc and friction stir welding have all been measured, as well as various materials. A recent review of the uses of the ENGIN-X instrument included archaeological materials, welding residual stresses, and characterisation of phase transformations in steels (Zhang et al., 2009). An important development is in situ measurement of welds (Woo et al., 2011).

There are some publications which have investigated neutron diffraction measurement in superalloys, however none of these related the residual stresses to the weld bead geometries. Dye et al. (2000) studied TIG welds on thin (2 mm) IN718, and found the longitudinal direction to be tensile in the weld metal (with strain of 1480 με) and drops to compressive further from the weld centreline (-800 με) before becoming slightly tensile again. A similar study on C263 by Korsunsky and James (2004) presented longitudinal measurements for strain and found that the weld metal was tensile with a peak of around 3000 με and compressive in the base material with

values around -2000 με. However, these studies avoided the complications found in the present study: namely a large material thickness (22 mm) and a large average grain size.

Large thickness provide difficulties with diffraction studies because of the increased neutron flight path through the material, which increases the absorption of the beam and therefore requires more measurement time to get a good diffraction peak. The grain size influences the measurement because the grains need to be orientated correctly with respect to the beam. If the sample has a large grain size, then the number of grains correctly orientated is reduced and therefore the data quality is poor. These problems may be addressed by using a large gauge volume, however this reduces the spatial resolution and results in a poorer quality of data.

5.1.3 Aims

The work in this chapter aims to:

1. To undertake a feasibility study of the use of neutron diffraction for residual stress measurement in thick, large grain sized nickel based superalloy castings;
2. To quantify the residual stresses developed in two separate samples of different weld bead geometry;
3. To relate the above to the cracking observed in the as-welded and PWHT conditions.

5.2 Experimental procedure

5.2.1 Material

Cast Rene 80 was used for these trials. This material had a chemical composition within the specification range shown in Table 2.1 and was produced as described in Chapter 2 with the smaller grain size. Prior to the welding trials it was solutionised (See Figure 2.5 in Chapter 2).

5.2.2 Welding trials

Each weld was performed on an individual block of material with dimensions 73 mm long, 43 mm wide and 22 mm thick (Figure 5.3). Prior to welding, the blocks are shot blasted, and then cleaned with an angle grinder and wire brush to ensure the surface was free of any surface contaminants. After cleaning, and prior to welding, the surface was degreased with acetone. Single pass autogenous bead-on-plate welds were laid on the cleaned surface, of approximately 50 mm length, as illustrated in Figure 5.3.

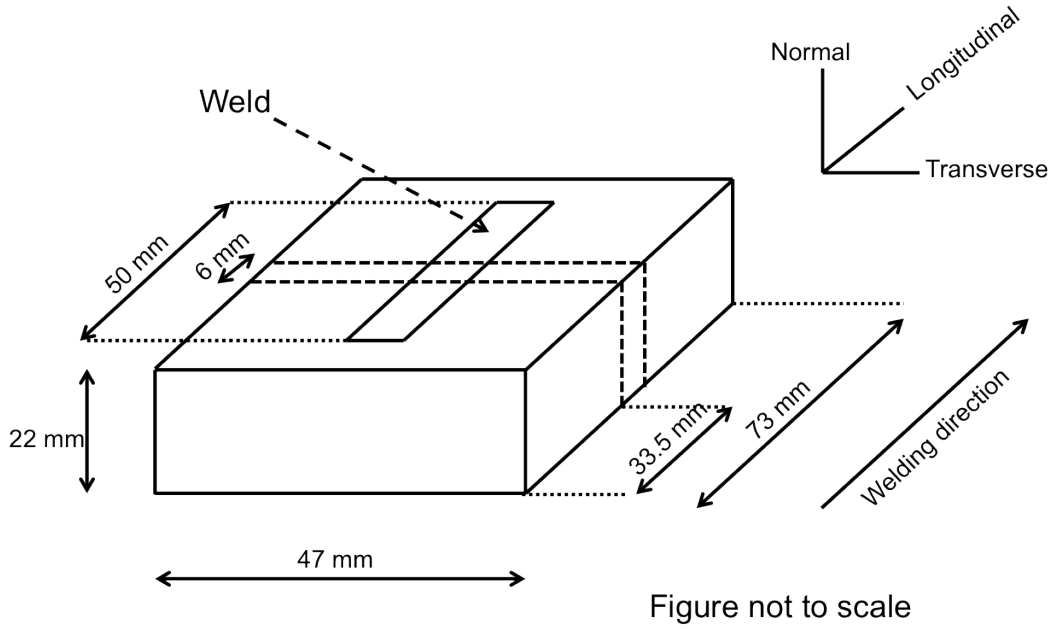

Figure 5.3 – Dimensions of the material used in these trials. Figure illustrates relative position of weld bead, dimension of weld bead, and location of 6 mm stress-free reference samples. Note that figure not to scale.

5.2.2.1 Parameter selection

The parameters were selected from the trials in Chapter 3 to produce four different aspect ratios (penetration to width) welds and are shown in Table 5.1. Figure 5.4 shows these parameters on a contour plot from Chapter 3 that predicts the likelihood of cracking. All the samples had identical heat input. The first three had identical power and welding speed, and only the beam diameter was varied to produce a low aspect ratio (sample 1), optimum aspect ratio (sample 2) and high aspect ratio (sample 3) weld. Sample 4 used the optimum aspect ratio, but with a lower heat input. Note that due to time restrictions it was only possible to do neutron diffraction measurements on samples 2 and 3.

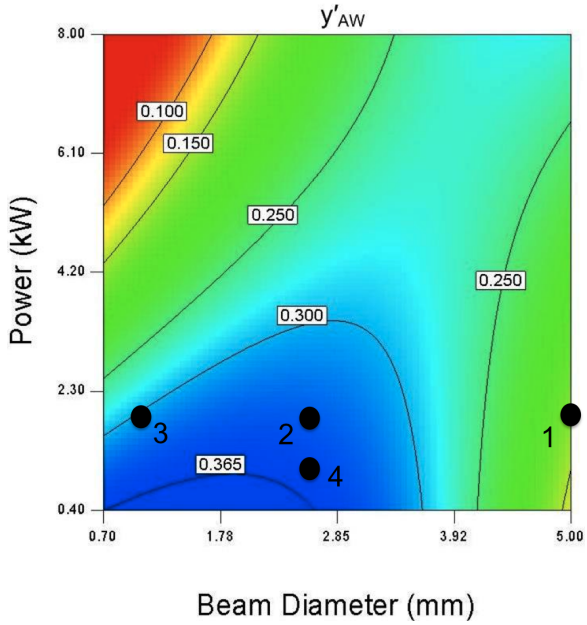

Figure 5.4 – Contour plot (Figure 3.5 from Chapter 3) showing points for each sample in these trials where parameters were selected.

Table 5.1 – Parameters used to produce welds in these trials. Desired aspect ratios based on previous trials in Chapter 3. *This is an assumed aspect ratio as this beam diameter was not used previously.

Sample	Power (kW)	Welding speed (mm/min)	Beam Diameter (mm)	Calculated heat input (kJ/mm)	Desired aspect ratio
1	2	600	5.0	0.2	0.19
2	2	600	2.5	0.2	0.55
3	2	600	1.2	0.2	> 0.65*
4	1	300	2.5	0.2	0.58

5.2.2.2 Welding procedure

The welds were produced using the same laser and robot as described in Chapter 3. A ten degree angle was applied to ensure protection from any back reflection. In these trials, a 500 mm focal length lens was used. The use of this lens is not significant because the beam profile was measured to ensure the exact beam diameters required were produced. However, this lens had an in focus beam diameter of 1.2 mm, and this is therefore the smallest diameter possible in these trials.

The robot position was fixed, and a single axis traverse motion was used, on which the samples were attached using vacuum clamps. The shielding gas was supplied using a nozzle inline with the welding direction at the leading edge of the weld pool. The same high purity argon gas was used at a flow rate of 12 L/min.

For each set of parameters, two samples were produced. One was machined to produce a stress free reference sample, while the other was used for stress measure-

ments in the diffraction study.

5.2.3 Neutron diffraction measurements

The measurements were performed using the ENGIN-X instrument on the ISIS pulsed neutron source, based at the Rutherford-Appleton Laboratory in Oxfordshire.

5.2.3.1 Stress-free reference samples

The weld that had the stress free reference cubes removed had a 6 mm thick section cut through the centre of the block, from which four cubes of 6 mm side length were machined. The location of these samples is shown in Figure 5.5. The cutting was completed using a wire EDM system to minimise any additional residual stresses input into the sample using standard cutting techniques, as well as ensuring the cubes were near perfect shape and dimensions.

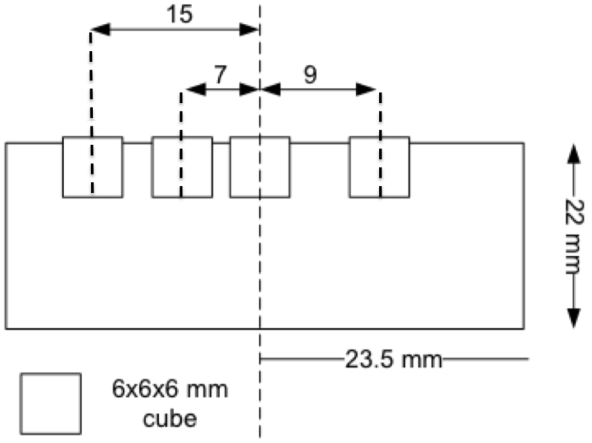

Figure 5.5 – Schematic of positions of stress-free reference cubes removed from section of weld.

5.2.3.2 Strain-measurement

The measurement points are shown in Figure 5.6 and were made from -2 mm to + 9 mm for the normal and transverse directions, and -2 mm to + 5 mm for the longitudinal directions (with 0 mm being the weld centreline). All of the points were measured 3 mm from the top surface. The d_0 measurements were taken with the beam aimed at the centre of the cube.

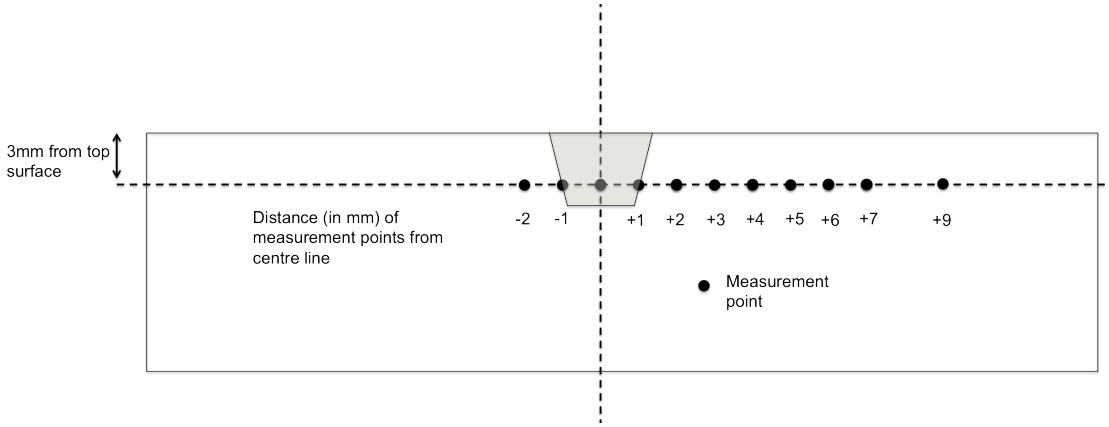

Figure 5.6 – Illustration of a cross section of sample, with positions of measurement annotated. Note figure not to scale, and shaded area is representative of location of weld bead.

Table 5.2 lists the measurement settings used. The count time is a measure of ensuring enough data has been collected for a sufficient diffraction profile. For the normal and transverse direction, 60 μA required an average of 50 mins of continual beam time, and for 100 μA it was approximately an average of 90 mins. During the measurements, there was often a loss of the beam, resulting in longer times than the average for some points.

Table 5.2 – Details of the specific point by point measurements during neutron diffraction measurements.

Sample/orientation	Gauge volume (mm^3)	Count time (μA per point)
d_0	2x2x2	20
Transverse / Normal	2x2x15	60
Longitudinal	2x2x2	100

The samples were positioned on an X-Y-Z orientation system within the measurement chamber. A general overview of the ENGIN-X instrument set up can be seen in Figure 5.7.

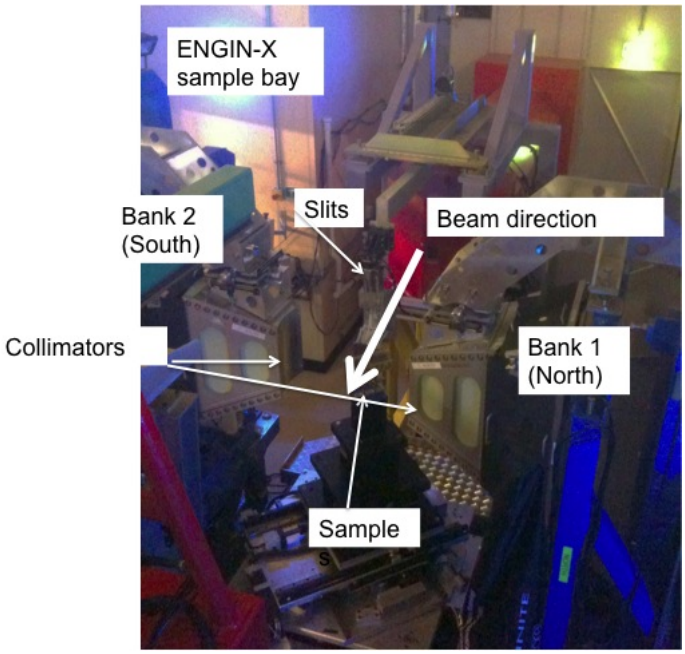

Figure 5.7 – Overview of the ENGIN-X Instrument and annotations of important components.

The beam was targeted onto the sample, and a gauge volume is produced according to the collimators and slit settings. The beam is then diffracted and reflected, and these are detected respectively by detectors in banks 1 and 2.

5.2.3.3 Analysis procedure

The analysis of the diffraction data involves fitting a mathematical model, either for a Rietveld refinement (multi-peak) or individual single peak. The data is then produced as either a lattice parameter (related to the cubic crystal) or d-spacing value (single peak).

The lattice parameter/d-spacing values are converted to strain using Eq. 5.3. The error for the strain is calculated using Eq. 5.6 and will be plotted as error bars in the strain plots.

$$\varepsilon_{error} = \sqrt{\left(\left(\frac{d_{error}}{d_0} \times 10^6\right)^2 + \left(\frac{d_{0error}}{d_0} \times 10^6\right)^2\right)} \tag{5.6}$$

During the analysis, the diffraction plots were checked for their quality. In the normal direction the plots were sufficient to produce the Rietveld refinement and individual studies on the {311} and {200} peaks. Although in most cases the transverse direction could produce a value for the Rietveld refinement and {200} data, the {311} peaks were strongest for this direction. However in the longitudinal direction it was only possible to obtain data from the {200} peaks.

5.2.3.4 Stress calculation

Once the strain has been calculated for each principal direction, the stress can be calculated based on Eq. 5.7:

$$\sigma_N = \frac{E_{hkl}}{(1+v_{hkl})(1-2v_{hkl})}\left[(1-v_{hkl})\varepsilon_N + v_{hkl}(\varepsilon_T+\varepsilon_L)\right]... \tag{5.7}$$

Where E_{hkl} is the Young's modulus for the {hkl} crystallographic plane, υ_{hkl} is the respective Poisson's ratio. For the transverse and longitudinal directions, the respective terms are swapped.

The Rene 80 material properties for the specific crystallographic planes are not available. The bulk data for Rene 80 is available, and the bulk and specific plane data for a similar alloys is also available. Therefore the material properties were assumed based on the ratio for the IN718 data found in Dye et al. (2000). This data is presented in Table 5.3.

Table 5.3 – Material properties used to calculate stress.

Material	E (GPa)	E_{200} (GPa)	υ	υ_{200}
IN718	204	163	0.299	0.340
Rene 80	208	167	0.30	0.341

5.2.4 Metallography

For the cracking study after the neutron diffraction measurements, the samples were split so that the welds which had the stress-free references taken from them were analysed in the as welded condition, and the samples that were measured at ISIS were sent for the standard post-weld heat treatment (See Figure 2.5). Samples were then taken to analyse cracking in the PWHT condition. In total, six sections from each weld were taken at positions along the sample. The same metallographic procedure as used described in Chapter 2 was used.

5.3 Results

5.3.1 Weld bead geometries

In Figure 5.8, the macros of each weld are shown. The weld bead geometries for each sample were averaged across each section and are presented in Table 5.4. Samples 3 and 4 have the highest penetration and have similar profiles. The samples produced to have the aspect ratios below and in the optimal aspect ratio range were unfortunately slightly out of the range desired (see Table 5.1).

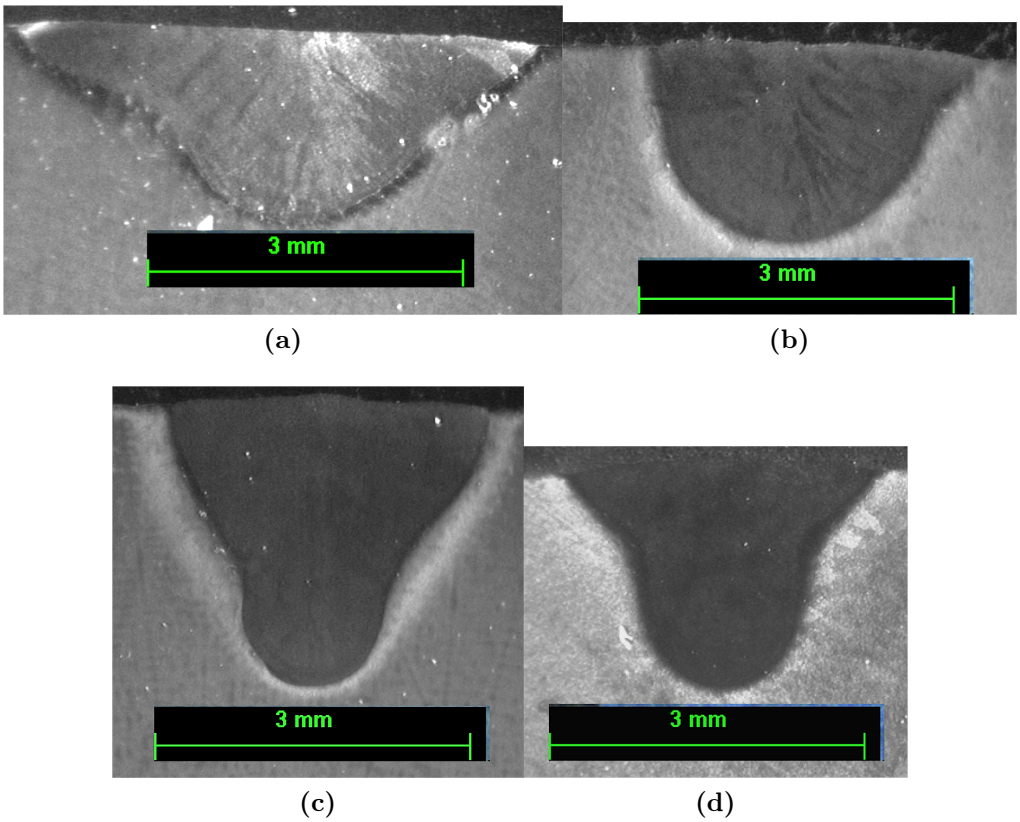

Figure 5.8 – Macros images of welds in these trials. (a) Sample 1 (Aspect ratio of 0.34). (b) Sample 2 (Aspect ratio of 0.65). (c) Sample 3 (Aspect ratio of 0.90). (d) Sample 4 (Aspect ratio of 0.74).

Table 5.4 – Summary of weld geometry data.

Sample	Width (mm)	Penetration (mm)	Aspect ratio
1	4.97	1.69	0.34
2	2.73	1.78	0.65
3	2.99	2.69	0.90
4	2.79	2.06	0.74

5.3.2 Cracking

All of the welds contained HAZ cracking, in both the as-welded and PWHT conditions. Table 5.5 summarises the cracking observed in these samples in both conditions.

Table 5.5 – Breakdown of cracking per section observed in samples.

Sample	As-welded		PWHT	
	ACL (μm)	StErr of the mean	ACL (μm)	StErr of the mean
1	311.2	89.2	295.9	53.2
2	92.0	29.0	1299.4	358.0
3	52.4	35.3	1210.6	379.2
4	68.7	68.7	734.7	142.1
	As-welded		PWHT	
Sample	TCL (mm)	StErr of the mean	TCL (mm)	StErr of the mean
1	1.14	0.32	2.13	0.59
2	0.12	0.05	3.58	0.63
3	0.35	0.24	3.28	0.56
4	0.09	0.10	4.42	0.69

In Figure 5.9, the ACL/section is plotted for each sample, for both conditions. For the as-welded condition, only sample 1 (which is the weld with the lowest aspect ratio of 0.34) had an ACL greater than 100 μm. All of the samples had small error bars illustrating that the variation across the weld was small. The ACL/section increases significantly after the PWHT is applied, particularly in the case of samples 2, 3 and 4, which had all previously showed small ACLs. The error bars are also large for sample 2 and 3.

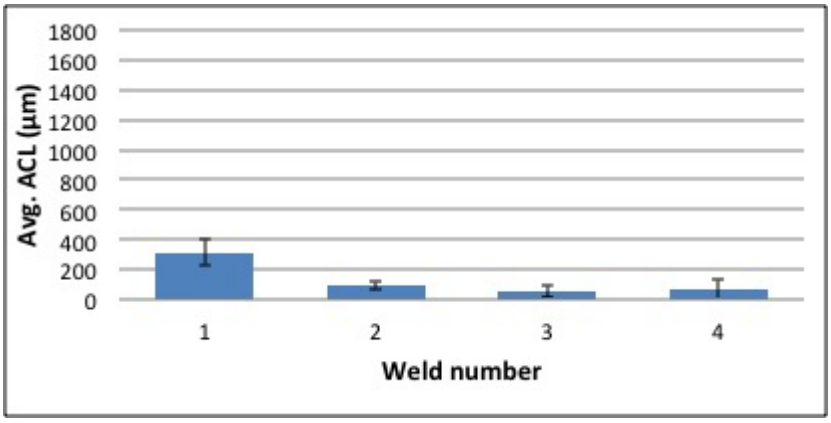

(a)

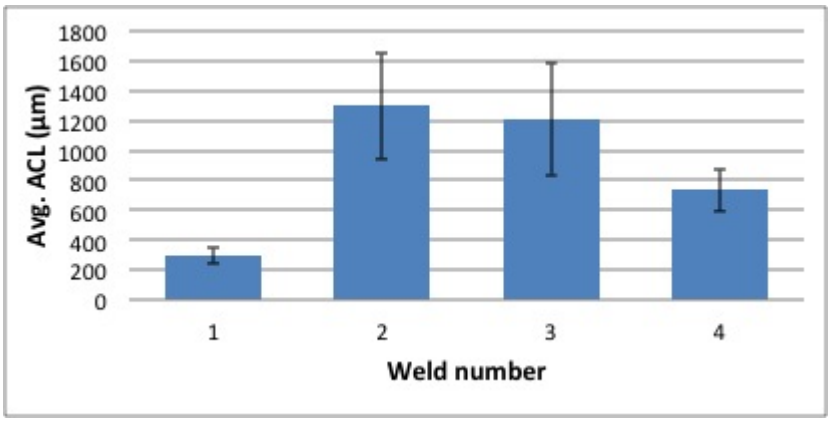

(b)

Figure 5.9 – Comparison of the average crack length (ACL) per section for (a) as-welded condition and (b) PWHT condition. The error bars represent the standard error of the mean across the 6 sections.

The TCL/section is plotted in Figure 5.10 for both conditions. The as-welded condition (Figure 5.10(a)) shows low cracking in samples 2, 3 and 4 as for the ACL values. However, the plot for the PWHT condition (Figure 5.10(b)) shows a large increase in TCL across all samples, as would be expected based on the ACL plots. The error bars are now similar for each sample in this plot, indicating that the variation in TCL across the whole weld was consistent.

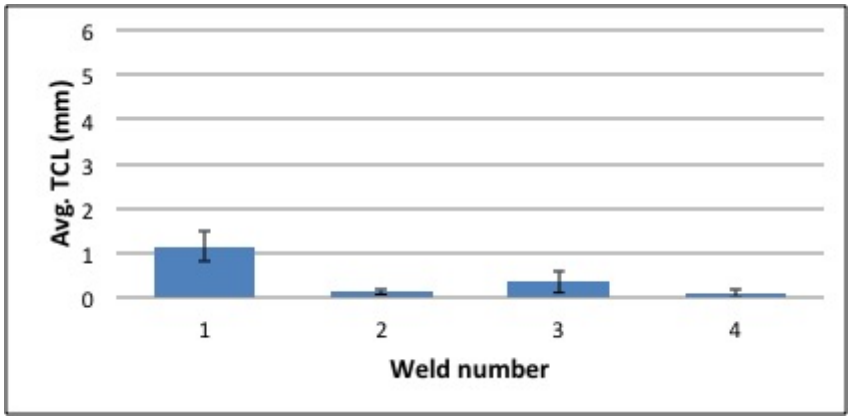

(a)

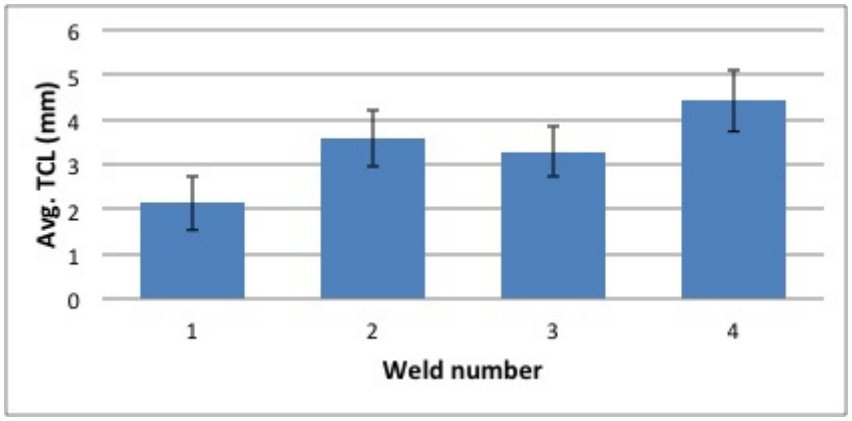

(b)

Figure 5.10 – Comparison of the total crack length (TCL) per section for (a) as-welded condition and (b) PWHT condition. The error bars represent the standard error of the mean across the 6 sections.

The large increase in cracking after PWHT appears to be partly due to a significant amount of weld metal cracking. In all PWHT samples this type of crack was visible, although samples 2, 3 and 4 had significantly larger examples. Examples of the cracks observed in the HAZ in both conditions, and weld metal cracks in the PWHT condition are in Figure 5.11.

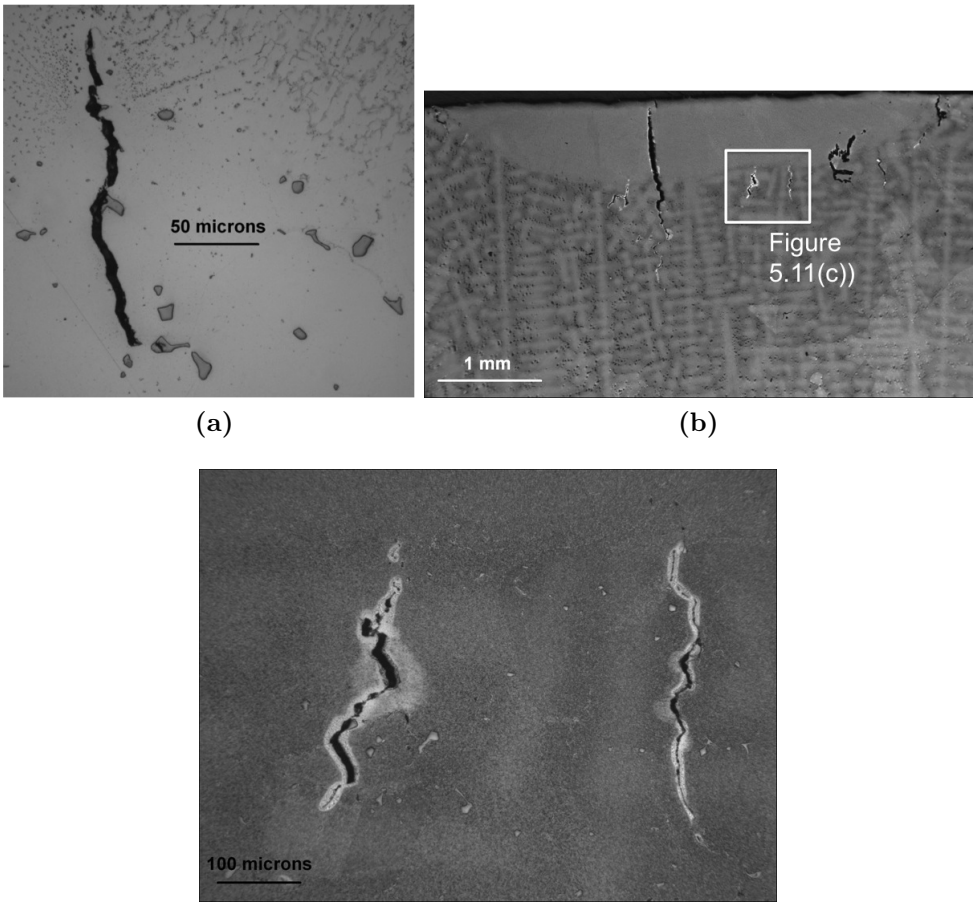

(a) **(b)**

(c)

Figure 5.11 – Examples of crack morphologies observed in sample 1. (a) as-welded HAZ crack, (b) PWHT weld metal cracking, and (c) PWHT HAZ crack.

5.3.3 Strain calculation results

The normal direction comparisons can be observed in Figure 5.12. These plots were created by using the average of banks 1 and 2 data for the stress-free reference. The first significant point is how similar the Rietveld refinement and {200} plots are for both samples. The {311} data appears to be more compressive in both samples than the {200}/Rietveld refinement.

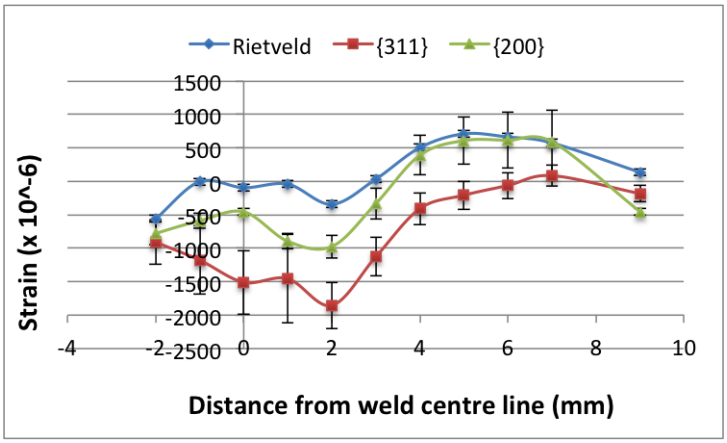

(a)

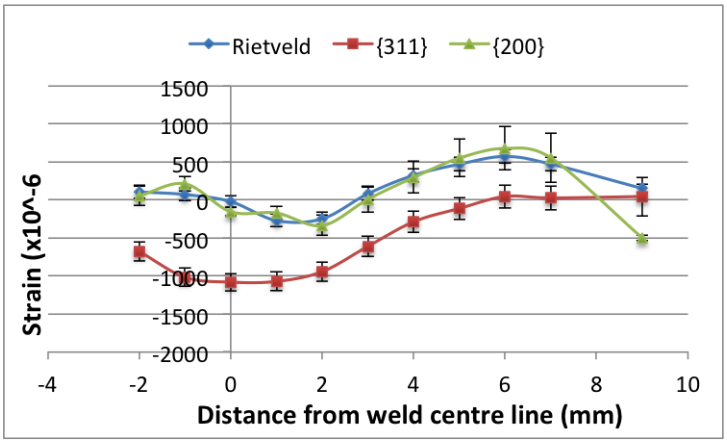

(b)

Figure 5.12 – The strain in the normal direction across the samples, comparing Rietveld refinement with {200} and {311} peaks. (a) Sample 2, and (b) Sample 3. Strain was calculated using the average of banks 1 and 2 for the stress-free reference data.

The plots in Figure 5.13 compare the Rietveld refinement and single peak profiles of both samples. It appears that for the Rietveld refinement, both samples are nearly identical for the normal direction. However, the {200} shows sample 2 is more compressive in the weld/HAZ area than sample 3. The error bars plotted on these figures show the error in the strain is smaller for Rietveld refinement than the {200} plot.

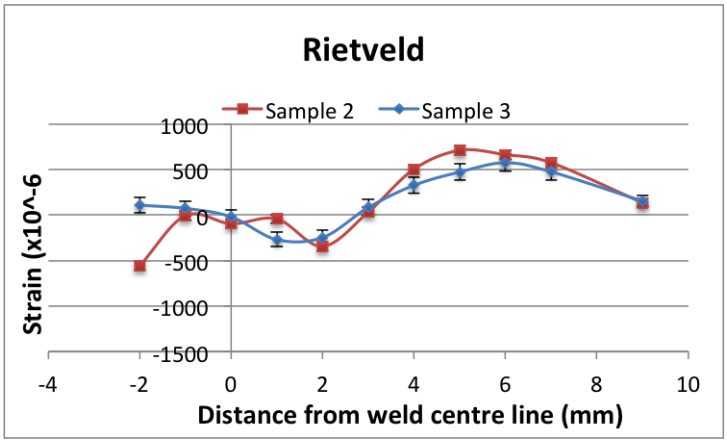

(a)

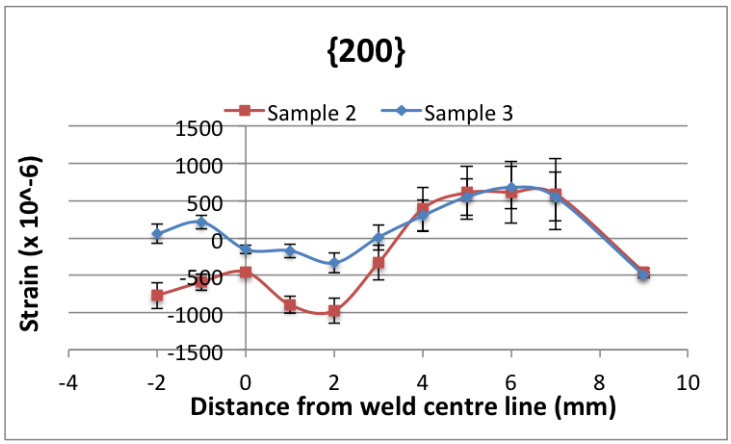

(b)

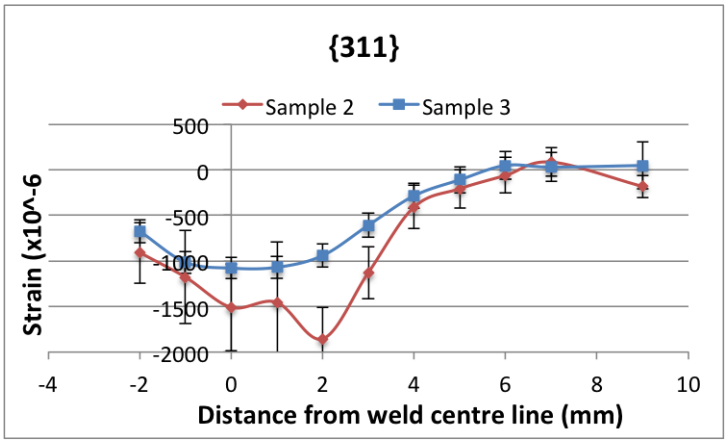

(c)

Figure 5.13 – Comparison of strain in the normal direction for (a) Rietveld refinement and (b) {200} and (c) {311} single peak, for both sample 2 and 3.

The transverse direction comparisons in Figure 5.14 show higher values of strain than in the normal direction. Again, the {311} peaks are more compressive than the Rietveld or {200}. In all directions the strain tends to zero as the measurements

tend towards the base material. Note also how the Rietveld data is only partially complete.

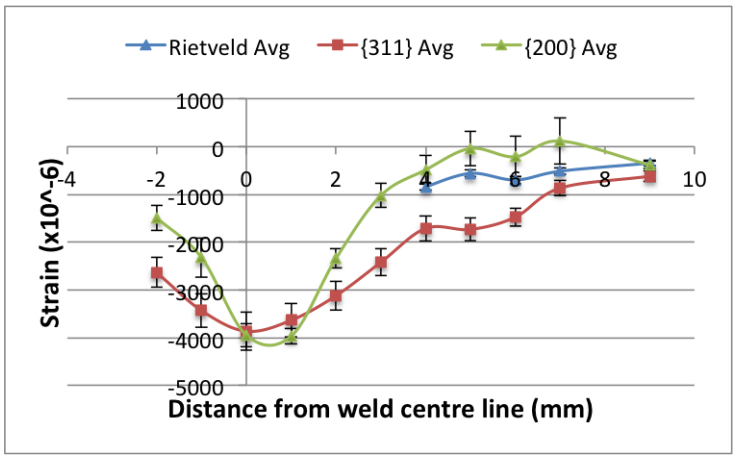

(a)

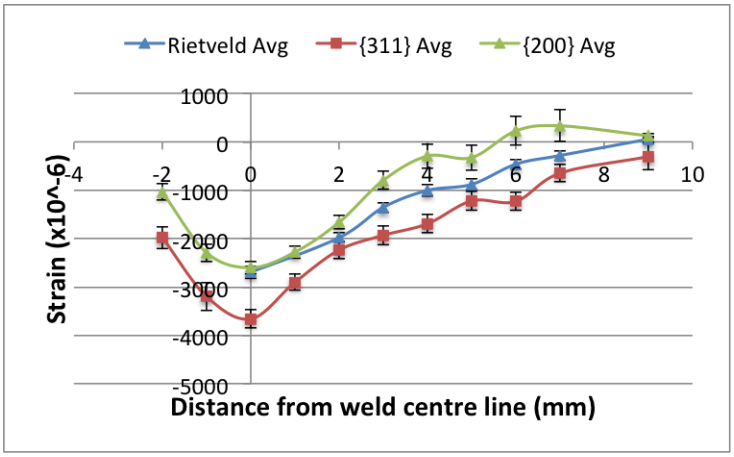

(b)

Figure 5.14 – The strain in the transverse direction across the samples, comparing Rietveld refinement with {200} and {311} peaks. (a) Sample 2, and (b) Sample 3. Strain was calculated using the average of banks 1 and 2 stress-free reference data.

Figure 5.15 compares the {311} and {200} individually for both samples. Both the {311} and {200} data show similar trends and values for both samples in the far HAZ/base material (again around 4 mm). However, in the weld zone/near HAZ area, the material is highly compressive in this direction in both cases.

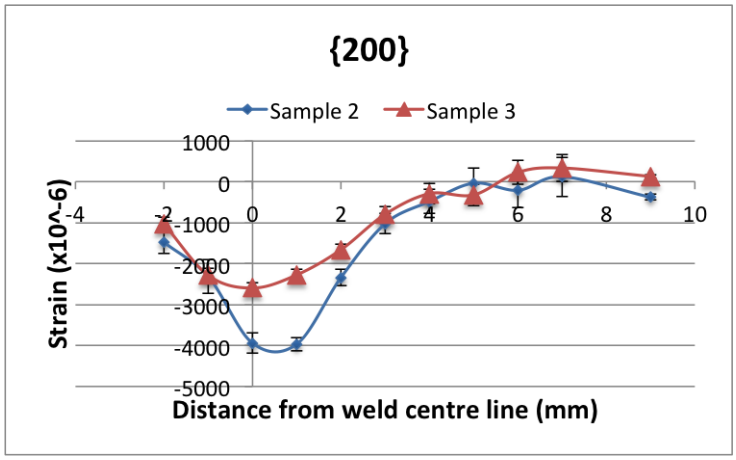

(a)

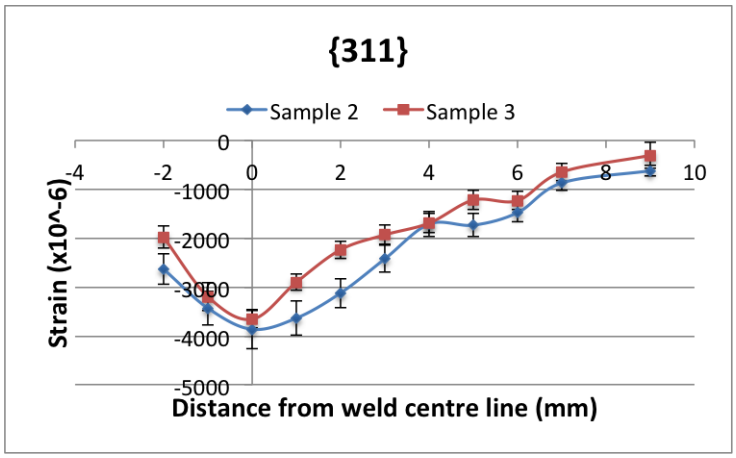

(b)

Figure 5.15 – Comparison of transverse direction for (a) {200} and (b) {311} single peaks, for both sample 2 and 3.

For the longitudinal direction, only the {200} data is presented in Figure 5.16. This figure shows both samples are highly compressive, with no tensile strain in the material at any point. The curves also show no significant trend for either sample. The error bars are also larger in this plot than in the transverse and normal case, indicating greater uncertainty.

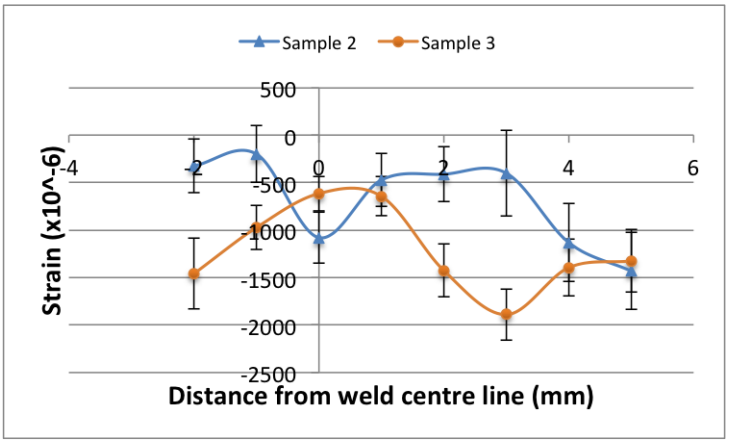

Figure 5.16 – Comparison of longitudinal direction for {200} single peak, for both sample 2 and 3.

5.3.4 Stress in {200} direction

The stress in each sample (for the {200} direction only) is plotted in Figure 5.17. The most surprising aspect of these plots is the longitudinal stresses aren't strongly tensile in the weld region. However, it does appear that the stresses in the transverse and normal directions are more compressive in sample 2 than in sample 3. Plots showing the comparison of each sample for each stress direction are individually shown in Appendix C.3.

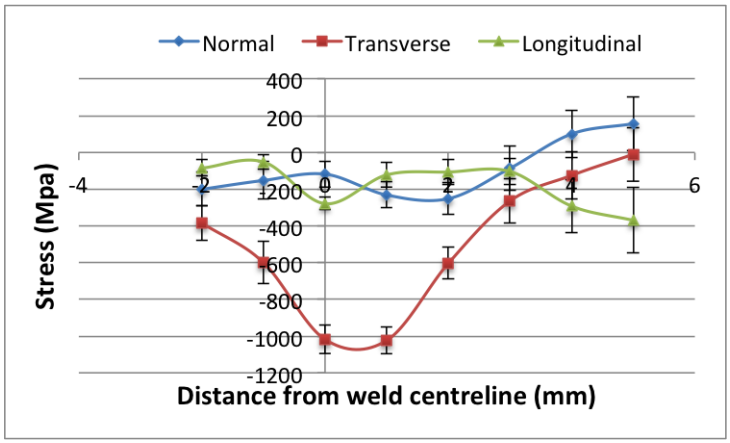

(a)

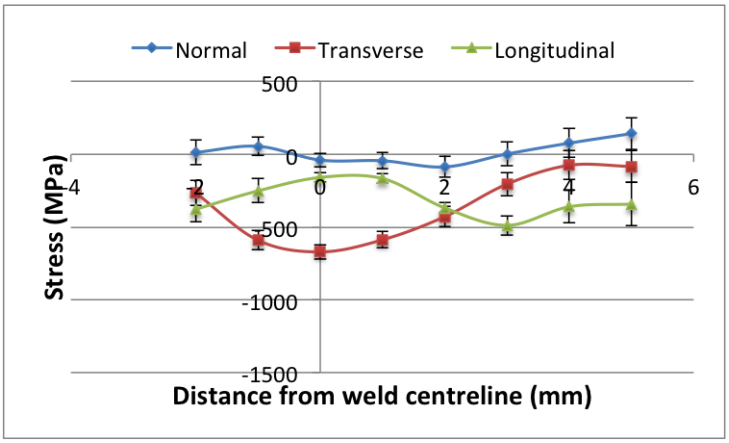

(b)

Figure 5.17 – Stress for each direction calculated from the {200} crystallographic plane. (a) Sample 2 and (b) Sample 3.

5.4 Discussion

5.4.1 Cracking

This chapter investigated some select welding conditions from Chapter 3 to determine whether there were any significant differences in the residual stresses. These welds were longer than those produced in Chapter 3 (60 mm versus 50 mm in the original study). Also, in this study the welds were not cut prior to the PWHT treatment, whereas in Chapter 3 the weld samples were cut into two sections, with one subsequently being given the PWHT. Hence these two factors are significant differences which may have influenced the interesting observations related to PWHT cracking in this chapter.

The results for the as-welded cracking partially supported the previous findings. Although all four samples had at least one section with cracking, the ACL/section for samples 2, 3 and 4 was below 100 μm, whilst the lowest aspect ratio sample (Sample

1) had an ACL/section of above 300 μm. This sample also had the highest amount of TCL. Hence, although the cracking was less for the sample near the optimal aspect ratio (Sample 2) than one with a low aspect ratio (sample 1) as expected; the low cracking in the high aspect ratio sample (Sample 3) was not expected.

Perhaps more surprising are the PWHT cracking results. Samples 2, 3 and 4 now appear to have significant levels of cracking. This is partly due to the significant increase in weld metal cracks, which were most prevalent in samples 2 and 3. There were some sections which had some large weld metal cracks, as was shown by the large values of ACL/section together with the larger error bars for these samples on Figure 5.9(b).

Another interesting aspect of the PWHT effects is that sample 1 - which had the highest amount of as-welded cracking - now appears to have the lowest amount of PWHT cracking, showing an actual reduction in the ACL/section, whilst also having the smallest increase in TCL/section. This could be because it cracked more during welding - as the as-welded sample showed - and as a result was less susceptible to PWHT because the cracks reduced the stresses within the material making PWHT cracking less likely.

To explain the differences between the two trials it is worth noting several differences in the experimental method. Firstly, unlike the previous trials in Chapter 3, the as-welded and PWHT cracking in these trials are studied on different blocks of material. Therefore the sample selected for PWHT had not been cut beforehand which would have partially relieved the stresses. Jiang et al. (2012) found that the length of repair weld has little effect on the longitudinal stress, although the transverse stresses decrease as the length of repair increases up to a value of 140 mm. As the samples in the present study are below this value, it is therefore possible that the significant difference in length of the welded material being heat treated could have an impact on the magnitude of transverse stress, which could have caused the increased in weld metal cracking after PWHT, compared to what has previously been observed in other trials.

One final reason is that the PWHT samples were all exposed to neutron radiation during the measurements. The exposure could be a reason for increasing the crack susceptibility of the material, which then produced the higher cracking after the PWHT treatment. This was observed in neutron irradiated stainless steels by Suzuki et al. (1999), who found that steels which had been subjected to neutron radiation had significantly increased cracking. However, the present study differs from the study on steels in that the welds had already been laid down, therefore unless the radiation caused embrittled areas of the weld material, the likelihood that this is a

factor caused the increase in weld metal and HAZ cracking is low.

5.4.2 Strain and residual stress results

The material studied in these trials is inherently difficult to measure using the neutron diffraction technique due chemistry of the alloy, the combination of large grain structure (meaning that the number of grains over which the measurements are made is reduced), and the large thickness (the neutron path through the material is greater than the 22 mm thickness due to the angle). Therefore for all the points, significantly higher measurement times (through increased neutron flux, e.g. 100 microamps for longitudinal and 60 for normal and transverse) were required to produce a sufficient diffraction peak. This resulted in longer than normal times required per point to achieve suitable diffraction patterns. This is something that was outlined by Santisteban et al. (2006), who showed that like for like tests for nickel and iron resulted in the requirement for double the amount of measurement time for nickel, which increased significantly with increasing depth of penetration (which is indicative of what would occur with increasing thickness).

However, despite these difficulties, all the measured directions were able to produce data for the {200} crystallographic plane. The use of the Rietveld refinement is generally preferred as this averages over the four main crystallographic planes for superalloys - {111}, {200}, {220} and {311}. However, although {200} can be used, the {111} and {311} directions are better for superalloys because they exhibit an approximately linear response in strain as plasticity starts to occur (Dye et al., 2001b; Webster and Withers, 2001).

For a weld after cooling to room temperature, the residual stress (and strain) in the longitudinal direction is commonly observed to be tensile in the weld metal (Kou, 2003b). Due to equilibrium and the Poisson effect, it is common to find that, when observing through the same measurement plane, the tensile and normal directions are compressive.

The results presented in sections 5.33 and 5.44 need to be compared with the published results on superalloys/similar materials for a full appreciation of their validity and significance. The stress data presented in Figure 5.17 suggests that both of the samples are compressive in all three directions within the weld material, with the transverse direction being the most compressive. Dye et al. (2000) studied single pass autogenous welds on thin plate (2 mm) IN718 and found that in the weld zone the material was tensile in the longitudinal direction, and compressive in the transverse and normal directions.

Similarly, in a study on thick plate (20 mm) high strength steel with clad layers applied, Jiang et al. (2010, 2012) found that the material is tensile for the longitudi-

nal and transverse directions in the weld zone, with the normal being compressive. Price et al. (2006) found that on 12 mm thick steel with partial penetration welds, the normal and transverse directions are compressive whilst the longitudinal is tensile, in the weld material.

It is therefore clear that the stress plots in Figure 5.17 show significant differences from the published works, both in terms of magnitude of stresses but also in the trends observed. As the stresses are calculated from the strain data as illustrated by Equation 5.7, it is logical to breakdown the results in terms of strain in each direction for each sample, to assess where any errors may lie in the data.

The longitudinal strain plots in Figure 5.16 show that the material is compressive in the weld material in this direction, whilst other authors found that the material should be tensile in this direction (Dye et al., 2000; Jiang et al., 2010, 2012; Price et al., 2006).

The normal and transverse direction plots in Figures 5.12 - 5.15 show that the material is compressive in the weld material in these directions, and as the measurements move away from the weld centreline the material tends to zero and tensile strain. As previously reported, this is in agreement with published data by Dye et al. (2000); Jiang et al. (2012, 2010); Price et al. (2006). However, the values of maximum strain for each direction proved contrasting, and offer some uncertainty.

For the normal direction, the data in this chapter reports maximum compressive strains of -400 με for the Rietveld multpieak data, whilst for the individual crystallographic peaks the values are much more varied. In fact, sample 3 is significantly more compressive than sample 2 when observing the {200} and {311} data in Figure 5.13 (b and c). The peak values for these are between -1000 to -1500 με. Dye et al. (2000) observed a normal strain in the weld material of between -1000 and -1500 με, whilst Price et al. (2006) obtained around -500 με for the normal direction.

Hence, the normal direction appears to show results which are in agreement with other works, and this is not surprising as this direction produced the best measurement data from the diffraction plots. The transverse direction is, however, producing questionable results. The data for both samples show significant compressive strain in the weld zone, reporting values of up to -4000 με. For comparison, Dye et al. (2000) found that the maximum observed in their study was -800 με, whilst Price et al. (2006) found -500 με in their study. Hence, the transverse direction for both samples, as well as the longitudinal direction data, are very likely to be inaccurate and not representative of what is actually occurring in the material.

There are obviously complications which would have lead to the poor data produced in these experiments. As was stated previously, the material is relatively

difficult to produce diffraction plots using the neutron technique due to the large thickness, the chemistry of the alloy and the large grain size. Therefore, the diffraction data for these two directions could have had a significant impact on the quality of the results.

The strain calculation as illustrated in Equation 5.3 uses the stress-free reference lattice parameter data, together with the lattice parameter recorded from the welded samples. Therefore, the stress-free data could also contribute to the poor results. The measurement of stress free reference samples was by a gauge volume of 2x2x2, but the cubes themselves were relatively larger, at 6x6x6 mm. There is a substantial difference in volume between the two, and therefore the measurement of the stress free data may have error due to not measuring over the full sample and thus taking into account the full compositional and microstructural variation in the cube. Also, because the cubes are quite large, it may be that there was not full relaxation of stress in them. Therefore, it would be logical for future experiments to produce smaller cubes for stress-free reference measurements.

5.4.3 Relationship with cracking

The strain and stress measured in these trials are residual, and as a result only offer a footprint of what occurred during the welding cycle. It is the in-situ transient stresses during the welding cycle which impact the formation of liquation cracks (Kou, 2003b). The analysis of the stress and strain data found that there are question marks over the validity of the results, with only the normal direction being usable for any comparison with the cracking data, due to the longitudinal and transverse directions being significantly different in magnitude and trend to what others have observed.

The strain data for the normal direction (see Figures 5.12 and 5.13) was shown to be compressive for both samples. Sample 2, which was the optimised aspect ratio sample, was found to have a higher amount of compressive strain than the other tested sample (which had the high aspect ratio). In Chapter 3 it was shown that the high aspect ratio samples are more susceptible to HAZ cracking than the optimised samples (although this was not the case in this Chapter). Recent research by Ola et al. (2011c,b,a) has suggested that compressive strain in welds acts to reduce the incidence of liquation cracking. In their research, Ola et al studied the application of linear friction welding to the joining of superalloys. As it is a solid state process, it was previously thought that liquation was not occurring in the samples because of this. However, evidence of liquated grain boundaries were observed, and the authors concluded that the compressive strains applied during the LFW process acted to stop the cracks forming.

Of course, the measured strain and stresses in this Chapter may not be truly representative of what is happening in the material. As was mentioned, there are uncertainties over the accuracy of the results. Further more, the in-situ stresses, which are difficult to measure, may be more compressive in the LFW welds resulting in the reduced crack formation, and this may also be true in the optimised aspect ratio samples. However, the LFW process has an externally applied load to generate the compressive stresses, whilst there is no externally applied load in the present study.

To improve these results, further measurements on more samples of varying aspect ratios, using the neutron diffraction should be undertaken. This includes the optimising of the measurement set up to increase the quality of the data. This may also mean that the samples should be thinner. Another area to help the study would be to produce a thermo-mechanical model which tracks the in-situ stresses in each direction during the welding cycle and subsequent cooling, which could test the different aspect ratios.

5.5 Conclusions

The following conclusions can be made:

1. Cracking in the as-welded condition in the samples partially validated the previous observations related to an optimised aspect ratio/parameters which reduce the incidence of cracking. Cracking in the high aspect ratio sample was low in this work, whereas previously it had been high;
2. PWHT cracking was significantly greater. This could be due to factors such as the higher restraint during the welding, longer weld samples, and the material not being cut to half the length prior to the PWHT. In particular, there was significant amounts of weld metal cracking after PWHT, which had not been observed previously;
3. Neutron diffraction measurements in nickel-based superalloys with thick section and large grains requires significant amounts of measurement time to produce quality diffraction profiles. The measurement of two samples, with only 11 points per sample, proved very time consuming. Only the normal direction appeared to produce suitable quality strain measurements. The normal direction appeared to be more compressive in sample 2 (optimal aspect ratio) than sample 3 (high aspect ratio);
4. The transverse and longitudinal directions were both difficult to measure. Whilst single peak data was attainable for each point for the transverse direction, this appeared to be highly compressive in the weld metal, more so than has been previously observed. Additionally, the longitudinal measurements are poor, with the trends observed not like those seen in previous work. The longitudinal direction appeared compressive across the weld section. The diffraction data for this direction was particularly poor;
5. From the data obtained, it appeared that the optimal aspect ratio weld (sample 2) is more compressive in the normal direction than the higher aspect ratio weld (sample 3). The higher compressive strain in the material may resist the formation of liquation cracks.

Chapter 6

Repair of casting defects using laser welding and hot isostatic pressing treatment

6.1 Introduction

The purpose of this chapter is to transfer the knowledge gained previously, into a repair procedure. The opportunity to use autogenous laser beam welding for repair of turbine blade castings with surface connected defects is of interest because it avoids a number of complications usually encountered when using standard repair processes, such as the use of lower strength filler alloys, and machining of surfaces to the original specified dimensions.

By using a laser to weld repair an area which is affected by defects such as surface connected porosity, the surface will in theory be closed. This will allow the the hot isostatic pressing process to be implemented to remove the defects within the sample. Hot isostatic pressing (HIP) is a materials processing treatment which utilises the combined application of a heat treatment and isostatic pressure. It has long been used as a method to repair casting defects (Koizumi and Nishihara, 1991). In this instance, the treatment will effectively heal any defects contained within the material, provided that there is no connection between the defect and the surface of the component. If there are defects, it is recommended that a seal is applied to the area, either by welding, or applying a coating to the area. Gandy et al. (2000) stated that HIP treatment after weld repair can effectively fix defects in most gas turbine components. A typical superalloy HIP cycle is illustrated in Figure 6.1.

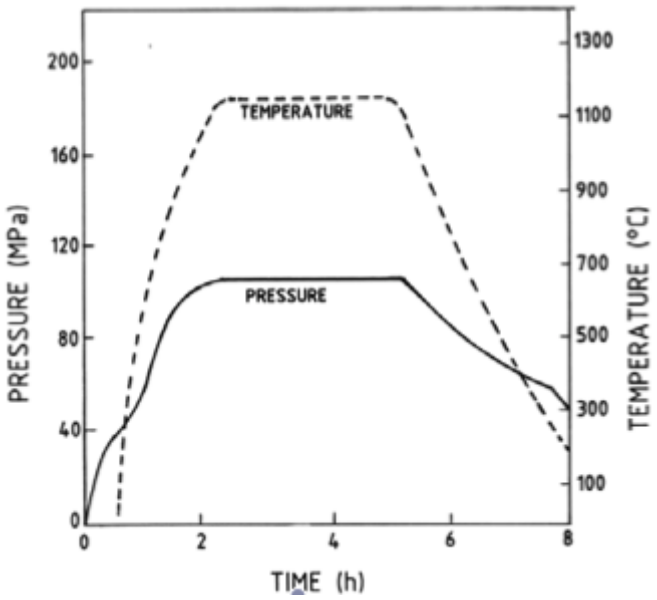

Figure 6.1 – A typical superalloy HIP cycle (After Appa Rao et al. (2012)).

This Chapter aims to:

1. Validate the optimised processing parameters developed in Chapter 3 in their avoidance of HAZ cracking, by applying to a repair weld;
2. Produce sealed surfaces which are successfully HIP treated and avoid other welding defects in samples;
3. Assess the repeatability of the optimised process;
4. Assess whether an already welded surface can be re-welded to seal any defects generated during the first repair.

6.2 Methodology

6.2.1 Samples

The samples used for these trials are considered to have a greater volume of porosity and other defects than a standard cast block or component as they are produced with the intention of containing defects to test the HIP process. A typical sample is illustrated in Figure 6.2(a), together with an example of the microstructure which contains a porosity defect (Figure 6.2(b)). It is of course only the near surface porosity which is of significance for the weld repair process. The blocks were cast from a different material batch to those studied previously, although the composition was within the ranges specified in Table 2.1.

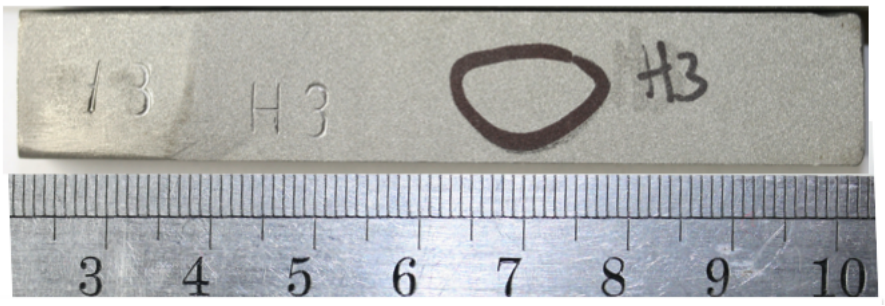

(a)

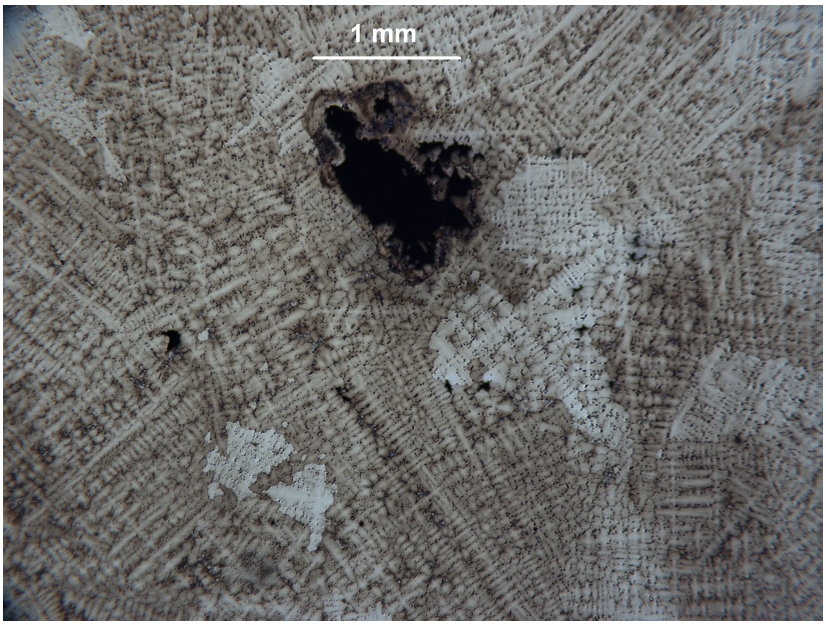

(b)

Figure 6.2 – (a) An example of the HIP sealing blocks used in these trials with an area of surface defects marked, and (b) the typical microstructure of the blocks showing the porosity contained with in them.

The samples were 80 mm long, 15 mm wide, and the thickness varied between 10 mm at the thinnest end to 15 mm at the thickest. The samples were prepared for the welding trials by cutting a very small layer off of the top surface, to expose the porosity within the sample and create a typical repair scenario. Once this had occurred, the samples were checked for defects by using dye penetrant inspection.

6.2.2 Initial trials

Prior to welding, the samples were first wiped with acetone, and then the surface was cleaned using a wire brush. Afterwards, they were cleaned using an ultrasonic bath with the samples in acetone. This ensured that any residual FPI fluid was removed from within the defects. After this, they were baked at approximately 100 ^{o}C to fully remove the residual acetone.

The welding was performed using the laser (with a 250 mm focal lens) and robot

system as outlined in Chapter 3. The samples were clamped using a vice (due to their small size). High purity argon (BOC N6) gas was used for shielding at 12 L/min flow rate and was supplied with a nozzle placed at the leading edge of the weld pool. Additionally, the laser head was set at a 10° angle as in Chapter 3 to ensure that the laser optics were protected from back reflection. Each sample was repaired with a minimum of six passes, each overlapping by 50 %. The HIP cycle applied to the samples was similar to that illustrated in Figure 6.1, however the exact details are proprietary information of the material supplier. The HIP cycle was undertaken by the material suppliers (the industrial sponsors), and it was a 100% argon environment.

The parameters were selected from those used in Chapter 3. From these samples, the following criteria were used to narrow the parameters from over 130 different combinations of power, beam diameter, and welding speed:

1. Based on Figure 3.4 which shows a plot of the likelihood of cracking versus power and beam diameter, a diameter of 2.5 mm was selected with a maximum power of 2 kW;
2. From Figure 3.5, an aspect ratio range of 0.25 - 0.65 was selected;
3. Minimal cracking in as welded and post-weld heat treatment condition;
4. Penetration of greater than 1 mm.

The fourth criterion was used because there is a minimum thickness of material required to ensure closure during HIP treatment without the surface breaking. This narrowed the parameters down to the combinations shown in Table 6.1. The majority of samples were analysed in the as-welded condition. Those which were analysed after the HIP treatment are marked in the table. Note that one of the samples marked with an asterisk was welded first with a high welding speed (1000 mm/min) and the remaining defective region was treated with the 150 mm/min weld.

Table 6.1 – Parameters used in the initial trials.

Power (kW)	Welding speed (mm/min)	Beam diameter (mm)	No of samples tested	No of samples where HIP treatment applied	Nominal aspect ratio†
0.5	50	2.5	1	0	0.31
0.5	100	2.5	1	1	0.27
0.5	150	2.5	6*	3	0.25
0.5	200	2.5	2	1	0.23
0.5	300	2.5	1	0	0.22††
0.5	600	2.5	1	0	0.20
0.5	1000	2.5	1*	0	0.35
0.5	2000	2.5	1	0	0.15
1	200	2.5	1	0	0.22
1	600	2.5	2	0	0.18

†This is measured from previous trials in Chapter 3, or †† assumed where parameters previously not tried.

6.2.3 Second trials

This set of trials was developed to test the repeatability of the optimised parameters found in the initial trials. The parameters used are listed in Table 6.2.

Table 6.2 – Optimised parameters used for repeatability trials.

Power	0.5	kW
Beam diameter	2.5	mm
Welding speed	150	mm/min

To ensure that the trials would be valid, a selection of samples were X-rayed and then visually inspected using dye penetrant to ensure that defects were present. This resulted in nine samples being suitable for testing. Each sample was welded using the same procedure as that used for the initial trials, except that a surrounding shielding device (see Figure 6.3) was used to avoid the formation of surface oxidation. High purity argon at a flow rate of 12 L/min was used. In addition, if defects were observed after the first laser treatment, further laser treatments were applied to heal these defects.

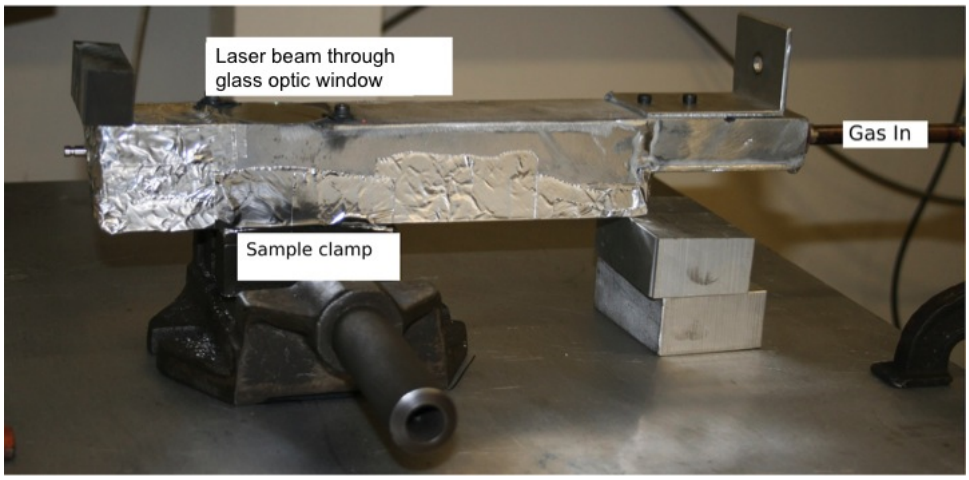

Figure 6.3 – Surrounding shielding device.

The samples for these trials were X-rayed after welding and after HIP treatment to understand what porosity was contained in the sample and how effective the HIP treatment had been. Additionally, during the welding trials the samples were checked using dye penetrant testing to check for surface defects (existing or those generated during welding), so that they could be re-treated where necessary.

There are two aspects of repeatability the process assessed in these trials. The first is in the number of samples being tested with the same parameters. The second aspect is how effective the repair treatment can be in re-sealing an already treated area.

6.2.4 Sample analysis

For the first trials, samples were sectioned either after welding, or the HIP treatment, with only one section per weld being taken. The procedure was identical to that used in Chapter 3.

For the final trials, three sections were taken from each sample after the HIP process had been applied (at different locations along the repaired area). In some cases, the regions were selected because the die penetrant indicated that there may be some defects in that area.

6.3 Results

6.3.1 Initial trials

6.3.1.1 Defect free samples

A breakdown of the results from these trials can be found in Appendix D.1. Of the samples from these trials, one of them contained no defects after the HIP treatment., and is shown in Figure 6.4. However, the rest of the samples all had defects of at least one type contained within them. These are described in the following sections.

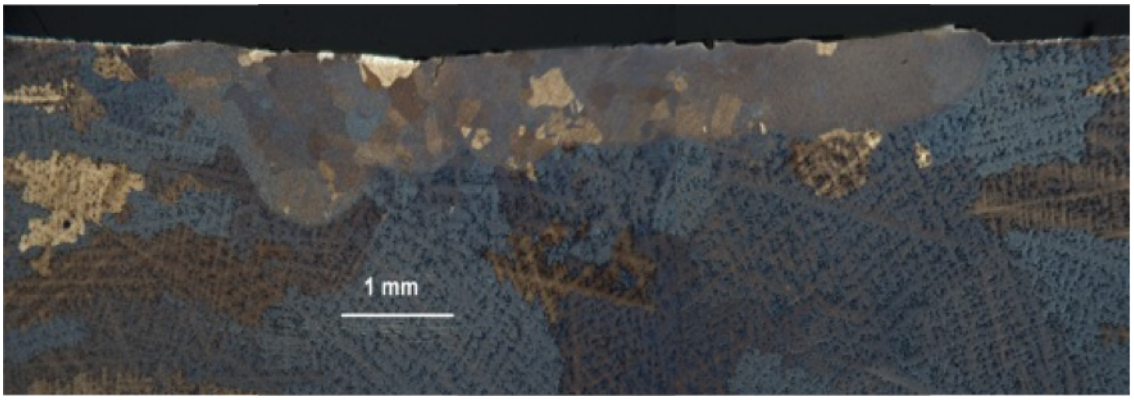

Figure 6.4 – Macro-section of defect free repair, after HIP treatment, produced using power of 0.5 kW, 150 mm/min welding speed and 2.5 mm beam diameter. Sample from initial trials.

6.3.1.2 Oxidation of weld surfaces

The majority of the welds had very poor weld surfaces. The welding speed had a significant effect on the surface's finish: below 500 mm/min oxidation was significant, while above this value it was significantly reduced. A comparison of weld surfaces with and without oxidation is illustrated in Figure 6.5. Even with reduced oxidation, the surface in Figure 6.5(b) isn't ideal and has a poor surface roughness, as well as significant surface breaking porosity.

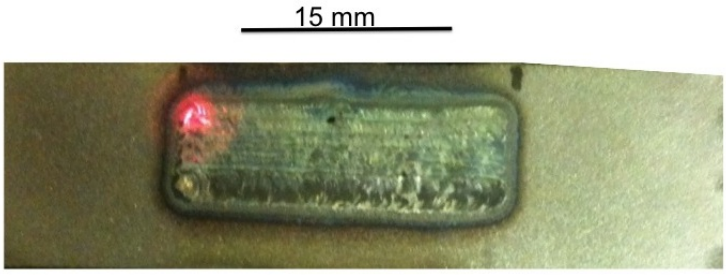

(a)

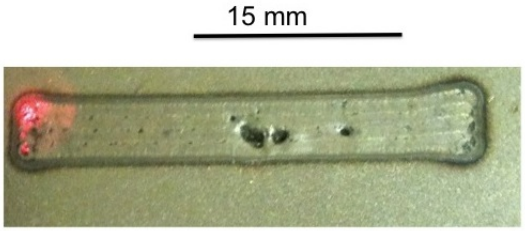

(b)

Figure 6.5 – Comparison of a weld surface produced at (a) 100 mm/min, and (b) 2000 mm/min.

6.3.1.3 Visible surface defects

The level of surface defects (cracks, porosity) was analysed qualitatively, with a relative scale from one (best case, Figure 6.6(a)) to five (worst case, Figure 6.6(b)) .

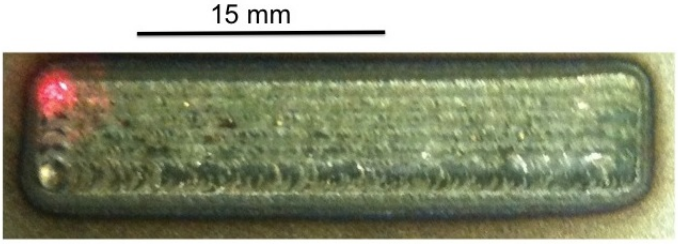

(a)

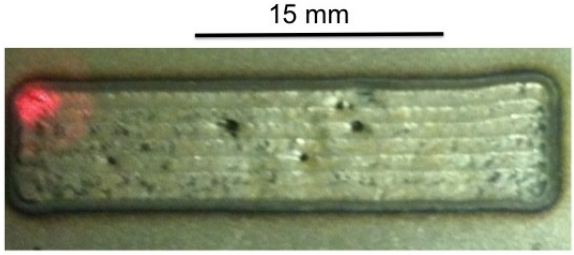

(b)

Figure 6.6 – Relative (a) best case (Sample 14) and (b) worst case (Sample 8) surface defect level.

A plot showing the relationship between this and the welding speed is shown in Figure 6.7. This chart indicates that the level of surface defects was reduced at welding speeds below 150 mm/min.

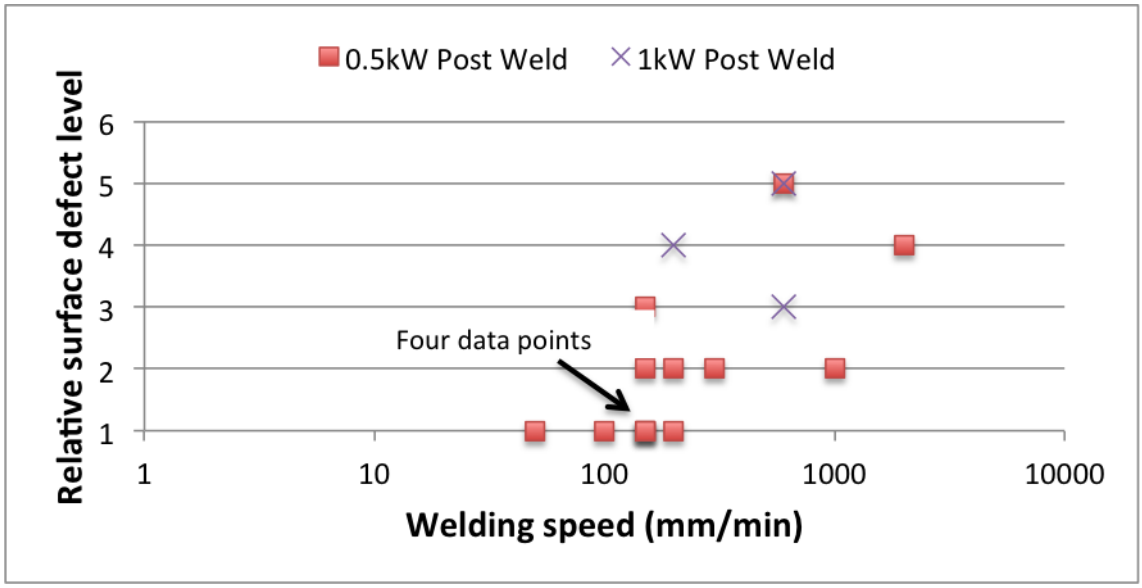

Figure 6.7 – Relative surface defects versus welding speed.

As was mentioned above, one sample from this trial was welded using two different sets of parameters: the first defective weld was subsequently treated with a low welding speed weld. Figure 6.8(a) shows the sample after the first weld repair with the poor surface quality and a large number of pores within the welded area. The parameters for this sample were 1 kW power and 1000 mm/min welding speed. It is clear that the fast welding speed has not allowed the entrapped porosity to escape from the molten pool. In Figure 6.8(c), this same sample was re-sealed using 0.5 kW power and 150 mm/min welding parameters, and the porosity was removed, although the surface oxidation was significantly worse.

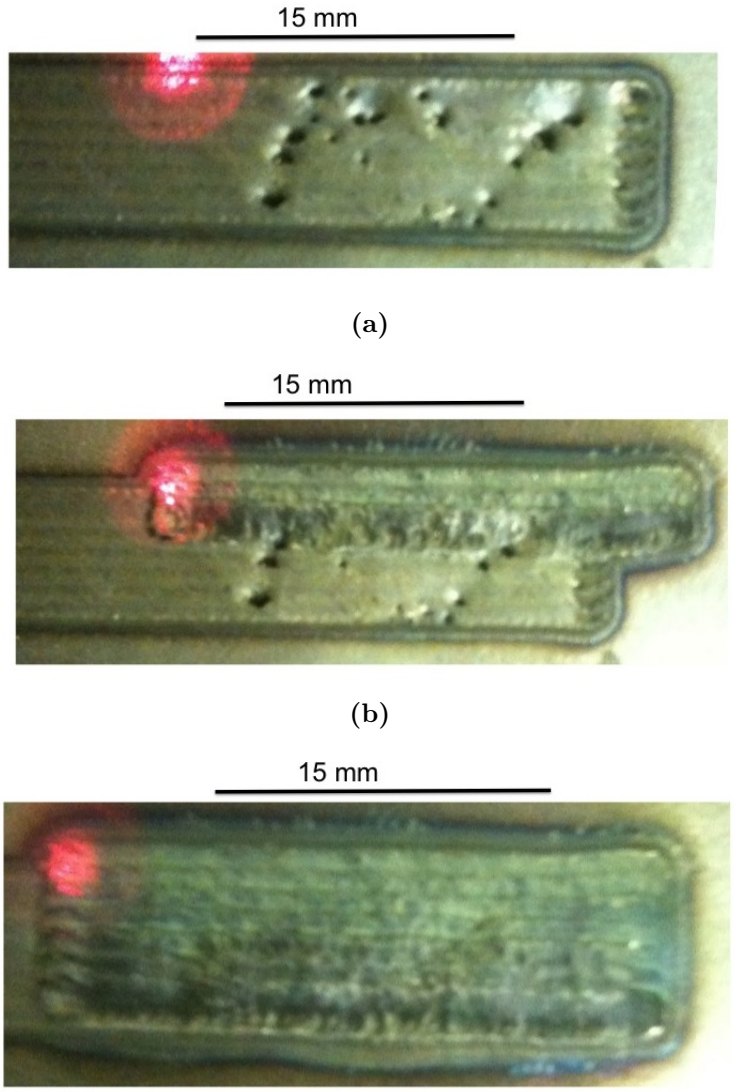

Figure 6.8 – Comparison of sample 16 & 17 from initial trials which was subjected to a re-seal of originally sealed area. Each sample was welded using the following parameters (a) 1 kW and 1000 m/min and (b) and (c) using 0.5 kW and 150 mm/min. (b) shows the sample after completing half the repair and (c) is the fully sealed sample.

An example of the severe porosity contained within one of the samples is shown in Figure 6.9. Despite the large porosity, there appears to be no defects within the weld or HAZ. This same sample however showed a large amount of porosity on the surface (see Figure 6.5(b)) and indicates the requirement for analysing more than one section.

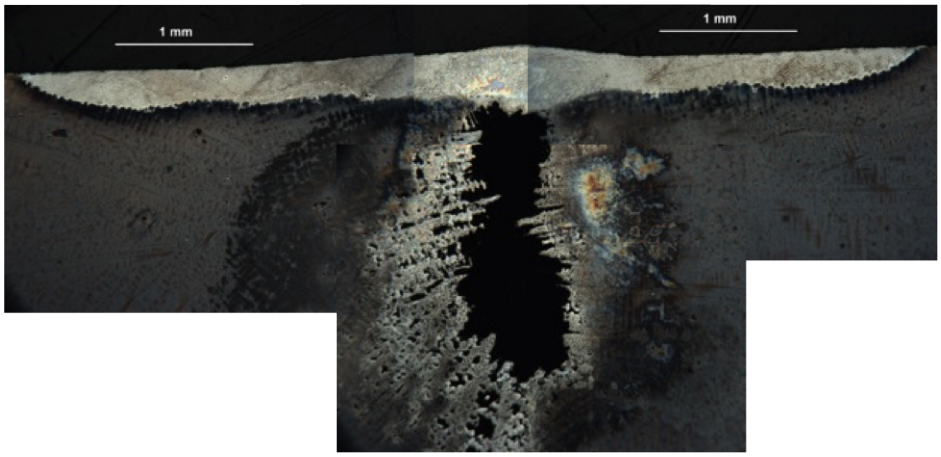

Figure 6.9 – Worst case porosity within microstructure. Parameters: 0.5 kW power and 2000 mm/min welding speed.

6.3.1.4 Cracking

In these trials, both solidification cracks and liquation cracks were observed. Two samples contained liquation cracks: one was produced at 0.5 kW and 300 mm/min and the other at 0.5 kW and 150 mm/min. However, there were four samples which had solidification cracking. Figure 6.10 shows the relationship between welding speed and solidification crack length, and shows that solidification cracking occurred at either the low welding speeds (at or below 100 mm/min) and at higher welding speeds (at or above 600 mm/min). The sample at 2000 mm/min didn't contain solidification cracking but did however contain a very large pore as was illustrated in Figure 6.9.

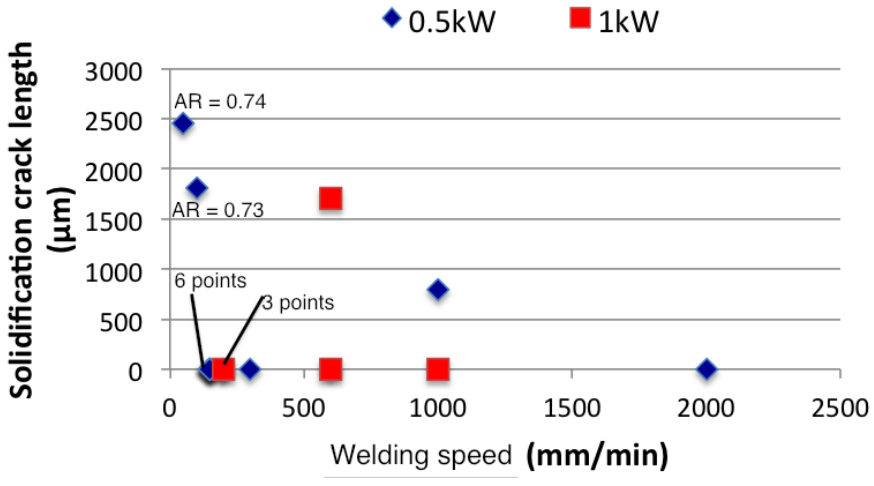

Figure 6.10 – Welding speed versus solidification crack length for initial trials, with data split into powers applied. Note that there was only one crack per section and as such is considered as a TCL and not ACL value. This plot also has the aspect ratios of the two samples with highest crack length annotated. Also, the data at 150 mm/min and 200 mm/min has 6 and 3 data points respectively.

6.3.2 Final trials

6.3.2.1 Pre-weld

The surfaces of the samples which showed surface connected defects prior to welding were qualitatively rated and are listed in Table 6.3. The full breakdown of the surface pre-weld condition of each sample in the final trials can be found in Appendix D.2. The best (i.e. smallest area of defects) and worst (largest area) samples are illustrated in Figure 6.11. The area was marked after the dye penetrant testing.

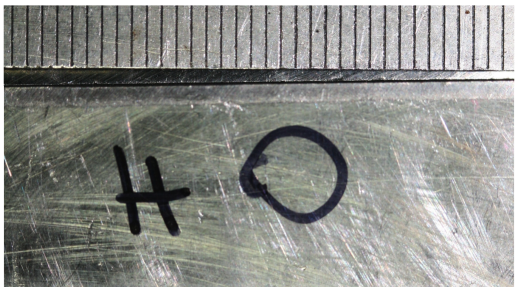

(a)

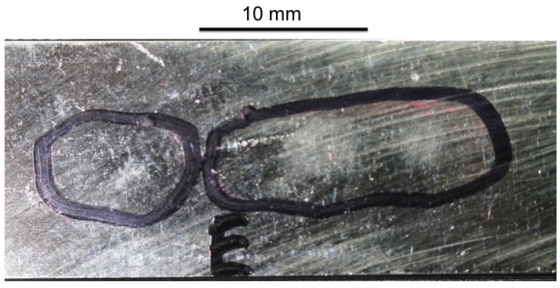

(b)

Figure 6.11 – Examples of samples from final trials, showing (a) best (smallest) and (b) worst (largest) areas affected with surface connected defects.

6.3.2.2 Post-weld and after HIP treatment

The summary of the samples is illustrated in Table 6.3. Only one sample (H) needed only one set of laser treatments, and sample C needed 5 treatments totalling 28 passes. Three of the nine samples were completely free of defects (See Figure 6.12 for example of a section from sample A). In fact, of the total of 27 sections analysed, only 8 contained any defects.

Table 6.3 – Details of results of final trials.

Sample	Defects Pre-weld	No of passes per repair cycle	Total no of passes	Surface defects post-weld	No of clean sections	No of defective sections	X-Rays	Details
A	2	6-4	10	1	3	0	Very small marks	-
C	5	7-3-8-7-3	28	4	1	2	Large area	Severe sub-weld porosity
D	4	5-4	9	2	2	1	Small area	Severe sub-weld porosity
E	5	6-7-7	20	2	2	1	Couple of small marks	Solidification cracks (in section taken from end of laser treatment)
H	1	6	6	1	3	0	Clear	-
I	3	6-3-4	13	2	3	0	Very small mark	-
K	4	6-4	10	3	2	1	Clear	Small crack in one (section taken from end of laser treatment)
M	2	6-2-11	19	3	2	1	Clear	Porosity escaping at surface
S	4	8-4-1-11	24	5	1	2	Large area	Severe sub-weld porosity

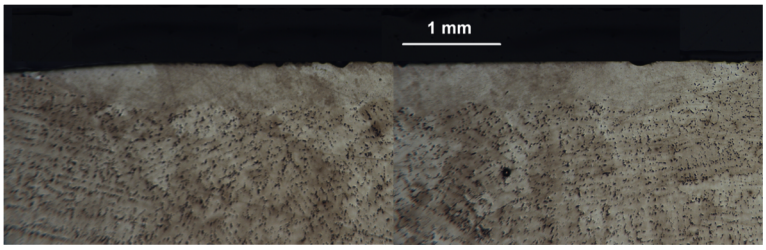

Figure 6.12 – Example section of sample A, which is completely free of defects.

The eight sections containing defects were from six different welds. Two of them were sections which contained only solidification cracking (See Figure 6.14(a and b) for example). One further sample had what appears to be a porosity at the surface which may have resulted from a porosity in the weld pool rising to the surface (Figure 6.14 (c)). The final five sections were all from samples C, D and S and all contained severe porosity. The porosity in these samples is illustrated by the examples in Figure 6.15. The porosity was observed in both the fusion zone and base material.

Prior to sectioning, the samples were tested using dye penetrant to see what surface defects were visible. A summary of this is in Table 6.3. Again, this is rated qualitatively, and the best (no defects, rated as one) and worst (significant, rated as five) are shown in Figure 6.13. Similar figures for all the samples can be found in Appendix D.2. Two of the samples which had severe porosity in them post-HIP (samples C and S) had high amounts of surface defects visible, although this was not true for sample D. The other samples which were all free of porosity in the microstructure (in all sections and visible on X-rays) were free of large areas of surface connected defects.

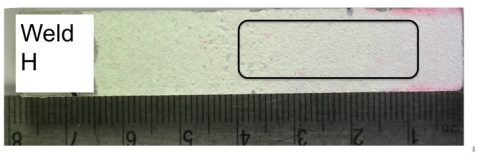

(a)

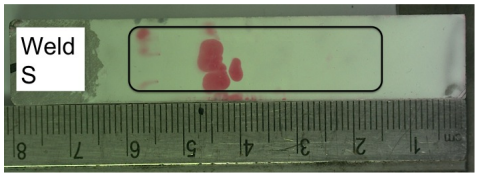

(b)

Figure 6.13 – (a) Sample H showing no visible dye penetrant indicating defects, and (b) Sample S showing significant amounts of dye penetrant indicating surface defects.

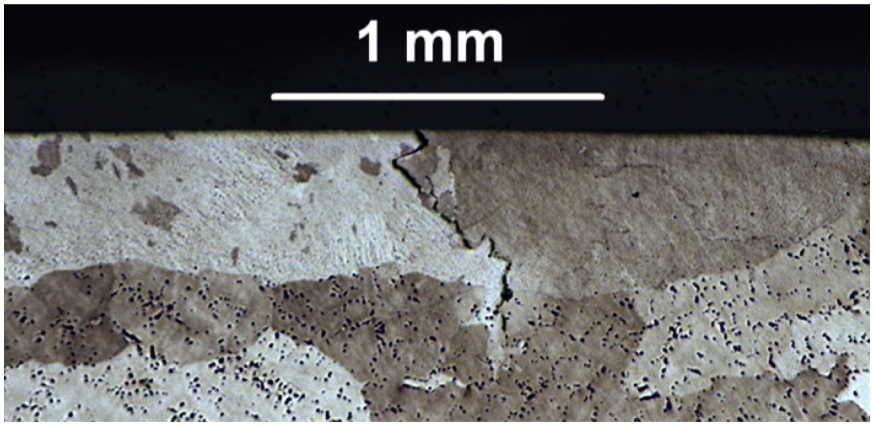

(a)

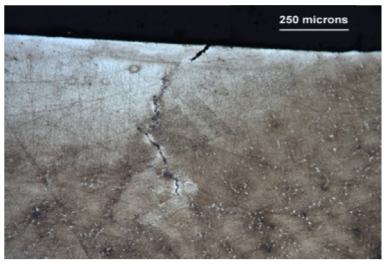

(b)

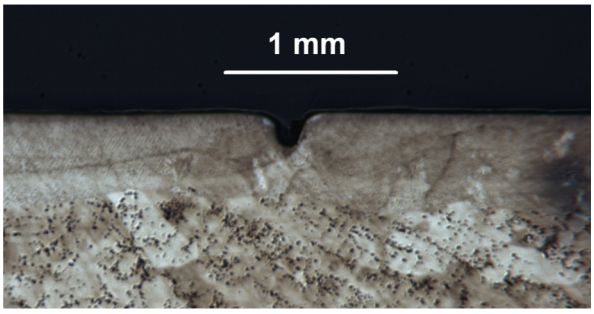

(c)

Figure 6.14 – Examples of sections from the final trials with the different intermediate defects observed. (a) solidification cracking in weld E, (b) solidification crack in weld C and (c) Porosity at surface in weld M.

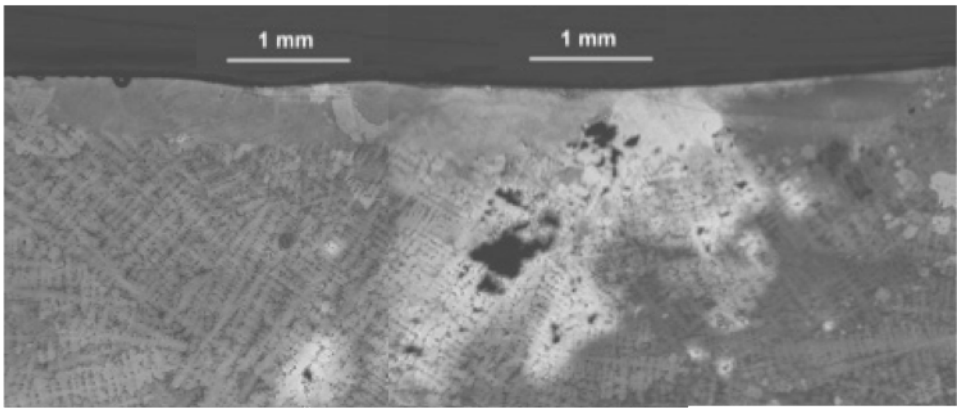

(a)

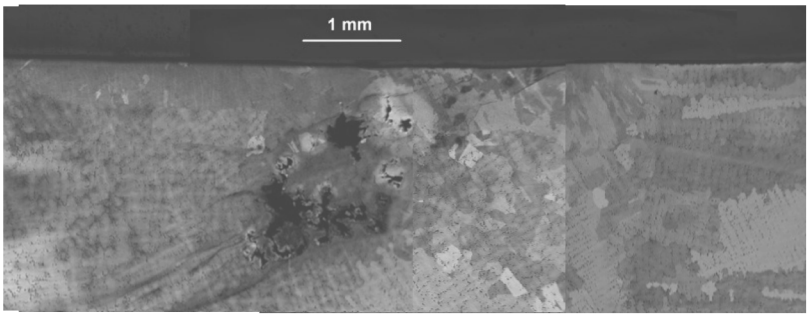

(b)

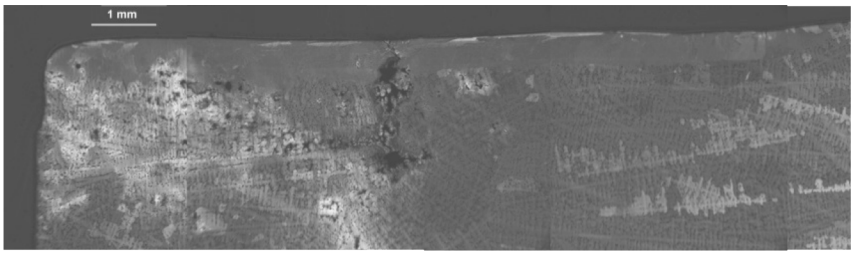

(c)

Figure 6.15 – Examples of sections from the final trials with the severe porosity defects observed. (a) severe porosity in weld C, (b) severe porosity in weld (D), and (c) severe porosity in weld S, which also shows a crack linked to the porosity in the weld metal.

Figure 6.16 relates the severity of the defects in the sample against the surface condition pre- and post-weld. Figure 6.16(a) suggests that the risk of having severe defects post-HIP (e.g. severe porosity) is increased when the pre-weld surface is severely affected by defects. There is also a similar link between the severity of defects and the post-weld surface defects identified from die penetrant testing in Figure 6.16 (b).

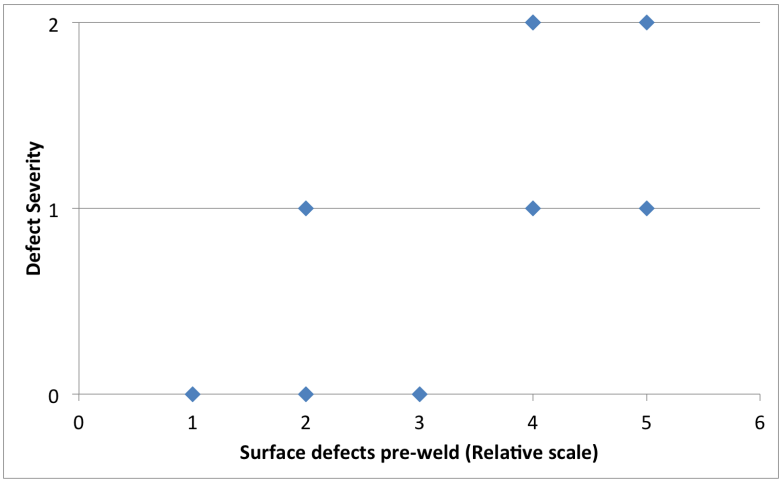

(a)

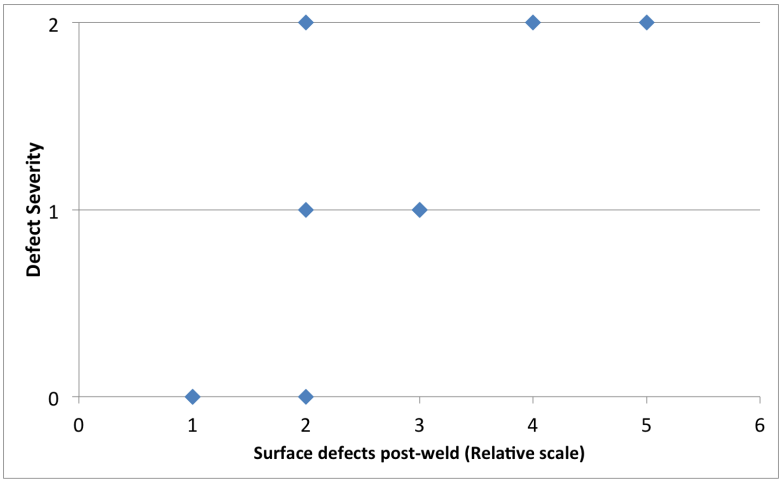

(b)

Figure 6.16 – Plots showing the severity of the defects versus (a) the relative surface defects pre-weld and (b) the relative surface defects post-weld. The severity of the defects is determined by 0 = no defects, 1 = intermediate (e.g. solidification cracks/small pore) and 2 = severe porosity. The relative scale of the surface defects is as was described previously, where the worst surface according to the dye penetrant testing is rated as a 5 and the other samples are scaled accordingly.

There was a variation in the number of treatments and total number of passes required to repair each sample. Figure 6.17(a) correlates the relationship between total number of passes required with the pre-weld surface rating, and shows that more passes are required to repair those samples with a greater amount of defects. In Figure 6.17(b), the severity of defects in the sample after HIP treatment is plotted against the number of laser passes. Generally, those samples that required the greatest number of passes could not be successfully repaired.

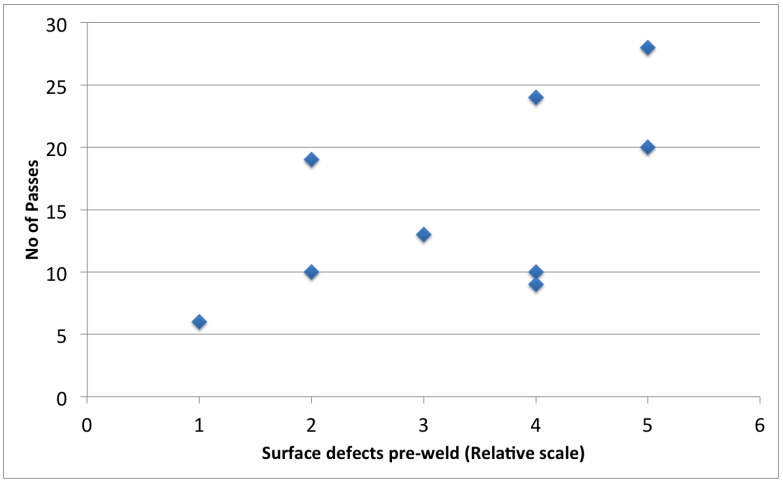

(a)

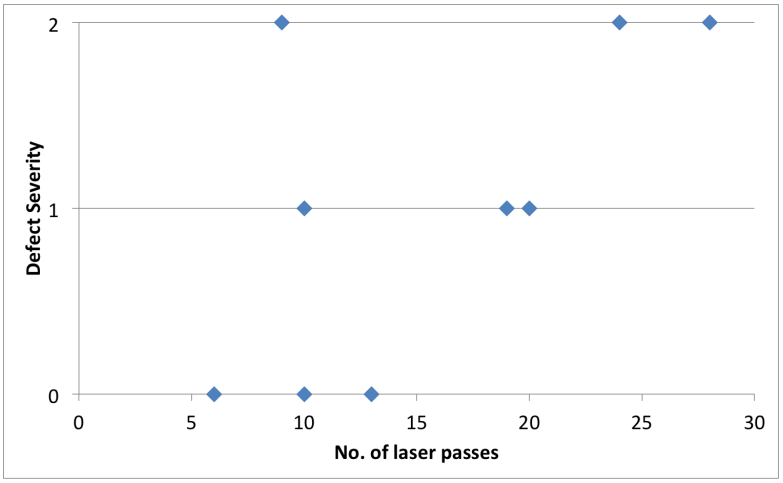

(b)

Figure 6.17 – Plots showing the relationship between total number of laser passes versus (a) the pre-weld surface rating and (b) severity of defects in sample. The severity of the defects is determined by 0 = no defects, 1 = intermediate (e.g. solidification cracks/small pore) and 2 = severe porosity. The relative scale of the surface defects is as was described previously, where the worst surface according to the dye penetrant testing is rated as a 5 and the other samples are scaled accordingly.

The issue with oxidation of the weld surface was eliminated with the use of the surrounding shielding device. Figure 6.18 compares welds produced with and without the trailing shielding device using identical welding parameters. It is clear that there is a significant improvement in surface quality, and also a reduction in small pores present across the weld surface. The quality of the surface shown in the sample with the shielding is replicated throughout all the welds.

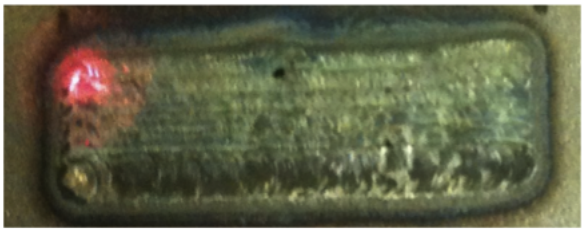

(a)

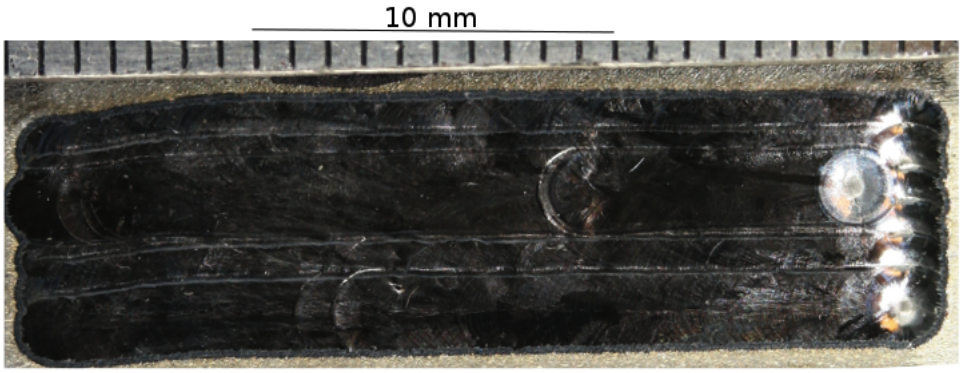

(b)

Figure 6.18 – Comparison of surfaces (a) without and (b) with surrounding shielding device. Welds produced using 0.5 kW power, 150 mm/min welding speed, and 2.5 mm beam diameter.

6.3.2.3 X-rays

Throughout the final trials, the samples were X-rayed. This was before the welding, after welding, and after the HIP treatment. A summary of the observations from the X-ray images after the HIP treatment was listed in Table 6.3. Generally, the samples which were found to be free of defects after the metallography were also clear on the X-ray. Also the X-ray appeared to show nothing where there was an intermediate defect. An example X-ray of sample H (which was clear) and sample C (which was severe porosity) is found in Figure 6.19. The X-rays for each stage (pre-weld, post-weld and post-HIP) for each sample can be found in Appendix D.2.

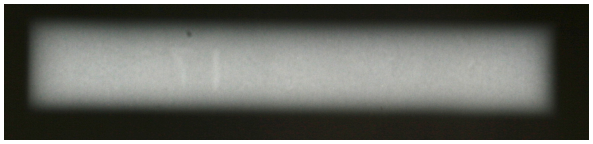

(a)

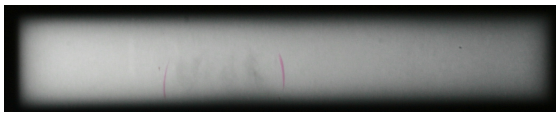

(b)

Figure 6.19 – Post-HIP X-rays of (a) Sample H (free of defects) and (b) Sample C (severe porosity defects).

6.4 Discussion

In all the trials described in this Chapter, it is important to recognise that the samples which are being tested contain significant amounts of porosity. This is because they are manufactured to do so, and are typically used for quality control of the HIP treatment. The defect levels in actual components is typically much lower; although the components would be of more complex geometry.

6.4.1 Initial trials

6.4.1.1 Validation of previous work

The occurrence of only two examples of HAZ (liquation cracking) in the initial trials, produces an excellent validation of the work produced in this thesis. Chapter 3 produced work which suggested optimised conditions that should reduce the incidence of HAZ cracking in superalloys. Although the optimised parameters in the initial trials were successful in this instance, there were other defects to be considered.

6.4.1.2 Defects

There were 17 samples from these trials, only one of which was completely free of any defects. The defects were studied based on their type, with solidification cracking and weld metal porosity being a significant issue. Also, the surface oxidation (whilst not a primary issue) is important to understand due to the implications on future repair of in-service components.

In the first set of trials, no surrounding shielding device was used. As a result, oxidation occurring below a threshold welding speed of 600 mm/min is down to the increased build up of heat with decreasing welding speeds. As the speed decreases, the power is applied to an area of the surface for longer. Therefore because the sample was hotter for longer, the shielding gas supplied was unable to protect the sample from oxidation. At faster welding speeds, the heat build up is less severe and

this issue was not observed. This issue was addressed with the surrounding shield device used in the second trials.

Solidification cracking was more of an issue in these trials than had previously been observed in this thesis. This crack was related to the welding speed in Figure 6.10, which suggested that the incidence was higher with both low and high welding speeds. Dye et al. (2001a) found that this type of cracking in superalloys occurs at low welding speeds, and also at high powers. However to observe the occurrences of faster speeds is interesting. Additionally, a high aspect ratio geometry is also suggested as a reason for increased amounts of this type of crack, because of the large angle formed between the opposite sides of columnar grain growth in the weld pool, whereas a lower aspect ratio has a shallower angle (Kou, 2003b).

However, a significant difference between these trials and those previously in this thesis is the number of passes. Whereas only one pass was previously laid, this work has seen that amount increase to a minimum of five. There could be an increased amount of strain in the material caused by the multi-pass process. Also, the multi-pass welding cycles could be decreasing the ductility of the weld metal, which obviously then will be more susceptible to solidification cracking as the material would no longer be able to resist the contraction stresses during solidification and cooling. These trials appeared to show that this type of crack was minimised in certain welding speed conditions - avoiding the low or high speeds - at around 150 mm/min.

The surface defects were more difficult to quantify, and were studied using a qualitative scale in Figure 6.6. This plot shows that the amount of defects generally reduced with decreasing welding speed. One reason is that the lower welding speeds keep the weld pool molten for longer, which allows any porosity to escape before solidification. At higher welding speeds, there was not enough time for this to occur, leaving the gas bubbles trapped in the solidifying metal. Note that the four repeat data points at 150 mm/min showed the repeatability of this result.

The key result in this trial was the sample where the porosity was eliminated after the HIP treatment (see Figure 6.4). This demonstrated that the repair technique was feasible provided all the surface connected porosity could be eliminated.

6.4.2 Final trials

The first trial was limited in a number of ways. Firstly, only one section was taken per weld, so it is possible that subsequent sections may reveal defective areas, e.g. compare Figure 6.9 with Figure 6.7(b). Secondly, repeating the same parameters on a number of samples will reveal whether the repeat method can be applied consistently to remove defects. Therefore nine repeat welds were produced with a

power of 0.5 kW and a welding speed of 150 mm/min.

These trials tested the repeatability of the repair process, and proved that the optimised parameters in the previous section were effective in repairing one third of samples, which were completely defect free. These samples required a relatively low number of passes to ensure a sealed surface. The samples - A, H and I - were samples which had a relatively low amount of surface defects pre-weld. The welding process improved the surface ratings and they showed either no defects, or very tiny indications on the dye penetrant.

Therefore it is clear that the success of a sample being repaired is linked to the amount of visible surface defects prior to and after the welding treatment. The likely success of the treatment can be easily determined using the dye penetrant non-destructive technique.

The intermediate defects - solidification cracks and the trapped porosity - depended on the surface quality and number of passes. These types of defects were visible in the dye penetrant testing of the surfaces post-weld. However, these samples didn't contain severe porosity after the HIP treatment, suggesting that the defects did not interact with the porosity within the material.

The intermediate defects may be avoided by optimising the process. Sample E, which had solidification cracking in one sample, had a large amount of pre-weld surface defects, and yet this managed to produce porosity free sections. The cracks were in the section taken from the end of the treated area. This is also true of the crack in sample K. Solidification cracks could affect the success of a repair, as if they penetrate into an area of porosity - as in sample S in Figure 6.15(c) - then the sample will not be successfully treated using the HIP cycle.

The end of the laser passes may have increased the incidence of these defects because there is a moment of time where the laser head is stationary whilst the power is left on. There is therefore a build up of heat at this area. According to Dye et al. (2001a), solidification cracks occur at low welding speeds and high powers. If there is zero welding speed, the process is in effect equivalent to a higher power compared to the rest of the treated area. Therefore the risk of solidification cracking forming in this region is increased, as was observed in these trials. By optimising the process so that the power is switched off/ramped down towards the end of the treated area, this problem could be avoided.

6.5 Conclusions

The following conclusions can be been made:

1. The use of laser sealing (with optimised parameters) and HIP treatment can produce repaired components free of defects;
2. The likelihood of success is higher when the surface porosity prior to treatment is less severe;
3. Dye penetrant testing can be used to determine whether the laser sealing treatment has been effective;
4. The optimised parameters and weld bead geometry, identified in Chapter 3, have been validated as reducing the incidence of HAZ cracking. Note however that solidification cracking, which was not a problem with the previous work proved a problem due to the multiple welding runs;
5. It appeared that (with further optimisation) the treatment could increase the chances of producing more repaired samples.

Chapter 7

Arc welding of Rene 80

7.1 Introduction

The previous chapters have shown a relationship between the welding process parameters and the crack susceptibility of Rene 80. By understanding this relationship, a suitable repair procedure for application to surface connected defects in cast components was developed. This utilises a laser with subsequent hot isostatic pressing.

By avoiding the use of a laser, components could be repaired without the expense of the laser equipment, and the safety issues that have to be considered. Arc based processes are the most commonly used repair processes for gas turbine components (Gandy et al., 2000) due to the ease with which a manual procedure can be used to repair the complex components.

This chapter highlights how two different arc based processes have been used to apply the knowledge obtained in Chapter 3: namely an aspect ratio of 0.5 reduces the incidence of cracking in the as-welded condition. A high frequency pulsed TIG power source and a plasma arc welding source were used due to their abilities to achieve the higher penetration depths required to achieve an aspect ratio of 0.5.

7.2 TIG and Plasma arc welding

Tungsten inert gas (TIG) and plasma arc welding (PAW) are non consumable arc processes. In terms of process energy densities they are lower than laser or electron beam, however plasma is capable of higher energy density levels than TIG (Figure 7.1). This extends the arc welding operating window and eliminates the need for the extremely expensive and often difficult to implement laser and electron beam processes. The evolution of the technologies has seen the operating windows for each process in Figure 7.1 expand.

One particularly interesting development has been in the use of high frequency

(greater than 5 kHz) pulsed waveforms, which according to Shimada and Gotoh (1976) improves arc stiffness, particularly at low average currents. Cook and Eassa (1985) also found that a high frequency (of greater than 5 kHz) pulsed arc can have arc pressure up to ten times higher than that of a comparable direct current (DC) arc (for the same equal power output). Similarly, Onuki et al. (2002) found for identical average currents, high frequency (HF) pulsing (up to 20 kHz) with a high peak current produces arc pressure three times that of the DC weld, with weld bead penetrations twice as deep. The authors also found that the arcs were highly constricted, which could be related to the higher arc pressure.

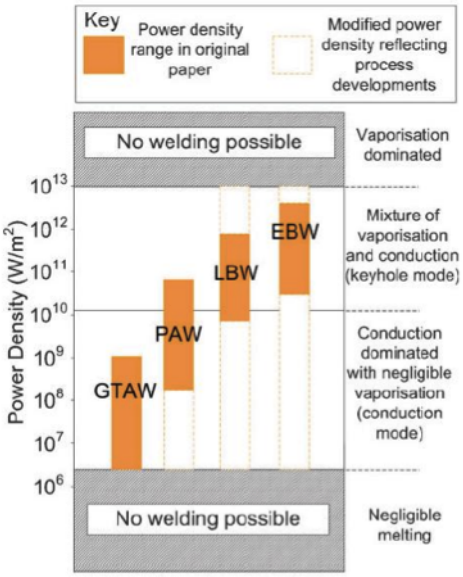

Figure 7.1 – Illustration of energy densities of common welding processes. (After Short, 2009).

An example of a high frequency power supply is the VBC Interpulse (also known as the VBC IE 175i). This utilises a constant high frequency (20 kHz) pulse current which can be used in conjunction with a DC current, or superimposed on a low frequency pulsed waveform - see Figure 7.2.

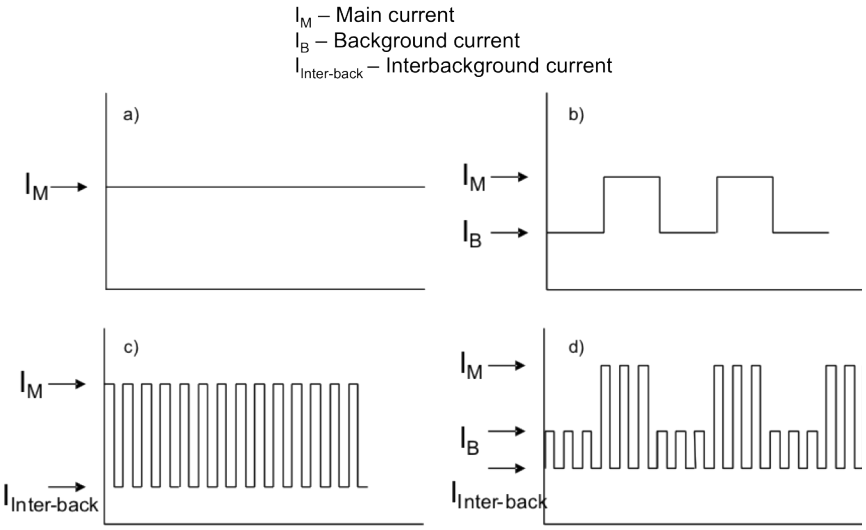

Figure 7.2 – Example waveforms produced using the HF constricted arc TIG power source (a) DC, (b) low frequency pulsed, (c) high frequency pulsed, (d) low + high frequency pulsed. Note waveforms not to scale.

This technology is sometimes designated constricted arc TIG or gas tungsten constricted arc welding (GTCAW). An initial study by Gregori (2006) for welding nickel superalloys found that using the process at low heat inputs (below 0.3 kJ/mm) produced crack free repair welds, although further development to improve the consistency of the procedure was recommended.

Plasma arc welding (PAW) differs from TIG welding by the constriction of the arc through a nozzle within the torch (Figure 7.3). Due to the constriction, the arc has a greater energy density than TIG, which means it can operate in keyhole mode like the power beam processes.

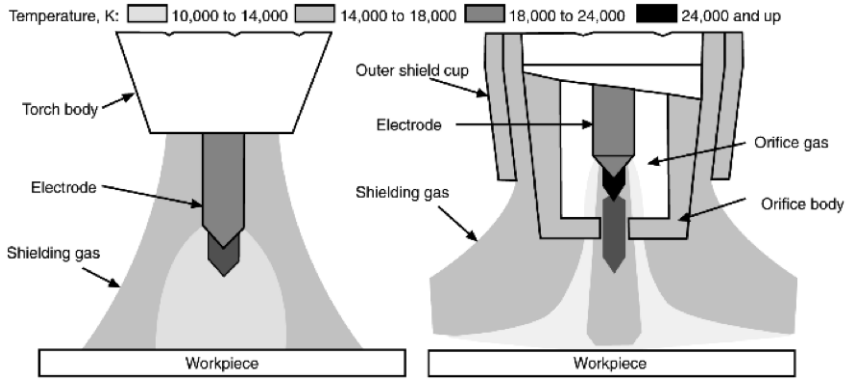

Figure 7.3 – Schematic illustrations of (a) TIG torch and (b) plasma torch, with areas of arc temperatures outlined.

The plasma gas operates at temperatures well in excess of those observed in TIG welding. Two gas supplies are used for PAW, one for the plasma gas, and another

for the shielding gas. Standard welding gases are used for both gas types, although specific gas compositions depend on the application. PAW also uses electrodes similar to TIG welding.

The torch of the plasma welding system features some intricate features, but the two main factors which affect the plasma arc are the orifice diameter, and the distance between the electrode tip and the orifice (or the electrode set back). The orifice diameter has been shown to influence width and penetration of weld beads, although the effect is greater on thin material (Short et al., 2011). Both of these parameters will be studied in this thesis.

Therefore, given the ability to operate with higher energy density and therefore create higher aspect ratio welds, this process has been used in addition to the constricted arc TIG process described previously.

The aims of this chapter are:

1. To obtain welds with the optimum aspect ratio found in Chapter 3;
2. To assess the effect of aspect ratio on cracking in arc welds;
3. To assess the suitability of TIG and PAW processes for the repair of Rene 80 components.

7.3 Methodology

7.3.1 Material

The Rene 80 alloy as outlined in previous chapters was used. The material was produced via the same procedures outlined in Chapter 2, and it had the smaller grain size. For the wire added trials, IN625 filler wire of 1.2 mm diameter was used. Please refer to Table 2.1 for the chemistries of the alloys. Prior to welding, the material was cleaned using a wire brush and acetone to degrease the surfaces.

7.3.2 Experiments

7.3.2.1 TIG trials

The TIG trials were performed using two different power sources. The majority of welds were produced using a VBC Interpulse 150 unit. This power source can produce the different waveforms shown in Figure 7.2, with three different current settings - main (I_M), background (I_B) and inter-background ($I_{Inter\text{-}back}$) - being used. Each of these had a maximum setting of 150A. For some comparative welds, a Migatronic TIG commander 400 was used, which only operates in DC or low-frequency pulsing mode. The power sources were connected to a Fanuc Arcmate 120iB robot. Shielding was provided by high purity N6 argon, and 1.6 mm thoriated tungsten

electrodes were used. Where used, wire was fed into the weld as illustrated in Figure 7.4 by a Migatronic KT-4 system. Table 7.1 lists the constant parameters used in these trials. A constant welding speed value was used for all trials, because of the previous findings related to their being no significant influence of welding speed on the incidence of HAZ cracking. Table 7.2 lists the variable parameters used in these trials. The plots in the results section are in some cases distinguished by the values of main and inter-background current relative to each other, for example a main of 100 A and inter-background of 20 A is defined as inter-background lower. Where there is a value for each of the three currents, this is designated as a pulsed + inter-background.

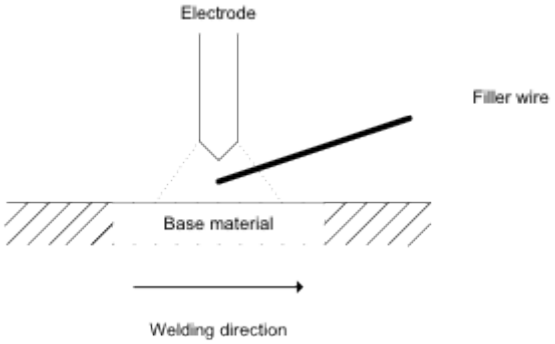

Figure 7.4 – Illustration of wire feeding position.

Table 7.1 – Constant parameters for all TIG welds.

Parameter	Value	Units
Welding speed	100	mm/min
Wire feed speed	600	mm/min
Electrode diameter	1.6	mm
Electrode type	Thoriated	-
Electrode angle	60	°
CTWD - Autogenous	2	mm
CTWD - Wire added	5	mm
Torch to plate distance* -Autogenous	12	mm
Torch to plate distance* -Wire added	15	mm
Shielding gas type	N6 Argon	-
Shielding gas flow rate	10	L/min
Low frequency pulsing	10	Hz

* This is the distance from the edge of the gas shroud to the plate surface.

Table 7.2 – List of current settings used in each TIG trial, both autogenous and wire-added. Note that parameter sets marked with an asterisk and the Migatronic DC welds were for autogenous conditions only. The average current is that obtained experimentally. The I_M is the main current, the $I_{IP}$is the inter-background current, and the I_B is the background current.

Average current (A)	DC (A)	Interpulse (A)o	Pulsed+Interpulse (A)	Migatronic DC (A)
30*	-	$I_M = 40$, $I_{IP} = 20$.	-	-
40*	-	$I_M = 55$, $I_{IP} = 25$.	-	-
		$I_M = 25$, $I_{IP} = 55$.		
45*	-	$I_M = 60$, $I_{IP} = 30$.	-	-
60	$I_M = 60$.	$I_M = 120$, $I_{IP} = 20$.	-	$I_M = 60$.
		$I_M = 80$, $I_{IP} = 40$.		
		$I_M = 20$, $I_{IP} = 120$.		
		$I_M = 40$, $I_{IP} = 80$.		
75	-	$I_M = 90$, $I_{IP} = 60$.	-	-
		$I_M = 60$, $I_{IP} = 90$.		
80	$I_M = 80$.	$I_M = 60$, $I_{IP} = 100$.	-	$I_M = 80$.
		$I_M = 100$, $I_{IP} = 60$.		
100	$I_M = 100$.	-	$I_M = 150$, $I_{IP} = 60$, I_B=130.	$I_M = 100$.
			$I_M = 130$, $I_{IP} = 80$, I_B=110.	
110	-	$I_M = 120$, $I_{IP} = 100$.		-
		$I_M = 100$, $I_{IP} = 120$.		
120	$I_M = 120$.	-	$I_M = 150$, $I_{IP} = 100$, I_B=130.	-
			$I_M = 120$, $I_{IP} = 140$, I_B=80.	
130	-	-	$I_M = 130$, $I_{IP} = 150$, I_B=110.	-

The base material was clamped to a flat surface, and welds of approximately 60 mm length were laid on the base material. A gap of 10 mm and 15 mm respectively was left between the edges of each autogenous and wire added weld to ensure no overlapping of HAZs. The blocks were allowed to cool to room temperature between each pass. All passes (including wire-added) were single pass bead on plate.

The waveforms for the Migatronic welds were recorded using an AMV 4000 arc watch system. For the VBC power source, a higher sampling rate was required, and a Yokogawa DL750 oscilloscope was used. The currents were measured using an LEM current transducer LF 205-S placed around the earth cable of the power source. This unit has a wide frequency bandwidth and is suitable for capturing the high frequency inter-background current due to the requirement of high sampling rate. This was connected to the oscilloscope and the voltage was measured by measuring the potential difference between the electrode and the workpiece. To protect the oscilloscope from back-EMF, the connections were established after the arc was struck.

7.3.2.2 Plasma trials

A Migatronic Plasma Commander power source was used with a Thermal Dynamics plasma torch. A Trio-motion six-axis motion system was used to manipulate the torch. The plates were clamped similarly to the TIG trials. The waveforms for these trials were measured using an AMV 4000 arc watch system. The samples were autogenously bead on plate welded, with a minimum gap of 10 mm between each weld. The material was allowed to cool to room temperature before the next weld was applied. The main parameters of interest were the electrode set back position (in the torch), current, and plasma gas flow rate. The constant parameters are shown in Table 7.3, and the variable ones are shown in Table 7.4. As in the TIG trials, a constant welding speed was used.

Table 7.3 – Constant parameters for all plasma arc welding trials.

Parameters	Value	Units
Welding speed	100	mm/min
Plasma gas type	N6 Argon	-
Shielding gas type	Pureshield argon	-
Shielding gas flow rate	12	L/min
Electrode diameter	4.8	mm
Electrode type	Thoriated	-
Electrode angle	60	°
Orifice diameter	Medium	-
Torch to plate working distance	4	mm

Table 7.4 – List of variable parameters used for plasma arc welding trials.

Current (A)	Electrode set back	Plasma gas flow rate (L/min)	Current (A)	Electrode set back	Plasma gas flow rate (L/min)
50	Maximum	1.3	75	Minimum	2.3
50	Maximum	1.7	100	Maximum	1.7
50	Maximum	2.0	100	Maximum	2.2
50	Minimum	1.3	100	Maximum	2.6
50	Minimum	2.0	100	Maximum	1.3
75	Maximum	1.5	100	Minimum	1.7
75	Maximum	1.9	100	Minimum	2.6
75	Maximum	2.3	150	Maximum	1.3
75	Minimum	1.5	150	Maximum	1.9

7.3.2.3 Metallography

Samples were only analysed in the as welded condition. One section was cut from each weld produced. The section was prepared using the metallographic procedure described in Chapter 2, and the same procedure for crack and weld measurement was also used.

Due to the smaller range of parameters used in these trials, and the relative ease with which the results could be interpreted, the design expert software was not used to analyse the results like the previous chapters.

7.4 Results

7.4.1 TIG welds

The results are presented in terms of the influence of the power source's waveform capabilities on both the weld bead geometry and the average crack length (ACL).

7.4.1.1 Process parameter effect on HAZ cracking

The only parameter of interest here is the power, and this is plotted against the ACL in Figure 7.5. The autogenous welds showed two samples with high average crack lengths, which is a result of weld metal solidification cracking. These two samples were produced at high power. It appears that cracking was avoided when the average power was below 800 W. Additionally, there appears to be no beneficial effect of the different waveform types. Of the 26 autogenous conditions investigated, only 7 exhibited cracking.

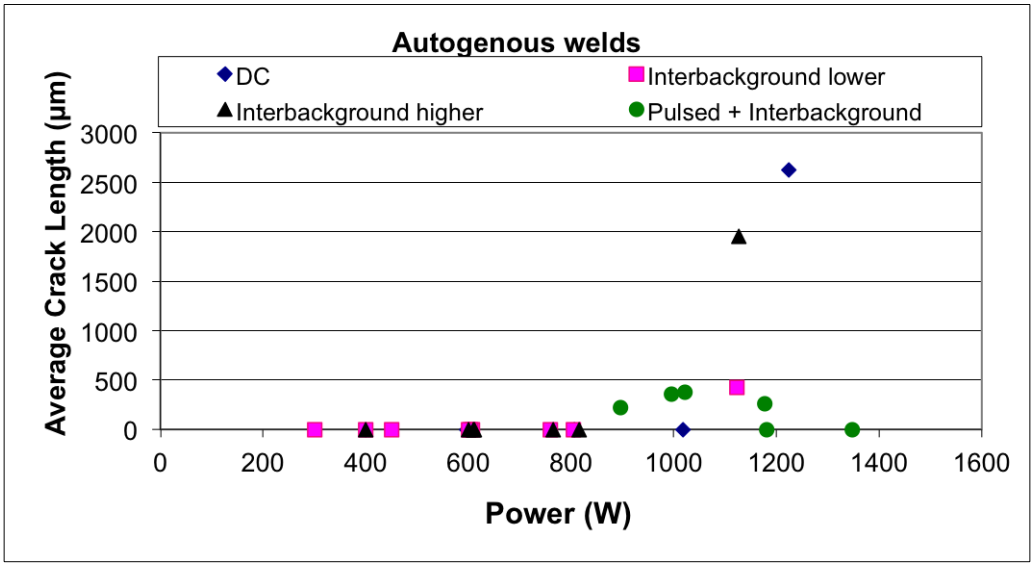

Figure 7.5 – Average crack length versus power for autogenous welds.

There are no occurrences of weld solidification cracks in the wire added welds (Figure 7.6). The average crack lengths of the wire-added welds appear to be in a similar range to those observed in the autogenous welds. Of the 17 wire added conditions, 10 exhibited cracking. Only the very lowest power levels avoided cracking in the as-welded condition.

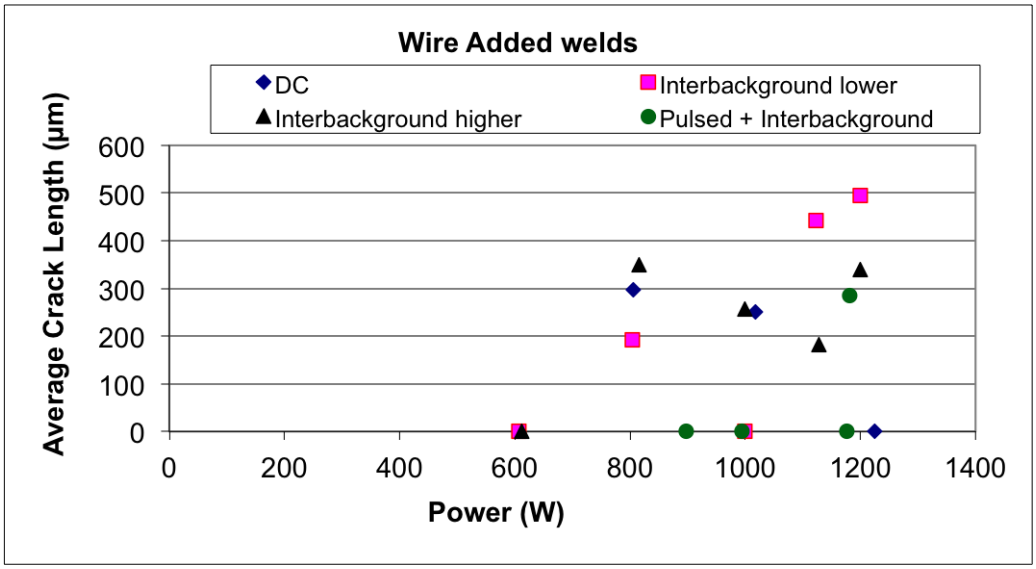

Figure 7.6 – Average crack length versus power for wire added welds.

7.4.1.2 Process parameter effect on weld geometry

The autogenous welds have a linear relationship between weld power and the geometry of the weld bead (Figures 7.7a, b and c). There also appears to be no influence of the type of waveform used to produce the bead geometries for these results. Note also that the comparative DC waveform results from the Migatronic power source also fit on the linear trend line. The TIG process (both power sources) was also only able to produce a weld pool (therefore producing a fusion zone) below 600 W (or 60 A average current) when using the high-frequency pulsing mode of the interpulse, using the waveform in Figure 7.2(c). The average power had little effect on the aspect ratio and all the welds were between 0.2 and 0.3.

For the wire added welds in Figure 7.8, the waveform type appeared to have an influence on the weld bead geometries. This is most prominent in the height results (Figure 7.8c). The influence of the waveform also appears to be most visible at the lower powers (and current), with a large difference being observed between the inter-background current being higher or lower than the main. There again appears to be a linear relationship between the respective geometry type and power. However, it was not feasible to produce a weld pool with any dilution at average powers below 600 W. It was also not feasible to achieve a weld pool for the wire-added welds using the DC waveform at 600 W, whereas the high frequency pulsing mode waveform was able to do so.

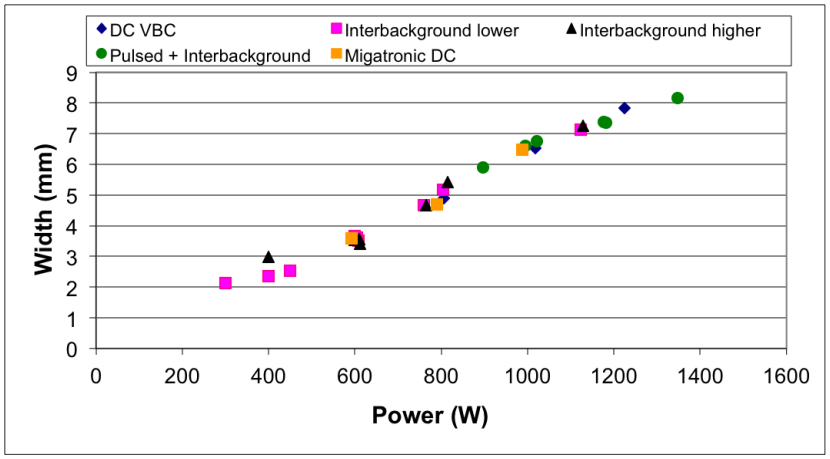

(a)

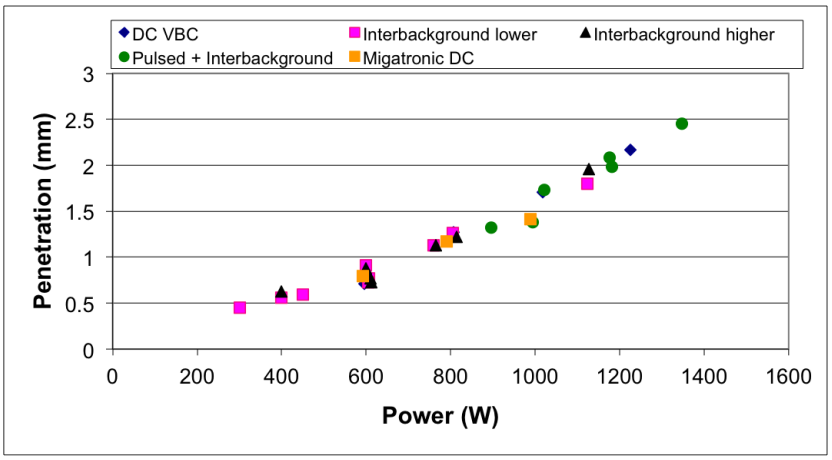

(b)

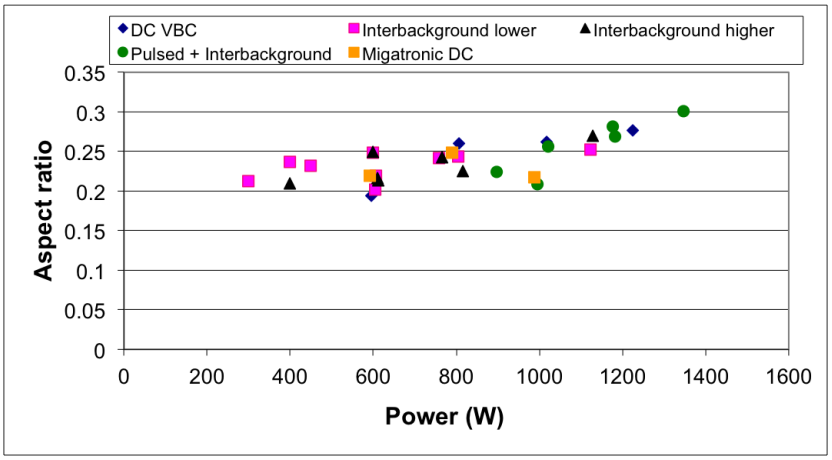

(c)

Figure 7.7 – Relationship between waveform type, power and (a) weld width, (b) weld penetration, and (c) aspect ratio, for autogenous TIG welds.

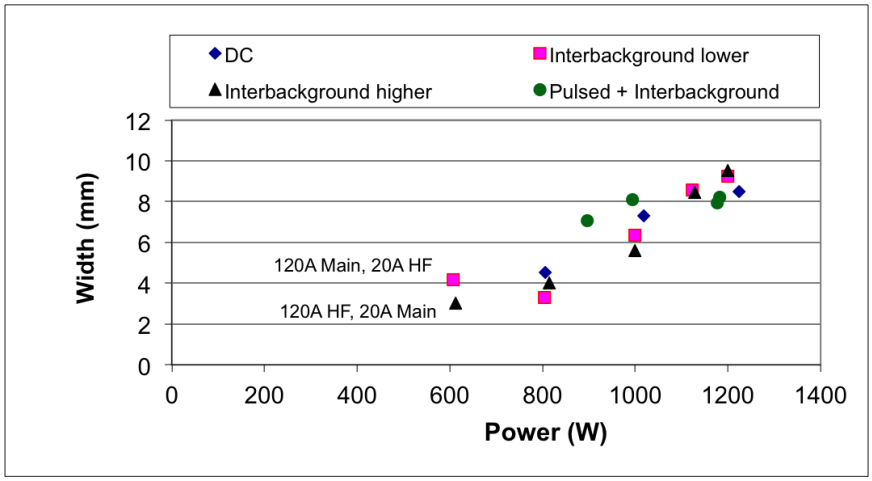

(a)

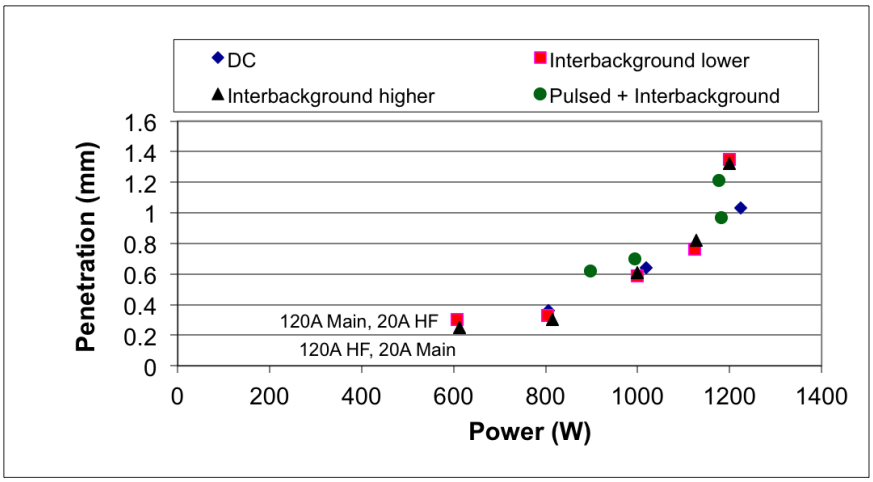

(b)

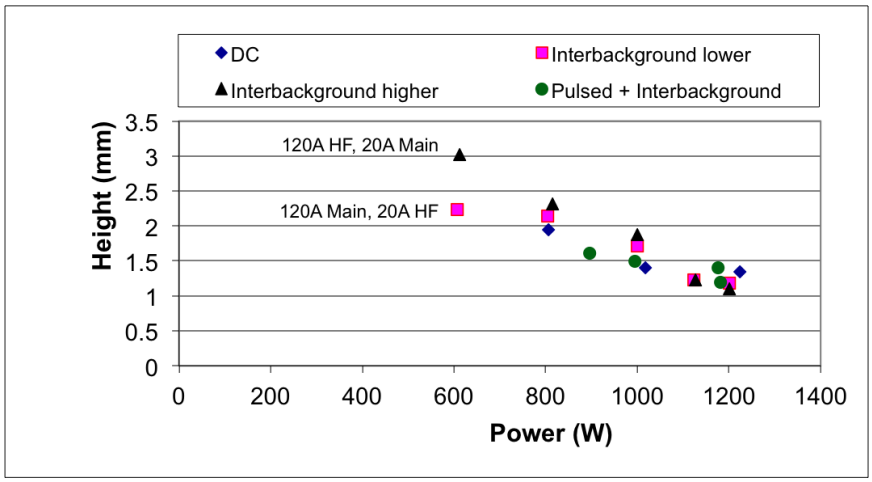

(c)

Figure 7.8 – Relationship between waveform type, power and (a) weld width, (b) weld penetration, and (c) weld height for wire added welds.

7.4.2 Plasma arc welds

A plot of the ACL versus aspect ratio for the PAW welds is illustrated in Figure 7.9. This shows there was a significant issue with cracking. Most of the cracks were weld metal solidification cracks at the higher aspect ratios. In general, nearly all samples had at least one crack.

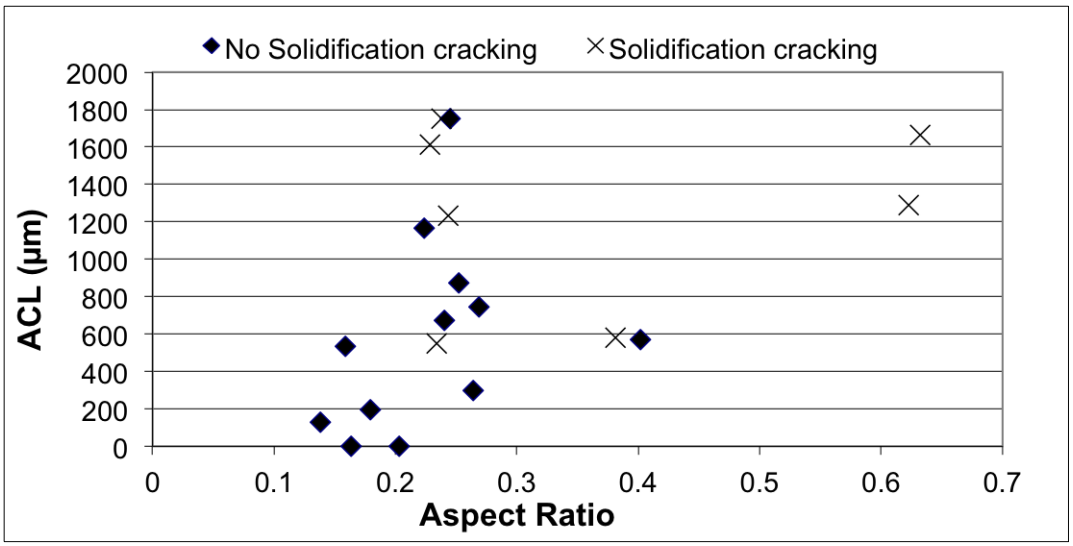

Figure 7.9 – Average crack length per weld versus aspect ratio for plasma arc welds.

A plot of the aspect ratio as a function of the power for the PAW is shown in Figure 7.10. Note that the aspect ratio particularly with high powers, was dependant on the plasma gas flow rate, which is also identified in this figure. It also appears that the aspect ratio was not influenced by the electrode position in the torch.

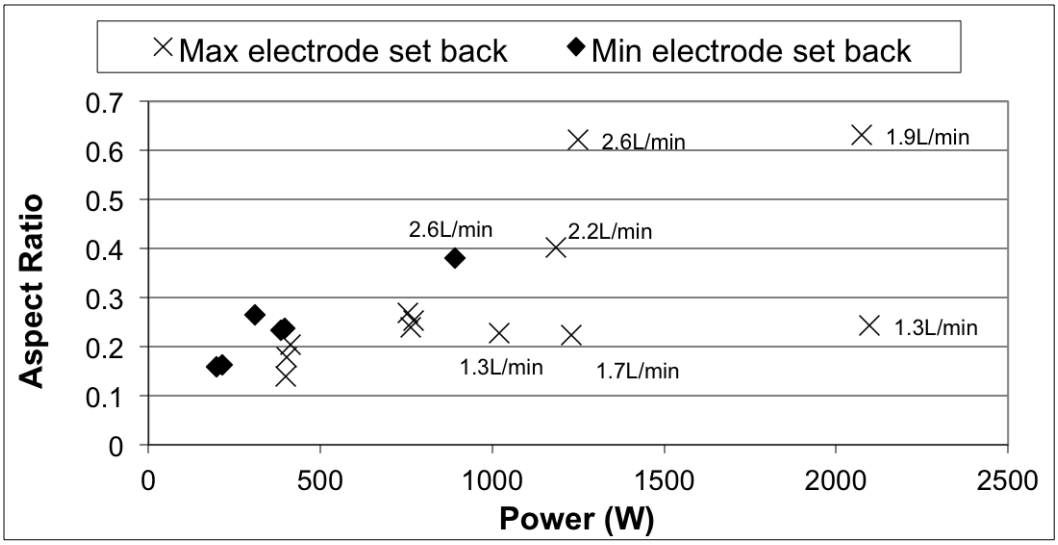

Figure 7.10 – Relationship between weld bead aspect ratio and power for plasma arc welding (plasma gas flow rates annotated as data labels).

The severity of the cracking issue is also exacerbated by the poor quality of the

weld surfaces. In most cases, the weld bead appeared severely oxidised (see Figure 7.11). In a number of cases, there were welds with one or more of the following defects: surface connected porosity, weld humping, and surface concavity.

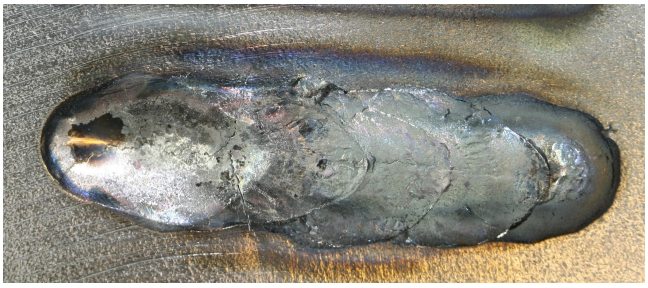

Figure 7.11 – Example of typical plasma weld surface condition.

7.5 Discussion

7.5.1 Cracking

It is significant that only a third of the TIG welds, and all the plasma welds, contained either HAZ liquation cracks, weld metal solidification cracking, or both. The TIG process was most suitable at powers below 800 W in the autogenous condition, and 600 W with wire added. This indicates that the use of the TIG process at low powers is suitable for producing crack free welds in superalloys. However, in terms of achieving the optimised aspect ratio as determined in Chapter 3, none of the autogenous TIG welds achieved the aspect ratios above 0.3. The two welds that produced weld metal solidification cracks were also two samples that were produced at a higher level of power. The TIG welds all appear to show an increasing incidence of cracking with increasing power, as was observed with the previous trials.

The application of HF TIG welding at low powers is favourable for crack free welding of superalloys. It is significant that Gregori (2006) found that superalloys Mar-M247 can be welded crack free using this process at heat inputs below 0.5kJ/mm, whilst in these trials the upper limit for autogenous welding was 0.48 kJ/mm, and for wire added it was 0.32 kJ/mm (calculated using Equation 7.1 where P is power in kW, and v is welding speed in mm/min).

$$HI = \frac{60.P}{v} \tag{7.1}$$

The lack of solidification cracking in the wire-added results are not surprising. It is however interesting to observe an increase in the number of samples that cracked with wire added. Normally, the addition of a more ductile filler metal reduces the susceptibility to cracking in nickel-based superalloys (Sidhu et al., 2005). In actual fact, the number of autogenous welds which contained cracking was at 27 %, whilst

this figure rose to 59 % for wire added welds.

It is very possible that the observed increase in cracking levels in the wire added welds is due to contamination of the wire. The contamination of the wire could have introduced lower melting point contaminants - such as those listed in Table 1.12 - which as a result may have lead to liquation cracks forming near the FZ boundary. Whilst the wire used was to a high aerospace quality, it is unfortunate that the wire may not have been thoroughly cleaned prior to the experiments. The wire feeder did have brand new liners in the system, so contamination from other wires (aluminium alloys, for example) was avoided. However, the working environment is still one with various different contaminants. This could be from contact between hands, or from the nozzle where the wire was fed from. The end of the wire could also be contaminated from the tools used to cut it. Therefore, even though the weld metal with autogenous welds is harder, they may have the advantage of fewer potential contamination sources.

To confirm that contamination of the wire lead to the exacerbated cracking problem, the best solution would be through a microstructural and chemical analysis of the cracks, which would show that (if contamination was the issue) the cracks were nucleated by liquation of low melting point segregates/contaminates, as discussed in section 1.4.1.

7.5.2 Aspect ratio

The optimal aspect ratio was defined in Chapter 3 as being between 0.25 and 0.65. As the results for the high frequency pulsed TIG process illustrated, only the lower limit of this range was achievable. This means that this process was difficult to use for a repair procedure which requires the generation of weld beads in this optimal range.

The plasma arc welding results however, produced a wider range of weld bead geometries, and proved that this process was capable of producing welds with sufficient penetration to achieve aspect ratios in and above the range, allowing for the process to be assessed for suitability. Unfortunately, as will be discussed in more detail below, this process produced poor quality weld beads, particularly when the higher aspect ratios were achieved.

The plasma welds were unable to avoid the formation of HAZ liquation cracks, and in some cases there were occurrences of weld metal solidification cracking. There were also instances of weld metal porosity, as well as severe surface porosity, oxidation, and concaved weld beads.

Plasma arc welding of superalloys, particularly in keyhole mode, is rarely used, especially in autogenous conditions. The most common application of PAW with

superalloys is cladding; where a powder/wire is introduced into the plasma jet (Su et al., 1997). The large amount of cracking suggests that the conditions required to achieve the higher aspect ratio welds also increased the risk of weld metal porosity and solidification cracking. The higher aspect ratios were achieved with a higher plasma gas flow rate, which created a higher keyhole pressure to increase the penetration of the weld bead. This may introduce turbulence, which may cause contamination of the weld metal, also causing cracking.

It may also be that plasma arc welding is typically used with higher welding speeds. One of the advantages of plasma welding is that it allows an increased rate of production compared to TIG welding, due to its ability to weld faster because of the higher penetration depths achieved compared to TIG. However, in this study the welding speed was kept constant and so it is difficult to comment on whether higher welding speeds would have a beneficial effect.

It is therefore clear that neither process can achieve the desired aspect ratio while producing high quality welds, which was the original aim.

7.5.3 High frequency pulsed TIG power source

It is claimed that a high frequency pulse into the waveform can produce an arc with higher energy densities, and a constricted arc leading to characteristics similar to a higher energy density process (Onuki et al., 2002). With a constricted arc, the greater arc pressure in comparison to DC or low frequency pulsed TIG welds at similar average currents, should produce welds that are of higher penetration, and as a result with higher aspect ratios.

This is part of the reason why the process was used in this chapter. The results in this chapter showed that the waveform had no effect on the weld bead profile for autogenous welds. Therefore the claim of higher arc pressure with the high frequency process is debatable. The process did however offer an important advantage: the ability to produce a weld pool at low average powers (or currents) where the DC and low frequency pulsing didn't produce a weld pool.

There was however a small influence of the different waveform types when a filler wire was introduced with low powers. It could be that the different waveforms influence the interaction between the arc and the filler wire, rather than between the arc and the weld pool. Unfortunately, the only published works which use this power source technology are on thin sheet titanium alloy (Leary et al., 2010) and use a matching filler wire, so understanding the difference is difficult.

The results presented in this thesis, show that when the HF current is set higher than the main, the weld beads are taller than comparable welds with the main current set higher. The width of the beads of the welds with HF current set higher

are also narrower than the comparable welds. There appears to be little difference in the penetration and dilution levels. However, emphasis must be stressed that these results appear to be true only at lower average powers/currents. When lower powers/currents at or below 600 W were used, it was not possible to melt the wire, or produce a weld pool except when using the interpulsing waveform.

A recent investigation on the impact of the parameters on titanium additive manufacture found similar results (Eze, 2009). However, the interesting finding from this thesis is that the effect of the magnitude of main current and HF pulsing current is reversed. In these results, when the main current is higher than the HF pulsing, a narrower but taller weld bead is formed, and conversely the bead is wider but flatter when the currents are reversed. This therefore casts a shadow over the true effect of the welding power source's parameter effects. This is especially true when it is considered that there appeared to be no influence on autogenous weld bead geometries.

7.6 Conclusions

This chapter has studied the suitability of high frequency TIG welding and plasma arc welding for the application of repair welding nickel superalloys. This was in an attempt to produce weld bead geometries with the optimal shape, as was outlined in Chapter 3. The following conclusions can be made from this work:

1. With the material studied in this chapter, the optimal aspect ratio range cannot be achieved with the high frequency TIG. However, the aspect ratio range can be achieved using the plasma arc process, although there are significant defects associated with these welds.
2. The plasma arc process produced significant levels of defects. Only two samples contained zero cracking, and there were significant issues with solidification cracking. When using the HF TIG power supply, cracking was minimised with low power inputs. It was not possible to establish a link with the weld bead geometry.
3. The TIG welding process produced crack free welds at average powers below 800 W for autogenous, and 600 W for wire-added welds. This confirms that low heat input arc welding is a viable process for repair of superalloys.
4. The high frequency TIG welds produced more cracking when filler wire was added, than autogenous welds. The most likely cause was contamination from the filler wire. An advantage of the autogenous process is there is one less source of contamination.

5. The HF TIG power source was able to produce autogenous welds in the material at powers below 600 W when using the high frequency pulsing waveform, which couldn't be achieved with the DC and HF pulsed + low frequency pulsed waveforms. The HF TIG power source was also able to produce a wire-added weld at 600 W, where the DC and HF pulsed + low frequency pulsed waveforms couldn't.
6. There is no influence of the different waveforms produced by the HF TIG power source on cracking, or the shape of the autogenous weld bead profiles. A small effect was observed with the wire-added welds at low powers.
7. It is difficult to validate the previous observations (Optimal aspect ratio) using the arc welding technologies in this study.
8. Based on the above conclusions, it is recommended that the HF TIG process is investigated further for its application to produce crack free repair welds in nickel based superalloys.

Chapter 8

Overall conclusions and future work

8.1 Conclusions

The following are the conclusions of this thesis:

1. Crack free welds have been produced on Rene 80, which is considered a highly crack susceptible nickel based superalloy.
2. A large parametric study using laser welding, with over 130 different parameter combinations, enabled the identification of welding parameters that reduced the incidence of liquation and post-weld heat treatment cracking.
3. The study found that for the as-welded condition, welding power significantly affects the incidence of cracking, but depended on the beam diameter: high power increased cracking with small beam diameters, while high power decreased cracking with large beam diameters. Overall, a beam diameter of 2.5 mm reduced the incidence of cracking for the range of powers investigated in this study.
4. The study on welding parameter effect found a significant relationship between the weld bead aspect ratio and the incidence of both types of crack. At aspect ratios in the range of 0.25 - 0.65 (for as-welded) and 0.35 and 0.65 (in the PWHT condition), the incidence of cracking is significantly reduced.
5. Welding speed effects were shown to be negligible in the as-welded condition, but appeared to have an affect on the post-weld heat treatment cracking. In this condition, cracking was lower at lower welding speeds.
6. The cracks produced during the parametric study where characterised and found to be produced via liquation of secondary phases such as MC type carbides, γ/γ' eutectic and secondary γ' precipitates. Additionally, there appeared to be one crack formed via stress-induced mechanism in an as-welded

sample. In the PWHT condition, there were cracks which had already formed during the welding cycle (e.g. liquation) and they appeared to extend in the PWHT condition, whilst some additional cracks nucleated. This was via the strain-induced mechanism.

7. Based on the optimised weld bead geometry and welding parameters, a novel repair procedure combining autogenous laser sealing with hot isostatic pressing was developed. This procedure avoids the complications associated with using ductile filler material, and had a high level of success in producing samples free of welding defects, and which were successfully HIP treated to heal surface-connected porosity.

8. Neutron diffraction measurement of the different strains and residual stresses in two different aspect ratio samples produced poor quality results. The results were affected by complications arising from the material's thickness, composition and grain size. As a result, no conclusions relating the aspect ratio to the cracking can be confidently made.

9. Advanced arc-welding processes were studied for their suitability for repair of Rene 80. This includes a low heat input MIG based process, which still appeared to form cracks in both conditions. Additionally, the effect of cast grain size was found to be significant, with larger grain sizes being more susceptible to cracking.

10. High frequency pulsed TIG welding was also studied for suitability for repair, and was found to produce crack free welds at powers below 800 W. Additionally, the addition of wire with this process appeared to produce more cracking compared to the autogenous welds. This process offered benefits of producing a weld pool at lower average powers than a comparable DC process. When used autogenously, the high frequency pulsing had no effect on the weld bead geometry. However, there was a small effect at low powers when filler wire is added.

11. The high frequency TIG and a plasma arc welding power source were both studied for the application as an arc-based repair procedure based on the laser-based one. However, in the case of the TIG power source it could not achieve the optimised aspect ratio ranges to reduce the incidence of cracking. The plasma process could produce the optimised aspect ratio range, but was severely affected by weld metal cracking due to process instabilities. However, the HF TIG process was shown to be suitable for crack free repair welds on superalloys at powers below 800 W.

8.2 Recommendations for future work

The following are suggestions to continue this research further, as well as some more general areas of interest related to superalloy weldability:

1. Develop thermo-mechanical FE models to understand the effect of the weld bead aspect ratio during welding cycle. This will include how the stresses in the HAZ develop and are influenced by the weld bead geometries.
2. Further evaluation of the weld bead aspect ratio effect by the neutron diffraction technique. In particular, in-situ measurements would greatly aid the understanding of the phenomenon.
3. Development of standardised crack susceptibility data for Rene 80 and other superalloys. This would involve a crack susceptibility test which would produce a more accurate understanding of an alloy's susceptibility to cracking.

Although the repair procedure developed in Chapter 6 has been partially successful, there are still some issues to resolve, such as identifying how to reduce the occurrence of solidification cracking, and improving the surface finish.

Further trials should be undertaken, which would investigate the following areas:

1. Increasing the amount of samples studied, thereby improving the statistics by having a greater sample range.
2. Improving the pre-weld surface preparation - increased cleanliness and reduced roughness.
3. Optimisation of weld paths - e.g. investigating effect of different overlap distances.
4. Application to real components.
5. Application to larger components which are more heavily restrained, and could therefore have larger residual stresses after welding, which could exacerbate cracking.
6. Modify the laser controller so that it turns the laser off prior to stopping the movement of the laser head. This should prevent the occurrence of defects at the end of travel.
7. Determine whether sealing the components with the TIG process is as effective when using a similar welding speed.

References

Andersson, J. and G. P. Sjoberg: 2012, 'Repair welding of wrought superalloys: Alloy 718, Allvac 718Plus and Waspaloy'. *Science and Technology of Welding and Joining* **17**(1), 49–59.

Appa Rao, G., M. Sankaranarayana, and S. Balasubramaniam: 2012, 'Hot Isostatic Pressing Technology for Defence and Space Applications'. *Defence Science Journal* **62**(1), 73–80.

Arjakine, N., J. Bruck, B. Gruger, D. M. Seger, and R. Wilkenhoener: 2008, 'Advanced weld repair of hot gas turbine components'. In: *Proceedings of ASME Turbo Expo*.

ASTM: 1988, 'Standard test method for determining the average grain size'. Technical Report E112-88.

Babu, S. S., S. A. David, J. W. Park, and J. M. Vitek: 2004, 'Joining of nickel base superalloy single crystals'. *Science and Technology of Welding and Joining* **9**(1), 1–12.

Banerjee, K., N. L. Richards, and M. C. Chaturvedi: 2005, 'Effect of filler alloys on heat-affected zone cracking in preweld heat-treated IN-738 LC gas-tungsten-arc welds'. *Metallurgical and Mat.Transactions A* **36**(7), 1881–1890.

Benoit, A., S. Jobez, P. Paillard, V. Klosek, and T. a. Baudin: 2011, 'Study of Inconel 718 weldability using MIG CMT process'. *Science and Technology of Welding and Joining* **16**(6), 447–482.

Betteridge, W. and A. W. Franklin: 1957, 'The effect of heat treatment and structure on the creep and stress rupture properties of Nimonic 80A'. *Journal of Institute of Metallurgy* **85**, 473–479.

Boucher, C., M. Dadian, and H. Granjon: 1977, 'Final report COST 50'. Technical report, Institute de Soudure, Paris .

Boucher, C., D. Varela, M. Dadian, and H. Granjon: 1976, 'Hot cracking and recent improvement of the weldability of nickel alloys of the inconel 718 and waspaloy types.'. *Revue de Metallurgie.Cahiers D'Informations Techniques* **73**(12), 817–832.

Bruckner, J.: 2005, 'Cold metal transfer has a future joining steel to aluminum'. *Welding Journal* **84**(6), 38–40.

Callister, W. D.: 2000, *Materials science and engineering : an introduction*. New York ; Chichester: Wiley, 5th edition.

Cao, W.-D.: 2005, 'Solidification and solid state phase transformation of Allvac® 718Plus™ alloy'. In: *Superalloys 718, 625, 706, and Various Derivatives*. pp. 165–177.

Carlton, J. B. and M. Prager: 1970, 'Variables influencing the strain-age cracking and mechanical properties of Rene 41 and related alloys'. *Welding Research Council Bulletin* pp. 13–23.

Chaturvedi, M. C.: 2007, 'Liquation cracking in heat affected zone in Ni superalloy welds'. *Materials Science Forum* **546-549**, 1163–1170.

Chen, W., M. C. Chaturvedi, N. L. Richards, and G. McMahon: 1998, 'Grain boundary segregation of boron in Inconel 718'. *Metallurgical and Mat.Transactions A* **29**(7), 1947–1954.

Clark, D., M. R. Bache, and M. T. Whittaker: 2008, 'Shaped metal deposition of a nickel alloy for aero engine applications'. *Journal of Materials Processing Technology* **203**(1-3), 439–448.

Cook, G. E. and H. E.-D. E. H. Eassa: 1985, 'Effect of high-frequency pulsing of a welding arc'. *IEEE Transactions on Industry Applications* **IA-21**(5), 1294–1299.

Courtot, B.: 2007, 'Repair welding of high temperature nickel superalloy castings'. Master's thesis, Cranfield University.

Czech, N., F. Staif, V. S. Savchenko, and K. A. Yushchenko: 1997, 'Evaluation of the weldability of the gas turbine blade materials IN738LC and Rene 80'. In: *Proceedings from Material Solutions '97 on Joining and Repair of Gas Turbine Components*. pp. 7–10.

Danis, Y., C. Arvieu, E. Lacoste, T. Larrouy, and J.-M. Quenisset: 2010, 'An investigation on thermal, metallurgical and mechanical states in weld cracking of Inconel 738LC superalloy'. *Materials and Design* **31**(1), 402–416.

David, S. A., J. M. Vitek, S. S. Babu, L. A. Boatner, and R. W. Reed: 1997, 'Welding of nickel base superalloy single crystals'. *Science and Technology of Welding and Joining* **2**(2), 79–88.

Dinda, G. P., A. K. Dasgupta, and J. Mazumder: 2009, 'Laser aided direct metal deposition of Inconel 625 superalloy: Microstructural evolution and thermal stability'. *Materials Science and Engineering A* **509**(1-2), 98–104.

Donachie, M. J. and S. J. Donachie: 2002, *Superalloys : a technical guide*. Materials Park, OH: ASM International, 2nd edition.

Doncasters: 2006, 'Rene 80 Microstructure report'. Technical report, Doncasters Group DPC.

Dudas, J. H. and F. R. Collins: 1966, 'Preventing weld cracks in high-strength aluminum alloys'. *Welding Journal* **45**(6).

DuPont, J. N., J. C. Lippold, and S. D. Kiser: 2009, *Welding metallurgy and weldability of nickel-base alloys*. Hoboken, NJ: Wiley.

Dye, D., O. Hunziker, and R. Reed: 2001a, 'Numerical analysis of the weldability of superalloys'. *Acta Materialia* **49**(4), 683–697.

Dye, D., S. M. Roberts, P. J. Withers, and R. C. Reed: 2000, 'Determination of the residual strains and stresses in a tungsten inert gas welded sheet of IN718 superalloy using neutron diffraction'. *Journal of Strain Analysis for Engineering Design* **35**(4), 247–259.

Dye, D., H. J. Stone, and R. C. Reed: 2001b, 'A two phase elastic–plastic self-consistent model for the accumulation of microstrains in Waspaloy'. *Acta Materialia* **49**(7), 1271–1283.

Dyrkacz, W. W.: 1979, 'Aerospace structural metals handbook'. Technical Report Code 4214- Rene 80, Mechanical Properties Data Center, Battelle Columbus Laboratories, Columbus, Ohio.

Egbewande, A., H. Zhang, R. Sidhu, and O. Ojo: 2009, 'Improvement in laser weldability of INCONEL 738 superalloy through icrostructural modification'. *Metallurgical and Materials Transactions A* **40**(11), 2694–2704.

Egbewande, A. T., R. A. Buckson, and O. A. Ojo: 2010, 'Analysis of laser beam weldability of Inconel 738 superalloy'. *Materials Characterization* **61**(5), 569–574.

Electric, G.: 1971, 'Patent US3615376A Cast nickel base alloy'.

Eze, E.: 2009, 'VBC welding system parameter effect on the shape and microstructure of additively manfactured Ti6Al4V titanium alloy'. Masters thesis, Cranfield University.

Gandy, D. W., G. Frederick, J. T. Stover, and R. Viswanathan: 2000, 'Overview of hot section component repair methods'. In: *ASM International Materials Solutions Conference 2000 Gas Turbine Materials Technology Session*.

Gittos, N. F. and M. H. Scott: 1981, 'Heat-Affected-Zone cracking of Al-Mg-Si alloys'. *Welding Journal* **60**(6).

Gregori, A.: 2003, 'Survey of welding and repairing of nickel super-alloys for gas turbines'. Technical Report 774/2003, TWI.

Gregori, A.: 2006, 'Repair of single crystal CMSX-10 blades and polycrystalline Mar-M247 vanes by high-frequency pulsed DCEN TIG welding'. Technical Report 856/2006, WI.

Haafkens, M. H. and J. G. Matthey: 1982, 'A new approach to the weldability of nickel-base as-cast and powder metallurgy Superalloys'. *Welding Journal* **61**, 25–30.

Halmoy, E.: 1979, 'Wire melting rate, droplet temperature and effective anode melting potential'. In: *Arc Physics and Weld Pool Behaviour*. pp. 49–57.

Harvey, M. D. F.: 1999, 'Advanced repair of hot section gas turbine components'. Technical Report TWI Proposal GP/ALS/1171-1, TWI.

Henderson, M. B., D. Arrell, R. Larsson, M. Heobel, and G. Marchant: 2004, 'Nickel based superalloy welding practices for industrial gas turbine applications'. *Science and Technology of Welding and Joining* **9**(1), 13–21.

Hong, H., I. Kim, B. Choi, Y. Yoo, and C. Jo: 2011, 'On the Role of Grain Boundary Serration in Simulated Weld Heat-Affected Zone Liquation of a Wrought Nickel-Based Superalloy'. *Metallurgical and Materials Transactions A* **43**(1), 173–181.

Huang, C. and S. Kou: 2002, 'Liquation mechanisms in multicomponent aluminum alloys during welding'. *Welding Journal* **81**(10), S211–S222.

Huang, C. and S. Kou: 2004, 'Liquation cracking in full-penetration Al-Cu welds'. *Welding Journal* **83**(2), S50–S58.

Hughes, W. P. and T. F. Berry: 1967, 'A study on the strain-age cracking characteristics in welded Rene 41 - phase 1'. *Welding Journal* **46**(8), 361s–370s.

Hussein, N. I. S., J. Segal, D. G. McCartney, and I. R. Pashby: 2008, 'Microstructure formation in Waspaloy multilayer builds following direct metal deposition with laser and wire'. *Materials Science and Engineering A* **497**(1-2), 260–269.

Idowu, O. A., O. A. Ojo, and M. C. Chaturvedi: 2007, 'Effect of heat input on heat affected zone cracking in laser welded ATI Allvac 718Plus superalloy'. *Materials Science and Engineering A* **454-455**, 389–397.

Ion, J. C.: 2005, *Laser processing of engineering materials : principles, procedure and industrial application*. Oxford: Elsevier.

Jahnke, B.: 1982, 'High-temperature electron beam welding of the nickel-base superalloy IN-738LC'. *Welding Journal* **61**(11), S343–S347.

Jena, A. K. and M. C. Chaturvedi: 1984, 'The role of alloying elements in the design of nickel-base superalloys'. *Journal of Materials Science* **19**(10), 3121–3139.

Jiang, W., Z. Liu, J. Gong, and S. Tu: 2010, 'Numerical simulation to study the effect of repair width on residual stresses of a stainless steel clad plate'. *International Journal of Pressure Vessels and Piping* **87**(8), 457–463.

Jiang, W., X. Xu, J. Gong, and S. Tu: 2012, 'Influence of repair length on residual stress in the repair weld of a clad plate'. *Nuclear Engineering and Design*.

Joseph, A., D. Harwig, D. Farson, and R. Richardson: 2003, 'Measurement and calculation of arc power and heat transfer efficiency in pulsed gas metal arc welding'. *Science and Technology of Welding and Joining* **8**(6), 400–406.

Kayacan, R., R. Varol, and O. Kimilli: 2004, 'The effects of pre- and post-weld heat treatment variables on the strain-age cracking in welded Rene 41 components'. *Materials Research Bulletin* **39**(14-15), 2171–2186.

Kelly, T. J.: 1990, 'Welding metallurgy of investment cast nickel-based superalloys'. *Proceedings of the conference of "Weldability of Materials" 8-12 October 1990* pp. 151–157.

Kim, D. Y., J. H. Hwang, K. S. Kim, and J. G. Youn: 2000, 'A study on fusion repair process for a precipitation hardened IN738 Ni-based superalloy'. *Journal of Engineering for Gas Turbines and Power* **122**(3), 457–461.

Koizumi, M. and M. Nishihara: 1991, *Isostatic pressing: technology and applications*. Springer.

Koren, A., I. Weisshaus, A. Kaufman, and M. Roman: 1982, 'Improving the weldability of Ni-base superalloy 713C'. *Welding Journal* **61**(11), 348. s–351. s.

Korsunsky, A. and K. James: 2004, 'Residual Stresses Around Welds in Nickel-based Superalloys'. *Journal of Neutron Research* **12**(1), 153–158.

Kou, S.: 2003a, 'Solidification and liquation cracking issues in welding'. *JOM* **55**(6), 37–42.

Kou, S.: 2003b, *Welding metallurgy*. Hoboken, NJ: John Wiley, 2nd edition.

Krawitz, A. D.: 2011, 'Neutron strain measurement'. *Materials Science and Technology* **27**(3), 589 – 603.

Leary, R. K., E. Merson, K. Birmingham, D. Harvey, and R. Brydson: 2010, 'Microstructural and microtextural analysis of InterPulse GTCAW welds in Cp-Ti and Ti-6Al-4 V'. *Materials Science and Engineering: A* **527**, 7694–7705.

Li, Y.: 2007, 'Mechanism of Repair Weld Cracking in Rene 80 Nickel Based Superalloy'. Master's thesis, University of Birmingham.

Lim, L. C., J. Z. Yi, N. Liu, and Q. Ma: 2002a, 'Cyclic overaging heat treatment for ductility and weldability improvement of nickel based superalloys'. *Materials Science and Technology* **18**(4), 413–419.

Lim, L. C., J. Z. Yi, N. Liu, and Q. Ma: 2002b, 'Cyclic overaging pre-weld heat treatment of Rene 80: Effect of solution treatment and end aging temperatures'. *Materials Science and Technology* **18**(4), 420–428.

Lim, L. C., J. Z. Yi, N. Liu, and Q. Ma: 2002c, 'Mechanism of post-weld heat treatment cracking in Rene 80 nickel based superalloy'. *Materials Science and Technology* **18**(4), 407–412.

Lingenfelter, A. C.: 1997, 'Welding metallurgy of nickel alloys in gas turbine components'. In: *Proceedings from Materials Solutions '97 on Joining and Repair of Gas Turbine Components, 15-18th September 1997*.

Liu, Y., Y. Li, and H. Peng: 2010, 'Laser Net Shape Manufacturing of Rene 80'. In: *Picalo: Pacific International Conference on Applications of Lasers and Optics*.

Meetham, G.: 1989, 'Steel and nickel alloys at high temperatures. Part D of 'The requirements for and limitations of materials at high temperatures". *Materials and Design* **10**(2), 77–92.

Messler, R. W.: 2004, *Joining of materials and structures: from pragmatic process to enabling technology*. Burlington, MA: Elsevier.

Metzger, G. E.: 1967, 'Some mechanical properties of welds in 6061 aluminum alloy sheet'. *Welding Journal* **46**(10).

Milman, Y. V., D. B. Miracle, S. I. Chugunova, I. V. Voskoboinik, N. P. Korzhova, T. N. Legkaya, and Y. N. Podrezov: 2001, 'Mechanical behaviour of Al3Ti intermetallic and L12 phases on its basis'. *Intermetallics* **9**(9), 839–845.

Modenesi, P.: 1990, 'Statistical modelling of the narrow gap gas metal arc welding process'. Ph.D. thesis, Cranfield University.

Montazeri, M. and F. M. Ghaini: 2012, 'The liquation cracking behaviour of IN738LC superalloy during low power Nd:YAG pulsed laser welding'. *Materials Characterization* **67**, 65–73.

Moradi, M. and M. Ghoreishi: 2010, 'Influences of laser welding parameters on the geometric profile of NI-base superalloy Rene 80 weld-bead'. *International Journal of Advanced Manufacturing Technology* **55**(1-4), 205–215.

Mousavizade, S. M., F. M. Ghaini, M. J. Torkamany, J. Sabbaghzadeh, and A. Abdollah-zadeh: 2009, 'Effect of severe plastic deformation on grain boundary liquation of a nickel-base superalloy'. *Scripta Materialia* **60**(4), 244–247.

Nakagawa, Y. G., A. Ohtomo, and Y. Saiga: 1976, 'Directional solidification of Rene 80'. *Trans Jpn Inst Met* **17**(6), 323–329.

Neidel, A., S. Riesenbeck, T. Ullrich, J. Völker, and C. Yao: 2005, 'Hot cracking in the HAZ of laser-drilled turbine blades made from René 80'. *Materialpruefung/Materials Testing* **47**(10), 553–559.

Nissley, N. E.: 2006, 'Intermediate temperature grain boundary embrittlement in nickel-base weld metals'. Ph.D. thesis, Ohio State University.

Norrish, J.: 1992, *Advanced welding processes*. Bristol: Institute of Physics Publishing. J. Norrish.

Norton, S. J.: 2002, 'Development of a Gleeble Based Test for Post Weld Heat Treatment Cracking in Nickel Alloys'. Ph.D. thesis, Ohio State University.

Ojo, O. and M. Chaturvedi: 2005, 'On the role of liquated gamma prime precipitates in weld heat affected zone microfissuring of a nickel-based superalloy'. *Materials Science & Engineering A* **403**(1-2), 77–86.

Ojo, O. A.: 2007, 'Intergranular liquation cracking in heat affected zone of a welded nickel based superalloy in as cast condition'. *Materials Science and Technology* **23**(10), 1149–1155.

Ojo, O. A., N. L. Richards, and M. C. Chaturvedi: 2004, 'Contribution of constitutional liquation of gamma prime precipitate to weld HAZ cracking of cast Inconel 738 superalloy'. *Scripta Materialia* **50**(5), 641–646.

Ojo, O. A., N. L. Richards, and M. C. Chaturvedi: 2006, 'Study of the fusion zone and heat-affected zone microstructures in tungsten inert gas-welded Inconel 738LC superalloy'. *Metallurgical and Materials Transactions A* **37**(2), 421–433.

Ola, O., O. Ojo, P. Wanjara, and M. Chaturvedi: 2011a, 'Analysis of Microstructural Changes Induced by Linear Friction Welding in a Nickel-Base Superalloy'. *Metallurgical and Mat.Transactions A* **42**(12), 3761–3777.

Ola, O., O. Ojo, P. Wanjara, and M. Chaturvedi: 2011b, 'Crack-Free Welding of IN 738 by Linear Friction Welding'. *Advanced Materials Research* **278**, 446–453.

Ola, O., O. Ojo, P. Wanjara, and M. Chaturvedi: 2011c, 'Enhanced resistance to weld cracking by strain-induced rapid solidification during linear friction welding'. *Philosophical Magazine Letters* **91**(2), 140–149.

Onuki, J., Y. Anazawa, M. Nihei, M. Katou, A. Onuma, and T. Funamoto: 2002, 'Development of a new high-frequency, high-peak current power source for high constricted arc formation'. *Japanese Journal of Applied Physics, Part 1* **41**(9), 5821–5826.

Osoba, L. O., R. K. Sidhu, and O. A. Ojo: 2011, 'On preventing HAZ cracking in laser welded DS Rene 80 superalloy'. *Materials Science and Technology* **27**(5), 897–902.

Österle, W., S. Krause, T. Moelders, A. Neidel, G. Oder, and J. Völker: 2008, 'Influence of heat treatment on microstructure and hot crack susceptibility of laser-drilled turbine blades made from René 80'. *Materials Characterization* **59**(11), 1564–1571.

Owczarski, W. A., D. S. Duvall, and C. P. Sullivan: 1966, 'A model for heat-affected zone cracking in nickel-base superalloy'. *Welding Journal* **45**(4), S145–S155.

Pepe, J. J. and W. F. Savage: 1967, 'Effects of constitutional liquation in 18-Ni maraging steel weldment'. *Welding Journal* **46**(9), S411–S422.

Pickin, C. G., S. W. Williams, and M. Lunt: 2011, 'Characterisation of the cold metal transfer (CMT) process and its application for low dilution cladding'. *Journal of Materials Processing Technology* **211**(3), 496–502.

Pickin, C. G. and K. Young: 2006, 'Evaluation of cold metal transfer (CMT) process for welding aluminium alloy'. *Science and Technology of Welding and Joining* **11**(5), 583–585.

Pinkerton, A. J., W. Wang, and L. Li: 2008, 'Component repair using laser direct metal deposition'. *Proceedings of the Institution of Mechanical Engineers, Part B: Journal of Engineering Manufacture* **222**(7), 827–836.

Pollock, T. M. and S. Tin: 2006, 'Nickel-based superalloys for advanced turbine engines: Chemistry, microstructure, and properties'. *Journal of Propulsion and Power* **22**(2), 361–374.

Prager, M. and C. S. Shira: 1968, 'Welding of precipitation-hardening nickel-base alloys'. *WRC Bulletin No 128 February* pp. 1–55.

Prager, M. and G. Sines: 1970, 'Mechanism for cracking during postwelding heat treatment of nickel- base alloys'. *Welding Research Council Bulletin* pp. 24–32.

Price, J., A. Paradowska, S. Joshi, and T. Finlayson: 2006, 'Residual stresses measurement by neutron diffraction and theoretical estimation in a single weld bead'. *International Journal of Pressure Vessels and Piping* **83**(5), 381–387.

Radhakrishnan, B. and R. G. Thompson: 1993, 'The effect of weld heat-affected zone (HAZ) liquation kinetics on the hot cracking susceptibility of alloy 718'. *Metallurgical Transactions A* **24**(6), 1409–1422.

Reed, R. C.: 2006, *The superalloys : fundamentals and applications*. Cambridge: Cambridge University Press, 1st edition.

Richards, N. L., R. Nakkalil, and M. C. Chaturvedi: 1994, 'The influence of electron-beam welding parameters on heat-affected-zone microfissuring in Incoloy 903'. *Metallurgical and Materials Transactions A* **25**(8), 1733–1745.

Ross, E. W.: 1971, 'Rene 80. A cast turbine blade alloy'. *Metal Progr* **99**(3), 93–94.

Safari, J. and S. Nategh: 2006, 'On the heat treatment of Rene-80 nickel-base superalloy'. *Journal of Materials Processing Technology* **176**(1-3), 240–250.

Santisteban, J. R., M. R. Daymond, J. A. James, and L. Edwards: 2006, 'ENGIN-X: A third-generation neutron strain scanner'. *Journal of Applied Crystallography* **39**(6), 812–825.

Savage, W. F., E. F. Nippes, and G. M. Goodwin: 1977, 'Effect of minor elements on hot-cracking tendencies of inconel 600'. *Welding Journal* **56**(8).

Schneider, K., B. Jahnke, R. Buergel, and J. Ellner: 1985, 'Experience with repair of stationary gas-turbine blades - view of a turbine manufacturer'. *Materials Science and Technology* **1**(8), 613–619.

Schnell, A., M. Heobel, and J. Samuleson: 2011, 'A study of the weldability of gamma prime hardened superalloys'. *Advanced Materials Research* **278**, 434–439.

Sexton, L., S. Lavin, G. Byrne, and A. Kennedy: 2002, 'Laser cladding of aerospace materials'. *Journal of Materials Processing Technology* **122**(1), 63–68.

Shahsavari, H. A., A. H. Kokabi, and S. Nategh: 2007, 'Effect of preweld microstructure on HAZ liquation cracking of Rene 80 superalloy'. *Materials Science and Technology* **23**(5), 547–555.

Shimada, W. and T. Gotoh: 1976, 'Characteristics of high frequency pulsed DC TIG welding process'. Technical Report XII-628-76, International Institute of Welding.

Shinozaki, K., H. Kuroki, X. Luo, H. Ariyoshi, and M. Shirai: 2000, 'Comparison of hot cracking susceptibilities of various Ni-base, heat-resistant superalloys by U-type hot cracking test (2nd report)'. *Welding Research Abroad* **46**(2), 10–17.

Short, A., D. McCartney, P. Webb, and E. Preston: 2011, 'Influence of nozzle orifice diameter in keyhole plasma arc welding'. *Science and Technology of Welding and Joining* **16**(5), 446–452.

Short, A. B.: 2009, 'Gas tungsten arc welding of Alpha + Beta titanium alloys: A review'. *Materials Science and Technology* **25**(3), 309–324.

Sidhu, R. K., O. A. Ojo, and M. C. Chaturvedi: 2007a, 'Microstructural analysis of laser-beam-welded directionally solidified Inconel 738'. *Metallurgical and Materials Transactions A* **38**(4), 858–870.

Sidhu, R. K., O. A. Ojo, and M. C. Chaturvedi: 2009a, 'Microstructural response of directionally solidified René 80 superalloy to gas-tungsten arc welding'. *Metallurgical and Materials Transactions A* **40**(1), 150–162.

Sidhu, R. K., O. A. Ojo, N. L. Richards, and M. C. Chaturvedi: 2009b, 'Metallographic and OIM study of weld cracking in GTA weld build-up of polycrystalline, directionally solidified and single crystal Ni based superalloys'. *Science and Technology of Welding and Joining* **14**(2), 125–131.

Sidhu, R. K., N. L. Richards, and M. C. Chaturvedi: 2005, 'Effect of aluminium concentration in filler alloys on HAZ cracking in TIG welded cast Inconel 738LC superalloy'. *Materials Science and Technology* **21**(10), 1119–1131.

Sidhu, R. K., N. L. Richards, and M. C. Chaturvedi: 2007b, 'Post-weld heat treatment cracking in autogenous GTA welded cast Inconel 738LC superalloy'. *Materials Science and Technology* **23**(2), 203–213.

Sidhu, R. K., N. L. Richards, and M. C. Chaturvedi: 2008, 'Effect of filler alloy composition on post-weld heat treatment cracking in GTA welded cast Inconel 738LC superalloy'. *Materials Science and Technology* **24**(5), 529–539.

STAT-EASE: 2008, 'Design Expert 7.1'.

Steen, W. M.: 2010, *Laser material processing*. Springer.

Stoloff, N. S., C. T. Sims, and W. C. Hagel: 1987, *Superalloys II*. New York: Wiley.

Su, C. Y., C. P. Chou, B. C. Wu, and W. C. Lih: 1997, 'Plasma transferred arc repair welding of the nickel-base superalloy IN-738LC'. *Journal of Materials Engineering and Performance* **6**(5), 619–627.

Suzuki, T., A. Kohyama, T. Hirose, and M. Narui: 1999, 'Evaluation of weld crack susceptibility for neutron irradiated stainless steels'. *Journal of Nuclear Materials* **271**, 179–183.

Thakur, A., N. L. Richards, and M. C. Chaturvedi: 2003, 'On crack-free welding of cast Inconel 738'. *International Journal for the Joining of Materials* **15**(4), 21–25.

Thompson, R. G., J. J. Cassimus, D. E. Mayo, and J. R. Dobbs: 1985, 'The relationship between grain size and microfissuring in alloy 718'. *Welding Journal* **64**(4), S91–S96.

Thompson, R. G., D. E. Mayo, and B. Radhakrishan: 1991, 'Relationship between carbon content, microstructure and intergranular liquation cracking in cast nickel alloy 718'. *Metallurgical transactions. A* **22**(2), 557–567.

Treager, I. E.: 1979, *Aircraft gas turbine engine technology*. New York: McGraw-Hill, 2nd edition.

Vishwakarma, K. R., N. L. Richards, and M. C. Chaturvedi: 2005, 'HAZ microfissuring in EB welded allvac 718 plus™ alloy'. In: *Proceedings of the International Symposium on Superalloys and Various Derivatives*. pp. 637–647.

Wallace, W., R. T. Holt, and T. Terada: 1973, 'The nature of the sulfo-carbides observed in nickel-base superalloys'. *Metallography* **6**(6), 511–526.

Wang, Z., Y. Liu, M. Zhao, and J. Bi: 2001, 'Mechanical properties of L12 structure intermetallics produced from elemental powder mixtures'. *Journal of Materials Science Letters* **20**(2), 171–173.

Watanabe, R. and T. Kuno: 1975, 'Design of nickel-base precipitation hardening superalloys'. *Journal of the Iron and Steel Institute of Japan* **61**(9), 2274–2294.

Webster, P. and P. Withers: 2001, 'Versailles Project on Advanced Polycrystalline materials – Determination of residual stresses by neutron diffraction'. Technical Report ISO/TTA 3:2001, International Organisation for Standardisation.

Withers, P. J. and H. K. D. H. Bhadeshia: 2001, 'Residual stress part 1 - Measurement techniques'. *Materials Science and Technology* **17**(4), 355–365.

Woo, W., Z. Feng, X. L. Wang, and S. A. David: 2011, 'Neutron diffraction measurements of residual stresses in friction stir welding: A review'. *Science and Technology of Welding and Joining* **16**(1), 23–32.

Wurst, J. C. and J. A. Nelson: 1972, 'Lineal intercept technique for measuring grain size in two-phase polycrystalline ceramics'. *Journal of The American Ceramic Society* **55**(2), 109–109.

Young, G., T. Capobianco, M. Penik, B. Morris, and J. McGee: 2008, 'The Mechanism of Ductility Dip Cracking in Nickel-Chromium Alloys: Subsolidus cracking

results from global stresses produced during fusion welding and local . . . '. *Welding journal* **87**(2), 31s–43s.

Zhang, J., T. Murakumo, H. Harada, Y. Koizumi, and T. Kobayashi: 2004, 'Creep deformation mechanisms in some modern single-crystal superalloys'. In: *Superalloys 2004*. pp. 189–195.

Zhang, S., E. Godfrey, B. Abbey, P. Xu, Y. Tomota, D. Liljedahl, O. Zanellato, M. Fitzpatrick, J. Kelleher, and S. Siano: 2009, 'Materials Structure and Strain Analysis Using Time-of-flight Neutron Diffraction'. *Proceedings of the World Congress on Engineering* **2**.

Zhong, M., H. Sun, W. Liu, X. Zhu, and J. He: 2005, 'Boundary liquation and interface cracking characterization in laser deposition of Inconel 738 on directionally solidified Ni-based superalloy'. *Scripta Materialia* **53**(2), 159–164.

Appendix A

Appendix for Chapter 2

Appendix A1 - Interpretation of R-Squared
Appendix A2 - Definitions of Outputs from ANOVA

A.1 Interpretation of R-Squared

The following text is taken from the Design Expert software's help section (STAT-EASE, 2008).

Experimenters frequently ask the question "What is a good R-squared value? How low can it be before the results are not valid?"

First of all, experimenters should be focusing on the adjusted R-squared and predicted R-squared values. The regular R-squared can be artificially inflated by simply continuing to add terms to the model, even if the terms are not statistically significant. The adjusted R-squared basically plateaus when insignificant terms are added to the model, and the predicted R-squared will decrease when there are too many insignificant terms. A rule of thumb is that the adjusted and predicted R-squared values should be within 0.2 of each other.

There is no commonly used "cut-off" value for R-squared. Focus on thinking about the objective of the experiment. If the objective is to create a model that will accurately model a process so that I can determine very precise optimum parameter settings (often this is with response surface or mixture designs), then it is desirable to have a high adjusted and predicted R-squared (preferably .70+). In this case you need more than just to identify significant factors, you need to make sure you are modeling HOW the factors affect the responses and that you are not leaving anything out.

The other objective is one where the primary concern is to simply identify factors and interactions that are affecting the response and generally learn if higher or lower factor levels are better (generally with factorial designs). In this case, you might have the situation where the model is statistically significant and there is no lack of fit, but the R-squared's are low. You can conclude that the significant terms identified are correct and the graphs will show the best directions to follow, but you have not yet found (or controlled) all the sources of variation in the process. There are other things left unidentified which may or may not also give even better results. So, there is no doubt that the factors found are correct and their model is correct. BUT, there is more to be investigated if it is economically beneficial to the company. Do NOT use the model for prediction because it doesn't explain enough of what is going on. A good next step would be to set the known factors at their best settings and then brain-storm about other possible factors and run another DOE.

A.2 ANOVA output definitions

Term	Definition
Model F-value	Test for comparing model variance with residual (error) variance. If the variances are close to the same, the ratio will be close to one and it is less likely that any of the factors have a significant effect on the response. Calculated by Model Mean Square divided by Residual Mean Square.
Model p-value (Prob >F)	Probability of seeing the observed F value if the null hypothesis is true (there is no factor effect). Small probability values call for rejection of the null hypothesis. The probability equals the proportion of the area under the curve of the F-distribution that lies beyond the observed F value. The F distribution itself is determined by the degrees of freedom associated with the variances being compared. (In "plain English", if the Prob>F value is very small (less than 0.05) then the terms in the model have a significant effect on the response.)
Factor p-value (Prob >F)	Probability of seeing the observed F value if the null hypothesis is true (there is no factor effect). Small probability values call for rejection of the null hypothesis. The probability equals the proportion of the area under the curve of the F-distribution that lies beyond the observed F value. The F distribution itself is determined by the degrees of freedom associated with the variances being compared. (In "plain English", if the Prob>F value is very small (less than 0.05) then the individual terms in the model have a significant effect on the response.)
Adequate Precision	This is a signal to noise ratio. It compares the range of the predicted values at the design points to the average prediction error. Ratios greater than 4 indicate adequate model discrimination.
R-Squared	A measure of the amount of variation around the mean explained by the model.
Adj R-Squared	A measure of the amount of variation around the mean explained by the model, adjusted for the number of terms in the model. The adjusted R-squared decreases as the number of terms in the model increases if those additional terms don't add value to the model.
Pred R-Squared	A measure of the amount of variation in new data explained by the model. The predicted R-squared and the adjusted R-squared should be within 0.20 of each other. Otherwise there may be a problem with either the data or the model. Look for outliers, consider transformations, or consider a different order polynomial.

Appendix B

Appendix for Chapter 3

Appendix B1 - Tables of parameters
Appendix B2 - Plots for individual sets of data

B.1 Parameters

Table B.1 – Parameters in set 1

Weld number	Power	Beam diameter	Welding speed	Weld number	Power	Beam diameter	Welding speed
	kW	mm	mm/min		kW	mm	mm/min
1	0.86	0.70	100	29	3.44	1.71	800
2	0.86	0.70	200	30	3.44	1.71	1000
3	0.86	0.70	400	31	3.44	1.71	2000
4	0.86	0.70	600	32	3.44	1.71	4000
5	0.86	0.70	800	33	6.9	1.71	100
6	0.86	0.70	1000	34	6.9	1.71	200
7	0.86	0.70	2000	35	6.9	1.71	400
8	0.86	0.70	4000	36	6.9	1.71	600
9	1.725	0.70	100	37	6.9	1.71	800
10	1.725	0.70	200	38	6.9	1.71	1000
11	1.725	0.70	400	39	6.9	1.71	2000
12	1.725	0.70	600	40	6.9	1.71	4000
13	1.725	0.70	800	41	1.72	1.71	100
14	1.725	0.70	1000	42	1.72	1.71	200
15	1.725	0.70	2000	43	1.72	1.71	400
16	1.725	0.70	4000	44	1.72	1.71	600
17	2.6	0.70	100	45	1.72	1.71	800
18	2.6	0.70	200	46	1.72	1.71	1000
19	2.6	0.70	400	47	1.72	1.71	2000
20	2.6	0.70	600	48	1.72	1.71	4000
21	2.6	0.70	800	49	0.4	0.70	100
22	2.6	0.70	1000	50	0.4	0.70	200
23	2.6	0.70	2000	51	0.4	0.70	400
24	2.6	0.70	4000	52	0.4	0.70	600
25	3.44	0.70	100	53	0.4	0.70	800
26	3.44	1.71	200	54	0.4	0.70	1000
27	3.44	1.71	400	55	0.4	0.70	2000
28	3.44	1.71	600	56	0.4	0.70	4000

Table B.2 – Parameters in set 2

Weld number	Power	Beam diameter	Welding speed	Weld number	Power	Beam diameter	Welding speed
	kW	mm	mm/min		kW	mm	mm/min
1	0.5	2.5	200	26	4	5.0	200
2	0.5	2.5	600	27	4	5.0	600
3	0.5	2.5	1000	28	4	5.0	1000
4	0.5	2.5	2000	29	4	5.0	2000
5	0.5	2.5	4000	30	4	5.0	4000
6	1	2.5	200	31	8	2.5	200
7	1	2.5	600	32	8	2.5	600
8	1	2.5	1000	33	8	2.5	1000
9	1	2.5	2000	34	8	2.5	2000
10	1	2.5	4000	35	8	2.5	4000
11	2	2.5	200	36	8	5.0	200
12	2	2.5	600	37	8	5.0	600
13	2	2.5	1000	38	8	5.0	1000
14	2	2.5	2000	39	8	5.0	2000
15	2	2.5	4000	40	8	5.0	4000
16	4	2.5	200	41	0.5	5.0	200
17	4	2.5	600	42	0.5	5.0	600
18	4	2.5	1000	43	0.5	5.0	1000
19	4	2.5	2000	44	0.5	5.0	2000
20	4	2.5	4000	45	0.5	5.0	4000
21	2	5.0	200	46	1	5.0	200
22	2	5.0	600	47	1	5.0	600
23	2	5.0	1000	48	1	5.0	1000
24	2	5.0	2000	49	1	5.0	2000
25	2	5.0	4000	50	1	5.0	4000

Table B.3 – Parameters in set 3

Weld number	Power	Beam diameter	Welding speed	Weld number	Power	Beam diameter	Welding speed
	kW	mm	mm/min		kW	mm	mm/min
1	0.5	2.5	50	16	0.5	5.0	50
2	0.5	2.5	100	17	0.5	5.0	100
3	0.5	2.5	150	18	0.5	5.0	150
4	0.6	2.5	50	19	0.6	5.0	50
5	0.6	2.5	100	20	0.6	5.0	100
6	0.6	2.5	150	21	0.6	5.0	150
7	0.8	2.5	50	22	0.8	5.0	50
8	0.8	2.5	100	23	0.8	5.0	100
9	0.8	2.5	150	24	0.8	5.0	150
10	1	2.5	50	25	1	5.0	50
11	1	2.5	100	26	1	5.0	100
12	1	2.5	150	27	1	5.0	150
13	1.5	2.5	50	28	1.5	5.0	50
14	1.5	2.5	100	29	1.5	5.0	100
15	1.5	2.5	150	30	1.5	5.0	150

B.2 Individual plot data

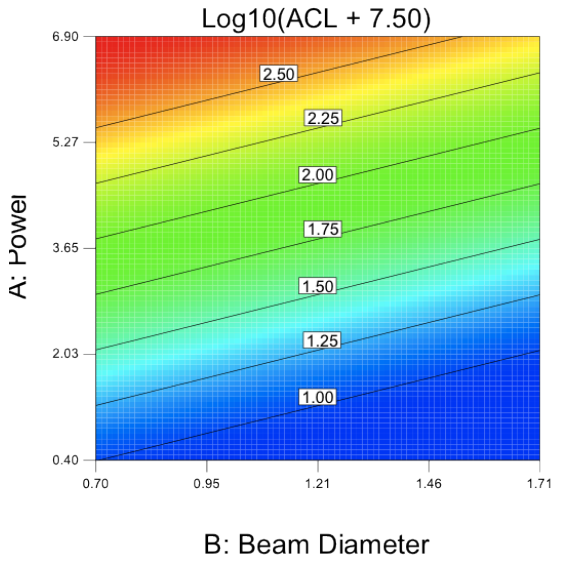

Figure B.1 – Contour plot of ACL data for the as-welded samples vs. beam diameter and power for set 1 data.

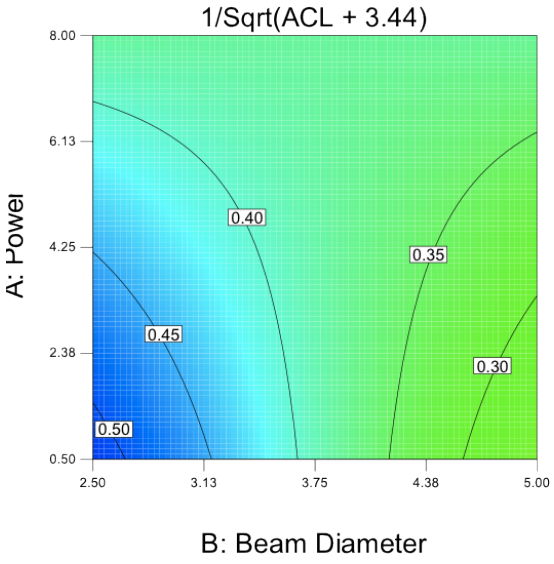

Figure B.2 – Contour plot of ACL data for the as-welded samples versus beam diameter and power for set 2 data.

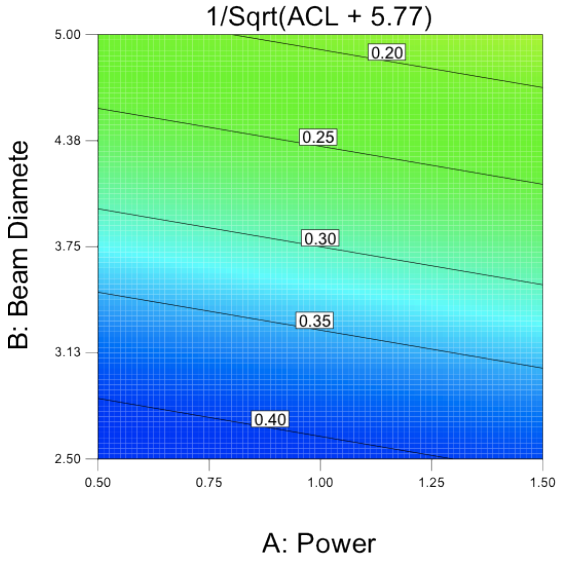

Figure B.3 – Contour plot of ACL data for the as-welded samples versus beam diameter and power for set 3 data.

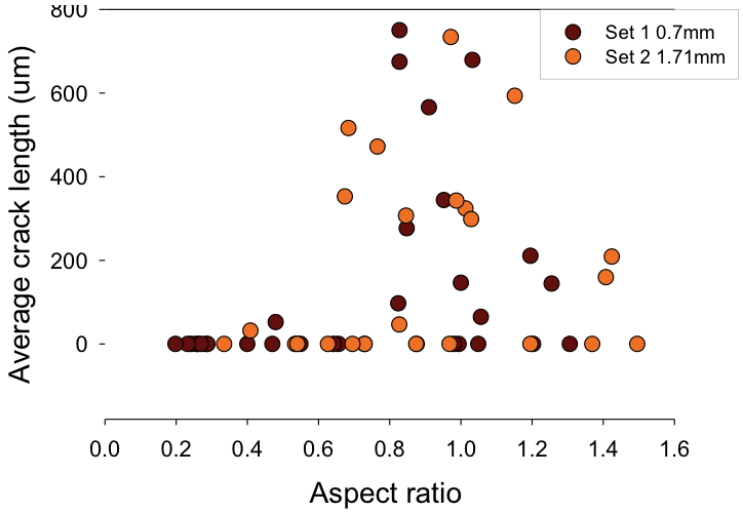

Figure B.4 – Aspect ratio versus ACL scatter plot, set 1, as-welded condition.

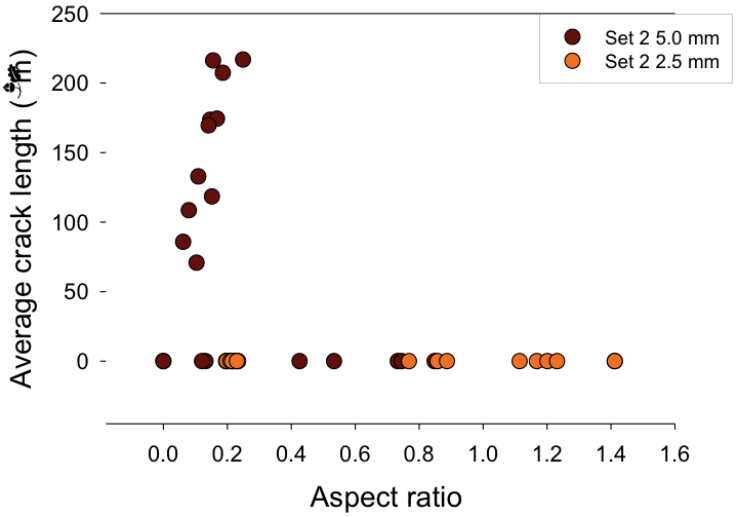

Figure B.5 – Aspect ratio versus ACL scatter plot, set 2, as-welded condition.

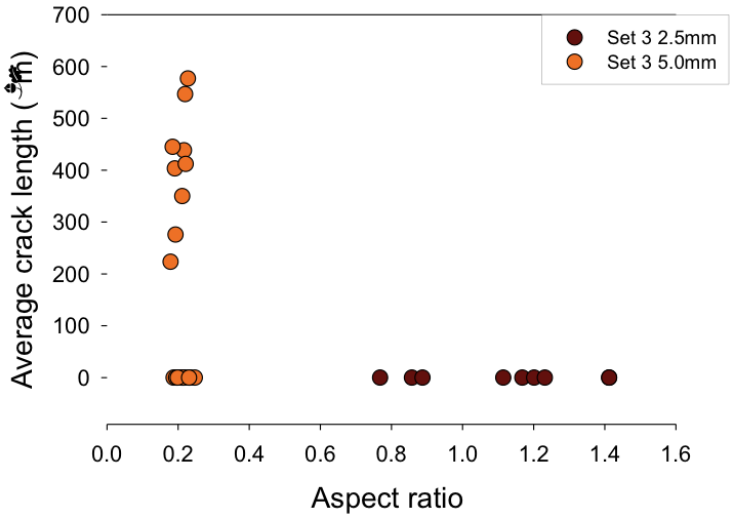

Figure B.6 – Aspect ratio versus ACL scatter plot, set 3, as-welded condition.

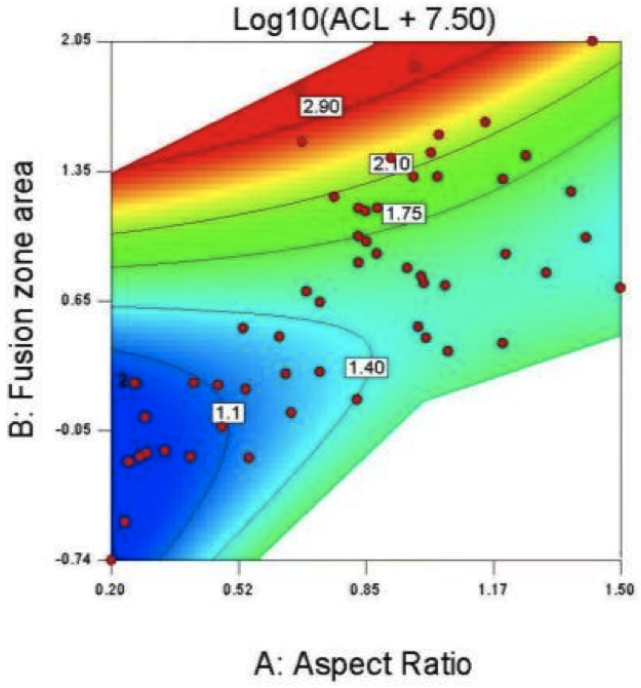

Figure B.7 – Contour plot showing the ACL of the as-welded samples versus the log of fusion zone area and aspect ratio for set 1 data.

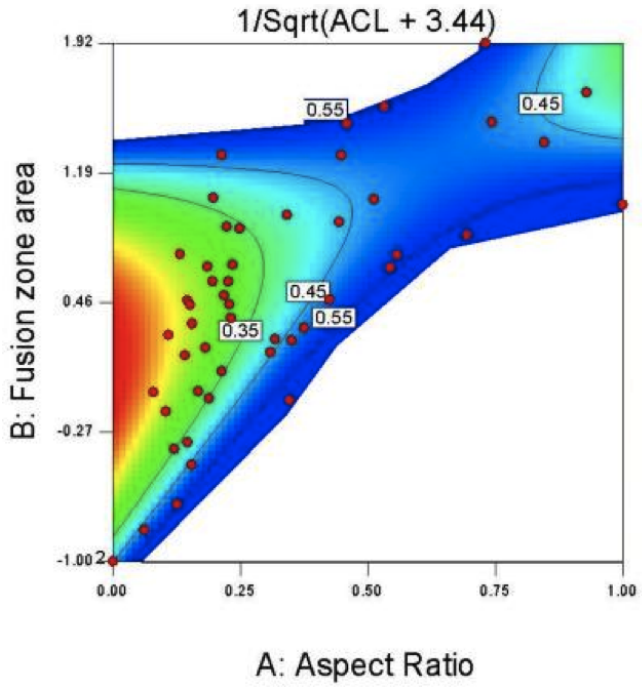

Figure B.8 – Contour plot showing the ACL of the as-welded samples versus the log of fusion zone area and aspect ratio for set 2 data.

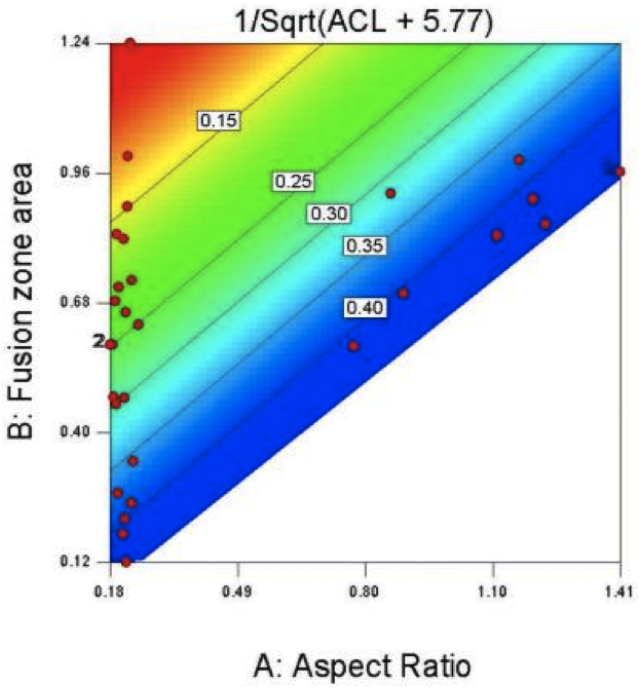

Figure B.9 – Contour plot showing the ACL of the as-welded samples versus the log of fusion zone area and aspect ratio for set 3 data.

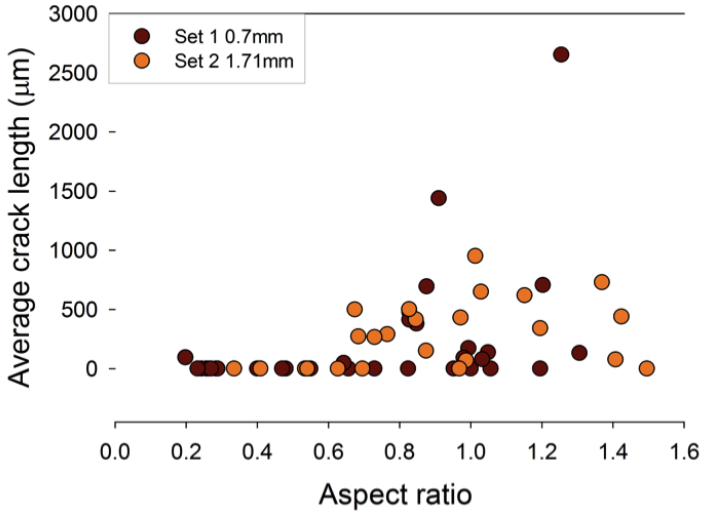

Figure B.10 – Aspect ratio versus ACL scatter plot, set 1, PWHT condition.

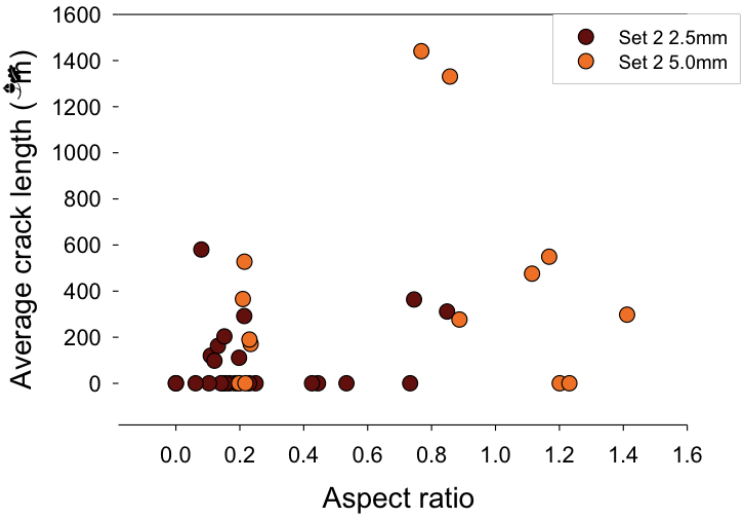

Figure B.11 – Aspect ratio versus ACL scatter plot, set 2, PWHT condition.

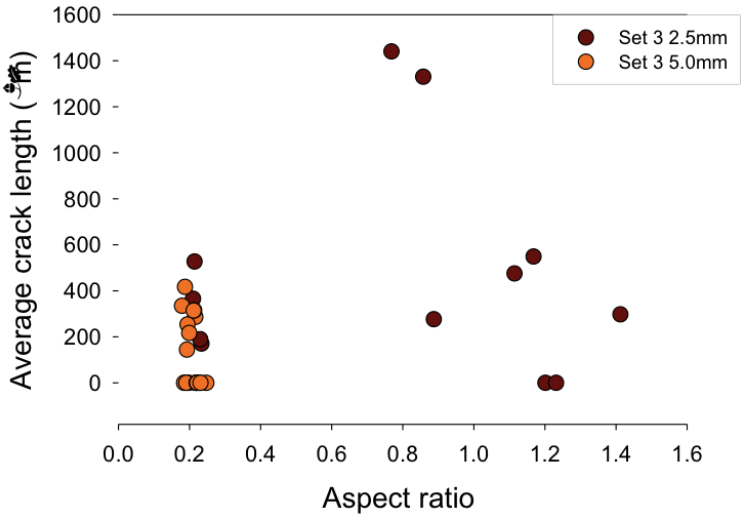

Figure B.12 – Aspect ratio versus ACL scatter plot, set 3, PWHT condition.

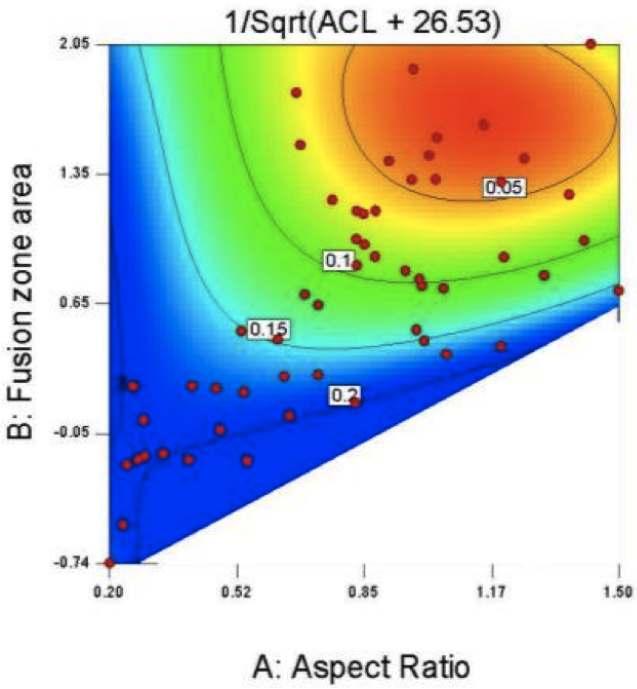

Figure B.13 – Contour plot showing the ACL of the PWHT samples versus the log of fusion zone area and aspect ratio for set 1 data.

Appendix C

Appendix for Chapter 5

Appendix C1 - Lattice parameter
Appendix C2 - Further lattice parameter plots
Appendix C3 - Stress plots

C.1 Lattice parameter

C.1.1 Lattice parameter results

The results from the diffraction plots are first presented as the raw lattice parameter readings. The data is from either the Rietveld (multi-peak) refinement applied to the diffraction profile, or specific crystallographic plane data (e.g. {311} or {200}) depending on the quality of the diffraction profile. In most cases (where available) the data from the single peaks is compared with the Rietveld refinement.

C.1.1.1 Stress-free reference

The plots for stress-free reference were created by interpolating the data according to the readings from the four cubes. The average of bank's 1 and 2 are presented for the {311} and {200} directions for each sample in Figure C.1. The plots for each bank for the Rietveld, {311} and {200} can be found in Appendix C.2.1. The plots for both samples show identical trends, with both overlapping up until about 5 mm from the weld centreline, where the d-spacing for the {200} direction appears to increase significantly. The plots also have error bars which is represented as the uncertainty from the reading.

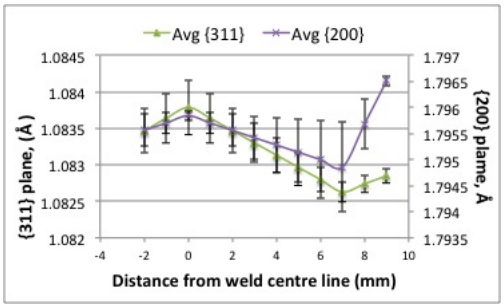

(a)

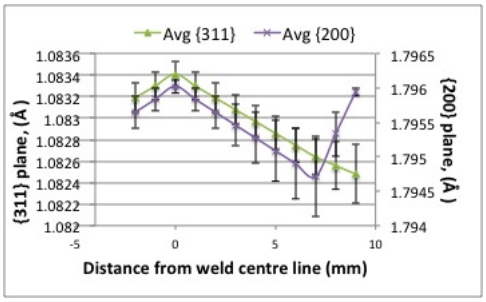

(b)

Figure C.1 – Average of stress-free lattice spacing for {311} and {200}, (a) sample 2 and (b) sample 3.

The data presented above is then converted into lattice parameter using Eq. 5.2 to allow for direct comparison between each Bragg plane data and the Rietveld refinement (again the average of banks 1 and 2) in Figure C.2 for both samples.

The most surprising aspect of these two plots is that there appears to be a different relationship between the Rietveld (multi-peak) curve and the single peak curve for the samples. Sample 2's Rietveld plot is flat until 6 mm from the weld centre, at which point it increases slightly, whereas sample 3's is very similar to the {311} profile. In both cases, the {200} is lower than the {311}.

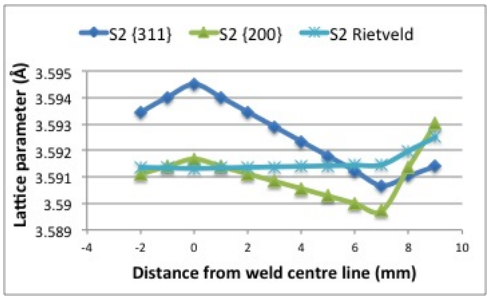

(a)

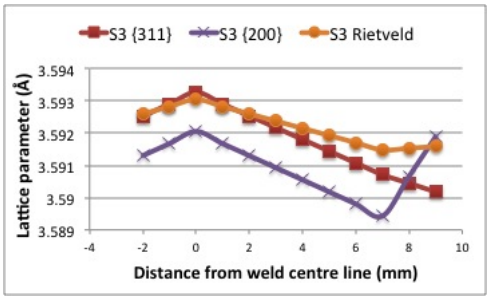

(b)

Figure C.2 – Comparison of the stress-free lattice parameter/d-spacings, for (a) sample 2 and (b) sample 3. The average of banks 1 and 2 for the {311} and {200} planes are both converted to lattice parameter, and compared with the Rietveld refinement.

C.1.1.2 Normal direction

The normal direction (bank 2, which is in reflection) generated good diffraction profiles for nearly all the positions. The Rietveld (multi-peak) refinement and {200} and {311} directions are plotted in Figure C.3 for both sample 2 and 3. Note that the {311} and {200} directions have been converted to lattice parameters by use of Eq. 5.2, and therefore the error bars are not included in these plots. The plots comparing each of these planes to their original state (including error bars) can be found in the Appendix C.2.2.

The plots show that the trends observed across the sample are the same for each peak/multi-peak, but the values of lattice parameter calculated for the {311} and {200} planes appear to be more compressive than the Rietveld data. Appendix C.2.2also contains the plots comparing the profiles for each multi-peak/single peak for each sample.

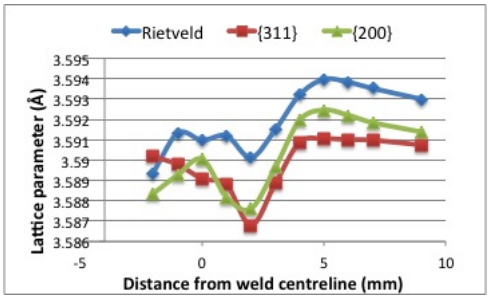

(a)

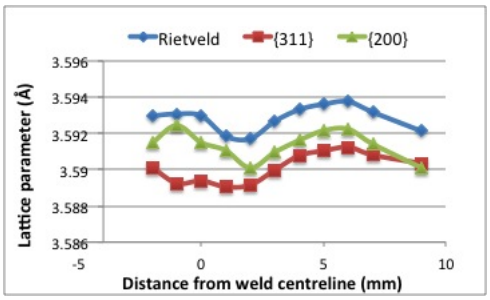

(b)

Figure C.3 – Comparison of the normal direction lattice parameter/d-spacings, for both sample 2 (a) and 3 (b). The Rietveld refinement is compared with the {311} and {200} (both converted to lattice parameter).

C.1.1.3 Transverse direction

The transverse direction was measured using bank 1 (which was in diffraction). Figure C.4 plots for each sample the lattice parameter profiles for the Rietveld, {311} and {200} (both converted using Eq. 5.2 to lattice parameter) peaks. The plots indicate that the Rietveld and {200} overlap and are very similar. Both also suggest that the {311} is generally more compressive (smaller lattice parameter). A full Rietveld refinement of sample 2 across all data points was not possible for the transverse direction. The original unconverted d-spacing plots can be found in Appendix C.2.3, together with plots which illustrate the comparison of both samples for each multi-peak/single peak.

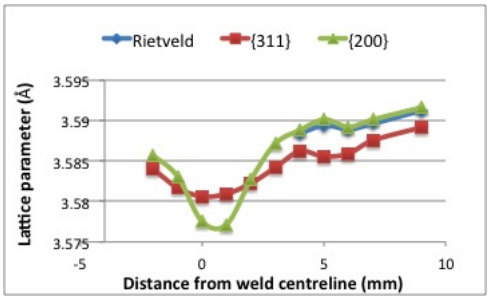

(a)

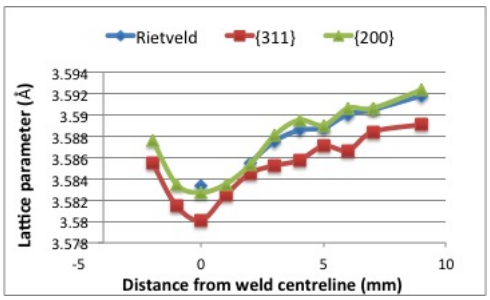

(b)

Figure C.4 – Comparison of the transverse direction lattice parameter/d-spacings, for both sample 2 (a) and 3 (b). The Rietveld refinement is compared with the {311} and {200} (both converted to lattice parameter).

C.1.1.4 Longitudinal direction

The longitudinal direction was measured using bank 1 in a separate run of measurements to the previous two directions. This direction presented the most difficulties in achieving good results. As per the other directions, a comparison of the Rietveld and {200} for each sample is presented in Figure C.5. The {311} data is no longer presented because for most data points the quality of the diffraction profiles was not sufficient to allow a good model to fit the single peak. However, to view any data that was achieved from this peak please see Appendix C.2.4. The plots for both samples in Figure C.5 do not appear to show any clear trend. To view the comparison of the {200} plane for both samples, see the Appendix C.2.4.

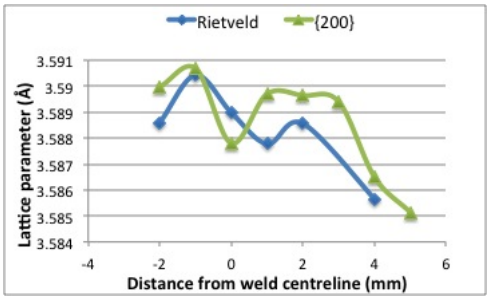

(a)

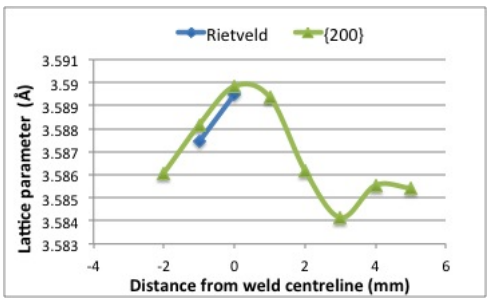

(b)

Figure C.5 – Comparison of the longitudinal direction lattice parameter/d-spacings, for both sample 2 (a) and 3 (b). The Rietveld refinement is compared with the {311} and {200} (both converted to lattice parameter).

In Appendix C.2.4 the comparison of plots of the lattice parameter/d-spacing for each peak and Rietveld refinements, with error bars are listed. The most significant point of these plots is that the error bars in the longitudinal measurements are significantly larger than the other directions.

C.2 Further lattice parameter plots

C.2.1 Stress-free reference lattice parameter/d-spacing v.s. distance

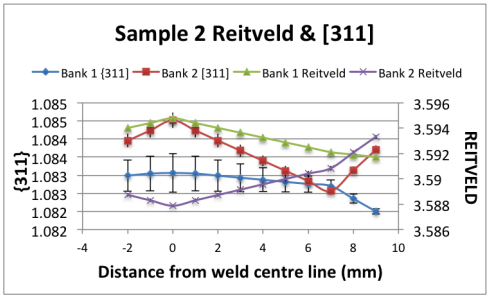

(a)

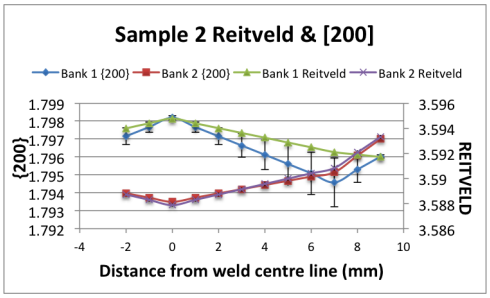

(b)

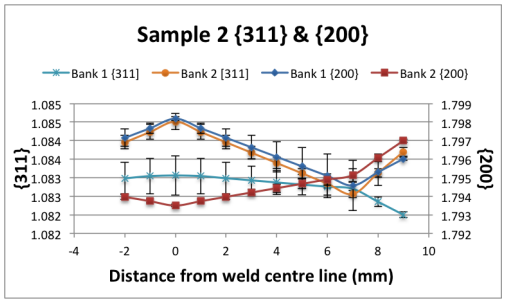

(c)

Figure C.6 – Sample 2 stress-free reference lattice parameter/d-spacing comparison (a) Rietveld and {311} d-spacing, (b) Rietveld and {200} d-spacing, (c) {311} and {200} d-spacings.

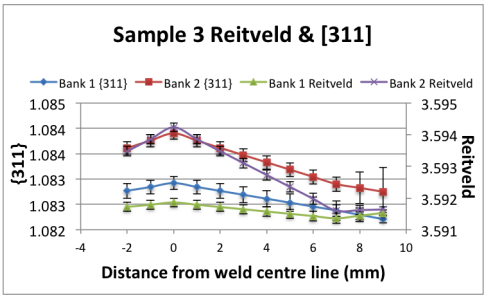

(a)

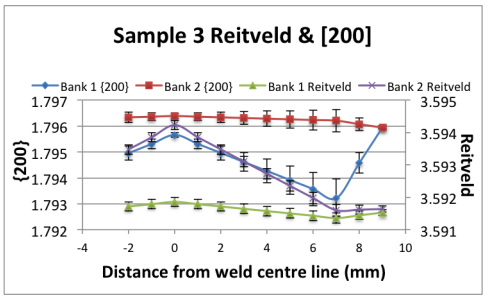

(b)

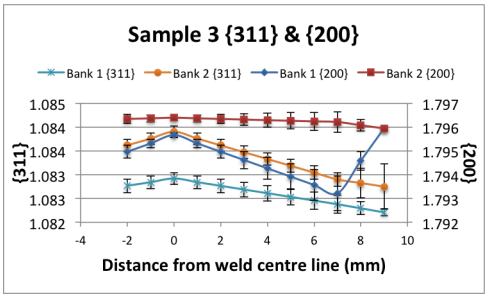

(c)

Figure C.7 – Sample 3 stress-free reference lattice parameter comparison (a) Rietveld and {311} direction, (b) Rietveld and {200} direction, (c) {311} and {200} direction.

C.2.2 Normal direction lattice parameter/d-spacing v.s. distance

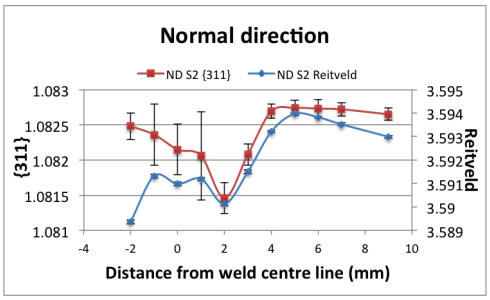

(a)

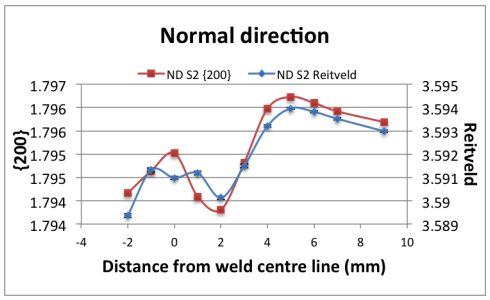

(b)

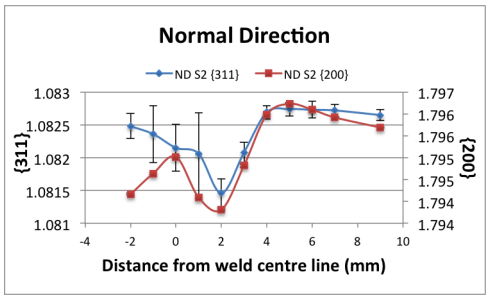

(c)

Figure C.8 – Sample 2 normal direction lattice parameter/d-spacing comparison (a) Rietveld and {311} direction d-spacing, (b) Rietveld and {200} d-spacing, (c) {311} and {200} d-spacings, and (d) Comparison of Rietveld with the {311} and {200} converted to lattice parameter.

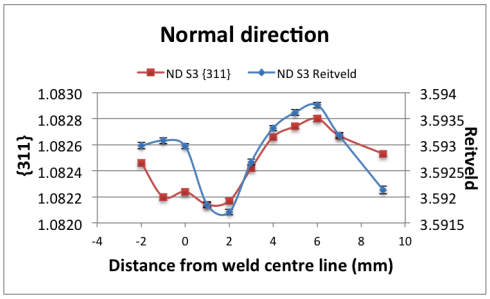

(a)

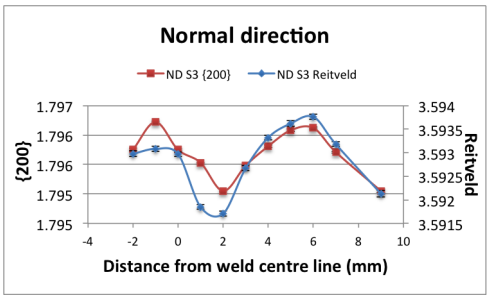

(b)

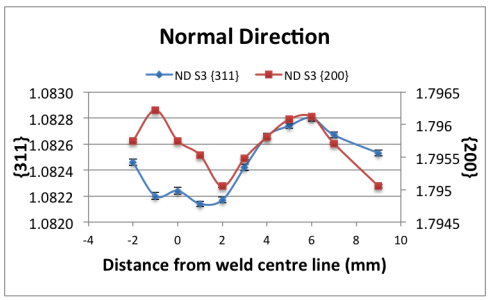

(c)

Figure C.9 – Sample 3 normal direction lattice parameter/d-spacing comparison (a) Rietveld and {311} direction d-spacing, (b) Rietveld and {200} d-spacing, (c) {311} and {200} d-spacings, and (d) Comparison of Rietveld with the {311} and {200} converted to lattice parameter.

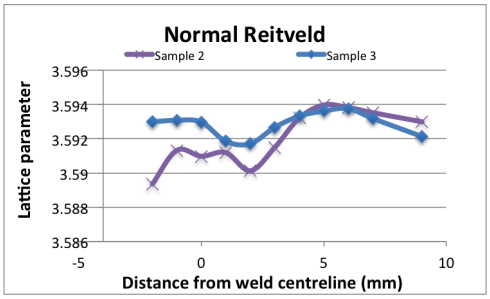

(a)

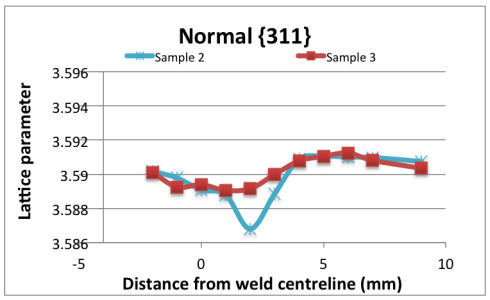

(b)

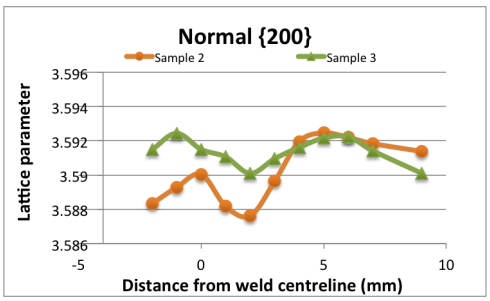

(c)

Figure C.10 – Comparison of both samples' normal direction lattice parameter for (a) Rietveld refinement, (b) {311} and (c) {200} (both these are converted to lattice parameter).

C.2.3 Transverse direction lattice parameter/d-spacing v.s. distance

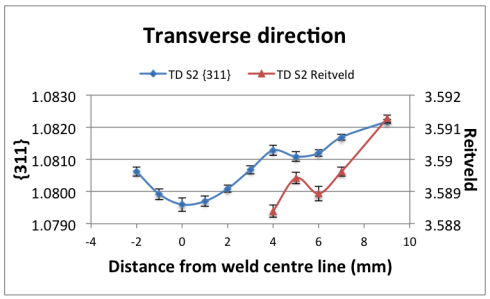

(a)

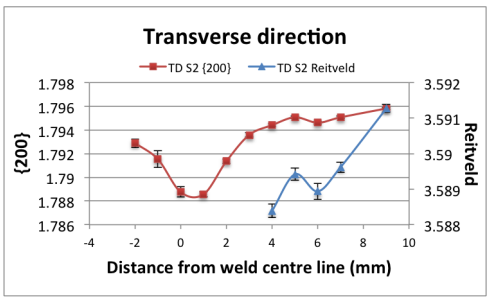

(b)

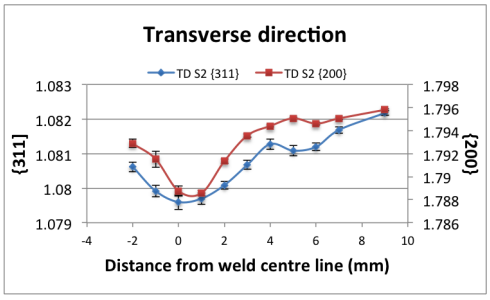

(c)

Figure C.11 – Sample 2 transverse direction lattice parameter/d-spacing comparison (a) Rietveld and {311} direction d-spacing, (b) Rietveld and {200} d-spacing, (c) {311} and {200} d-spacings.

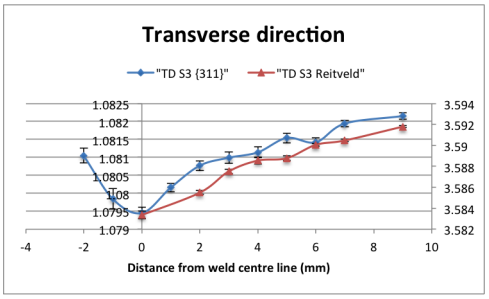

(a)

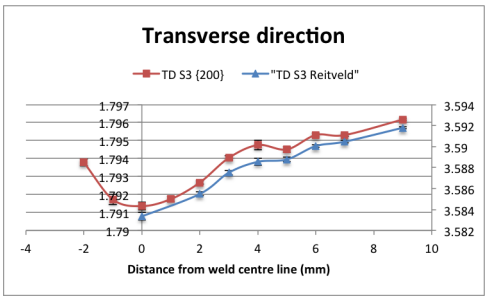

(b)

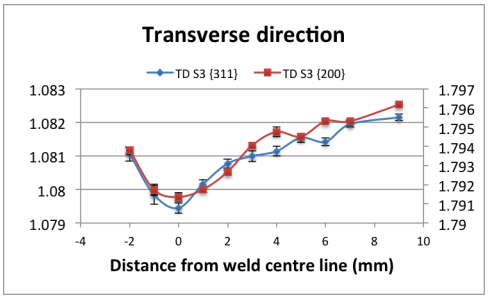

(c)

Figure C.12 – Sample 3 transverse direction lattice parameter/d-spacing comparison (a) Rietveld and {311} direction d-spacing, (b) Rietveld and {200} d-spacing, (c) {311} and {200} d-spacings.

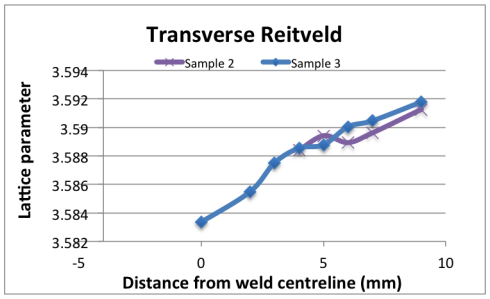

(a)

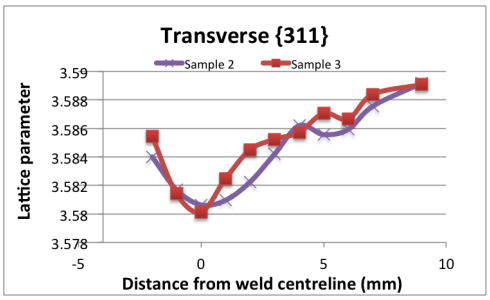

(b)

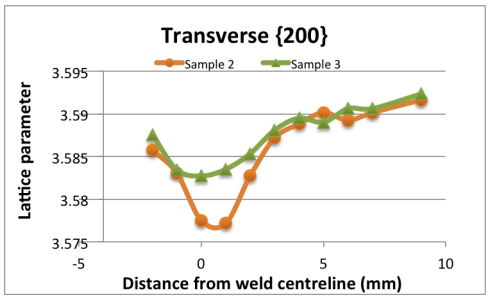

(c)

Figure C.13 – Comparison of both samples' transverse direction lattice parameter for (a) Rietveld refinement, (b) {311} and (c) {200} (both these are converted to lattice parameter).

C.2.4 Longitudinal direction lattice parameter/d-spacing v.s. distance

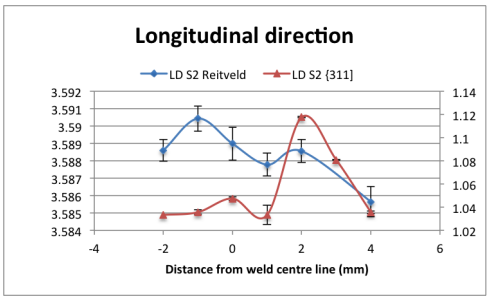

(a)

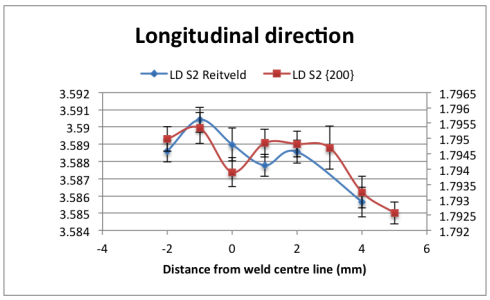

(b)

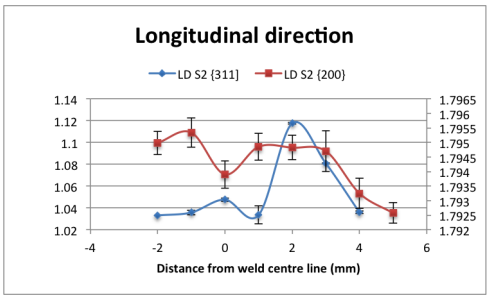

(c)

Figure C.14 – Sample 2 longitudinal direction lattice parameter/d-spacing comparison (a) Rietveld and {311} direction d-spacing, (b) Rietveld and {200} d-spacing, (c) {311} and {200} d-spacings.

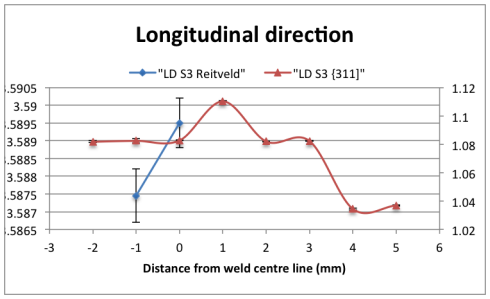

(a)

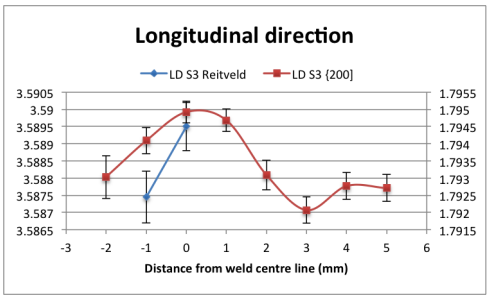

(b)

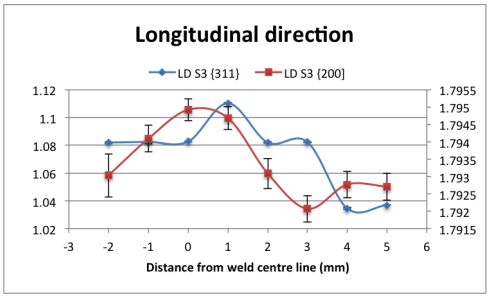

(c)

Figure C.15 – Sample 3 longitudinal direction lattice parameter/d-spacing comparison (a) Rietveld and {311} direction d-spacing, (b) Rietveld and {200} d-spacing, (c) {311} and {200} d-spacings.

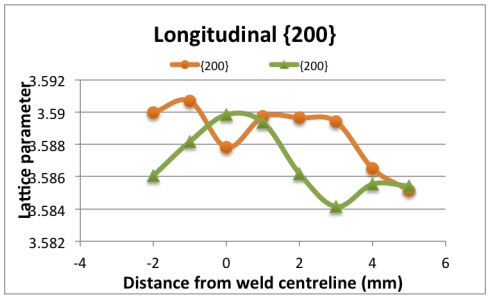

Figure C.16 – Comparison of both samples' normal direction lattice parameter for the {200} single peak (these are converted to lattice parameter).

C.3 Stress plots

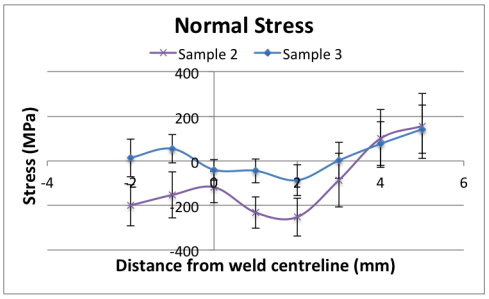

Figure C.17 – Normal direction stress comparison

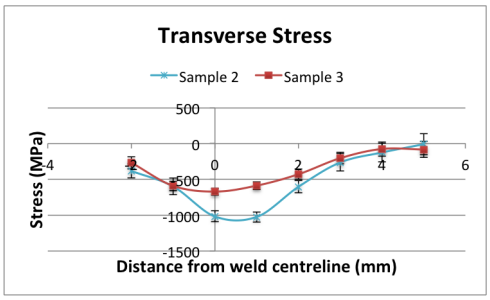

Figure C.18 – Transverse direction stress comparison

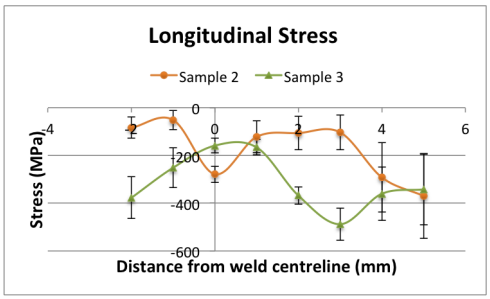

Figure C.19 – Longitudinal direction stress comparison

Appendix D

Appendix for Chapter 6

Appendix D1 - Details of results from initial trials
Appendix D2 - Images of all final trial samples

D.1 Details of results from initial trials

Table D.1 – Details of results from initial trials.

Sample	Power (kW)	Welding speed (mm/min)	No of passes	Condition	Oxidation	Defects
1	0.5	150	6	As welded	Yes	Weld & base metal porosity
2	1	600	6	As welded	No	Solidification cracks & base metal porosity
3	0.5	300	6	As welded	Yes	Weld & base metal porosity, Liquation cracks
4	0.5	600	6	As welded	No	Weld & base metal porosity
5	0.5	200	6	As welded	Yes	Minor amount of base metal porosity
6	1	200	6	As welded	Yes	Weld & base metal porosity
7	0.5	150	6	As welded	Yes	Weld & base metal porosity
8	0.5	50	5	As welded	Yes	Solidification crack
9	1	600	6	As welded	Yes	Weld & base metal porosity
10	0.5	150	6	HIP	Yes	None
11	0.5	150	6	HIP	Yes	Liquation cracks
12	0.5	200	6	HIP	Yes	Weld & base metal porosity
13	0.5	100	6	HIP	Yes	Weld & base metal porosity, Solidification crack
14	0.5	150	6	HIP	Yes	Weld & base metal porosity
15	0.5	1000	6	HIP	No	Solidification crack
16*	1	1000	6	As welded	No	Weld & base metal porosity
17*	0.5	150	7	As welded	Yes	Weld & base metal porosity
18	0.5	2000	6	As welded	No	Base metal porosity

*Sample 17 are parameters applied to repair sample 16, as was discussed in Chapter 6. This was the same piece of material.

D.2 Images of all final trial samples

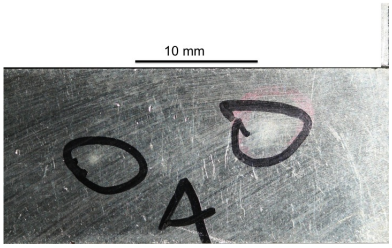

(a)

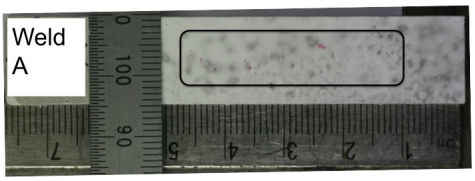

(b)

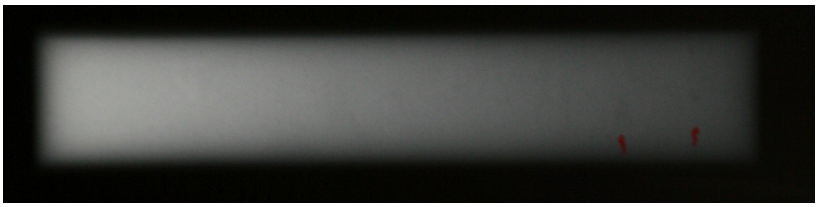

(c)

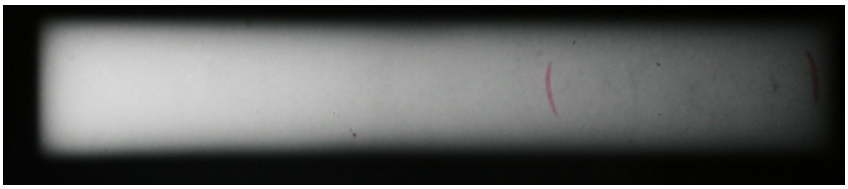

(d)

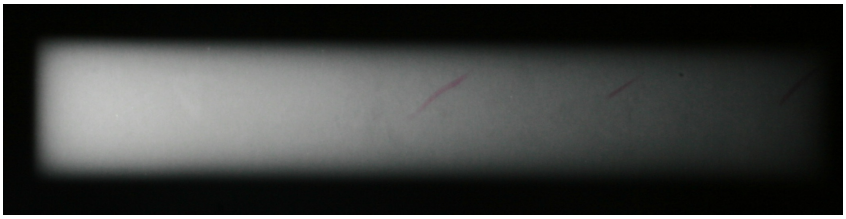

(e)

Figure D.1 – Sample A - (a) Area of surface defects pre-weld (b) surface of post-weld surface with dye penetrant (c) X-Ray pre-weld (d) X-Ray post-weld and (e) X-Ray post HIP

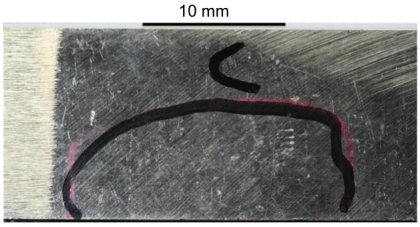

(a)

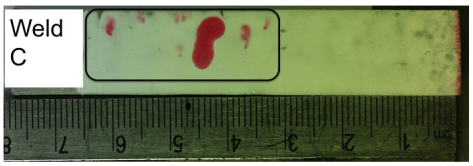

(b)

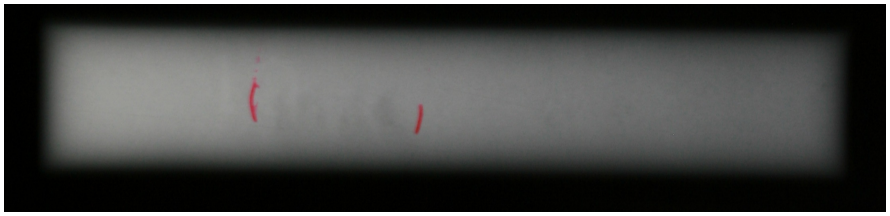

(c)

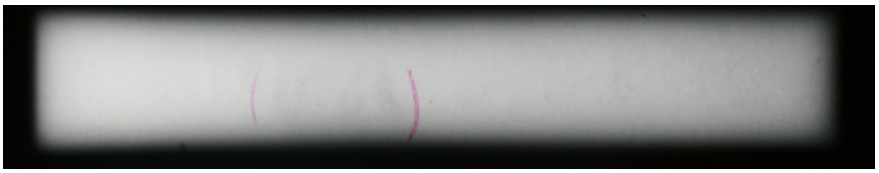

(d)

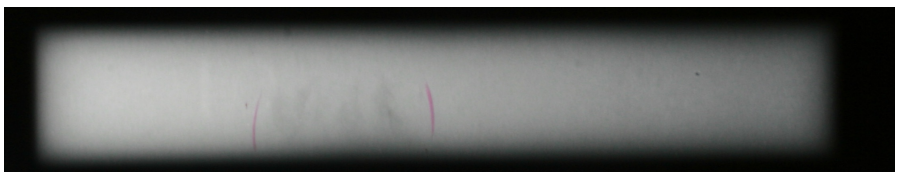

(e)

Figure D.2 – Sample C - (a) Area of surface defects pre-weld (b) surface of post-weld surface with dye penetrant (c) X-Ray pre-weld (d) X-Ray post-weld and (e) X-Ray post HIP

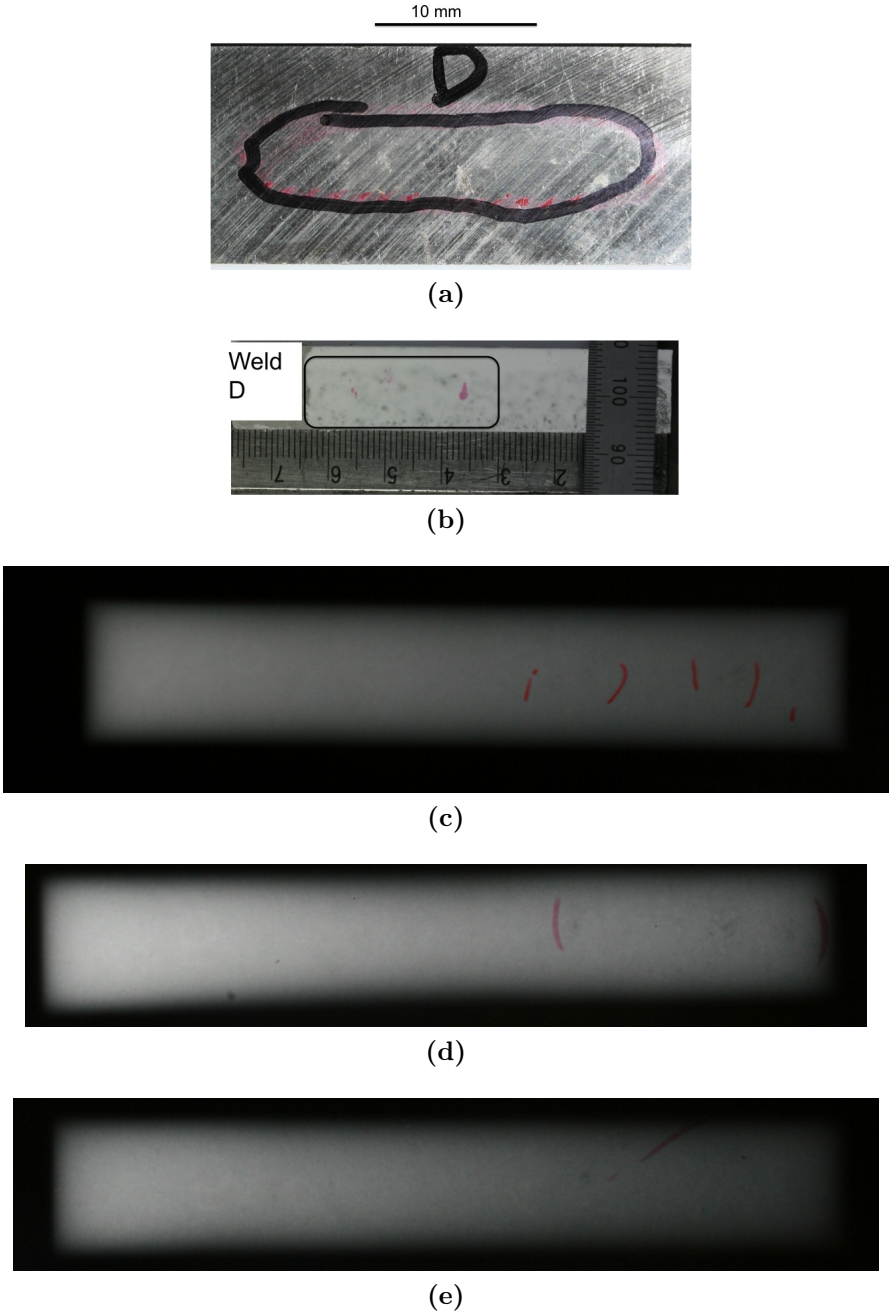

(a)

(b)

(c)

(d)

(e)

Figure D.3 – Sample D - (a) Area of surface defects pre-weld (b) surface of post-weld surface with dye penetrant (c) X-Ray pre-weld (d) X-Ray post-weld and (e) X-Ray post HIP

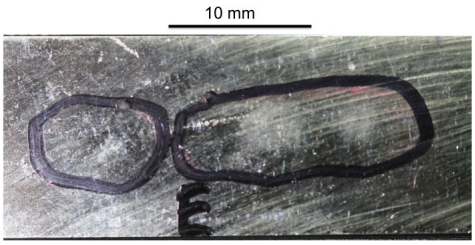

(a)

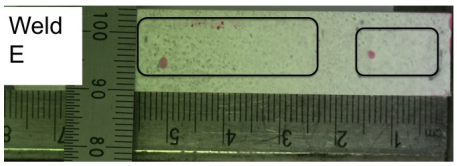

(b)

(c)

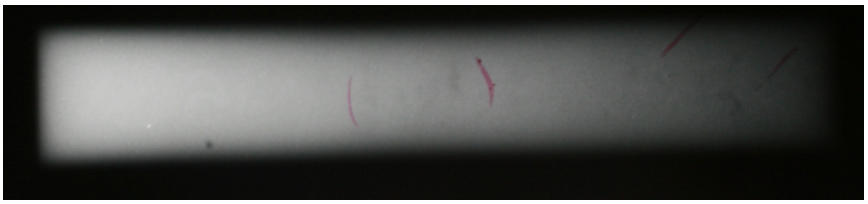

(d)

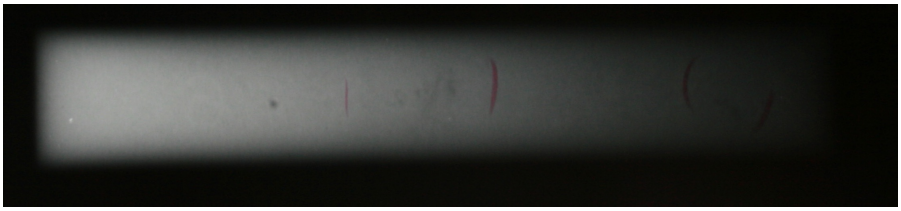

(e)

Figure D.4 – Sample E - (a) Area of surface defects pre-weld (b) surface of post-weld surface with dye penetrant (c) X-Ray pre-weld (d) X-Ray post-weld and (e) X-Ray post HIP

(a)

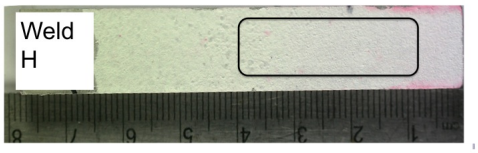

(b)

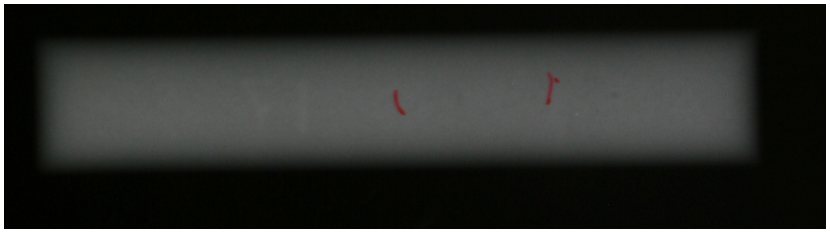

(c)

(d)

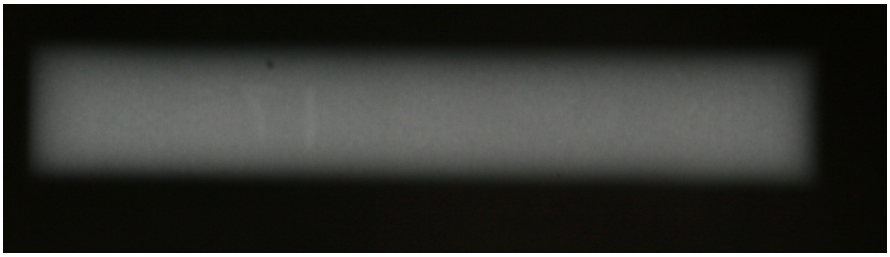

(e)

Figure D.5 – Sample H - (a) Area of surface defects pre-weld (b) surface of post-weld surface with dye penetrant (c) X-Ray pre-weld (d) X-Ray post-weld and (e) X-Ray post HIP

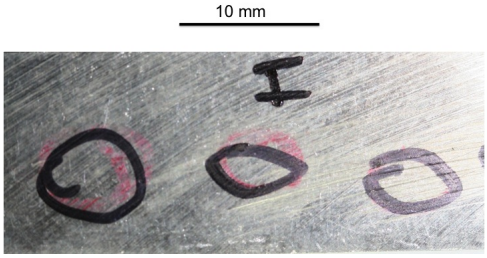

(a)

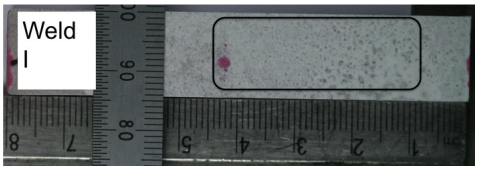

(b)

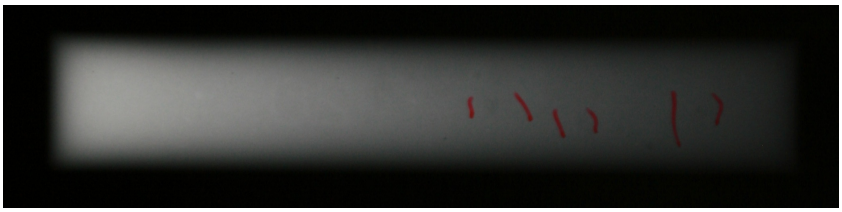

(c)

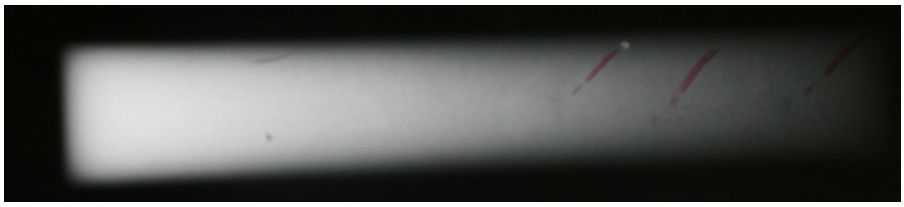

(d)

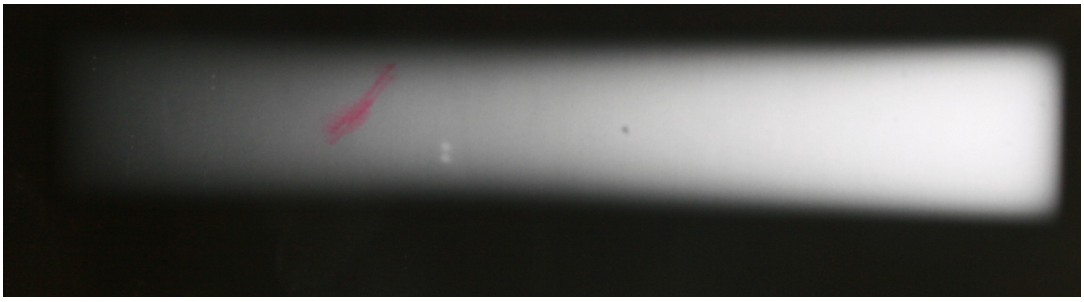

(e)

Figure D.6 – Sample I - (a) Area of surface defects pre-weld (b) surface of post-weld surface with dye penetrant (c) X-Ray pre-weld (d) X-Ray post-weld and (e) X-Ray post HIP

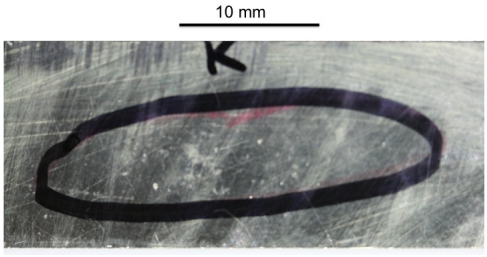

(a)

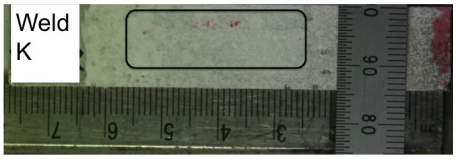

(b)

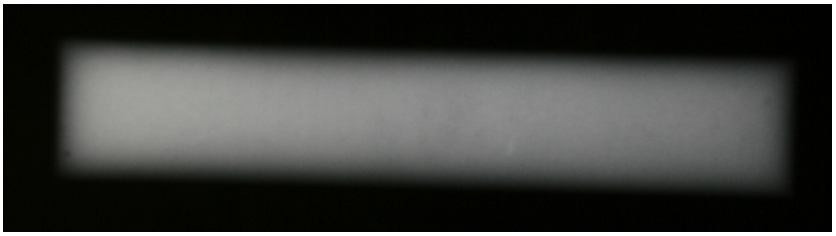

(c)

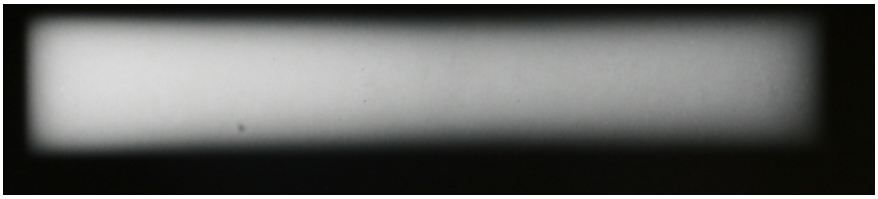

(d)

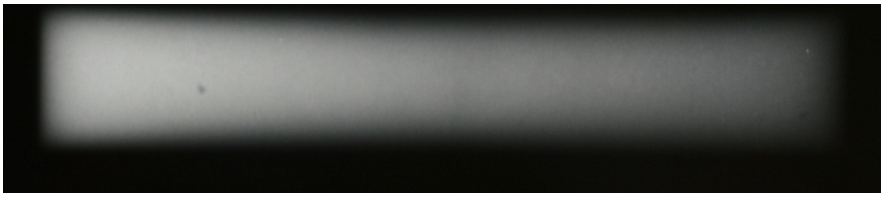

(e)

Figure D.7 – Sample K - (a) Area of surface defects pre-weld (b) surface of post-weld surface with dye penetrant (c) X-Ray pre-weld (d) X-Ray post-weld and (e) X-Ray post HIP

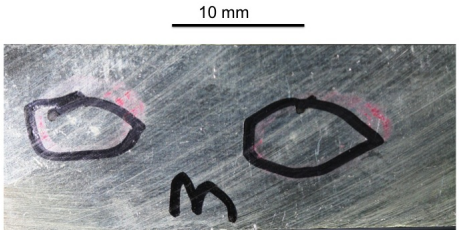

(a)

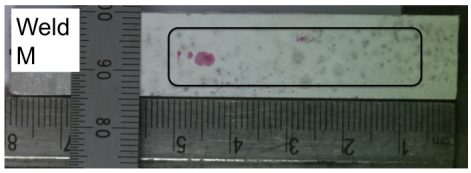

(b)

(c)

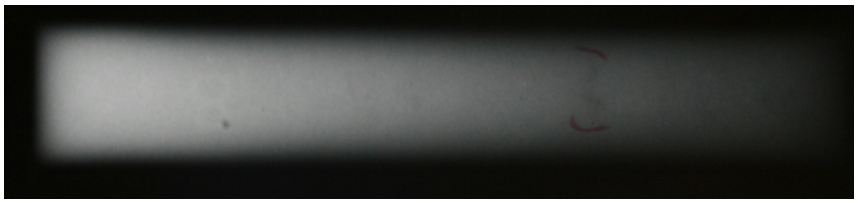

(d)

(e)

Figure D.8 – Sample M - (a) Area of surface defects pre-weld (b) surface of post-weld surface with dye penetrant (c) X-Ray pre-weld (d) X-Ray post-weld and (e) X-Ray post HIP

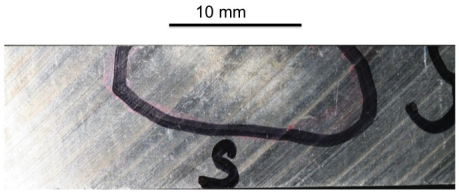

(a)

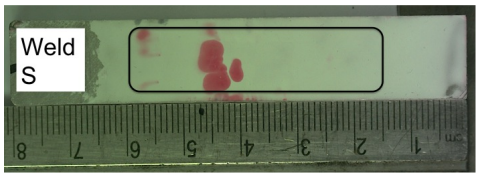

(b)

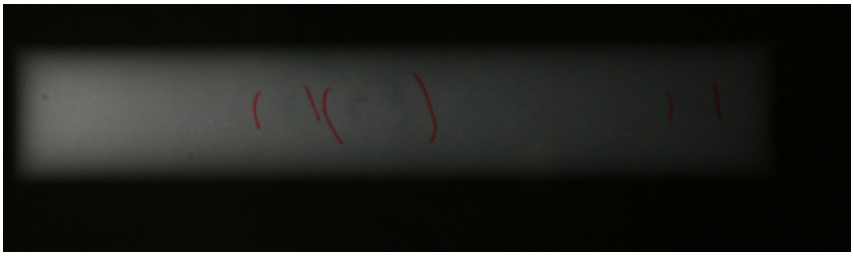

(c)

(d)

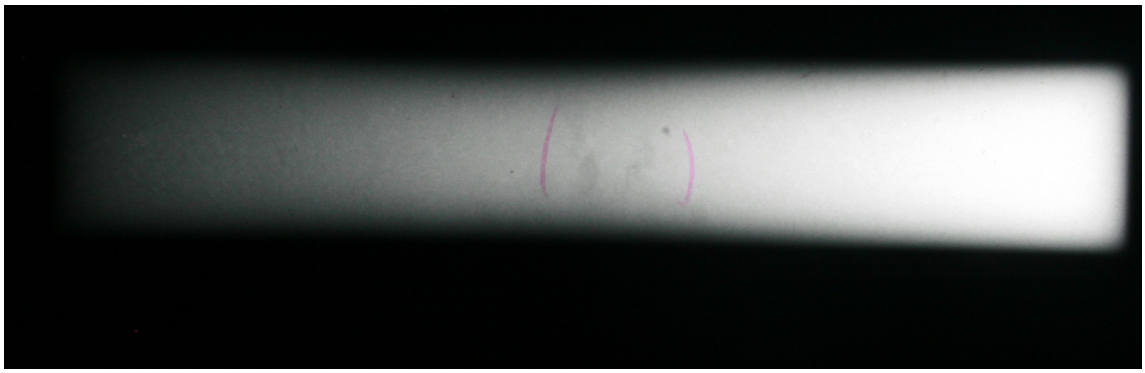

(e)

Figure D.9 – Sample S - (a) Area of surface defects pre-weld (b) surface of post-weld surface with dye penetrant (c) X-Ray pre-weld (d) X-Ray post-weld and (e) X-Ray post HIP